

CHARACTERISING THE CARDIAC EFFECTS OF DYSREGULATED PROPIONATE METABOLISM USING A MOUSE MODEL OF PROPIONIC ACIDAEMIA

Kyung Chan Park

A THESIS SUBMITTED FOR THE DEGREE OF DOCTOR OF PHILOSOPHY

HILARY TERM 2021

THE QUEEN'S COLLEGE

UNIVERSITY OF OXFORD

Mum

Dad

Haena

Haemi

Christopher

Wang-Jae

Kayne

Kyle

Clarise

Annalyn

Ben

Abstract

Propionate is a naturally-occurring monocarboxylate short-chain fatty acid in humans derived from the mitochondrial metabolism of multiple substrates. There is evidence for dysregulated propionate metabolism (and hence its accumulation), in common metabolic disorders, such as diabetes and obesity. However, the most extreme accumulation of propionate occurs in the inherited metabolic disease, propionic acidaemia (PA). Despite its rarity, PA is one of the commonest organic acidaemias. PA results from a defect in mitochondrial propionyl-CoA carboxylase, the rate-limiting step to propionate metabolism (as propionyl-CoA), resulting in the accumulation of propionate, and other related metabolites such as propionyl-carnitine and 2-methylcitrate. Interestingly, diastolic dysfunction, cardiomyopathy and arrhythmias account for significant morbidity and mortality in PA patients. However, the underlying mechanisms are yet to be fully elucidated.

The aim of this thesis was to characterise the effects of dysregulated propionate metabolism on the heart. This was primarily addressed by using a mouse model of PA (*Pcca*$^{-/-}$ A138T), in which the levels of propionate generated *in vivo* are sufficient to produce a metabolic signature of the human disease, but allows the animal to reach adulthood, thereby facilitating the study of cardiac physiology *in vivo* and in isolated cells. However, there is little information available on how (or whether) the heart is affected in these animals.

Several readouts were used to characterise the cardiac function in PA animals, at the whole-organ level (metabolomics, ECG, cine-MRI), and the cellular level (Ca^{2+} signalling). These investigations revealed a metabolic signature of PA in the heart, early signs of contractile dysfunction *in vivo*, and dysregulated cardiomyocyte Ca^{2+} handling. Due to previous evidence for propionate acting as a histone deacetylase (HDAC) inhibitor, as well as it being a substrate for histone propionylation, whole-exome sequencing was performed in PA hearts to characterise changes in gene expression. The majority of differentially expressed genes that were sensitive to propionate could be explained by the canonical mechanism of HDAC inhibition. The most significant gene was upregulation of *Pde9a*, a well-recognised driver of diastolic dysfunction via reduced cGMP-PKG signalling, which can explain the cardiac phenotype. Importantly, *Pde9a* is a potentially important therapeutic target in PA that warrants further investigation.

Published Works During DPhil

Manuscripts

- Chung YJ, **Park KC**, Tokar S, Eykyn TR, Fuller W, Pavlovic D, Swietach P, Shattock MJ. SGLT2 inhibitors and the cardiac Na^+/H^+ exchanger-1: the plot thickens. *Cardiovasc Res* 2021;cvab184.
- Zervou S, McAndrew DJ, Whittington HJ, Lake HA, **Park KC**, Cha KM, Ostrowski PJ, Eykyn TR, Schneider JE, Neubauer S, Lygate CA. Subtle role for adenylate kinase 1 in maintaining normal basal contractile function and metabolism in the murine heart. *Front Physiol* 2021; 12:623969.
- **Park KC**, Krywawych S, Richard E, Desviat L, Swietach P. Cardiac complications in propionic and other organic acidemias. Corresponding author. *Front Cardiovasc Med* 2020;22(7):617451.
- **Park KC**, Donovan K, Mckechnie S, Ramamurthy N, Klenerman P, Swietach P. Single-cell oxygen saturation imaging shows that gas exchange by red blood cells is not impaired in COVID-19 patients. *Br J Haem* 2020;190:e229-e232.
- Chung YJ, **Park KC**, Tokar S, Eykyn TR, Fuller W, Pavlovic D, Swietach P, Shattock MJ. Off-target effects of SGLT2 blockers: empagliflozin does not inhibit Na+/H+ exchanger-1 or lower $[Na^+]_i$ in the heart. *Cardiovasc Res* 2020:cvaa323.
- Chung YJ, Luo A, **Park KC**, Loonat AA, Lakhal-Littleton S, Robbins PA, Swietach P. Iron-deficiency anemia reduces cardiac contraction by downregulating RyR2 channels and suppressing SERCA pump activity. *JCI Insight* 2019;4(7):e125618.
- Michl J, **Park KC**, Swietach P. Evidence-based guidelines for controlling pH in mammalian live-cell culture systems. *Commun Biol* 2019;2:144.

Abstracts

- **Park KC**, Ford K, Hulikova A, Smart N, Swietach P. Propionate anions produce acute and sustained remodelling of Ca^{2+} transients in rat ventricular myocytes. *J Inherit Metab Dis* 2018;41:S50.
- **Park KC**, Roseman G, Chung YJ, Ford KL, Hulikova A, Swietach P. Propionate anions accumulated in propionic acidaemia influences the cardiac gene expression landscape. *Heart* 2018;104:A4-A5.

Acknowledgements

This DPhil has been a remarkable journey. Not only did I develop as a scientist, but I grew substantially as a person. I would not have reached this point without the many wonderful people along the way – family, friends and mentors – who supported me, and all played a role in my personal and professional development. To that end, I have many people I would like to acknowledge, but I would like to first recognise the animals that were sacrificed in order to carry out the work in this thesis. I would also like to thank the British Heart Foundation and its patrons, for funding my Studentship and the research presented in this thesis.

I would like to express my sincere gratitude to my primary supervisor, Prof. Pawel Swietach. *Pawel*, thank you for your knowledge, guidance, and patience throughout my doctorate. I developed tremendously as a scientist in your lab, and I will always remember your mentorship during any success that I may have in the future. I also extend this gratitude to my co-supervisor, Assoc. Prof. Nicola Smart. *Nicola*, thank you for your valuable mentorship, expertise in molecular biology and for your unwavering belief in me. You helped me get back on track when I felt discouraged and lost. I would like to thank our Doctoral Training Programme Director, Prof. David Greaves, as well as our Programme's Co-Directors, Profs. Kim Dora and Nicola Smart, for their continued support and providing me a positive graduate student experience. I would also like to thank Dr Steve Krywawych from Great Ormond Street Hospital for clinical advice and expertise on propionic acidaemia throughout the project. Finally, I gratefully acknowledge Maria Ward for supporting me during my doctorate.

My training as a scientist ultimately began during my undergraduate degree at King's College London. I would like to thank mentors from the earlier stages of my career: Dr Sarah Salvage, Dr Richard Siow, Dr Michael Curtis and Prof. Michael Marber. In particular, I would like to thank Prof. Michael Shattock from KCL, who's laboratory I first trained in, continues to mentor me today, and without whom I would not have made it to Oxford.

I was fortunate to have been surrounded by truly fantastic people on a daily basis in the Swietach Group. I learnt so much from all of you and forever grateful for your support. My biggest appreciation goes to my day-to-day supervisor, Dr Alzbeta Hulikova. *Betka*, I'm truly grateful. Thank you for training me and for your extraordinary patience, especially during my early days. I really admire your approach as a scientist and I hope to know as much as you one day. *Yujin*, thank you for helping me find my feet and get started on my project. *Kate*, thank you for

training me in all things mouse physiology. *Andreas*, you are science's true handyman. Thank you for teaching me how to fix essentially any item. *Johanna*, thank you for teaching me the importance of work-life balance. I would have burnt out otherwise. *Mark*, thank you for imparting me your expertise in cardiomyocyte physiology and everything there is to know about isolations, as well as for schooling me on life in and out the lab. I'd also like to acknowledge the fellow students in the lab. *Mala*, thanks for welcoming into Oxford. *Wiktoria*, you were a great desk-buddy and I enjoyed our coffee runs.

Finally, from the lab, I would like to specially acknowledge the valuable friendships of Drs Aminah Loonat and Stefania Monterisi. *Aminah*, thank you for your endless knowledge in protein biochemistry and for helping me find the 'mers of phospholamban. I promise we will eventually make it to Gail's. *Stefania*, during these past 4 years, we have somehow managed to communicate using only two words from the Italian dictionary: 'si' and 'prego'. As well as your expertise in molecular biology, thank you for your overwhelming kindness. You were always there for me and I'll never forget that.

My time at Oxford would not have been so enjoyable without the support of my amazing friends. I want to first acknowledgement my course-mates, Drs Abigail Wilson and Lisa Simpson. *Abbie & Lisa*, this DPhil would have been a very different experience if it were not for the both of you. I cannot express how grateful I am for our comradery through thick and thin. Thank you both for your shared knowledge, the laughter, and for helping me stay positive. I would also like to extend that gratitude to my wonderful friends from College: Anna, Caroline, Eri, James, Maarten, Sam, Sofia and Vangelis. I'm grateful for all the good times and I'll fondly look back on our trips to the Rusty Bicycle. Lastly, I want to mention my lovely group of friends from as far back as Hinchley Wood School. Thank you all for your continued friendship over the past ~15 years, for your belief in me, and for helping me smile when times were difficult.

Last but not least, I would like to give my heartfelt thanks to all my family, for their continuous support and encouragement: my parents, sisters, brothers-in-law, and my lovely nephews and nieces. I am truly blessed, and your unconditional love and belief in me underlie my achievements. I dedicate this thesis to all of you. My greatest appreciation though, is for my mum and my sisters. I am truly sad for the difficult times experienced in our earlier lives and for all the sacrifices you had to make. However, the path I am on now, was from a culmination of our earlier experiences. My hope, is that this thesis shows you that some good has come from them. Thank you, with all my heart.

Statement of authorship

All the work presented in this thesis was by the Author, Kyung Chan Park, with some exceptions. Whilst experimental planning, sample preparation, data analysis, and interpretation of data were conducted by the Author:

- The mouse model was generated by Dr Michael Barry (Mayo Clinic, US). A Material Transfer Authority was successfully obtained. To establish the colony in Oxford, heterozygous mice were provided by Dr Lourdes Desviat (Centro de Biología Molecular Severo Ochoa, Spain);
- Original ImageJ and MATLAB macros were written by Prof. Pawel Swietach;
- *Chapter 3*: IC-MS was conducted on a collaborative basis by Dr David Hauton (Department of Chemistry, University of Oxford), at the metabolomics facility of Prof. James McCullagh. The acyl-carnitines LC-MS/MS was performed on a collaborative basis by Dr Steve Krywawych (Great Ormond Street Hospital, London);
- *Chapter 5*: RNA extraction for sequencing was performed by Dr Kerrie Ford for the *in vitro* cardiomyocyte experiment, whilst RNA extraction for the *in vivo* heart tissue experiment was performed by the Author. In both cases, library preparation and next-generation sequencing was performed by the Oxford Genomics Centre (University of Oxford), as a paid service, and bioinformatic analysis was performed by Prof. Pawel Swietach.

Finally, throughout this thesis, particularly in Chapter 1, material was reproduced from a review article published by the Author. This article was originally written by the Author, and permission was obtained from the Principle Investigator (Prof. Pawel Swietach) to reproduce the material in this thesis. The reference for this article is below:

Park KC, Krywawych S, Richard E, Desviat L, Swietach P. Cardiac complications in propionic and other organic acidemias. *Front Cardiovasc Med* 2020;22(7):617451.

Table of Contents

ABSTRACT I

PUBLISHED WORKS DURING DPHIL II

ACKNOWLEDGEMENTS III

STATEMENT OF AUTHORSHIP V

TABLE OF CONTENTS VI

ABBREVIATIONS XII

LIST OF FIGURES XIX

LIST OF TABLES XXII

CHAPTER 1. INTRODUCTION 1

1.1 ACID-BASE AND ORGANIC ANION PHYSIOLOGY 2

1.1.1 Acid-base balance and disturbances 2

1.1.2 Intracellular pH and the heart 2

1.1.3 Inherited metabolic diseases and organic acidaemias 3

1.1.4 Accumulation of organic anions in OAs 5

1.1.5 Organic anions as biologically potent molecules 6

1.2 PROPIONATE AND METABOLISM 7

1.2.1 Overview of cardiac metabolism 7

1.2.2 Normal propionate metabolism 8

1.2.3 Fates of propionate and propionyl-CoA when metabolism is disrupted 10

1.2.4 Sources of propionate and propionyl-CoA in the heart and their transport mechanisms 11

1.3 PROPIONIC ACIDAEMIA (PA) 16

1.3.1 Discovery of PA 16

1.3.2 Molecular basis of PA 20

1.3.3 Biochemical features, clinical presentation and management 21

1.4 CARDIAC COMPLICATIONS IN PA 25

1.4.1 Background to the types of cardiac pathologies encountered in PA 25

1.4.2 Typical clinical features of heart disease in PA 28

1.4.3 Liver transplantation for the treatment of PA: insight into mechanisms of cardiac dysfunction 32

1.4.4 Possible mechanisms causing cardiac dysfunction in PA 34

1.4.4.1 Energetic deficiency and oxidative stress 35

1.4.4.2 Metabolic dysfunction....36
1.4.4.3 MicroRNAs....37
1.4.4.4 Gene expression: histone acetylation and propionylation....38
1.5 BIOLOGICAL MODELS USED IN THIS THESIS....40
1.5.1 *In vivo* model of PCC disruption: FVB *Pcca*$^{-/-}$ A138T hypomorphic mouse....41
1.5.2 *In vitro* models of propionate actions: Wild-type SD rats....46
1.6 CENTRAL HYPOTHESIS....47
1.7 SUMMARY AND THESIS AIMS....47

CHAPTER 2. GENERAL METHODS....48

2.1 ANIMAL MODELS....49
2.1.1 General overview of animal procedures....49
2.1.2 Genotyping *Pcca*$^{-/-}$ A138T mice....49
2.2 EXPERIMENTAL METHODS....52
2.2.1 Animals and euthanisation....52
2.2.2 Primary adult ventricular myocyte isolation....53
2.2.2.1 Adult mouse ventricular myocytes (AMVMs)....55
2.2.2.2 Adult rat ventricular myocytes (ARVMs)....56
2.2.3 Primary neonatal ventricular myocyte isolation and culture....57
2.2.4 Preparation of cell culture media and treatment conditions....59
2.2.5 Mouse heart and plasma collection....60
2.2.6 Heart homogenisation and sample preparation....61
2.2.7 Determination of protein concentration....62
2.2.8 SDS-PAGE and western blot....62
2.3 STATISTICAL ANALYSIS....64

CHAPTER 3. CHARACTERISATION OF THE CARDIAC PHENOTYPE OF PCC-DEFICIENT MICE....65

3.1 INTRODUCTION....66
3.1.1 Metabolomics as a tool for studying cardiac metabolism....66
3.1.2 The ECG in mice....67
3.1.3 Cardiac function in mice....68
3.1.4 Aims of this Chapter....71
3.2 SPECIFIC METHODS....72
3.2.1 Biological models....72
3.2.2 Untargeted metabolomics: anion-exchange mass spectrometry....72

3.2.3 Mouse organ weight measurements....74
3.2.4 Cardiomyocyte cell size....74
3.2.5 SRB *in vitro* hypertrophic assay....75
3.2.6 ECG recordings....76
3.2.7 Cine-MRI....78
3.3 RESULTS....81
3.3.1 Effect of PCC disruption on the metabolome....81
3.3.2 Effect of PCC disruption on organ weights....84
3.3.3 Effect of PCC disruption and exogenous propionate on cardiomyocyte cell size....86
3.3.3.1 Ventricular myocyte cell size in PCC-deficient hearts....86
3.3.3.2 In vitro hypertrophic assay in cardiomyocytes treated with propionate....87
3.3.4 Effect of PCC disruption on the ECG....89
3.3.5 Effect of PCC disruption on contractile function....92
3.4 DISCUSSION....97
3.4.1 PCC disruption has a metabolic signature in the heart....98
3.4.2 Maladaptive cardiac hypertrophy does not occur in PA....101
3.4.3 Assessment of cardiac electrophysiology in PCC-deficient mice by surface ECGs....102
3.4.4 Evidence of early contractile dysfunction in the PA mouse....104
3.4.5 Discrepancy in heart rates recorded in ECG platform vs cine-MRI experiments....108
3.5 SUMMARY....110

CHAPTER 4. EFFECTS OF PROPIONATE ON CARDIOMYOCYTE EXCITATION-CONTRACTION COUPLING....111

4.1 INTRODUCTION....112
4.1.1 Cardiac excitation-contraction coupling....112
4.1.1.1 The ventricular action potential....112
4.1.1.2 The Ca^{2+} transient and myofilament activation....114
4.1.2 Control of cardiomyocyte Ca^{2+} handling....116
4.1.3 Ca^{2+} handling in propionic acidaemia....123
4.1.4 Aims of this Chapter....125
4.2 SPECIFIC METHODS....126
4.2.1 Biological models....126
4.2.2 Primary cardiomyocyte isolation....127
4.2.3 Solutions....128
4.2.4 Myocyte superfusion....130
4.2.5 Whole-cell epifluorescence microscopy....131
4.2.6 Ca^{2+} imaging....132

4.2.6.1 Ca^{2+} transients in adult myocytes 132
4.2.6.2 Ca^{2+} transients in neonatal myocytes 136
4.2.7 Membrane potential imaging 137
4.2.8 Ca^{2+}-handling proteins western blot 138
4.3 RESULTS 139
4.3.1 Effects of PCC disruption on cardiomyocyte physiology 139
4.3.1.1 Effect of PCC disruption on Ca^{2+} handling in 8-week-old animals 140
4.3.1.2 Effect of PCC disruption on Ca^{2+} handling in 20-week-old animals 144
4.3.1.3 Effect of PCC disruption on Ca^{2+} handling protein expression 148
4.3.2 Effects of *in vitro* application of propionate on cardiomyocyte physiology 150
4.3.2.1 Effect of acute propionate exposure on Ca^{2+} handling 150
4.3.2.2 Effect of chronic propionate exposure on AP-CaT coupling 152
4.3.2.3 Effect of chronic propionate exposure on APD 154
4.3.2.4 Effect of chronic propionate exposure on electrically-evoked CaTs 155
4.4 DISCUSSION 157
4.4.1 Ca^{2+} handling is remodelled following PCC disruption 158
4.4.2 Diastolic and resting [Ca^{2+}] are raised in 8-week amPA females 159
4.4.2.1 Resting Ca^{2+} 160
4.4.2.2 Diastolic Ca^{2+} 161
4.4.2.3 Interpretation of Ca^{2+} handling in 8-week amPA females 162
4.4.3 CaT amplitude and SR Ca^{2+} load are increased in 20-week amPA females 164
4.4.4 Sex-specificity of the effect on Ca^{2+} handling in PCC-deficient animals 165
4.4.5 *In vitro* application of propionate on WT cardiomyocytes 167
4.4.5.1 Acute exposure to propionate 167
4.4.5.2 Chronic exposure to propionate 167
4.5 SUMMARY 171

CHAPTER 5. EFFECTS OF PROPIONATE ON CARDIAC EPIGENETICS AND GENE EXPRESSION 173

5.1 INTRODUCTION 175
5.1.1 Gene expression: structural considerations 175
5.1.1.1 Histones and the epigenome 175
5.1.1.2 Nuclear organisation 176
5.1.2 Metabolic regulation of gene expression 178
5.1.2.1 Writers and erasers: KATs and HDACs 179
5.1.2.2 Lysine propionylation: propionyl-CoA as a substrate for PTMs 183
5.1.2.3 Acyl-CoA accessibility and compartmentalisation 184

5.1.3 Histone modifications in cardiovascular disease 185
5.1.4 Aims of this Chapter 186
5.2 SPECIFIC METHODS 187
5.2.1 Biological models 187
5.2.2 Sample preparation 188
5.2.2.1 Total RIPA lysates 188
5.2.2.2 Histone extraction 188
5.2.2.3 RNA extraction 189
5.2.3 Poly(A)+ RNA-sequencing 190
5.2.3.1 Assessment of RNA sample quality 190
5.2.3.2 Library preparation, sequencing and analysis pipeline 191
5.2.4 RT-qPCR 193
5.2.5 Western blot 194
5.2.6 Whole-cell ELISA 195
5.2.7 Immunofluorescence 197
5.3 RESULTS 199
5.3.1 Effect of propionate application *in vitro* on cardiac gene expression 199
5.3.2 Effect of propionate application *in vitro* on cardiomyocyte histone acetylation and propionylation 207
5.3.3 Concentration-dependence of propionate-evoked histone acetylation *in vitro* 208
5.3.4 Propionate induces a consistent spatial pattern of nuclear H3K9ac and H3K27ac 210
5.3.5 Effect of PCC disruption on cardiac histone propionylation and H3K9ac 214
5.3.6 Effect of PCC disruption on cardiac non-histone protein propionylation 215
5.3.7 Effect of PCC disruption on cardiac gene expression 217
5.4 DISCUSSION 229
5.4.1 RNA-seq reveals major effect of propionate on cardiac gene expression *in vitro* 230
5.4.2 Gene expression is epigenetically regulated by propionate *in vitro* 231
5.4.2.1 Cardiomyocyte HDAC inhibition and histone acetylation 231
5.4.2.2 Cardiomyocyte histone propionylation 235
5.4.3 Cardiac gene expression is significantly altered in mice with PCC disruption *in vivo* 236
5.4.3.1 Epigenetic mechanisms in vivo 238
5.4.3.2 Sex effect 241
5.4.3.3 DEGs of cardiac interest 243
5.4.4 Protein propionylation as a post-translational modification in the heart 245
5.5 SUMMARY 246

CHAPTER 6. FINAL SUMMARY AND INTEGRATED DISCUSSION 248
6.1 SUMMARY OF KEY FINDINGS 249
6.2 INTEGRATED DISCUSSION AND IMPLICATIONS OF FINDINGS 251
6.2.1 Ca^{2+} handling and contractile function 251
6.2.1.1 At 8 weeks of age, early changes are being detected 251
6.2.1.2 PDE9A, cGMP-PKG signalling, and diastolic dysfunction 255
6.2.2 Epigenetics and gene expression 257
6.2.3 Sex-dependence of cardiac dysfunction in PA 259
6.2.4 Other potential mechanisms 261
6.3 SUMMARY OF MECHANISMS 263
6.4 FUTURE PERSPECTIVES 266
6.5 FINAL CONCLUSION 268

REFERENCES 269

APPENDIX: RESEARCH DURING THE COVID-19 PANDEMIC 301

Abbreviations

ACSS	Acyl-CoA synthetase short-chain family member
A.U.	Arbitrary units
AM	Acetoxy-methyl ester
amPA	Adult mouse with propionic acidaemia
AMVM	Adult mouse ventricular myocytes
amWT	Wild-type adult mouse
ANOVA	Analysis of variance
AP	Action potential
APD	Action potential duration
APD_{90}	Action potential duration at 90% repolarisation
ARVM	Adult rat ventricular myocytes
ATP	Adenosine triphosphate
BCA	Bicinchoninic acid
BCAA	Branched-chain amino acids
B_{max}	Maximum buffering capacity
BNP	Brain-type natriuretic peptide
bp	Base pairs
bpm	Beats per minute
BSA	Bovine serum albumin
Bu	Butyrate
C2	Acetyl-carnitine
C3	Propionyl-carnitine
CACT	Carnitine-acylcarnitine translocase
cAMP	3'-5'-cyclic adenosine monophosphate
CAG	Cytomegalovirus early enhancer

CaMKII	Ca^{2+}/calmodulin-dependent protein kinase II
CaT	Ca^{2+} transient
CaT_{90}	Time to 90% Ca^{2+} transient recovery
cDNA	Complementary DNA
cGMP	3'-5'-cyclic guanosine monophosphate
ChIP	Chromatin immunoprecipitation
CICR	Ca^{2+}-induced Ca^{2+}-release
CO	Cardiac output
CoA	Coenzyme A
cPA	Compensated propionic acidaemia
cpm	Counts per million
CRAT	Carnitine acetyltransferase
cSNARF-1	5,6-carboxy-seminaphthorhodofluor-1
DCM	Dilated cardiomyopathy
DEG	Differentially expressed gene
DMEM	Dulbecco's Modified Eagle's Medium
DMSO	Dimethyl sulfoxide
DNA	Deoxyribonucleic acid
E-C	Excitation-contraction
EC_{50}	Half-maximal effective concentration
ECG	Electrocardiogram
ECL	Enhanced chemiluminescence
EDTA	Ethylenediamine tetra-acetic acid
EDV	End-diastolic volume
EF	Ejection fraction
eGFP	Enhanced green fluorescent protein

EGTA	Ethylene glycol-bis(2-aminoethylether)-*N,N,N',N'*-tetra-acetic acid
ELISA	Enzyme-linked immunosorbent assay
ESV	End-systolic volume
ETC	Electron transport chain
F	Female
FC	Fold-change
FCS	Foetal calf serum
F/F_0	Fluorescence emission intensity normalised to baseline
FFAR	Free fatty acid receptor
fps	Frames per second
Fl-Acetate	Fluoroacetate
FR	Fura Red
FVB	Friend virus B-type susceptibility
G	Gauge
GO	Gene ontology
GPR	G-protein coupled receptor
H3	Histone 3
H3K9ac	Histone 3 lysine 9 acetylation
H3K27ac	Histone 3 lysine 27 acetylation
HAT/KAT	Histone acetyltransferase/lysine acetyltransferase
HCM	Hypertrophic cardiomyopathy
HDAC	Histone deacetylase
HEPES	4-(2-hydroxyethyl)-1-piperazineethanesulfonic acid
HF	Heart failure
HFpEF	Heart failure with preserved ejection fraction
HNDC	Hypokinetic non-dilated cardiomyopathy

HRP	Horse radish peroxidase
HR	Heart rate
HS	Horse serum
HW:BW	Heart weight to body weight ratio
HW:TL	Heart weight to tibia length ratio
Hz	Hertz
IC_{50}	Half-maximal inhibitory concentration
ICC	Intraclass correlation
IC-MS	Anion-exchange chromatography mass spectrometry
$I_{Ca,L}$	L-type Ca^{2+} current
IMD/IEM	Inherited metabolic disease/inborn error of metabolism
I.U.	International units
IP	Intraperitoneal
IRES	Internal ribosome entry site
Kac	Lysine acetylation
K_d	Dissociation constant
kDa	Kilodaltons
KEGG	Kyoto Encyclopedia of Genes and Genomes
K_m	Michaelis constant
KO	Knock-out
Kpr	Lysine propionylation
LA	Left atrium
LTCC	L-type Ca^{2+} channel
LC-MS	Liquid chromatography-mass spectrometry
LED	Light-emitting diode
LQTS	Long QT syndrome

LT	Liver transplantation
LV	Left ventricle
LVNC	Left ventricular non-compaction cardiomyopathy
M	Male
M199	Medium 199
MCT	Monocarboxylate transporter
MeCit	2-methylcitrate
MEF	Myocyte enhancer factor
MMA	Methylmalonic acidaemia
MME	Membrane metalloendopeptidase
MΩ	Megaohms
MRI	Magnetic resonance imaging
mRNA	Messenger RNA
MS	Mass spectrometry
MS-MS	Tandem mass spectrometry
NaBu	Sodium butyrate
NaPr	Sodium propionate
NCS	Neonatal calf serum
NCX	Na^+/Ca^{2+}-exchanger 1
NHE	Na^+/H^+-exchanger 1
nm	Nanometres
NRVM	Neonatal rat ventricular myocytes
NT	Normal Tyrode's solution
NT-BC	Bicarbonate-buffered Normal Tyrode's solution
NT-HEPES	HEPES-buffered Normal Tyrode's solution
OA	Organic acidaemia

OCFA	Odd-chain fatty acid
OPD	O-phenylenediamine dihydrochloride
P1/P2	Post-natal day 1 or 2
PA	Propionic acidaemia
PBS	Phosphate-buffered saline
PCA	Principle component analysis
PCC	Propionyl-CoA carboxylase
PCCA	Propionyl-CoA carboxylase α-subunit
PCCB	Propionyl-CoA carboxylase β-subunit
PCR	Polymerase chain reaction
PDE9A	Phosphodiesterase 9A
pH	Power of hydrogen
pH_i	Intracellular pH
PKA	Protein kinase A
PKC	Protein kinase C
PKG	Protein kinase G
PLN	Phospholamban
PLN_{pSer16}	Phospholamban serine 16 phosphorylation
PLN_{pThr17}	Phospholamban threonine 17 phosphorylation
PMCA	Plasma membrane Ca^{2+}-ATPase
Pr	Propionate
PTM	Post-translational modification
PVDF	Polyvinylidene fluoride
RCF	Relative centrifugal force
RIN	RNA integrity number
RIPA	Radioimmunoprecipitation assay

RNA	Ribonucleic acid
RNA-seq	RNA-sequencing
RPM	Revolutions per minute
RT-qPCR	Reverse transcription quantitative real-time polymerase chain reaction
RyR	Ryanodine receptor 2
SAM	Sequence alignment/map
SCFA	Short-chain fatty acid
sCMOS	Scientific complementary metal oxide semiconductor
SDS-PAGE	Sodium dodecyl sulphate-polyacrylamide gel electrophoresis
SEM	Standard error of the mean
SERCA	Sarcoplasmic reticulum Ca^{2+}-ATPase 2a
SR	Sarcoplasmic reticulum
SRB	Sulforhodamine B
STAR	Spliced Transcripts Alignment to a Reference
SV	Stroke volume
TAE	Tris-acetate-EDTA buffer
TBS-T	Tris-buffered saline with Tween 20
T-tubule	Transverse tubule
uPA	Uncompensated propionic acidaemia
UV	Ultraviolet
Vm	Membrane potential
WT	Wild-type
3-OH-Pr	3-hydroxypropionate

List of Figures

Figure 1.1. Normal propionate metabolism. 9

Figure 1.2. Intrinsic and extrinsic sources of propionate and propionyl-CoA in cardiomyocytes and their cellular compartmentalisation. 15

Figure 1.3. Strategy for the generation of *Pcca*$^{-/-}$ A138T hypomorphic mice. 44

Figure 2.1. Langendorff apparatus for the isolation of adult mouse myocytes. 56

Figure 2.2. Langendorff apparatus for the isolation of adult rat myocytes. 57

Figure 2.3. Neonatal rat ventricular myocyte (NRVM) culture protocol. 59

Figure 3.1. Recording of surface ECGs from isoflurane-anaesthetised adult mice. 77

Figure 3.2. Cine-MRI setup. 79

Figure 3.3. Metabolomic analyses of cardiac and plasma extracts. 82

Figure 3.4. Measurement of plasma acyl-carnitines by LC-MS/MS. 84

Figure 3.5. Body and organ weights of 8-week-old adult PA mice. 85

Figure 3.6. cSNARF-1 fluorescence imaging to determine cardiomyocyte cell size. 86

Figure 3.7. Sulforhodamine B (SRB) staining of NRVMs treated in propionate 88

Figure 3.8. Summary of key ECG parameters determined from surface recordings of isoflurane-anaesthetised mice. 90

Figure 3.9. Assessment of *in vivo* contractile function and chamber morphology by cine-MRI. 92

Figure 3.10. Summary histograms of key functional indices measured by cine-MRI. 95

Figure 4.1. Superfusion setup for adult and neonatal myocytes. 131

Figure 4.2. Protocol for the recording of electrically-evoked CaTs and caffeine-evoked Ca^{2+} release. 134

Figure 4.3. Averaged time-courses of electrically-evoked CaTs and caffeine-evoked Ca^{2+} release in 8-week-old mouse myocytes. 141

Figure 4.4. Ca^{2+} handling summary parameters from 8-week-old mouse myocytes. 142

Figure 4.5. Averaged time-courses of electrically-evoked CaTs and caffeine-evoked Ca^{2+} release in 20-week-old mouse myocytes. 145

Figure 4.6. Ca^{2+} handling summary parameters from 20-week-old mouse myocytes. 146

Figure 4.7. Western blotting of key Ca^{2+} handling proteins in ventricular lysates. 148

Figure 4.8. Electrically-evoked CaTs and caffeine-evoked Ca^{2+} release in wild-type myocytes acutely exposed to propionate. 151

Figure 4.9. APs and CaTs recorded in electrically-paced NRVMs cultured for an extended period in propionate. 153

Figure 4.10. APD_{90} in NRVMs cultured for an extended period in propionate 154

Figure 4.11. CaTs in NRVMs cultured for an extended period in propionate. 156

Figure 4.12. Summary of remodelling to Ca^{2+} handling in female amPA cardiomyocytes. 165

Figure 5.1. Principle component analysis of RNA-seq in NRVMs treated with propionate or butyrate *in vitro*. 200

Figure 5.2. Analysis of differentially expressed genes (DEGs) determined by RNA-seq. 201

Figure 5.3. Genes differentially expressed in NRVMs by propionate treatment *in vitro*. 203

Figure 5.4. Genes differentially expressed in NRVMs by butyrate treatment *in vitro*. 204

Figure 5.5. Validation of DEGs by RT-qPCR. 206

Figure 5.6. Western blotting for lysine propionylation and H3K9ac in histones extracted from NRVMs treated with propionate *in vitro*. 208

Figure 5.7. Whole-cell ELISA for H3K9ac in NRVMs treated for 24 hrs over a range of propionate concentrations. 209

Figure 5.8. Immunofluorescence for H3K9ac and H3K27ac in the nuclei of adult and neonatal rat ventricular myocytes treated with propionate *in vitro*. 212

Figure 5.9. Western blotting for lysine propionylation and H3K9ac in cardiac histones extracted from 8-week-old mice. 214

Figure 5.10. Western blotting for lysine propionylation in total RIPA lysates from 8-week-old mouse hearts. 216

Figure 5.11. Converted Bioanalyzer electropherograms of total RNA samples extracted from 8-week-old mouse hearts. 218

Figure 5.12. Principle component analysis of RNA-seq samples in 8-week-old mouse hearts. 219

Figure 5.13. Heat map of DEGs in 8-week-old mouse hearts. 221

Figure 5.14. Venn diagram of the number of DEGs in amPA hearts and cardiomyocytes exposed to propionate *in vitro*. 222

Figure 5.15. Enhanced volcano plots of DEGs in 8-week-old mouse hearts. 225

Figure 5.16. DEGs in 8-week-old mouse hearts also changed by propionate *in vitro* with a butyrate-like effect. 226

Figure 5.17. DEGs in 8-week-old mouse hearts also changed by propionate *in vitro* but not butyrate-like. 227

Figure 5.18. Selected genes of interest that were differentially expressed in female amPA hearts and *in vitro*. 228

Figure 5.19. Summary of mechanisms involved in epigenetic remodelling of cardiac gene expression by propionate. 247

List of Tables

Table 1.1. Comparative analysis of biochemical parameters in PA patients. 22

Table 1.2. Overview of biological models used in this thesis and example readouts. 41

Table 2.1. Genotyping PCR conditions. 51

Table 2.2. Solutions used for adult myocyte isolations. 53

Table 2.3. Basic treatment conditions used for *in vitro* experiments based on patient serum data. 60

Table 3.1. ECG parameters determined from surface recordings in isoflurane-anaesthetised mice. 91

Table 3.2. *In vivo* cardiac function as measured by cine-MRI in isoflurane-anaesthetised mice. 96

Table 4.1. Overview of experimental solutions used for superfusion studies. 129

Table 4.2. Antibodies used for Ca^{2+} handling western blot experiments. 139

Table 4.3. Analysis of Ca^{2+} transient parameters in 8-week-old mice using standard vs. hierarchical statistical tests. 143

Table 4.4. Analysis of Ca^{2+} transient parameters in 20-week-old mice using standard vs. hierarchical statistical tests. 147

Table 5.1. Primer sequences used for RT-qPCR experiments. 194

Table 5.2. Antibodies used for western blot experiments. 195

Table 5.3. Antibodies used for whole-cell indirect ELISA. 196

Table 5.4. Antibodies used for immunofluorescence experiments. 198

Chapter 1. Introduction

1.1 Acid-base and organic anion physiology

1.1.1 Acid-base balance and disturbances

The maintenance of a favourable pH is a homeostatic priority, which is manifested by the observation that plasma pH is regulated within a narrow range of 7.35 to 7.45 (Berend *et al.*, 2014). The principal pH buffer present in plasma is CO_2/HCO_3^-, therefore the concentration of H^+ ions, HCO_3^- ions and CO_2 gas is in a dynamic equilibrium. Acid-base disturbances can emerge from a change in $[HCO_3^-]$ at constant partial pressure of CO_2 (pCO_2), referred to as a metabolic acidosis (fall in $[HCO_3^-]$) or metabolic alkalosis (rise in $[HCO_3^-]$) (Berend *et al.*, 2014).

Clinically, many disturbances of pH are classified as metabolic acidosis, defined as an arterial pH < 7.35 with plasma bicarbonate < 22 mmol/L in the uncompensated state (Berend *et al.*, 2014). Its causes are widespread, but ultimately, they can be broadly classified into physiological (e.g. exercise-induced lactic acidosis), acquired (e.g. ischaemia, diabetic ketoacidosis) and genetic (inherited metabolic diseases; organic acidaemias) causes.

1.1.2 Intracellular pH and the heart

The maintenance of intracellular pH (pH_i) within the physiological set-point (near 7.20) is permissive for a myriad of biological processes. H^+ ions are generated or consumed metabolically. pH_i is regulated by the balance of H^+ (or H^+ equivalent) fluxes on sarcolemmal transporter proteins (e.g. Na^+/H^+-exchanger) (Vaughan-Jones *et al.*, 2009). The heart is exquisitely sensitive to pH_i and a wealth of information is available on the effects of H^+ ions on

the heart (Vaughan-Jones *et al.*, 2009; Garciarena *et al.*, 2013; Wakabayashi *et al.*, 2013). By acting as post-translational modifiers of proteins, H^+ ions can alter biological functions by protonating amino acid residues, such as histidine. The low extracellular pH in uncompensated metabolic acidoses can modulate the heart by directly acting on surface-expressed proteins (Saegusa *et al.*, 2011). Additionally, extracellular acidity can drive a fall in intracellular pH (Sun *et al.*, 1996), and thus gain access to a myriad of intracellular targets, most of which show some degree of pH-sensitivity, including most elements of excitation-contraction coupling (Vaughan-Jones *et al.*, 2009; Casey *et al.*, 2010; Schonichen *et al.*, 2013). For example, even minor reductions in pH_i from its physiological set-point (near 7.2) are capable of eliciting acute contractile depression (myofilament Ca^{2+} sensitivity), deranged Ca^{2+} handling, intracellular Na^+ overload, and triggering of arrhythmias (Bers, 2001; Vaughan-Jones *et al.*, 2009).

1.1.3 Inherited metabolic diseases and organic acidaemias

Inherited metabolic disorders (IMDs), classically known as inborn errors of metabolism (IEMs), are a collection of over 500 diseases, each caused by an inherited defect in genes coding for a metabolic enzyme (Lanpher *et al.*, 2006). Although individually rare, as a collective they affect 1 in 2,000 births worldwide (Waters *et al.*, 2018). IMDs exist for essentially every metabolic pathway, from fatty acid oxidation, to the urea cycle, and a number of them can be detected during newborn screening by tandem mass spectrometry (MS/MS) and multi-omic technologies (Argmann *et al.*, 2016). Recently, the role of whole-exome sequencing was

evaluated as an innovative methodology to aid in the diagnosis of infants with abnormal MS/MS screens (Adhikari *et al.*, 2020).

Organic acidaemias (OAs), sometimes referred to as organic acidurias, are a subset of seventeen IMDs that are characterised by the excessive accumulation of organic acids in body fluids. OAs have been divided into three categories: (1) systemic, (2) cerebral and (3) ketolytic/ketogenic (Chapman, 2019), although this naming system is problematic because changes related to the brain are common in all OAs and the canonical cerebral OAs can also develop non-neurologic manifestations (Dimitrov *et al.*, 2020). With the advent of chemical assays capable of defining the metabolite milieu of blood, OAs have been related to specific metabolic signatures, some of which have diagnostic value. Modern genetic techniques have described the gene mutations that give rise to the metabolite disorder, and even provided some degree of insight into gene-function relationships (Lanpher *et al.*, 2006).

A feature of many OAs is the accumulation of organic acid metabolites that directly relate to the mutated enzyme, typically accompanied by a build-up of various other acidic metabolites particularly during stages of metabolic decompensation, such as lactate, 3-hydroxybutyrate or acetoacetate. The clinical management of OAs is broadly based on the same principles, namely the reversal or prevention of catabolism, limiting exposure to precursors of the substrate that cannot be metabolised, and scavenging toxic intermediates (Chapman, 2019).

OAs are severe diseases that can affect multiple organ systems. Many OAs present in the neonatal or infantile period with a wide anion gap, metabolic acidosis and hyperammonaemia. Of the 17 known OAs, around half are known to cause cardiac dysfunction (Organic Acidemia Association, 2020). However, among the disorders most strongly associated with cardiac sequelae is the life-threatening disease, propionic acidaemia.

1.1.4 Accumulation of organic anions in OAs

The body's pH-regulatory apparatus is primarily designed to sense and handle H^+ ions rather than organic anions. Taking the heart for example, there are several sarcolemmal transporter proteins that act in concert to maintain pH_i: Na^+/H^+-exchange, Na^+-HCO_3^--cotransport, Cl^--HCO_3^--exchange and Cl^--OH^-exchange. This is in contrast to only one mechanism, the monocarboxylate transporter, as a mechanism of organic anion transport (Vaughan-Jones *et al.*, 2009). Therefore, organic anions may accumulate with little homeostatic oversight.

Organic acids, which accumulate in OAs, have two distinct chemical components: H^+ ions (which determine pH) and the conjugate organic anions. In aqueous solution, these ionic species are, in essence, fully dissociated, and can elicit effects via separate mechanisms. However, as organic acids accumulate in OAs, the concentrations of H^+ ions and organic anions increase in tandem, but since the former is heavily buffered, its relative rise is orders of magnitude smaller (Aiken, 2013). Whereas the drop in pH during a metabolic acidosis may be equivalent to a sub-micromolar change in free $[H^+]$, the accumulation of organic anions in blood may

reach millimolar levels, for example such as in the case of propionate in propionic acidaemia patients (Rasmussen *et al.*, 1972; Merinero *et al.*, 1981; Coude *et al.*, 1982).

OAs can result in the production of several different types of organic anions (e.g. lactate, propionate), and their collective concentration can be estimated from the so-called anion gap, usually calculated as $[Na^+] + [K^+] – [Cl^-] – [HCO_3^-]$. A high anion gap metabolic acidosis is a frequent observation in OAs, attributable to a high collective concentration of organic acids that are not measured routinely in blood tests (Berend *et al.*, 2014). A metabolic acidosis can become compensated by hyperventilation to reduce pCO_2. Whereas this compensatory manoeuvre can restore normal pH, albeit at a reduced pCO_2 and $[HCO_3^-]$, it does not *per se* remove the organic anion disturbance. Longer-term, increased production and tubular reabsorption of bicarbonate by the kidneys aid in the compensation of metabolic acidosis.

1.1.5 Organic anions as biologically potent molecules

To date, investigations of metabolic acidosis have conventionally focussed on the effects of H^+ ions and largely ignored the actions of the organic anion (conjugate base). However, it is becoming increasingly clear that organic anions are not biologically inert (Pietrocola *et al.*, 2015; Sun *et al.*, 2017; Tang *et al.*, 2019; Kimura *et al.*, 2020), and at least some of the common presentations of OAs are attributable to actions of these metabolites, rather than the pH *per se*. This notion is exemplified by the fact that not all OAs are associated with cardiac disease. For example, heart disease is not observed in isovaleric acidaemia (Grünert *et al.*, 2012) or pyroglutamic acidaemia (5-oxoprolinaemia) (Dempsey *et al.*, 2000), two examples of OAs

associated with profound metabolic acidosis. Therefore, in studying the metabolic acidoses, it is therefore important to distinguish the actions of H^+ ions and the organic anions.

The organic anion that is the topic of study in this thesis is propionate. Since the most extreme systemic accumulation of propionate occurs in the OA, propionic acidaemia, this disease has been used as a model to study the actions of propionate. Detail is provided in the remainder of this Chapter.

1.2 Propionate and metabolism

1.2.1 Overview of cardiac metabolism

A characteristic feature of cardiomyocyte maturation is the shift in myocardial substrate preference, from glycolytic to oxidative metabolism (Maroli & Braun, 2021). That is, in the adult heart, there is increased transport of fatty acids in the mitochondria and it primarily relies on fatty acid oxidation (FAO) as its primary substrate for ATP production (Maroli & Braun, 2021). However, it also displays a remarkable ability to utilise different substrates, including ketone bodies and amino acids, with a so-called 'metabolic flexibility' (Kolwicz *et al.*, 2013). Despite this flexibility, a hallmark of pathological hypertrophy and heart failure is a 'switch' in substrate-dependence from fatty acids towards glucose and ketone bodies (Neubauer, 2007; Ritterhoff & Tian, 2017). Interestingly, there is evidence for sex differences in myocardial metabolism at baseline, e.g. in acyl-carnitine and triglyceride metabolism (Murphy *et al.*, 2017).

Furthermore, it is well established that there are sex differences in cardiometabolic disorders (Murphy *et al.*, 2017; Gerdts & Regitz-Zagrosek, 2019).

1.2.2 Normal propionate metabolism

Propionate is a naturally-occurring monocarboxylate short-chain fatty acid (SCFA) in humans. It is derived from the metabolism of multiple substrates in the mitochondrial matrix, primarily in the liver: (1) catabolism of branched-chain amino acids (BCAAs; valine, isoleucine), methionine and threonine; (2) β-oxidation of odd-chain fatty acids (OCFAs); (3) oxidation of the side-chain of cholesterol (Baumgartner *et al.*, 2014). Note, whilst muscle can metabolise BCAAs, liver cannot, from lacking the essential enzyme BCAA aminotransferase (BCAT) (Salway, 2017). Another major source of propionate is the direct production of propionic acid by the gut microbiome from the fermentation of carbohydrates (Koh *et al.*, 2016). Using stable isotopes in patients, it has been estimated that the precursors (OCFAs, BCAAs and colonic fermentation) accounting for approximately 25, 50 and 25% respectively, of the propionate pool (Leonard, 1997). The liver is the major site for propionate metabolism accounts for ~90% of total first-pass propionate metabolism, with the remainder reaching the peripheral circulation (Wong *et al.*, 2006; Wilson *et al.*, 2017).

Propionate is metabolised in the esterified form, propionyl-coenzyme A (CoA). The primary metabolic fate of propionyl-CoA in mitochondria is anaplerosis through multiple reaction steps, that favour moving excess propionyl-CoA into the Krebs cycle as succinyl-CoA (Trefely et al., 2020). The first step is the carboxylation of propionyl-CoA to D-methylmalonyl-CoA by

propionyl-CoA carboxylase (PCC), a biotin-dependent enzyme. D-methylmalonyl-CoA is subsequently racemised by methylmalonyl-CoA epimerase (methylmalonyl-CoA racemase) to L-methylmalonyl-CoA. Finally, L-methylmalonyl-CoA is isomerised by methylmalonyl-CoA mutase to succinyl-CoA to enter the Krebs cycle (Siliprandi et al., 1991; Trefely et al., 2020) (Figure 1.1).

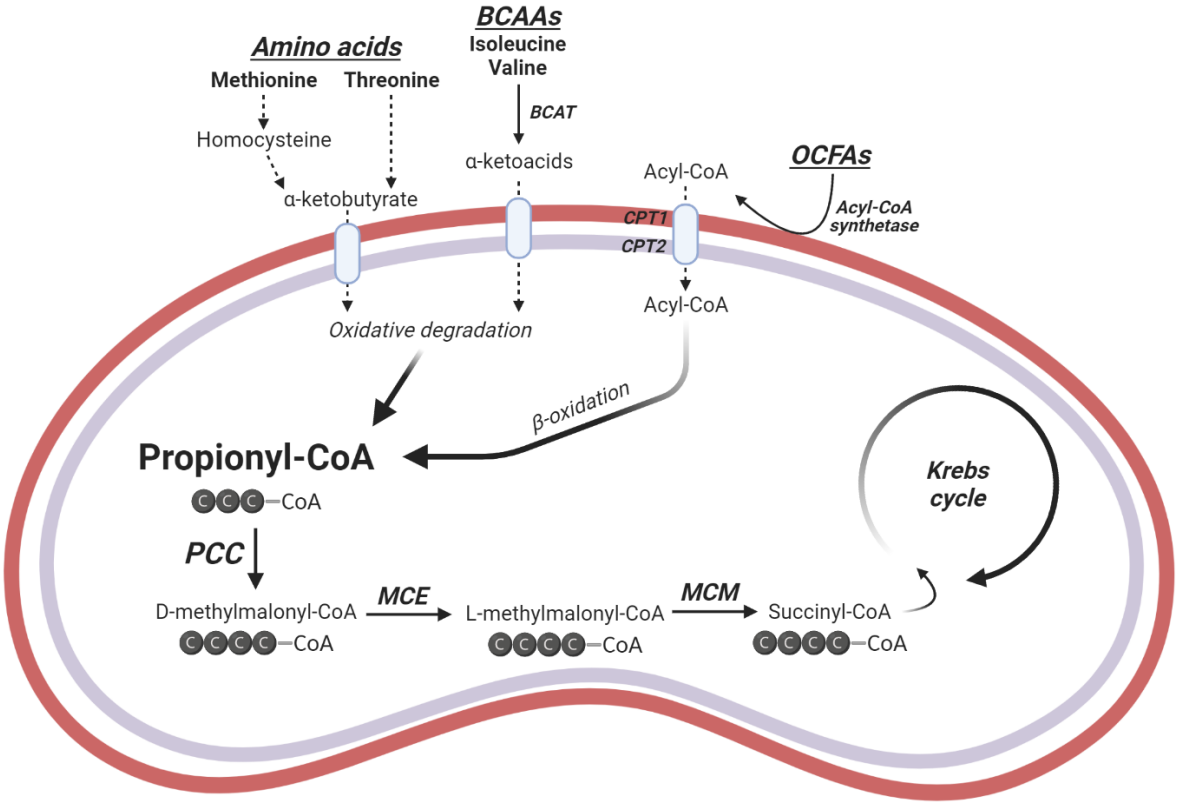


Figure 1.1. Normal propionate metabolism. Schematic of a mitochondrion with the key sources of propionyl-CoA and its subsequent metabolism via the Krebs cycle. There are specialised transport processes for each substrate (not shown for clarity). The essential amino acids methionine and threonine are first converted to α-ketobutyrate, whilst branched-chain amino acids (BCAAs; isoleucine and valine) first undergo transamination to different α-ketoacids, prior to oxidative degradation in the mitochondrial matrix, yielding propionyl-CoA. Odd-chain fatty acids (OCFAs) are first esterified to their acyl-CoA, prior to transport into the mitochondria via the carnitine palmitoyltransferase shuttle system (CPT1/CPT2). Dashed arrows indicate multiple reaction steps. Faded arrows represents metabolic pathways. BCAAs, branched-chain amino acids; BCAT, branched-chain amino acid aminotransferase; CoA, coenzyme A; CPT, carnitine palmitoyltransferase; MCM, methylmalonyl-CoA mutase; MCE, methylmalonyl-CoA epimerase; OCFA, odd-chain fatty acids; PCC, propionyl-CoA carboxylase.

1.2.3 Fates of propionate and propionyl-CoA when metabolism is disrupted

In circumstances where the metabolic activity of PCC is disrupted, for example such as in the case of propionic acidaemia (Section 1.3), there is an excessive accumulation of propionate and propionyl-CoA. Under these circumstances, there is a capacity for propionate and propionyl-CoA to be converted to a variety of downstream propionate-related metabolites. These are briefly described below.

Propionyl-carnitine. Propionyl-carnitine is generated from propionyl-CoA in mitochondria by the actions of carnitine acetyltransferase (CRAT). Contrary to the name, CRAT has the highest substrate-preference and activity for propionyl-CoA. CRAT is also highly abundant in the heart (Roe *et al.*, 1984; Wang *et al.*, 2018). Although not tested, presumably propionyl-carnitine can be converted back to propionyl-CoA via CRAT, since the reaction is known to be bidirectional (Trefely *et al.*, 2020). Indeed, such is the case for acetyl-CoA and acetyl-carnitine (Pietrocola *et al.*, 2015). However, the conversion of propionyl-carnitine to propionyl-CoA would be subject to CoA availability and the prevailing propionyl-CoA/CoA ratio, which in itself is homeostatically maintained (Roe *et al.*, 1984; Armstrong *et al.*, 2021).

2-methylcitrate. Propionyl-CoA, when conjugated with the Krebs cycle intermediate oxaloacetate, can act as an alternative substrate for citrate synthase to generate 2-methylcitrate (MeCit) (note, the condensation of oxaloacetate and acetyl-CoA, instead of propionyl-CoA, generates citrate) (Wongkittichote *et al.*, 2017; Armstrong *et al.*, 2021). MeCit however acts as

an endogenous inhibitor of citrate synthase, as well as isocitrate dehydrogenase (Cheema-Dhadli *et al.*, 1975).

3-hydroxypropionate. 3-hydroxypropionate (3-OH-Pr) is thought to be produced by β-oxidation of propionic acid (Ando *et al.*, 1972a; Siliprandi *et al.*, 1991; Wongkittichote *et al.*, 2017).

Propionyl-glycine. Propionyl-CoA is thought to interfere with glycine cleavage. Thus, under circumstances by which PCC activity is reduced, and [propionyl-CoA] is increased, there is also an increase in glycine concentration. It is speculated that the conjugation of propionate with glycine is pH-sensitive and favoured during periods of lower pH (such as during metabolic acidosis), generating propionyl-glycine which is then excreted in urine (Scholl-Bürgi *et al.*, 2012).

1.2.4 Sources of propionate and propionyl-CoA in the heart and their transport mechanisms

It is unknown whether the quantitatively, or indeed, the functionally important source of propionate in the heart, is circulating propionate, or that generated intrinsically by the heart. Since the liver accounts for ~90% of total propionate metabolism, with the remainder entering the circulation (Wong *et al.*, 2006; Wilson *et al.*, 2017), it seems intuitive that circulating propionate would be the major source for the heart. Regardless, the possible sources of propionate and propionyl-CoA in the heart are discussed below, following review of the best available evidence. The transport mechanisms are also discussed. The content from this sub-section are illustrated in Figure 1.2.

Intrinsic source of propionate: propionyl-CoA. The heart possesses the enzymes to metabolise BCAAs and OCFAs (Kolwicz *et al.*, 2013), therefore, it is able to generate its own propionyl-CoA (Wang *et al.*, 2018). Because of this, any propionate generated within the heart would be ultimately sourced from propionyl-CoA, from the metabolism of BCAAs and OCFAs in the mitochondrial matrix, and thus the metabolic rate of the heart would influence [propionyl-CoA]. The mitochondrial membrane, however, is impermeable to CoA-esters. For short-chain acyl-CoAs (e.g. acetyl-CoA and propionyl-CoA) to leave the mitochondria, they require conversion to their respective acyl-carnitine by mitochondrial CRAT (carnitine acetyltransferase; note, long-chain acyl-CoAs require conversion by carnitine palmitoyltransferase 1, also known as carnitine acyltransferase 1) (Wang *et al.*, 2018; Trefely *et al.*, 2020). Propionyl-carnitine is shuttled across the inner mitochondrial membrane by carnitine-acylcarnitine translocase (CACT), which then partitions across the outer mitochondrial membrane to access the cytosol (Trefely *et al.*, 2020). Thus, the combined actions of CRAT and CACT allow the two-way movement of short-chain acyl groups across the mitochondrial membrane.

Once in the cytosol, propionyl-carnitine could freely leave the myocyte, since short-chain acyl-carnitines can partition the cell membrane (Wikoff *et al.*, 2007). Alternatively, propionyl-carnitine could be converted back to propionyl-CoA via CRAT (Pietrocola *et al.*, 2015; Trefely *et al.*, 2020). Thereafter, propionyl-CoA could be metabolised to other related downstream metabolites (Section 1.2.3), or freely access other important cellular compartments, such as the

nucleus, since small molecules (< 9 nm/< 40 kDa) can freely diffuse through nuclear pore complexes (Görlich & Kutay, 1999).

Extrinsic sources of propionate: propionate and propionyl-carnitine. The two main extrinsic sources of propionate for the heart would be propionate itself and propionyl-carnitine. Short-chain acyl-carnitines, such as propionyl-carnitine, can freely permeabilise the cell membrane (Wikoff *et al.*, 2007). Therefore, any propionyl-carnitine in the circulation, could enter the heart. Through the actions of CRAT, it could then be converted to propionyl-CoA, as described above. As for circulating propionate, it is expected for free propionate in plasma to exist primarily in its anion form, since propionic acid has a low pKa (4.87), and dissociates at near-neutral pH. The lipid bilayer of cell membranes is highly permeable to weak acids (e.g. propionic acid), which can then freely enter cardiomyocytes and subsequently deprotonate, in equilibrium with intracellular pH. This circulating propionate could be sourced from the gut microbiome or the liver (i.e. propionate that has not been metabolised). Propionate could also enter cardiomyocytes, alongside a H^+ ion, via a proton-linked plasma membrane transporter, the monocarboxylate transporter (MCT) (Halestrap & Wilson, 2012). Once in the cardiomyocyte cytosol, propionate can access various cellular compartments, such as the nucleus through the aforementioned nuclear pore complexes (Görlich & Kutay, 1999). It could also partition across the inner mitochondrial membrane by crossing in the protonated form, or by MCT1 expressed on the inner membrane (Halestrap & Wilson, 2012).

There are also various metabolic fates of propionate. Aside from contributing to the common downstream propionate metabolites (e.g. propionyl-carnitine; Section 1.2.3), it can also be used to generate propionyl-CoA, through the actions of acyl-CoA synthetase short-chain family members (ACSS). ACSS catalyses the ATP-dependent ligation of short-chain acyl moieties (e.g. propionate, acetate) to CoA, to generate acyl-CoA (Trefely *et al.*, 2020). There are separate ACSS isoforms for different cellular compartments: ACSS1 and ACSS3 are expressed in mitochondria, whereas ACSS2 is localised to the cytosol and nucleus (Sivanand *et al.*, 2018; Haws *et al.*, 2020).

The intrinsic and extrinsic sources of propionate and propionyl-CoA in the heart and their transport mechanisms are summarised in Figure 1.2.

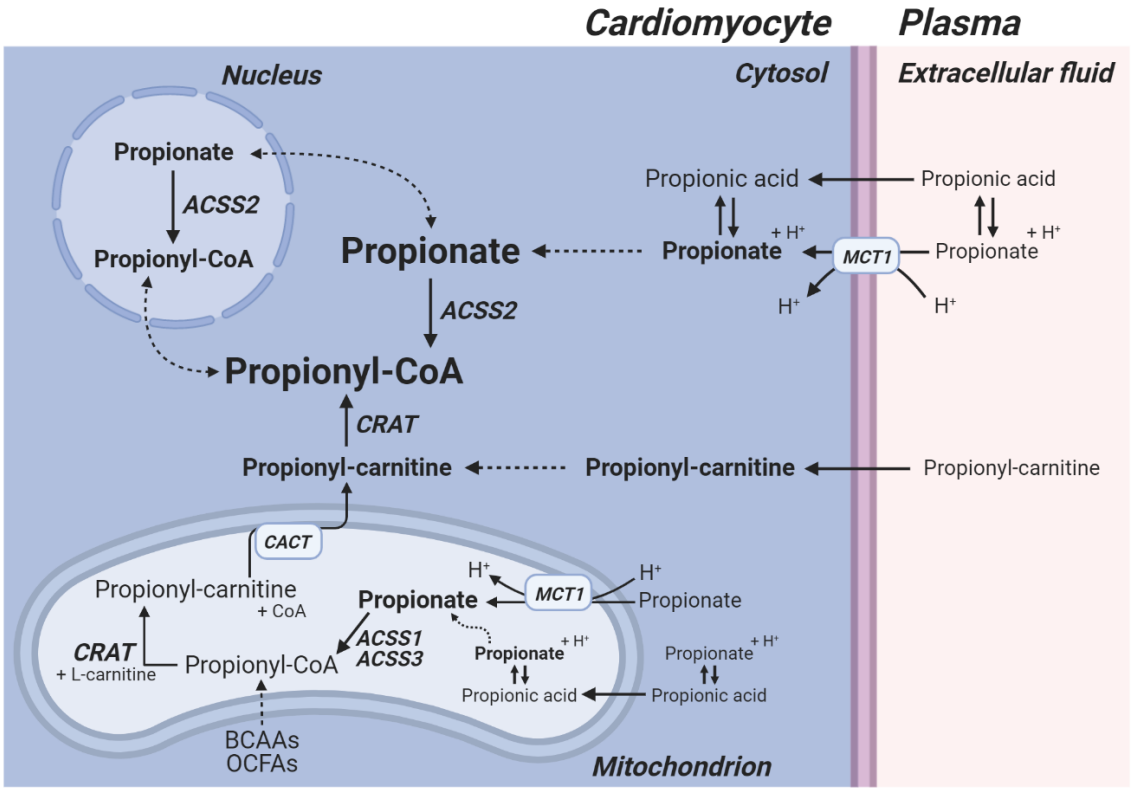


Figure 1.2. Intrinsic and extrinsic sources of propionate and propionyl-CoA in cardiomyocytes and their cellular compartmentalisation. Propionate can freely enter the myocyte as propionic acid or propionyl-carnitine. Propionate can also enter myocytes via the proton-linked monocarboxylate transporter 1 (MCT1). Once inside the cell, propionate can contribute to the propionyl-CoA pool through conversion by acyl-CoA synthetase short-chain family member 2 (ACSS2). Propionate can also freely access the nucleus (through nuclear pore complexes), or the mitochondria (by partitioning across the inner mitochondrial membrane either in the protonated form, or via MCT1 expressed on the inner membrane). Within those compartments, they can again be converted to propionyl-CoA by ACSS (ACSS2 in nucleus; ACSS1 and ACSS3 in mitochondria). At the mitochondrial level, propionyl-CoA can be generated from the metabolism of branched-chain amino acids (BCAAs) and odd-chain fatty acids (OCFAs). To exit the mitochondria, propionyl-CoA is converted to its carnitine ester by carnitine acetyltransferase (CRAT) using L-carnitine as a co-substrate. Propionyl-carnitine is shuttled through the inner mitochondrial membrane by carnitine-acylcarnitine translocase (CACT), and then freely partitions across the outer mitochondrial membrane to access the cytosol. Propionyl-carnitine can contribute to the propionyl-CoA pool through conversion by cytosolic CRAT. Note, CRAT and CACT can operate in both directions and thus facilitates bidirectional shuttling of propionyl groups between the cytosol and mitochondria. ACSS, acyl-CoA synthetase short-chain family member; BCAA, branched-chain amino acid; CACT, carnitine-acylcarnitine translocase; CRAT, carnitine acetyltransferase; MCT1, monocarboxylate transporter 1; OCFA, odd-chain fatty acids.

1.3 Propionic acidaemia (PA)

Elevated propionate has been linked to common metabolic conditions such as diabetes and obesity (Butte *et al.*, 2015; Gao *et al.*, 2016). In particular, plasma [propionyl-carnitine] is raised two-fold in type-2 diabetes (Mihalik *et al.*, 2010). However, the greatest increase in systemic propionate occurs in propionic acidaemia (PA), a relatively frequent type of OA that is characterised by an accumulation of propionate and other related metabolites, resulting in widespread end-organ damage (Fraser & Venditti, 2016). Acute illness in PA is typically a result of metabolic decompensation and acidosis (Chapman *et al.*, 2012). Interestingly, a common complication in PA patients is cardiomyopathy and arrhythmia, although the underlying mechanisms are not yet fully established (Baumgartner *et al.*, 2014; Park *et al.*, 2020). Therefore, combined with the fact that in PA, there is a direct defect in propionate metabolism, PA presents as an attractive model to study the effects of dysregulated propionate metabolism on the heart.

1.3.1 Discovery of PA

The discovery of PA was the least straightforward of all the OAs, spanning a decade of research between the 60s and 70s. The index patient was a Caucasian male born in 1957 and admitted to Johns Hopkins Hospital at 8 months of age with numerous signs and symptoms, including vomiting, intellectual disability, ketosis, hyperglycinaemia and hyperglycinuria in the neonatal period. The seminal report was published by Dr. Barton Childs in 1961, with the disorder

initially being referred to as 'idiopathic hyperglycinaemia', based on the most unusual biochemical finding being significantly raised plasma glycine (Childs *et al.*, 1961). Their key observation was that when specific amino acids were administered (leucine, isoleucine, valine, threonine, methionine), the patient's symptoms worsened, whereas a decrease in blood acidosis, glycine, and ketones was observed when these amino acids were restricted in the diet (Nyhan *et al.*, 1961).

Interestingly, the first hint of the basic defect underlying idiopathic hyperglycinaemia was borne not from studying the disease itself, but rather the closely related, methylmalonic acidaemia (MMA). Following the discovery of MMA by Oberholzer *et al.* (1967), a study published by a team from Yale (Rosenberg *et al.*, 1968) provided speculation that the primary biochemical lesion in idiopathic hyperglycinaemia was at the level of PCC.

The first report actually using a term close to PA was a case report published by Hommes *et al.* (1968) from the Netherlands, describing fatal 'propionic acidaemia' in a male neonate with severe metabolic acidosis and very high propionic acid in blood (5.4 mmol/L). The boy presented at 60 hours of age with hyperventilation and marked hypotonia but died at 104 hours of age. Initial laboratory studies showed a mild ketosis, and notably a severe metabolic acidosis (pH 6.98). Importantly, Hommes *et al.* applied the gas-liquid chromatography (GLC) method developed by Tanaka *et al.* (1966) employed in the discovery of isovaleric acidaemia (another OA), to measure plasma SCFAs. Although isovaleric acid was absent, there was a large peak coinciding with that of propionic acid, which was calculated as being 40,000 µg/100 mL (5.4

mmol/L) using the chromatogram peak area; Tanaka *et al.* (1966) reported a normal value of 28 µg/100 mL (3.8 µmol/L) propionic acid in healthy control children. Based on this observation, and given that a biosynthetic route of propionate is through the oxidation of OCFAs, Hommes *et al.* performed GLC for free fatty acids and triglycerides on post-mortem liver tissue, finding that C_{15}/C_{17} OCFAs were raised. Taken together, given the block in conversion of propionic acid to methylmalonic acid, and the increased number of OCFAs (C_{15}/C_{17}) detected in liver, the authors postulated that the observed disorder was consequent to an absence of PCC.

Subsequent reports consolidated on the findings by Hommes *et al.* (1968), although their coining of 'propionic acidaemia' was not immediately adopted by all research groups, with some authors still referring to it as idiopathic hyperglycinaemia. Hsia *et al.* (1969) published a study on propionate metabolism in peripheral leukocytes obtained from a patient with 'ketotic hyperglycinaemia', and one with MMA. The authors had renamed the term idiopathic hyperglycinaemia to distinguish the condition from other diseases that manifest hyperglycinaemia, but without ketoacidosis (Wolf *et al.*, 1981). In leukocytes from a ketotic hyperglycinaemia patient, Hsia *et al.* (1969) found normal metabolism of methylmalonate, but a failure to metabolise propionate. In contrast, leukocytes from an MMA patient could not metabolise methylmalonate, but propionate could be successfully metabolised. The authors concluded that the biochemical lesion in ketotic hyperglycinaemia (i.e. PA) was in the carboxylation of methylmalonate and speculated this was due to defective PCC.

The study by Gompertz *et al.* (1970) performed PCC and MCM enzyme activity assays on mitochondria isolated from post-mortem liver in a patient with fatal 'propionic acidaemia'. Gompertz and colleagues found the level of PCC in the patient to be 9.7% that of controls, whilst MCM activity was normal, definitively localising the enzymatic defect in PA to PCC. In a subsequent study, Hsia *et al.* (1971) performed flux isotope tracer studies in cultured fibroblasts from a patient with 'ketotic hyperglycinaemia' and found that they were unable to oxidise propionate-^{14}C to $^{14}CO_2$, but oxidised methylmalonate-^{14}C and succinate-^{14}C normally. PCC activity was determined to be <2% normal activity in the fibroblasts. Furthermore, PCC activity was ~50% of normal in both parents of the patient. Based on the collective evidence from their study, combined with the work of Gompertz *et al.* (1970), Hsia *et al.* (1971) concluded that 'ketotic hyperglycinaemia' and 'propionic acidaemia' are the same disease, caused by defective PCC, and that the defect is inherited as an autosomal recessive trait.

Although propionate and propionyl-CoA are the first and primary metabolites to accumulate with PCC dysfunction, they are challenging substances to measure accurately from a technical standpoint. Thus, the diagnosis of PA has relied on more downstream metabolites directly borne from excess propionate. The markers used clinically today to diagnose PA include elevations of propionyl-carnitine, MeCit, 3-OH-Pr and propionyl-glycine in physiological fluids (Wikoff *et al.*, 2007; Baumgartner *et al.*, 2014). Isotope tracer studies are frequently employed to study propionate metabolism (or rather, IMDs in general), and the discovery of these markers were borne from such studies. The use of MeCit and 3-OH-Pr as clinical markers of PA were

initially reported from the laboratory of Dr William Nyhan in the 1970s through studying the metabolic flux of [*1*-^{14}C] propionate intravenously infused into PA and MMA patients (Ando *et al.*, 1972a; Ando *et al.*, 1972b). Indeed, these markers have stood the test of time, being the principle biochemical markers by which PA is diagnosed today.

1.3.2 Molecular basis of PA

PA is caused by defects in the biotin-dependent enzyme PCC, a α6β6 heterododecamer composed of PCCA and PCCB subunits encoded by the genes *PCCA* and *PCCB* respectively. PA can be caused by mutations in either subunit and missense, nonsense and splicing mutations can occur in both *PCCA* and *PCCB* (Deodato *et al.*, 2006; Richard *et al.*, 2015). More than 150 variant alleles in each gene have been reported (Wongkittichote *et al*., 2017; Human Gene Mutation Database Professional 2020.3 Release). In both genes, missense mutations are predominant (~50%) and functional analyses have been used to identify functionally 'null' mutations associated with the most severe phenotypes, as well as some hypomorphic alleles correlating with milder, late-onset presentations (Desviat *et al.*, 2004; Rivera-Barahona *et al.*, 2018). However, most patients are compound heterozygotes, hindering the establishment of genotype-phenotype correlations in most cases (Pena *et al.*, 2012; Sutton *et al.*, 2012). Regardless of which mutation is involved, the ensuing defect in PCC results in the metabolic and clinical features of PA.

1.3.3 Biochemical features, clinical presentation and management

Biochemical features. PA is an inborn error of propionate catabolism. A biochemical lesion in PCC results in the accumulation of propionate and a myriad of its metabolites, that are detected during plasma and urinary screening, including propionyl-carnitine, MeCit, 3-OH-Pr, propionyl-glycine, and glycine (Baumgartner *et al.*, 2014). Whilst these biomarkers are usually utilised for diagnosis, there is building evidence that these biochemical markers can also act as surrogates for disease activity and predict the clinical course (Armstrong *et al.*, 2021).

Patients transition between periods of fully- or partially-compensated metabolic acidosis, to acute metabolic decompensation. Common laboratory abnormalities include ketonuria, reduced bicarbonate and hyperammonaemia (Deodato *et al.*, 2006; Richard *et al.*, 2015); hyperammonaemia is frequently observed because propionyl-CoA has been shown to inhibit the rate-limiting enzyme of the urea cycle, *N*-acetylglutamate synthase (Armstrong *et al.*, 2021). Notably, serum profiles typically show a raised anion gap (estimated concentration of 'unmeasurable anions') and reduced base excess (amount of base) (Baumgartner *et al.*, 2014). Though not routinely measured, these parameters suggest propionate anions can be accumulating to several millimolar in blood (Table 1.1). Indeed, early case reports have shown that propionic acid can accumulate up to several millimolar (~6 mmol/L) in acutely decompensated patients (Rasmussen *et al.*, 1972; Merinero *et al.*, 1981; Coude *et al.*, 1982).

Table 1.1. Comparative analysis of biochemical parameters in PA patients.

Parameter	Reference range	Compensated PA (cPA)		Uncompensated PA (uPA)	
		Mean*	No. of measurements from 16 patients*	Weighted mean**	No. of measurements from 42 patients**
Arterial pH	7.37 to 7.43	7.39	312	7.37	285
Bicarbonate (mM)	18 to 28	24	288	18.6	392
Anion gap (mM)	3 to 16	16	96	19.9	259
Base excess (mM)	-2 to +3	-0.9	313	-7.62	392
Ammonia (μM)	20 to 100	123	496	206.3	392

Collated serum data from stable (*compensated PA*) and decompensated PA patients (*uncompensated PA*) from two main clinical studies of PA patients. *From Zwickler *et al.* (2014). **Calculated combined weighted mean from Zwickler *et al.* (2014) and Rafique (2013).

Presentation. MMA and PA are often considered in tandem because their enzymatic defects occur along the same metabolic pathway and because they share a similar biochemical profile and presenting symptoms (note, MMA patients uniquely have systemic accumulation of methylmalonyl-CoA and methylmalonic acid) (Fraser & Venditti, 2016). MMA and PA generally manifest with a more severe early-onset neonatal form, and a milder late-onset form presenting later in infancy, childhood, or adolescence (although there is no clear definition of what is considered 'late') (Fraser & Venditti, 2016). In the neonatal onset form, patients typically present with pancytopenia and encephalopathy, as well as a string of metabolic disturbances, including high anion gap metabolic acidosis, ketoacidosis, hyperammonaemia. Chronically, MMA and PA typically present with similar signs and symptoms, such as developmental delay, dystonia, recurrent vomiting with ketoacidosis, and failure-to-thrive. However, critically, MMA and PA differ clinically with disease progression, whereby MMA patients predominantly

develop chronic renal failure, whilst PA patients commonly present with cardiomyopathy and prolonged QT intervals (Baumgartner *et al.*, 2014; Fraser & Venditti, 2016). Since cardiac dysfunction is rarely observed in MMA, it suggests that propionate, the principle substrate that accumulates in PA, may have a unique biological action in the heart to drive disease (Park *et al.*, 2020).

Treatment strategies. There is no cure for PA and patients are treated palliatively. The goals in managing the PA patient are to achieve normal development and prevent metabolic decompensations, whilst providing good quality-of-life care and minimising complications (Baumgartner *et al.*, 2014). Treatment is centred around reducing the propionate load: (i) broad-spectrum antibiotics (to suppress gut floral production of SCFAs/propionate); (ii) low-protein diet (to minimise mitochondrial propionyl-CoA production); (iii) L-carnitine supplementation (Baumgartner *et al.*, 2014).

CoA-esters are less toxic than carnitine-esters (Sauer *et al.*, 2008), and L-carnitine supplementation has been shown to be beneficial by enhancing propionyl group elimination via urine, by converting propionyl-CoA to propionyl-carnitine (in the mitochondria, catalysed by CRAT; Section 1.2.3) (Roe *et al.*, 1984; Davies *et al.*, 1991). Liver transplantation has also shown to be an effective treatment for PA (Baumgartner *et al.*, 2014), although it has a high mortality rate (Charbit-Henrion *et al.*, 2015).

Liver transplantation is discussed further in Section 1.4.3, as it has relevance to the potential mechanisms underlying cardiac dysfunction. More recently, in a study aimed at validating a small molecule therapy for PA patients, it was found that the small molecule HST5040 (2,2-dimethylbutanoic acid), reduced [propionyl-CoA] in a dose-dependent manner in primary hepatocytes isolated from PA patients (Armstrong *et al.*, 2021). The mechanism of HST5040 is hypothesised to involve the conversion of HST5040 to HST5040-CoA, which drives the redistribution of free and conjugated CoA pools. This is thought to reduce [propionyl-CoA] by either slowing the production of propionyl-CoA (by increasing demand on the free CoA pool) or by enhancing the clearance of propionyl-CoA (to replenish the mitochondrial CoA pool) (Armstrong *et al.*, 2021). HST5040 is entering phase 2 clinical trials for PA (and MMA patients) in the United States.

1.4 Cardiac complications in PA

The cardiac pathologies classically encountered in PA patients are dilated cardiomyopathy and long QT syndrome. For completeness, a general description of all cardiac pathologies previously documented in PA is provided in Section 1.4.1, prior to describing these disorders in the context of PA in Section 1.4.2.

1.4.1 Background to the types of cardiac pathologies documented in PA

Maladaptive cardiac hypertrophy. The heart is a remarkably plastic organ which can undergo physiological remodelling (hypertrophy) in response to a variety of stimuli, such as pregnancy and exercise training, in order to normalise wall stress from increased haemodynamic demands (Laplace's law) (Nakamura & Sadoshima, 2018). However, the heart can also undergo adverse hypertrophic remodelling due to pathological insults, for example hypertension (pressure overload) or mitral valve regurgitation (volume overload), which is initially compensatory but eventually contributes to disease pathophysiology and exacerbates the condition. Therefore, it is important that maladaptive hypertrophy is identified. Physiological and pathological remodelling is considered to occur due to distinct signalling pathways (e.g. IGF1/PI3K/Akt in physiological hypertrophy; $G_{q/11}$/PLC/NFAT in pathological hypertrophy) (Nakamura & Sadoshima, 2018).

Hypertrophic cardiomyopathy (HCM). Adverse cardiac hypertrophy can also occur as HCM, a monogenic disease defined as the presence of a hypertrophied, non-dilated ventricle, in the

absence of haemodynamic causes that are capable of eliciting wall thickening (e.g. physiological hypertrophy due to exercise, or pathological hypertrophy due to aortic stenosis) (Lipshultz *et al.*, 2019). The genetic causes of HCM are almost exclusively due to mutations of sarcomeric genes (Watkins *et al.*, 2011). HCM has been associated with several IMDs (Lipshultz *et al.*, 2019).

Left ventricular non-compaction cardiomyopathy (LVNC). LVNC is characterised by an outer compacted myocardial layer, and an inner noncompacted layer featuring prominent trabeculations coincident with large intertrabecular recesses (Arbustini *et al.*, 2016). Trabeculae are finger-like projections, which are a distinguishing feature of the developing embryonic heart. Since early embryonic hearts are devoid of coronary vascularisation, trabeculae serve to facilitate the diffusion of nutrients and oxygen, until they collapse in later stages of maturation ('compaction') and give rise to capillaries (Samsa *et al.*, 2013). LVNC occurs due to a failing of this compaction phase.

Hypokinetic non-dilated cardiomyopathy (HNDC). HNDC is a relatively new category of cardiomyopathy introduced to describe patients that have LV or biventricular systolic dysfunction (hypokinesia, or decreased 'wall-motion'), in the absence of dilatation or hypertrophy, or abnormal loading conditions and coronary artery disease (Pinto *et al.*, 2016).

Dilated cardiomyopathy (DCM). DCM is defined by the presence of left-ventricular (LV) or biventricular dilatation, and systolic dysfunction (based on ejection fraction; EF), in the absence of abnormal loading conditions (hypertension, valve disease), or coronary artery disease. DCM

can occur due to disorders isolated to the heart, for example from mutations in classical 'disease genes' such as the sarcomeric proteins titin (*TTN*) and myosin heavy chain 7 (*MYH7*). However, unlike HCM, it can also be due to mutations in genes accounting for different aspects of cell function, such as those involved in energy production, myofilament activation and Ca^{2+} handling (Watkins *et al.*, 2011). Notably, DCM can also occur due to myocardial damage secondary to systemic diseases, such as metabolic disorders (Pinto *et al.*, 2016; Riemersma *et al.*, 2017; Lipshultz *et al.*, 2019). Key complications with DCM include arrhythmias, decompensated heart failure (HF), and cardiogenic shock (Lee *et al.*, 2017). Diastolic dysfunction can also co-exist with DCM (Jefferies & Towbin, 2010).

Long QT syndrome (LQTS). LQTS is characterised by prolongation of the QT interval in the ECG and occurs due to abnormal cardiac repolarisation. The QT interval is a manifestation of the cardiac action potential which is carried by a number of ionic currents (described further in Section 4.1.1) (Moss & Kass, 2005). QT is usually reported as corrected QT (QTc) which normalises for heart rate (as cardiac repolarisation adapts to heart rate) and aids standardisation. QT prolongation is a major pro-arrhythmic substrate that can cause sudden cardiac death from life-threatening arrhythmias, notably torsades de pointes (polymorphic ventricular tachycardia) and ventricular fibrillation (Moss & Kass, 2005). Clinically, patients often first present after episodes of syncope and/or seizure (Bohnen *et al.*, 2017). LQTS can either be congenital or acquired. There are 15 congenital LQT sub-types (LQT1-LQT15), each associated with their own gene. Acquired LQTS, the most likely form to occur in metabolic

syndromes, can be due to a number of causes, including bradycardia, drugs, and electrolyte disturbances (Antzelevitch & Shimizu, 2002). Non-genetic factors (demographic and environmental) can also act as disease modifiers in LQTS, including for example, autonomic nervous system neurotransmitter signalling (Amin *et al.*, 2013). It has been shown that the reduction or inhibition of the channel encoded by *KCNH2* (hERG; I_{Kr}) accounts for almost all cases of acquired LQTS (Mitcheson *et al.*, 2000; Moss & Kass, 2005).

1.4.2 Typical clinical features of heart disease in PA

Heart disease in the form of cardiomyopathy was first reported in PA by Massoud and Leonard (1993) in a series of 19 paediatric patients. Cardiac complications account for significant morbidity and mortality in PA patients, most commonly in the form of DCM and prolonged QT intervals (Pena *et al.*, 2012; Baumgartner *et al.*, 2014). Increased myocyte size and focal fibrotic lesions have been noted (Pena *et al.*, 2012), implicating possible involvement of adverse cardiac remodelling (Nakamura & Sadoshima, 2018). Although HCM (Mardach *et al.*, 2005) and possibly LVNC (Lee *et al.*, 2009) have been reported, patients typically have DCM. In one of the largest case series to date, cardiomyopathy had a prevalence rate of 23% occurring in 6 out of 26 patients, all of whom had DCM, with a mean age of the onset of 7 years (Romano *et al.*, 2010). The incidence of LQTS has been reported as being as high as 70% (Baumgartner *et al.*, 2007).

More recently, a longitudinal observational monocentric study of 18 PA patients spanning 28 years was published by Kovacevic *et al.* (2020). Here, patients were categorised into 'early' or 'late-onset' (PA symptoms within 28 days, or after 28 days of life). Most patients (14/17; 82%) had an early-onset form of PA, and cardiomyopathy was seen in 7 patients (7/18; 39%), all of whom were from the early-onset cohort. 2 of the patients with cardiomyopathy (2/18; 11%) had DCM (LV dysfunction and dilatation) whilst 5 patients (5/18; 28%) had HNDC (LV dysfunction only). QTc in these patients were mildly prolonged on average (445 ± 18 ms). Interestingly, there was no difference in QTc between early-onset and late-onset patients, and no ventricular arrhythmias were recorded in either group. Furthermore, longer QTc was associated with a larger LV end-diastolic diameter (LVEDD), and critically, the number of metabolic decompensations per case had no significant effect on either the onset of cardiomyopathy or QTc duration. The latter point supports the idea that PA-induced cardiac dysfunction is uniquely due to propionate and its metabolites, as opposed to an effect due to pH disturbances.

Interestingly, diastolic function was also assessed in the study by Kovacevic *et al.* (2020) using Doppler echocardiography, which had not been previously done in PA patients. Pulsed-wave Doppler was used to measure the mitral E/A wave ratio, a marker determined by the left atrial (LA)-LV pressure gradient during different phases of diastole. A higher E/A is predictive of increased LV filling pressure (which would impose greater diastolic wall stress, 'preload'). E-wave velocity (LA-LV pressure gradient in early-diastole) is dependent on LV relaxation, whilst

A-wave velocity (LA-LV pressure gradient during late-diastole) is dependent on LV stiffness and LA contractility (Nagueh, 2020). Kovacevic *et al.* found evidence for diastolic dysfunction (based on E/A ratios) in 61% (11/18) of their PA patient cohort, and diastolic dysfunction typically preceded the cardiomyopathy seen in the 7 patients (7/18; 39%) in this study; 4 patients (4/18; 22%) had diastolic dysfunction in the absence of any LV systolic dysfunction.

Despite the observations in the study by Kovacevic *et al.* (2020), QT prolongation is an established observation in PA (Baumgartner *et al.*, 2007; Grünert *et al.*, 2013; Baumgartner *et al.*, 2014). In a large multi-centre study of 55 paediatric and adolescent PA patients from 16 European metabolic centres, 22% of patients (12/55) had a prolonged QTc (Grünert *et al.*, 2013).

Baumgartner *et al.* (2007) found a higher incidence of prolonged QTc intervals in their longitudinal study of 10 PA patients (median age of 9 years). Patients underwent cardiology investigation including 12-lead ECG, 24-hour Holter monitoring, exercise-tolerance test (where possible) and echocardiography. Prolonged QTc > 440 ms was found in 70% (7/10) of patients, with a markedly prolonged QTc > 460 ms in 60% (6/10) of patients. In this subset of patients, abnormal repolarisation was evident in the form of pre-terminal T wave inversion (which can be a sign of ventricular hypertrophy). 20% (2/10) of these children were found to have arrhythmic events including sinus bradycardia, ventricular ectopic beats (ventricular premature beats) and couplets (salvos). LV function (LV fractional shortening) was reduced in 40% (4/10) of patients with prolonged QTc, and one patient had DCM. Intriguingly, no correlation was

found between prolonged QTc and biochemical and metabolic indices (pH, ammonia, amino acids, acyl-carnitines, etc.).

Although the arrhythmias documented by Baumgartner *et al.* (2007) were relatively innocuous, life-threatening arrhythmias in conjunction with QT prolongation have indeed been documented in PA. A 13-year-old girl (who was diagnosed with PA as a newborn) was reported by Jameson and Walter (2008), with sudden cardiac arrest whilst playing netball. She was successfully resuscitated and her investigatory echocardiogram was normal, with no evidence of cardiomyopathy. However, 24-hour Holter showed QTc prolongation of 450 ms, which was confirmed on exercise testing when QTc increased to ~500 ms during the recovery phase. The patient recovered well and was discharged with β-blockade therapy. However, cardiac arrest in association with cardiomyopathy in PA has also been described. Tan *et al.* (2018) reported a 25-year-old man confirmed with PA at 2-years-of-age, who collapsed whilst jogging. Following cardiopulmonary resuscitation, paramedics identified VF which was successfully defibrillated. Initial investigation showed raised anion gap metabolic acidosis and lactic acidaemia, but normal cardiac biomarkers and serum ammonia. QTc was normal (425 ms) and was unchanged from previous clinic ECGs as part of routine PA follow-up. However, post-arrest echocardiography showed LVEF to be reduced (35%), which was a further decrease from 3 months prior to cardiac arrest (49%).

1.4.3 Liver transplantation for the treatment of PA: insight into mechanisms of cardiac dysfunction

Liver transplantation (LT) requires discussion in more detail as it provides insights into the potential mechanisms of PA-induced cardiac dysfunction. LT has been proposed to be an effective way to treat PA by Leonard (1995). The liver is the major site for propionate metabolism (Wilson *et al.*, 2017). Since PCC is expressed in all tissues of the body, LT is not expected to be a metabolic cure, but rather to stabilise patients and minimise decompensations. Indeed, LT has been shown to be effective in improving clinical outcome in PA and to largely eliminate keto-lactic-acidosis crises (Vara *et al.*, 2011; Critelli *et al.*, 2018). Intriguingly, there have been several studies to suggest that LT can resolve cardiomyopathy in PA, beginning with the seminal report in 2 patients by Romano *et al.* (2010), and indeed, LT is now considered a valid treatment for cardiac disease in PA. More recently, however, Berry *et al.* (2020) reported a child whose cardiomyopathy had recurred following LT. This child was diagnosed with PA at 5 months and presented with signs of congestive HF at 9 years of age; subsequent echocardiogram found DCM with reduced LV EF (20%), and prolonged QTc (480 ms). These complications were successfully managed with inotropes and diuretics and cardiac function resolved. He received a successful LT at 10 years for other clinical indications. However, at 14 years of age, he presented with cardiogenic shock and significantly elevated plasma propionyl-carnitine, 2-methylcitrate and glycine. He died at 18 years with pulmonary oedema secondary to HF.

The pathogenesis of cardiomyopathy in PA is unclear. It appears to be unrelated to metabolic crises, since LT successfully reduces these episodes and improves overall outcomes. It should be noted, however, that propionate metabolites can remain elevated post-transplantation (Kasahara *et al.*, 2012; Berry *et al.*, 2020). This leads to the credence that these 'propionate metabolites' may be the key drivers of cardiac pathogenesis.

There are several reasons why the accumulation of propionate and its metabolites, including propionyl-CoA, propionyl-carnitine, 3-OH-Pr, and MeCit, is central to the pathophysiology of PA: (1) PA patients develop normally *in utero*, despite raised concentrations of propionate metabolites (e.g. propionic acid, 2-methylcitrate), and only develop symptoms following birth, as it is assumed that propionic acid crossing into the maternal circulation will be cleared by maternal hepatic PCC (Dai *et al.*, 2020); (2) management of PA is centred around reducing the propionate-load, through dietary interventions and suppression of the gut flora; (3) although LT has largely shown success in managing PA as a 'clinical syndrome', propionate metabolites remain elevated post-transplant and recurrence of cardiomyopathy has been reported; (4) despite being closely related biochemically, cardiac complications are far more common in PA compared to MMA, where there is less accumulation of propionate and its metabolites (Park *et al.*, 2020).

1.4.4 Possible mechanisms causing cardiac dysfunction in PA

While the underlying mechanisms driving heart disease in PA are not yet fully established, notable achievements have been made recently (Park *et al.*, 2020). There are several pathogenic mechanisms proposed to underpin cardiac dysfunction in PA. Broadly, two 'systems' have been used in studying cardiac dysfunction in PA: (1) *in vitro* systems, using patient-derived cells, immortalised cell lines, or primary rodent cells (which may or may not have been exogenously treated with propionate metabolites); (2) *Pcca*$^{-/-}$ A138T mice, an *in vivo* mouse model of PA generated by Dr Michael Barry (Mayo Clinic, US).

The *Pcca*$^{-/-}$ A138T mouse is a hypomorphic model of PA, which instead of murine *Pcca*, expresses human *PCCA* with an A138T nucleotide point mutation. This mutation has been identified in human PA patients that have mild-to-moderate symptoms, resulting in reduced PCCA protein levels and a hypomorphic version of PCC (Ugarte *et al.*, 1999; Desviat *et al.*, 2004). *Pcca*$^{-/-}$ A138T mice are estimated to have ~2% PCC activity as measured by a radiometric activity assay in liver homogenates (Guenzel *et al.*, 2013). Since knockout of *Pcca* results in neonatal lethality, this residual level of activity results in the necessary minimum clearance of propiogenic substrates to allow these animals to survive to adulthood. Guenzel *et al.* (2013) found these animals present with a mild-to-moderate PA phenotype, and have raised plasma markers characteristic of PA, such as propionyl-carnitine and MeCit. Furthermore, these animals have raised *Nppb* in their hearts, which encodes for the hormone brain-type natriuretic peptide (BNP), a classical biomarker released during haemodynamic stress (e.g. when ventricles are dilated, hypertrophic,

or subjected to increased wall tension) (Braunwald, 2008). More detail on this mouse model is provided in Section 1.5.

The possible mechanisms causing cardiac dysfunction in PA are summarised below.

1.4.4.1 Energetic deficiency and oxidative stress

The heart is a highly energy-demanding organ, with an average adult human heart consuming ~6 kg of ATP per day, despite only having enough stored for a few heartbeats (Ritterhoff & Tian, 2017). Thus, perhaps not surprisingly, mitochondrial dysfunction has been implicated as a major driver of pathological cardiac remodelling in cardiomyopathy (Ritterhoff & Tian, 2017). Although decreased energy supply is considered the main consequence of mitochondrial dysfunction, recent advances have shown that it contributes to the pathogenesis of HF, beyond the idea of simply inadequate energy provision (Zhou & Tian, 2018). The available evidence suggests mitochondrial dysfunction is an underlying aetiological factor contributing to cardiomyopathy in PA, in the form of ultrastructural changes, electron transport chain (ETC) deficiency, oxidative stress, and metabolic dysfunction (Pena *et al.*, 2012; Richard *et al.*, 2015).

The accumulation of propionate metabolites can impair or interfere with mitochondrial biochemical pathways. Propionyl-CoA has been shown *in vitro* to be a major mitochondrial toxin in PA and to impair oxidative phosphorylation through the synergistic inhibition of pyruvate dehydrogenase complex, α-ketoglutarate dehydrogenase complex and ETC complex III (Schwab *et al.*, 2006). Deficiencies in ETC complex I (Mardach *et al.*, 2005) and ETC

complexes III/IV (de Keyzer *et al.*, 2009) have also been detected in the hearts of PA patients. Baruteau *et al.* (2014) presented a PA patient with severe DCM who was found to have enlarged mitochondria, atypical cristae, reduced complex IV activity, as well as markedly reduced coenzyme Q_{10} (ubiquinone) on myocardial biopsy. Interestingly, the DCM improved with ubiquinone supplementation, which may be related to positive effects from reducing oxidative stress *(see next)*.

There is a wealth of literature supporting that oxidative stress has a detrimental effect on the heart, including pathological remodelling, fibrosis, and contractile dysfunction (Takimoto & Kass, 2007). Since oxidative phosphorylation is inhibited in PA, a redox imbalance and increased oxidative stress are predicted for PA hearts. Indeed, oxidative stress has been implicated as a mechanism involved in the pathophysiology of PA (Richard *et al.*, 2018), which is likely to be involved in PA-induced cardiac dysfunction. Increased intracellular hydrogen peroxide has been detected in PA patient fibroblasts, indicating increased oxidative stress in PA (Gallego-Villar *et al.*, 2013). Increased superoxide production has been shown in the hearts of *Pcca*$^{-/-}$ A138T mice (Gallego-Villar *et al.*, 2016). In a subsequent study, treatment of *Pcca*$^{-/-}$ A138T mice with antioxidants was found to normalise the increase in expression of *Nppb* in the heart (Rivera-Barahona *et al.*, 2017a).

1.4.4.2 Metabolic dysfunction

Using an isotope-based metabolic flux approach in Langendorff-perfused rat hearts, Wang *et al.* (2018) found that the perfusion of propionate led to an accumulation of propionyl-CoA. This

accumulation caused significant mitochondrial CoA trapping and altered pool sizes of Krebs cycle intermediates. FAO was inhibited, with a concomitant increase in glucose oxidation, despite glycolysis being unchanged (i.e. switch from oxidative to glycolytic metabolism). Interestingly, supplementing the hearts with L-carnitine did not relieve the CoA trapping or reverse the fuel-switch mediated by propionate, because the authors showed that the heart lacks the specific enzyme that catalyses this reaction. Thus, there is good evidence for metabolic dysfunction contributing toward cardiac dysfunction in PA. Furthermore, this hindering of cardiac energy metabolism is likely to be exacerbated by MeCit, a commonly elevated PA metabolite, which has been shown to act as an inhibitor of Krebs cycle enzymes (Cheema-Dhadli *et al.*, 1975).

1.4.4.3 MicroRNAs

Whilst only 3% of the human genome codes for proteins, the remainder is still extensively transcribed, producing long non-coding RNAs (>200 nucleotides) and microRNAs (miRNAs; ~22 nucleotides), which are recognised to play important roles in transcriptional regulation (Romaine *et al.*, 2015). miRNAs are short, non-coding, single-stranded RNAs that anneal with complementary mRNA sequences to suppress protein expression. There are a plethora of miRNAs that have been discovered which have been implicated as key players in the pathophysiology of heart disease, and are uniquely detected in different cardiac pathologies like arrhythmia, cardiac hypertrophy and heart failure (van Rooij & Olson, 2012).

Dysregulated miRNAs have also been detected in a range of tissues (e.g. brain, liver) in *Pcca*$^{-/-}$ A138T mice (Rivera-Barahona *et al.*, 2017b). More recently, Fulgencio-Covian *et al.* (2020) performed analysis of cardiac-enriched miRNAs in a cohort of PA patient plasma and in two experimental models: (1) the hearts of *Pcca*$^{-/-}$ A138T mice, and (2) propionate treatment in HL-1 cells, an immortalised atrial cell line. The authors found a significant upregulation of several miRNAs involved in cardiac pathology in *Pcca*$^{-/-}$ A138T mouse hearts, for example miRNA-22 which has been implicated in cardiac hypertrophy and fibrosis that acts via the PI3K/AKT pathway. To support the relevance of these findings, Fulgencio-Covian *et al*. found upregulation of several genes involved in the PI3K/AKT pathway that are important for the heart (e.g. *Fos*, *Jun*). Finally, experiments were performed on HL-1 cells treated with propionate, which confirmed the upregulation of several miRNAs increased in PA mice, providing evidence that propionate is a toxic metabolite in PA.

1.4.4.4 Gene expression: histone acetylation and propionylation

DCM is frequently inherited through mutations in the 'classical DCM genes' such as *TTN* (titin) and *LMNA* (lamin A/C) (Pinto et al., 2016). Although the evidence to-date shows that cardiomyopathy in PA occurs without a change in expression of the DCM genes, a possibility remains that PA acts as a modifier of an 'unknown' DCM-related gene, or of genes critical to normal cardiac function (Riemersma *et al.*, 2017). Despite this, there is substantial evidence suggesting propionate can affect gene expression.

Post-translational modifications of histone proteins, in the form of acylation, is a major mechanism of regulating gene expression, and epigenetic alternations in cardiac gene expression programmes are known to be involved in adverse cardiac remodelling (Liu & Tang, 2019). It is established that acetyl-CoA is not the only metabolite that can participate in this process, but rather a plethora of metabolites such as butyryl-CoA, succinyl-CoA and notably, propionyl-CoA (Sabari *et al.*, 2017). There are two pathways implicated as potential mechanisms in the epigenetic regulation of gene expression in PA: (1) the inhibition of histone deacetylases (HDACs) by propionate (Waldecker *et al.*, 2008; Koh *et al.*, 2016), promoting histone acetylation, which is known to be involved in pathological cardiac remodelling (Bagchi & Weeks, 2019); (2) propionyl-CoA acting as a substrate for lysine acetyltransferases to result in histone propionylation. With respect to SCFAs, butyrate (C_4) is a well-established potent inhibitor of HDACs, and propionate (C_3) has also been shown to have HDAC inhibition properties (Waldecker *et al.*, 2008). Therefore, it would be expected that the accumulation of propionate in PA would result in HDAC inhibition, and thus an increase in histone acetylation. Histone 3 propionylation at lysine 14 (H3K14pr) has recently shown to be a modification that is a signature of transcriptionally active chromatin. The study by Kebede *et al.* (2017) showed that H3K14pr is present in the liver of *Pcca*$^{-/-}$ A138T mice and that it is mediated *in vivo* by KATs. They also showed that H3K14pr levels return to baseline wild-type levels in those mice that underwent *PCCA* gene therapy.

1.5 Biological models used in this thesis

The experimental models used in this thesis can be divided into two categories, based on the status of PCC:

- **Mouse model:** Where PCC is disrupted *in vivo* in genetically modified mice and an intrinsic source of propionate accumulates (FVB *Pcca*$^{-/-}$ A138T);
- **Propionate-treated cardiomyocytes:** Where PCC is intact in wild-type (WT) animals, but exogenous propionate is applied to cells *in vitro*.

The aim for using the **mouse model** was to first characterise the consequences of dysregulated propionate metabolism (PCC disruption) on the heart *in vivo.* The obvious advantage of this system is that it is the most physiological model, which recapitulates the biochemical changes in PA patients that have hypomorphic PCC activity (Guenzel *et al.*, 2013). However, since with disrupted PCC, accumulating propionate and propionyl-CoA are enzymatically converted to downstream propionate-related metabolites, (e.g. MeCit), it would be unknown whether these metabolites contribute to any observed cardiac phenotype. Experiments conducted on **propionate-treated cardiomyocytes** are intended to circumvent this problem, but also apply a level of stimulus that is likely to engage all relevant pathways fully. By exposing WT cardiomyocytes to high levels of propionate (still within reported levels in PA) and correlating against findings made in the mouse, it is possible to attribute responses to propionate, as opposed to other chemicals or secondary compensatory changes. An overview of biological models used in this thesis is presented in Table 1.2.

Table 1.2. Overview of biological models used in this thesis and example readouts.

Model	Abbreviations used	Sample type	Readouts & *techniques*
8-week-old young adult *Pcca*$^{-/-}$ A138T FVB mouse	*Pcca*$^{+/+}$ A138T WT controls, **amWT** *Pcca*$^{-/-}$ A138T PA animals, **amPA** Adult mouse ventricular myocytes, **AMVM**	*In vivo*	• Cardiac function: *ECG, cine-MRI.*
		Primary ventricular myocytes	• Physiology: *[Ca^{2+}]$_i$.*
		Ventricular tissue	• Metabolic profile: *metabolomics*; • Protein biochemistry: *protein expression levels, histone PTMs;* • Transcriptomic profile: *RNA-sequencing.*
		Plasma	• Metabolic profile: *metabolomics*
Adult WT SD rat	Adult rat ventricular myocytes, **ARVM**	Primary ventricular myocytes	• Physiology: *[Ca^{2+}]$_i$;* • Histone PTMs: *immunofluorescence*
Neonatal WT SD rat	Neonatal rat ventricular myocytes, **NRVM**	Cultured ventricular myocytes	• Physiology: *[Ca^{2+}]$_i$, membrane potential;* • Histone PTMs: *ELISA, immunoblotting, immunofluorescence;* • Transcriptomic profile: *RNA-sequencing.*

am, adult mouse; $[Ca^{2+}]_i$, intracellular Ca^{2+} concentration; ECG, electrocardiogram; ELISA, enzyme-linked immunosorbent assay; FVB, Friend virus B-type susceptibility; MRI, magnetic resonance imaging; PA, propionic acidaemia; PTM, post-translational modifications; SD, Sprague Dawley; WT, wild-type.

1.5.1 *In vivo* model of PCC disruption: FVB *Pcca*$^{-/-}$ A138T hypomorphic mouse

Background to the PA mouse model. PCC is encoded in humans by the genes *PCCA* and *PCCB*. Knock-out of the murine orthologue *Pccb* is embryonically lethal (MRC Harwell, International Mouse Phenotyping Consortium). In contrast, animals with complete knock-out of *Pcca* (*Pcca*$^{-/-}$) develop normally and have no phenotypic abnormalities at birth. However, they die due to accelerated ketoacidosis within 24-36 hrs post-natal (Miyazaki *et al.*, 2001). These

animals can be rescued by liver-specific PCC expression, the main metabolic organ of propionate (Wong *et al.*, 2006; Wilson *et al.*, 2017). In order to understand the pathophysiology of PA, a model is required which survives beyond 36 hrs. Therefore, a mouse was generated in which PCC was dysfunctional, yet retained the minimum level of activity required for survival: the *Pcca*$^{-/-}$ A138T mouse model, reported by Guenzel *et al.* (2013) from the laboratory of Dr Michael Barry (Mayo Clinic, US). *Pcca*$^{-/-}$ A138T mice have a full knock-out of murine *Pcca*, but survive into adulthood due to the human A138T transcript (encoding a hypomorphic version of *PCCA*). Since ~50% of PA patients are observed to have hypomorphic enzyme activity, models such as *Pcca*$^{-/-}$ A138T have clinical value (Guenzel *et al.*, 2013).

Pcca$^{-/-}$ A138T animals are estimated to have ~2% PCC activity as measured by a radiometric activity assay in liver homogenates (Guenzel *et al.*, 2013). Although this residual level of activity may seem too low, it has been shown to result in the necessary minimum clearance of propionate and propiogenic substrates, exemplified by the fact that these animals are able to survive to adulthood. Importantly, these mice present with a mild PA phenotype. Guenzel *et al.* (2013) found these animals have raised plasma markers characteristic of PA such as MeCit and propionyl-carnitine. There is also evidence for these biomarkers being detected at higher levels in female vs. male mouse plasma, suggesting an effect of sex in PA (Guenzel *et al.*, 2015).

Generation of the model. Traditionally, there are two distinct technologies for modifying the mouse genome: gene targeting (knock-out/knock-in) and insertional transgenesis (Davis *et al.*, 2012). The *Pcca*$^{-/-}$ A138T model was created by knockout of *Pcca* through homologous

recombination (Miyazaki *et al.*, 2001), and transgenic insertion of human *PCCA* cDNA bearing an A138T nucleotide point mutation (Guenzel *et al.*, 2013), a mutation originally identified in human PA patients with mild-to-moderate symptoms (Ugarte *et al.*, 1999; Desviat *et al.*, 2004). This mutation in exon 5 results in reduced PCCA protein levels in patient cells, and thus reduced PCC activity. *PCCA* A138T cDNA was generated and cloned into a vector containing a CAG promoter (cytomegalovirus early enhancer; a ubiquitously active promoter to drive expression across all tissues) and an internal ribosome entry site-enhanced green fluorescent protein (IRES-EGFP) cassette, to aid in phenotyping founder mice. This cassette was microinjected into fertilised eggs of FVB (friend virus B-type susceptibility) mice, a commonly used background strain for transgenesis. A schematic of the generation strategy is shown in Figure 1.3.

Transgene copies. As this colony was in-bred, all animals had ≥ 1 copy of the transgene (determined by qPCR; Transnetyx Genotyping, US); indeed, the transgene integrates in a random manner within a site of the genome, as either a single copy, or (more commonly) as concatemers (Davis *et al.*, 2012). Although the number of transgene copies was not controlled for in the work presented in this thesis, it is appreciated that different levels of the mutant allele may affect PCC expression levels and lead to biological variability (Davis *et al.*, 2012).

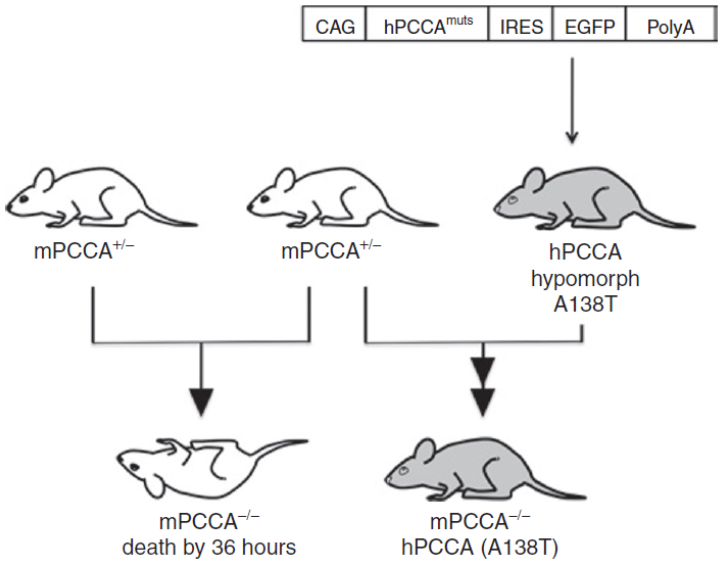


Figure 1.3. Strategy for the generation of *Pcca*$^{-/-}$ A138T hypomorphic mice. The schematic of the insertion cassette that was microinjected into fertilised eggs of FVB mice is shown *(top)*. The A138T hypomorph construct ('mut') was injected, with an integrated IRES-EGFP DNA sequence, to aid in genotyping founder mice *(bottom)*. CAG, cytomegalovirus early enhancer; EGFP, enhanced green fluorescent protein; hPCCA, human *PCCA*; IRES, internal ribosome entry site; mPCCA, mouse *Pcca*; muts, A138T point mutation. Figure from Guenzel *et al.* (2013).

Breeding strategy and animals used. The breeding strategy used in this thesis was based on murine *Pcca* expression (vs. a strategy based on transgene copy number). All other studies published to date using this mouse model performed experiments on pups born from homozygous (*Pcca*$^{-/-}$ A138T) dams. However, this may not be considered physiological. Since PA is a multi-organ system disorder associated with severe morbidity (as well as deficits in neurological development), PA patients do not have pregnancies. That is, exposure to elevated levels of propionate *in utero* is not physiological. Therefore, to model the consequences of propionate *accumulation*, as is the case in PA patients, only heterozygous (*Pcca*$^{+/-}$ A138T) dams which are phenotypically normal, were used for breeding. Indeed, pups from homozygous

dams were developmentally stunted vs. pups from heterozygous dams, which only showed a PA phenotype from weaning (Guenzel *et al.*, 2013).

All animals used in this thesis were either *Pcca* wild-type (*Pcca*$^{+/+}$ A138T) for control experiments, or homozygous knockout (*Pcca*$^{-/-}$ A138T) animals, referred to as amWT and amPA respectively, for wild-type adult mouse (amWT) and adult mouse with propionic acidaemia (amPA) (Table 1.2). Finally, due to significant evidence for a sex effect in PA (Guenzel *et al.*, 2015), as well as a sex effects in normal heart physiology and cardiometabolic disorders (Murphy *et al.*, 2017; Gerdts & Regitz-Zagrosek, 2019), experiments were sex-balanced (in contrast to other studies using this model which typically focussed on males).

Experimental timepoint. The main experimental timepoint in this thesis was young adults that were 8 weeks of age. The primary rationale for selecting this timepoint was to capture early changes that might precede compensatory changes, or more complex remodelling related to chronic oxidative damage and micro-RNAs, noted in older 5 to 8-month-old amPA from homozygous dams (Rivera-Barahona *et al.*, 2017a; Rivera-Barahona *et al.*, 2017b; Fulgencio-Covian *et al.*, 2020; Tamayo *et al.*, 2020). Indeed, PA is a disease predominantly affecting neonates, infants and pre-adolescents. In order to best model the human condition, arguably even 8 weeks could be regarded as too old; mice reach sexual maturity ~ 6 weeks of age (Dutta & Sengupta, 2016). However, since amPA animals have a partial dysfunction of PCC, changes may occur on a slower timescale, compared to human PA. Therefore, an aim of Chapter 3, the first results chapter, was to confirm whether 8 weeks was an appropriate timepoint.

1.5.2 *In vitro* models of propionate actions: Wild-type SD rats

Wild-type Sprague-Dawley (SD) rats were used for the *in vitro* experiments to determine the actions of propionate. The idea of comparing results from a rat and mouse model, may seem problematic. However, the rat and mouse are similar, both in their genome (Gibbs *et al.*, 2004) and in their cardiac physiology (e.g. electrophysiology, excitation-contraction coupling) (Bers, 2002a). Furthermore, more cardiomyocytes can be isolated from each rat, due to their greater size, therefore reducing the overall number of animals required (3R principle of animal research; NC3Rs, UK). Therefore, WT rats were favoured as a replacement model to WT mice.

1.6 Central hypothesis

Propionate is an epigenetic modifier that, when abnormally elevated, can drive cardiac dysfunction by the differential expression of cardiac genes.

1.7 Summary and thesis aims

Cardiac complications account for significant morbidity and mortality in PA. However, the molecular mechanisms underlying this dysfunction, particularly in the early phase prior to compensatory measures, are yet to be described. The only *in vivo* model available to study PA, and the consequences of dysregulated propionate metabolism, is the *Pcca*$^{-/-}$ A138T mouse model, in which PCC is disrupted (retaining ~2% of wild-type activity) (Guenzel *et al.*, 2013). However, there is little information available on how (or whether) the heart is affected in these animals. Therefore, the aims of this thesis were as follows:

i. Confirm PCC deficiency has an effect on the metabolic profile of the heart and plasma, in line with the PA phenotype;
ii. To characterise the effect of PCC deficiency on *in vivo* cardiac electrophysiological and contractile function at the organ level;
iii. To relate the *in vivo* phenotype to changes taking place at the cellular level, with respect to Ca^{2+} signalling, a key determinant of contraction;
iv. To describe changes in cardiac gene expression, and identify those that are a likely consequence of propionate, as a possible epigenetic driver of cardiac dysfunction.

Chapter 2. General methods

An overview of methods and biological resources used throughout this thesis are provided in Chapter 2. Any chapter-specific details are provided where appropriate.

2.1 Animal models

2.1.1 General overview of animal procedures

All animal procedures conducted in this thesis followed The Animals (Scientific Procedures) Act 1986. Wild-type adult and neonatal Sprague Dawley (SD) rats were obtained from Charles River UK Ltd. Mouse experiments using the *Pcca*$^{-/-}$ A138T model were authorised under a Project Licence (PPL #P01A04016). The use of this model at the University of Oxford was agreed by the original author Dr Michael Barry (Mayo Clinic, US). Mice to establish the colony were provided by Dr Lourdes Desviat (Centro de Biología, Madrid). Mice were bred and housed in individually ventilated cages at the University of Oxford Biomedical Services Unit. Animal husbandry was provided by facility technicians. All animals were sacrificed using an appropriate method of humane killing (Schedule 1), and where possible, following >24 hours acclimatisation to the Sherrington Building (site of work) to minimise the stress response.

2.1.2 Genotyping *Pcca*$^{-/-}$ A138T mice

All mice used in this thesis were from the *Pcca*$^{-/-}$ A138T mouse line generated by Guenzel *et al.* (2013). Mice used were either wild-types (*Pcca*$^{+/+}$ A138T) for control experiments, or homozygous (*Pcca*$^{-/-}$ A138T) animals, herein referred to as amWT and amPA respectively. Only heterozygous *Pcca*$^{-/+}$ A138T dams were used for breeding. The number of copies of the transgene in both homozygous and wild-type mice was not controlled for in experiments.

To genotype mice, pups were ear-clipped by facility technicians after post-natal day 10 and stored at -20°C until use. Clips were digested overnight at 55°C with gentle mixing (500 RPM) (ThermoMixer C, Eppendorf) in 100 µL of digestion buffer: 50 µg w/v Proteinase K, 10 mM Tris pH 8.3, 5 mM EDTA, 300 mM sodium acetate, 1% v/v Triton-X 100. Post-digestion, clips were centrifuged at 380 RCF for 2 mins at room temperature. The supernatant was diluted 1:5 in 10 mM Tris (pH 8.3) and 2 µL of digestion product was used for each polymerase chain reaction (PCR).

Due to the highly different amplicon sizes and annealing temperatures, a duplex reaction was not possible and separate PCRs were required to identify the wild-type and mutant alleles. PCRs were set up on ice and performed with a thermal cycler (SimpliAmp, Applied Biosystems) using reaction conditions outlined in Table 2.1. For identification of the endogenous *Pcca* allele, primers against *Pcca* intron 3 (CTAGAAAGTAAATGTTTACCAGAA) and *Pcca* exon 4 (AGAACTGGC ATCAACATCACTGTG) was used. For identification of the knockout allele, primers were used against the neomycin resistance gene (TGCTCCTGCCGAGAAAGTATCCATCATGGC) and for *PCCA* intron 3 upstream of the knocked-out exons (GGCAGCAAAGATGGTCTCAGGC). A PCR mix containing *Taq* DNA polymerase was used (Bioline BioMix 2x PCR mix) and the final concentration of primers in the reaction was 500 nM. A non-template control reaction using water instead of DNA sample was performed for each genotyping experiment.

For electrophoresis of PCR products, a 1.5% agarose gel was hand-cast using TAE buffer (in mmol/L): 40 Tris-base, 19 acetate, 1 EDTA. To enable fluorescent detection of DNA, GelRed nucleic acid stain, a non-mutagenic and non-hazardous alternative to ethidium bromide, was added at 1:10,000 to the molten agarose (Biotium, #41003). 12.5 µL of each PCR product was loaded and electrophoresed for 50 minutes at 120 V in TAE buffer. A 100 bp ladder was loaded as reference (New England Biolabs, #N0551S). Bands were visualised using a UV transilluminator.

Table 2.1. Genotyping PCR conditions.

Reaction stage	*Wild-type allele reaction*	*Knockout allele reaction*
Stage 1 *Initial denaturation*	94°C / 3 mins (x 1 cycle)	94°C / 3 mins (x 1 cycle)
Stage 2	(x 35 cycles)	(x 40 cycles)
Denaturation	94°C / 30 secs	94°C / 30 secs
Annealing	56.5°C / 30 secs	68°C / 30 secs
Extension	72°C / 1 min	72°C / 3 mins
Stage 3 *Final extension*	72°C / 10 mins (x 1 cycle)	72°C / 10 mins (x 1 cycle)
Approximate amplicon size	340 bp	900 bp

Bp, base pair.

2.2 Experimental methods

2.2.1 Animals and euthanisation

Adult mouse. All adult mouse experiments used male and female 8-week-old homozygous mice and wild-type litters from the *Pcca*$^{-/-}$ A138T colony, bred and maintained at the University of Oxford Biomedical Services Unit. Euthanisation was performed by a lethal overdose of sodium pentobarbital injected intraperitoneally (IP) pre-mixed with sodium heparin to prevent clotting (Schedule 1 method). The mix was prepared at a 2:1 ratio of pentobarbital (200 mg/mL) to heparin (5,000 IU/mL). An appropriate volume (~200-300 µL) of the anaesthetic mix was injected IP per mouse via a 26 G needle (adjusted for animal weight). Death was confirmed by cervical dislocation in myocyte isolation studies and by exsanguination in plasma collection studies.

Adult rat. All adult rat experiments used male wild-type SD rats (275-300 g) obtained from Charles River UK. Schedule 1 in adult rats was also performed by IP injection of 1 mL of sodium pentobarbital/heparin (as above) via a 23 G needle. Death was confirmed by cervical dislocation.

Neonatal rat. All neonatal rat experiments used multiple wild-type post-natal day 1-2 SD rats also obtained from Charles River UK. Neonatal pups were sacrificed by cervical dislocation and death confirmed by exsanguination.

2.2.2 Primary adult ventricular myocyte isolation

Primary adult ventricular myocytes from the rat and mouse (ARVM and AMVM respectively) were isolated by Langendorff-perfused hearts *in vitro* using a combination of enzymatic (~1 mg/mL Collagenase, Worthington Biochemical Corporation; 0.025 mg/mL Type XIV Protease, #P5147, Sigma-Aldrich/Merck) and mechanical dispersion. The method used to isolate adult ventricular myocytes from the mouse and rat are principally similar. Any technical differences are outlined in Sections 2.2.2.1 and 2.2.2.2. Although the isolation solutions used for the two species were different, the modifications made to the respective stock solution was the same (Table 2.2).

Table 2.2. Solutions used for adult myocyte isolations.

Stock solution	Components
Adult mouse isolation stock solution	Made with ultra-pure 18.2 MΩ water containing (in mmol/L): 130 NaCl, 5.6 KCl, 5 HEPES, 0.45 NaH_2PO_4, 10 glucose, 20 taurine, 3.5 $MgCl_2$; pH adjusted to 7.40 at 37 °C with NaOH.
Adult rat isolation stock solution	Made with ultra-pure 18.2 MΩ water containing (in mmol/L unless stated otherwise): 120 NaCl, 4 KCl, 10 HEPES, 2 NaH_2PO_4, 11 glucose, 20 taurine, 1.2 $MgCl_2$, 0.0173% v/v pyruvic acid; pH adjusted to 7.40 at 37 °C with NaOH.
Modified solution	**Components added to stock solution**
Pre-digestion solution	5 I.U/mL sodium heparin
Enzyme solution	~1 mg/mL Collagenase (Type IV in mouse, Type II in rat) ~0.025 mg/mL Type XIV Protease
Resuspension solution 1	200 µM $CaCl_2$ 1% v/v bovine serum albumin
Resuspension solution 2	500 µM $CaCl_2$
Resuspension solution 3	1 mM $CaCl_2$

Isolation and cannulation of the heart. In both species, following Schedule 1, the thoracic cavity was rapidly accessed to expose the heart. After blunt dissection of the pericardium, the aorta was cut and cannulated in pre-digestion solution. Retrograde Langendorff perfusion was performed at 37°C at a constant flow rate (provided in subsequent sections) using a peristaltic pump (Gilson MINIPULS3). Before proceeding with tissue digestion, the hearts were perfused with pre-digestion solution until the coronary effluent was clear.

Enzymatic digestion and preparation of cardiomyocytes. After residual blood in the coronary vessels had cleared, the hearts were enzymatically digested by perfusing with enzyme solution containing collagenase and protease. The heart was digested in Ca^{2+}-free solution, and to prevent Ca^{2+} paradox (Piper, 2000), isolated myocytes were re-introduced to Ca^{2+} in a stepwise manner (beginning at 200 µM). Following digestion of the heart, the major vessels and atria were removed and the remaining (left and right) ventricular tissue was placed into the first resuspension solution containing 200 µM $CaCl_2$ and 1% BSA to quench enzymatic activity. The tissue was finely minced and cells were collected by filtering through a 400 µm nylon mesh. The remaining tissue was further dissociated through subsequent digestions for 5 mins using 5-7 mL of enzyme solution (at 37°C) combined with gentle trituration. These digestions were repeated up to 5 times and filtered cells were collected separately after each digestion; viable myocytes were typically yielded in later digestions. The collected cells were centrifuged at 40 RCF for 1 min in a swing-out rotor centrifuge (O'Haus, FC5714). The supernatant (containing dead cells) was removed and replaced with resuspension solutions containing 500 µM $CaCl_2$,

followed by a final step to 1 mM $CaCl_2$. Cells were allowed to settle by gravity between these resuspension steps. Myocytes were allowed to rest in 1 mM Ca^{2+} for ≥ 30 mins prior to use. Only quiescent, Ca^{2+}-tolerant myocytes that were rod-shaped with clear striations, were selected for experiments.

2.2.2.1 Adult mouse ventricular myocytes (AMVMs)

Cannulation of mouse hearts was performed '*in vivo*' under magnification using a stereoscopic microscope and a halogen cold light source (Schott, KL1500 LCD). The time from extracting the heart to steady-state perfusion was ~4 mins. After accessing the mediastinum, extraneous organs (lungs, thymus) and pericardium was dissected with spring scissors (FST, #10525-10). A 4-0 U.S.P silk suture (Look SP116) was threaded under the aorta using 5/45 angled forceps (FST, #11251-35). The aorta was cut and cannulated onto a blunted 23G hypodermic needle with two double-knotted sutures. After gently flushing the heart with pre-digestion solution (via a 2 mL syringe), the cannula was mounted onto a Langendorff system and perfused at 2 mL/min (pump set to 3.75 RPM, Gilson MINIPULS 3) (Figure 2.1). The enzyme solution was not recycled during perfusion. The preparation of myocytes from the digested heart was as described in Section 2.2.2.

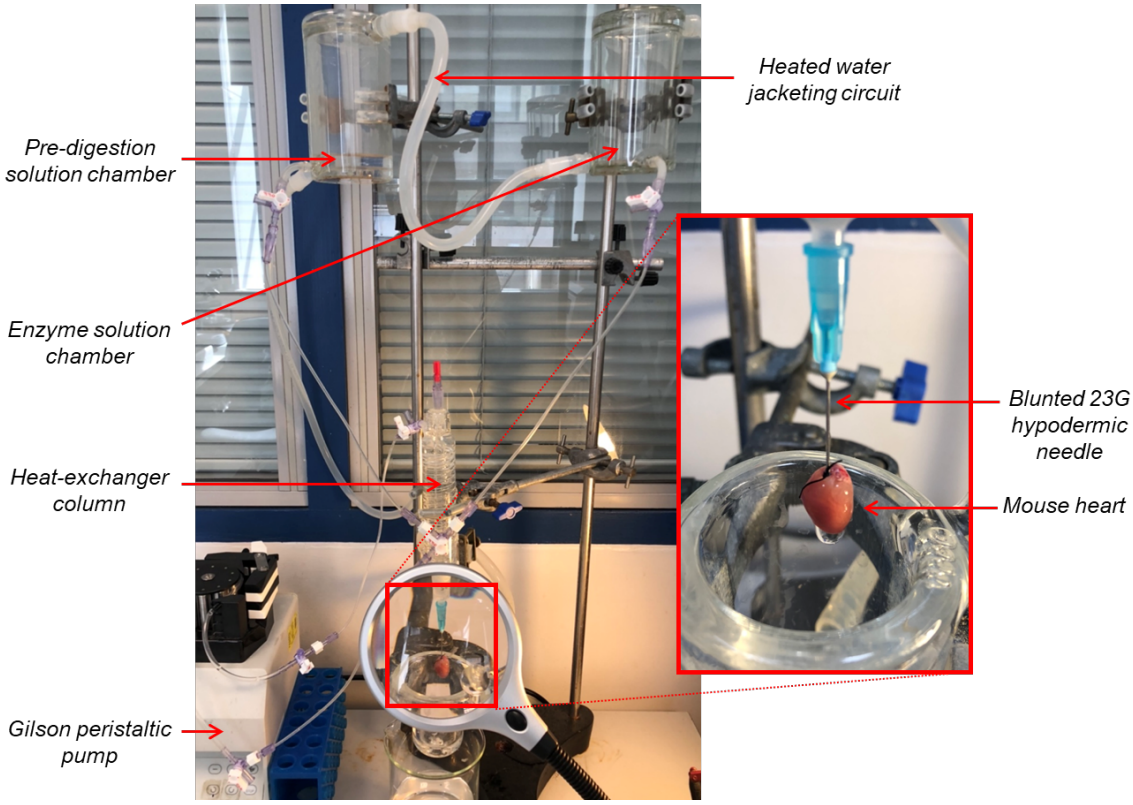


Figure 2.1. Langendorff apparatus for the isolation of adult mouse myocytes. The Langendorff system is warmed by the water jacketing circuit to ensure the solution temperature is 37°C when it enters the heart. Hearts were perfused through a converted 23 G hypodermic needle at a constant flow rate via a peristaltic pump.

2.2.2.2 Adult rat ventricular myocytes (ARVMs)

Cannulation of rat hearts was performed '*ex vivo*' and the time from extracting the heart to steady-state perfusion was ~2 mins. The heart was gently massaged in pre-digestion solution after excision and any extraneous tissue (e.g. lungs, thymus) and vessels were dissected away. Care was taken to ensure the pericardium was removed. The heart was secured with surgical knots onto a blunted 19G hypodermic needle mounted on the Langendorff system (Figure 2.2). A well-perfused heart had a perfusion pressure of ~30-40 mmHg, measured with a mercury manometer. Hearts were perfused at 8 mL/min (15 RPM, Gilson MINIPULS 3) and the enzyme

solution was recycled during perfusion. The preparation of myocytes from the digested heart was as described in Section 2.2.2.

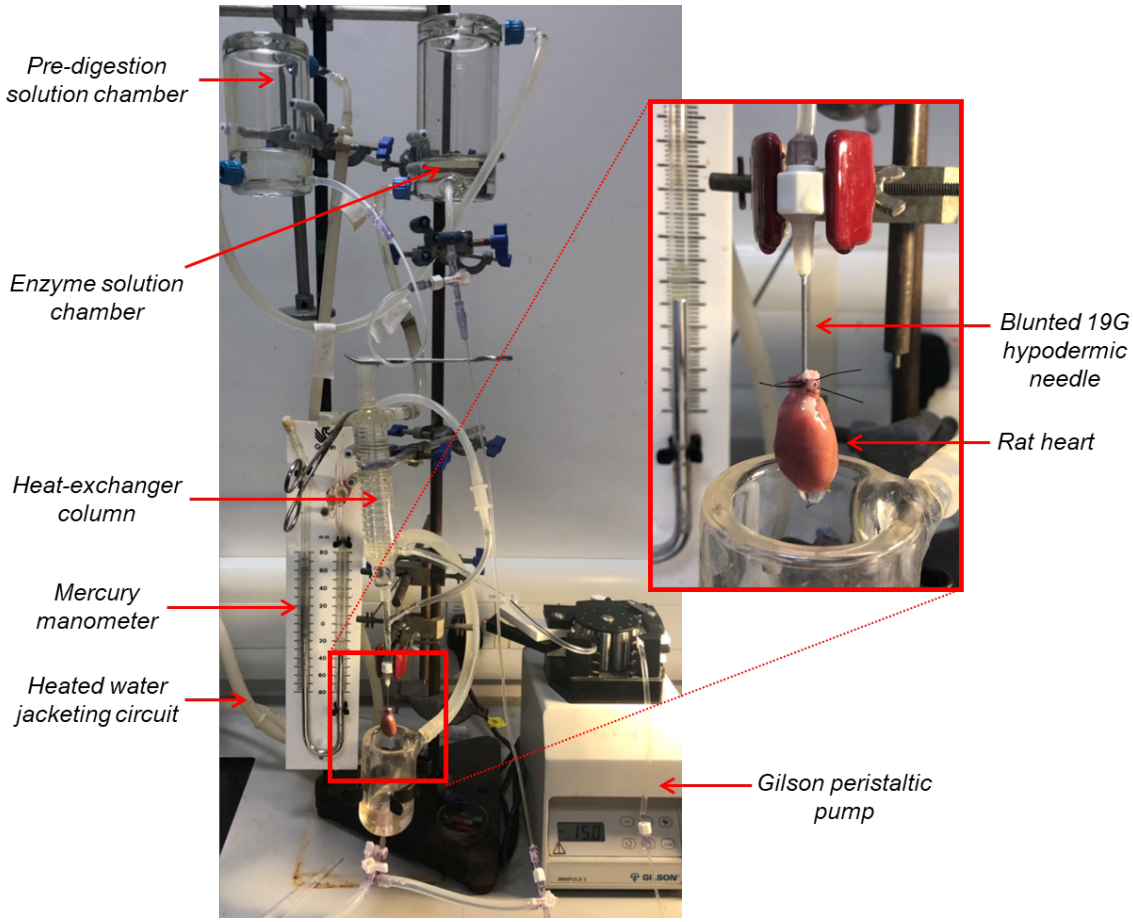


Figure 2.2. Langendorff apparatus for the isolation of adult rat myocytes. The Langendorff system is warmed by the water jacketing circuit to ensure the solution temperature is 37°C when it enters the heart. Hearts were perfused through a converted 19 G hypodermic needle at a constant flow rate via a peristaltic pump. The system was connected to a mercury manometer to monitor perfusion pressure and ensure consistency between hearts.

2.2.3 Primary neonatal ventricular myocyte isolation and culture

NRVM isolation. Primary neonatal rat ventricular myocytes (NRVMs) were isolated from post-natal day 1-2 (P1/P2) SD rats. Hearts were pooled from a litter of 12 pups for the isolation of myocytes. After Schedule 1 of the rat, its heart was excised and washed ice-cold 1x ADS buffer,

containing (in mmol/L): 106 NaCl, 5.3 KCl, 20 HEPES, 0.8 NaH_2PO_4, 0.4 $MgSO_4$, 5 glucose; pH adjusted to 7.40 at 37°C with NaOH. After removing the atria under a stereoscopic microscope, the ventricles were finely minced in groups of 6 and digested with 0.45 mg/mL Type A Collagenase (Roche) and 1.25 mg/mL Pancreatin (Sigma-Aldrich/Merck) for 5 mins at 37°C with gentle stirring.

The digestions and following steps were conducted under sterile conditions in a laminar-flow tissue culture hood. The supernatant from the first digestion was discarded, which contains most the pericardial collagen. The remaining tissue was digested for 20 mins at 37°C with gentle stirring. The supernatant (containing myocytes and fibroblasts) was collected and enzymatic activity was quenched using newborn calf serum (NCS). The cells were then centrifuged at 250 RCF for 5 mins in a swing-out rotor centrifuge and the pellet was resuspended in fresh pre-equilibrated 'M1' medium containing 10% horse serum (HS) and 5% NCS (Section 2.2.4) and stored in a humidified 5% CO_2 incubator. The digestion/collection process was repeated until all ventricular tissue was digested, which typically took 3-4 rounds of digestion. The final supernatant was 'pre-plated' on untreated 10 cm petri-dishes for 2 hours at 37°C to promote the attachment of fibroblasts, after which, the myocyte-enriched supernatant was collected and seeded (at an optimised density) on the appropriate cell culture platform (dish, slide, etc.) pre-coated with fibronectin.

NRVM culture. The NRVM culture regimen is shown in Figure 2.3. Cells were cultivated in M1 media, in 5% CO_2 at 37°C. On day-1 post-isolation, cells were rinsed with 1x PBS containing

1 mM $CaCl_2$ and 1 mM $MgCl_2$. Media was then replaced with fresh 'M2' (same composition as M1 media but with 10-fold reduction of serum; 1% HS, 0.5% NCS). On day-2 post-isolation cells were completely serum-starved (0%). Myocytes were treated on day-3 for either 24 or 48 hrs in serum-free conditions: 24 hr treatment for protein biochemistry experiments (e.g. histone modifications) and 48 hr treatment for physiological experiments (e.g. Ca^{2+} transients).

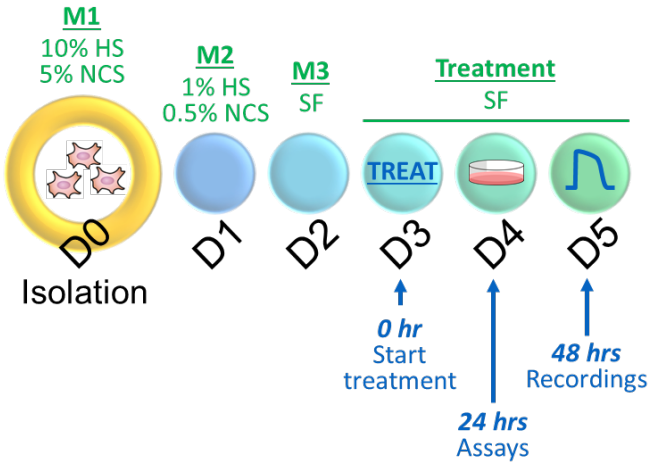


Figure 2.3. Neonatal rat ventricular myocyte (NRVM) culture protocol. Myocytes were isolated in M1 (15% serum) and seeded on the appropriate dish or plate. Media was replaced on day-1 post-isolation with M2 media (1.5% serum). Cells were serum-starved by day-2 and treated on day-3 for either 24 or 48 hrs according to application. D, day; HS, horse serum; M, media; NCS, neonatal calf serum; SF, serum-free.

2.2.4 Preparation of cell culture media and treatment conditions

Stock media preparation. Culture media was based 20% (v/v) M199 (Sigma-Aldrich/Merck, M4530) and 80% (v/v) $NaHCO_3$-free DMEM (Sigma-Aldrich/Merck, D7777) supplemented with 24 mM $NaHCO_3$ and 20 mM NaCl (to adjust osmolality to physiological levels). 1% (v/v) penicillin-streptomycin was included in media (100 U/mL penicillin, 100 µg/mL streptomycin; Sigma-Aldrich/Merck, P4333). All media was prepared using ultra-pure 18.2 MΩ water, sterile-

filtered (0.22 µm filter) and stored at 4°C. Before use on cells, media was pre-equilibrated in a humidified 5% CO_2 incubator for a minimum period of 1 hour to achieve equilibration of pH and temperature (Michl *et al.*, 2019).

NRVM culture media. NRVM isolation 'M1' media was as described above (80% DMEM and 20% M199) supplemented with 10% (v/v) HS, 5% (v/v) NCS and. 'M2' media contained 10-fold less serum (1% HS, 0.5% NCS). 'M3' media was completely serum-free.

Experimental treatment media. Treatment media was prepared using $NaHCO_3$-free DMEM (D7777) supplemented with various concentrations of $NaHCO_3$, NaCl (to balance osmolality), and where appropriate, sodium propionate and sodium butyrate (Table 2.3). All experimental treatment was serum-free.

Table 2.3. Basic treatment conditions used for *in vitro* experiments based on patient serum data.

Treatment group	Salts added (in mmol/L)					Total osmolytes added (mOsm)	Measured/ derived pH
	$NaHCO_3$	NaCl	NaPr	NaBu	NH_4Cl		
Control	24	6				60	7.4
Acidosis	18	12				60	7.3
3 mM cPA	24	3	3			60	7.4
6 mM cPA	24		6			60	7.4
6 mM uPA	18	5.8	6		0.2	60	7.3
Butyrate	24			6		60	7.4

Above modifications were made to media for *in vitro* culture experiments. pH values were calculated using the Henderson-Hasselbalch equation and derived by measuring Phenol Red absorbance at 560/430 nm. cPA, compensated propionic acidaemia; NaBu, sodium butyrate; NaPr, sodium propionate; uPA, uncompensated propionic acidaemia.

2.2.5 Mouse heart and plasma collection

Mice were anaesthetised by IP injection of sodium pentobarbital pre-mixed with heparin as described in Section 2.1.1. Upon confirmation of anaesthesia, mice were secured in the supine position and a thoracotomy was performed to access the heart. The heart was rapidly excised by incising the aorta and blood was allowed to pool in the thoracic cavity. The heart was promptly arrested in ice-cold 1x PBS and blood was cleared as much as possible by gentle massage. The atria were dissected away and the total ventricle was blotted on tissue before being snap-frozen in liquid nitrogen. Pooled whole blood in the thoracic cavity was then collected by gentle aspiration with a 1 mL syringe into a tube pre-sprayed with lithium heparin (BD Vacutainer, #368495) and kept on ice. To collect plasma, blood was centrifuged at 1,200 RCF at 4°C for 10 mins; the red cells and buffy coat were discarded. Heart and plasma samples were stored at -80°C for subsequent use.

2.2.6 Heart homogenisation and sample preparation

Snap-frozen hearts were cryoground on dry ice using a bespoke stainless-steel pestle and mortar. Any unused powdered tissue sample was stored at -80°C until for future use. The powdered tissue was mechanically homogenised in 2 mL cryovials using disposable probes (Qiagen TissueRuptor II) on ice, either in RIPA (containing in mmol/L: 150 NaCl, 20 Tris-HCl, 1 EDTA, 1 EGTA, 1% v/v Triton X-100, 0.5% w/v sodium deoxycholate; pH 7.50 at room temperature), or another lysis buffer specific for the downstream application (detailed in relevant section). The lysis buffer contained protease and phosphatase inhibitors where appropriate (Roche cOmplete ULTRA protease inhibitor cocktail, #5892953001; Roche PhosSTOP phosphatase

inhibitor cocktail, #4906845001). The homogenate was transferred to a 1.5 mL microcentrifuge tube and centrifuged at 12,000 RCF for 20 mins at 4°C in order to pellet insoluble material. The supernatant was recovered and used for subsequent experiments.

2.2.7 Determination of protein concentration

The concentration of samples (total lysate, histones) were quantified colorimetrically using the Pierce BCA Protein Assay Kit (Thermo Scientific, #23227) according to manufacturer's instructions. The assay was performed in clear 96-well microplates in technical triplicates. An 8-point protein concentration standard curve was generated using supplied albumin standards at a range appropriate for the expected protein concentration. After adding BCA reagent, the plate was incubated for 30 mins at 37°C. Absorbance was read at 562 nm using a plate-reader (Cytation 5, BioTek) and the average of each triplicate was used for analysis. Protein concentration of samples was determined using a standard curve generated by plotting albumin concentration against absorbance at 562 nm.

2.2.8 SDS-PAGE and western blot

Sample preparation and SDS-PAGE. Protein samples were separated by mass using SDS-PAGE. Samples were prepared in either 2x or 4x Laemmli sample buffer (Bio-Rad) and diluted accordingly to reach a final concentration of 1x. β-mercaptoethanol was included and samples were boiled at 100°C for 5 mins. Samples were loaded in either pre-cast gradient or hand-cast tris-glycine SDS-PAGE gels (various percentages of resolving gel) with a 4% stacking gel.

Electrophoresis was performed at constant voltage through the stacking gel at 90 V (~20-25 mins) and through the resolving gel at 120 V (~40-100 mins).

Western blot. Western blotting was performed after SDS-PAGE for the immunodetection of proteins and post-translational modifications of interest. Gels and methanol-activated 0.2 µm polyvinylidene fluoride (PVDF) membranes (Bio-Rad) were equilibrated for 1 min in transfer buffer (25 mM Tris-base, 192 mM glycine, 20% v/v methanol) prior to transfer. All proteins were wet-transferred at constant voltage using an electrophoretic transfer cell (Bio-Rad) for 90 mins at 90 V (unless stated otherwise) with ice blocks in the tank. Following transfer, non-specific binding sites were blocked by incubating the membrane in 5% milk in TBS-T (20 mM Tris-base, 137 mM NaCl, 0.1% v/v Tween 20, pH 7.40 at room temperature) for 1 hr at room temperature. Primary antibodies were prepared in TBS-T with 1% BSA and membranes were subsequently probed overnight at 4°C. Blots were then washed with TBS-T for 5 mins x 5 and probed with HRP-conjugated secondary antibodies for 1 hr at room temperature. After incubation with the secondaries, the TBS-T washes were repeated and blots were developed, unless stated otherwise, using enhanced chemiluminescence (ECL) substrate prepared in-house, that used *p*-coumaric acid as an enhancer (Haan & Behrmann, 2007). The ECL contained (in mmol/L): 100 Tris-HCl (pH 8.5 at room temperature), 2.5 luminol, 0.4 *p*-coumaric acid. H_2O_2 (from a 30% stock solution) was added fresh before use: 3 µL of H_2O_2 stock in 10 mL ECL. Blots were developed on a chemiluminescence imaging system (ChemiDoc, Bio-Rad).

Blot analysis and densitometry. Blots were analysed using commercial software (Bio-Rad, Image Lab v 6.0.1). For densitometric analysis, bands were quantified as the total band volume normalised to total loaded protein, as recommended for quantitative western blotting (Fosang & Colbran, 2015). For normalisation, total protein was measured by ImageJ from scanned blots that were stained overnight with Coomassie (QC Colloidal Coomassie Stain, Bio-Rad, #1610803).

2.3 Statistical analysis

All data in this thesis are shown as mean ± SEM. Conventional statistical methods (i.e. t-test, ANOVA) were used to analyse data that are independent (e.g. hearts in western blotting). Such analyses were performed either in Microsoft Excel or GraphPad Prism 9.

All cardiomyocyte data were analysed using the hierarchical statistics model published by Sikkel *et al.* (2017) in RStudio to account for any potential effects of clustering. First, clustering was quantified by the intraclass correlation coefficient (ICC). Low levels of clustering (low ICC) indicates each cell's behaviour is independent of the animal it came from; such data were then analysed by conventional methods. However, data with a high ICC (determined by the hierarchical statistical model and effective sample size) were analysed with hierarchical clustering analysis (Sikkel *et al.*, 2017).

Chapter 3. Characterisation of the cardiac phenotype of PCC-deficient mice

The PA mouse model (*Pcca*$^{-/-}$ A138T) was first described in 2013 and was found to exhibit a metabolic profile in plasma that recapitulated that of PA patients. However, the consequences of PCC disruption on the heart were largely overlooked. Therefore, the aims of this Chapter were to first ascertain whether there was an effect of PCC disruption on the metabolic profile of the PA mouse in heart and plasma. Having determined that propionate metabolites were indeed increased in the hearts of these mice, the next set of experiments sought to ascertain whether there was any evidence of maladaptive cardiac hypertrophy and establish whether there was any consequence to cardiac electrophysiological and contractile function *in vivo*. Importantly, these experiments were performed in 8-week-old animals in an attempt to capture early changes that precedes remodelling noted by other authors in 8-month-old mice when more complex pathology is expected.

3.1 Introduction

3.1.1 Metabolomics as a tool for studying cardiac metabolism

Metabolomics, an analytical approach that aims to characterise the metabolites of a biological system, is appreciated as an important tool for cardiac research (Griffin *et al.*, 2011; Ussher *et al.*, 2016). Whilst the transcriptome gives rise to the proteome, the proteome in turn influences the metabolome. Importantly, these different networks do not exist in isolation. That is, there is enzymatic feedback inhibition and modulation of the protein network by the metabolome. Moreover, there is also direct modulation of gene expression and transcription by metabolites (Ussher *et al.*, 2016).

Metabolite profiling can be performed in a targeted or untargeted manner. Whereas targeted metabolomics is usually 'hypothesis-led' and aims to analyse a predefined set of identified metabolites, untargeted metabolomics is 'hypothesis-generating' and aims to profile the entire set of metabolites found in a cell, tissue or organism. There are advantages and disadvantages to both these approaches. Whilst targeted metabolomics is considered more quantitative (since samples are spiked by internal standards), untargeted metabolomics has the potential for biomarker discovery (Griffin *et al.*, 2011; Ussher *et al.*, 2016).

A metabolomics workflow typically involves sample collection and extraction, sample filtration with a molecular weight cut-off filter (typically 10 kDa, to filter out proteins). Samples are then

separated by chromatography (e.g. ion-exchange chromatography, IC) followed by running these samples through the mass spectrometer (MS) (Walsby-Tickle *et al.*, 2020).

3.1.2 The ECG in mice

The ECG is the surface manifestation of cellular electrophysiology and is one of the most important diagnostic tools in modern clinical medicine, allowing the clinician to non-invasively obtain a rapid assessment of cardiac electrophysiology. The ECG has also become a popular tool in mouse models for cardiovascular research, such as for studying cardiac arrhythmias.

However, due to prominent differences in electrophysiology between the human and small rodent (rat and mouse), the shape of the action potential between these species are very different (discussed further in Chapter 4), and as such manifest dissimilar ECGs. There are even differences in the murine ECG between strains of mice (Wehrens *et al.*, 2000). Consequently, translation of electrophysiological findings between these species can be difficult since remodelling of electrophysiology in rodents may not directly mimic humans (Kaese & Verheule, 2012). Perhaps the most striking feature of the mouse ECG, which is not typical of the human, is the absence of an isoelectric ST segment and the presence of a characteristic J wave, which represents early repolarisation (Boukens *et al.*, 2014). As such, there has been a greater appreciation of understanding the differences between human and murine ECGs,

owing to prominent differences in body mass and cellular electrophysiology (Kaese & Verheule, 2012).

The QT interval approximates action potential duration and is ordinarily measured from the start of the Q wave to the end of the T wave (Roussel *et al.*, 2016). QT is a parameter of interest as its prolongation is a major pro-arrhythmic substrate (Moss & Kass, 2005). In humans, the QT interval is inversely related to heart rate (i.e. QT increases with slower heart rates). Therefore, it is common clinical practice to adjust the QT for heart rate and express it as the corrected QT interval (QTc), when heart rate is between 60-100 beats per minute. However, obtaining an accurate QTc in mice is challenging and there is currently no standardised approach (Boukens *et al.*, 2014; Roussel *et al.*, 2016). Moreover, in contrast to humans, there is little evidence for a relationship between QT and RR (i.e. heart rate) in mice (Roussel *et al.*, 2016). Finally, there are known to be sex differences in QT intervals in human ECGs (QTc is longer in females), although sexual dimorphism in QT duration appears to be less so a factor in the mouse (Salama & Bett, 2014).

3.1.3 Cardiac function in mice

Of Mice and Men. There are substantial differences in cardiac physiology between the human and mouse (Kaese & Verheule, 2012). Owing to the exponentially higher surface-to-volume ratio, thermostasis is a key homeostatic challenge to the mouse, met by heart rate (HR) being ~10-fold higher compared to the human (HR scales with body mass with an exponent of

approximately −1/4) (Kaese & Verheule, 2012). There are notable differences in cardiac performance between the human and mouse. At rest, cardiac output (CO) normalised to body surface area (cardiac index, CI) is ~10-fold higher in mice vs humans. This is driven by differences in heart rate (HR), since stroke volume (SV) normalised to body weight is ~1 µL/g in both species (CO = HR * SV). However, the human heart has a better capacity to increase its performance according to physiological demands. Whilst humans can increase HR by ~200-300%, mice have a smaller chronotropic reserve and can increase HR by only ~30-40%. With increasing HRs, diastolic filling time and ventricular end-diastolic volumes are reduced, which are exacerbated by the basally higher HR in mice. Furthermore, mice also have a smaller force-frequency relationship (Georgakopoulos & Kass, 2001). Together, these factors contribute to mice having a much smaller cardiac reserve, being able to raise CO only by a small amount, in comparison to humans where CO can increase by a factor of 5-6 (Kaese & Verheule, 2012).

Assessment of in vivo cardiac function in mice. There are three general approaches to measuring *in vivo* cardiac function in mice: echocardiography, magnetic resonance imaging (MRI) and haemodynamics (Lindsey *et al.*, 2018). Each method has its own advantages and caveats. Haemodynamics is the only method by which the pressure-volume relationship can be assessed, independent of load. However, as well as being a terminal procedure, it also requires the highest level of technical skill. Echocardiography has the highest temporal resolution of all techniques, and allows the assessment of a wide range of physiological parameters (e.g. diastolic function). However, it is prone to technical variability without a trained operator. Indeed, guidelines have

been recently published in effort to standardise echocardiographic measurements (Zacchigna *et al.*, 2021). In contrast to echocardiography, MRI has a higher spatial resolution, as well as high accuracy and reproducibility. However, it has a lower temporal resolution and has signal-to-noise ratio limitations (Lindsey *et al.*, 2018).

There are a multitude of other factors that should be considered during experimental design which can influence cardiac function measurements, including the features of the mouse (strain, age, sex) as well as the type (and amount) of anaesthesia (Lindsey *et al.*, 2018).

3.1.4 Aims of this Chapter

Whilst the PA mouse model (*Pcca*$^{-/-}$ A138T) generated by Guenzel *et al.* (2013) has been shown to exhibit a metabolic profile in plasma that recapitulates PA, it is unknown whether the heart is affected in this model. Since the best available evidence suggests that it is the accumulation of propionate and its metabolites that causes heart disease, it would be important to first determine whether there is an increase in PA metabolites in the hearts of PA mice, as a form of validation prior to cardiac phenotyping. Such phenotyping should then investigate whether there is any evidence of DCM or prolonged QT intervals, since these are the common cardiac complications observed in PA. Therefore, the aims of this Chapter were to:

a) Confirm that PCC-deficient mice between 8-12 weeks of age have a metabolic signature in heart and plasma;
b) Determine whether the ECG is affected in 8-week-old PCC-deficient mice;
c) Assess cardiomyocyte size as well as cardiac function *in vivo* for any evidence of maladaptive hypertrophy or DCM in 8-week-old PCC-deficient mice.

3.2 Specific methods

3.2.1 Biological models

Pcca$^{-/-}$ *(A138T) mouse.* To characterise the physiological consequences of PCC disruption *in vivo*, experiments were performed in 8-week-old adult PA and wild-type animals (*amPA* and *amWT*, respectively) from the *Pcca*$^{-/-}$ (A138T) mouse line.

amPA AMVMs and wild-type NRVMs. In a small subset of experiments in this Chapter, AMVMs from amPA animals and wild-type NRVMs (cultured in propionate) were used to determine whether there was any evidence of maladaptive cardiomyocyte hypertrophy, as described in Sections 3.2.4 and 3.2.5, respectively.

3.2.2 Untargeted metabolomics: anion-exchange mass spectrometry

Untargeted metabolomics was performed by anion-exchange chromatography coupled to high-resolution orbitrap MS (IC-MS) in the Department of Chemistry, University of Oxford, as recently described (Walsby-Tickle *et al.*, 2020). Metabolites were MeOH-extracted from heart tissue and plasma samples that were prepared as described in Sections 0 and 2.2.6.

Metabolite extraction from heart tissue and plasma. Metabolites were extracted from cryoground heart tissue by adding 500 µL of 80% (v/v) MS-grade MeOH to 50 mg of tissue. The sample underwent 2-3 rounds of brief homogenisation (~10 secs) then centrifuged at 21,000 RCF for 20 mins at 4°C. The pelleted insoluble material was discarded and the supernatant was processed in 10 kDa cut-off ultracentrifugation filter columns to remove proteins (Amicon

Ultra-0.5 Centrifugal Filter Units, Merck/Sigma-Aldrich, UFC501096). Prior to using the filters, contaminant preservatives (primarily glycerol) were removed from the cellulose membrane by adding 500 µL of 80% (v/v) MeOH and centrifuging for 10 mins at 21,000 RCF. Samples were then centrifuged in the cellulose filters at 21,000 RCF for 20 mins at 4°C. Plasma samples were also processed by ultracentrifugation, but neat, without MeOH dilution. The infranatant (containing the metabolites) was then transferred into Protein LoBind tubes (Eppendorf) and kept on ice. Nucleic acid concentration was estimated with a spectrophotometer (NanoDrop, Thermo Fisher) and all samples were diluted to sample with the lowest concentration using 80% MeOH. These samples were then submitted for IC-MS as described by Walsby-Tickle *et al.* (2020). Metabolites were identified from the mass-to-charge (m/z) ratios by alignment with the Human Metabolome Database (Wishart *et al.*, 2018). Downstream analysis and volcano plot generation was performed in MATLAB.

Measurement of plasma acyl-carnitines. Plasma acyl-carnitines (acetyl-carnitine and propionyl-carnitine) were measured separately using liquid chromatography tandem mass spectrometry (LC-MS/MS) by Dr Steve Krywawych, Great Ormond Street Hospital (London).

3.2.3 Mouse organ weight measurements

After induction of anaesthesia and excision of the heart (Sections 2.2.1 and 0), the heart and lungs were weighed using an analytical scale (heart weight and wet lung weight, respectively). The left tibia was harvested from each animal for normalisation of heart weights. The lungs were dried overnight and re-weighed (dry lung weight).

3.2.4 Cardiomyocyte cell size

AMVMs were isolated from amPA and amWT mice as described in Section 2.2.2. Myocytes were AM-loaded with the fluorescent indicator, cSNARF-1. cSNARF-1 was prepared by reconstituting 1 mg dye with 1 mL DMSO (Invitrogen, C1272) and loaded for 6 mins at room temperature at 1:100 v/v, to give a final concentration of 17.6 μM. Myocytes were imaged on a Zeiss LSM 700 inverted confocal microscope to acquire the outline of the cell (excitation 555 nm/emission 580 nm and 640 nm). Images were analysed in MATLAB to obtain cell length, width and area.

3.2.5 SRB *in vitro* hypertrophic assay

Cardiomyocyte hypertrophy was assessed for using a quantitative *in vitro* assay utilising sulforohdamine B (SRB), a bright-pink amino-xanthene dye with two sulfonic groups that bind to basic amino acid residues (Loonat *et al.*, 2019). Isolated NRVMs were plated on specialised 96-well microplates (Ibidi µ-Plate 96-Well Black, #89626) at 60,000 cells per 200 µL well and treated for 48 hrs under serum-free conditions, as described in Section 2.2.4. After treatment, cells were rinsed in ice-cold PBS and fixed in 4% (w/v) paraformaldehyde/PBS (pH 7.4) for 10 mins at 4°C. The remaining steps were performed at room temperature. After fixation, cells were permeabilised in 0.5% (v/v) Triton-X 100 for 10 mins. Myocytes were then stained with the nuclear dye Hoechst-33342 (Invitrogen, #H3570) for 5 mins (0.1% v/v in PBS), before staining with 0.004% (w/v) SRB dissolved in 1% (v/v) acetic acid for 10 mins. Wells were then rinsed four times with 1% acetic acid and dried. Plates were then imaged on a BioTek Cytation 5 plate-reader system with a dry ×4 objective and sequential excitation at 377 nm and 531 nm. Fluorescence was then measured at 417-477 nm and 630-650 nm, respectively. The Hoechst and SRB images were analysed in MATLAB to quantify nuclear and extra-nuclear regions (nSRB and eSRB, respectively) and data were presented as the eSRB/nSRB ratio.

3.2.6 ECG recordings

Surface ECGs were acquired from unconscious amWT and amPA mice during the diurnal period using a non-invasive surgical monitoring platform (Indus Instruments MouseMonitor$^+$; courtesy of Dr Carolyn Carr, University of Oxford) (Figure 3.1a). Anaesthesia was induced in an anaesthetic chamber by 2.5% isoflurane in oxygen and nitrous oxide (O_2:N_2O 4:1, total of 2 L/min). After an adequate depth of anaesthesia was reached, the mouse was transferred to the Indus monitoring platform and anaesthesia was maintained using a nose cone at 1.8-2% for the duration of the experiment (O_2:N_2O 4:1, total of 2 L/min). Conductive electrode cream (Indus Instruments ECG Electrode Crème, #600-0001-01-S) was applied to the paws of the forelimb and hindlimb and secured onto the contact electrodes with hypoallergenic tape (3M Micropore). The platform was heated to ~40°C to achieve a core temperature as close as possible to 37°C, monitored via a rectal probe.

To minimise noise in the ECG signal, the bottom of the platform was insulated using appropriate material. Signals were grounded to the chassis and filtered as follows: high-pass filter 1 Hz, low-pass filter OFF, notch filter 50 Hz. The following physiological parameters were recorded during each acquisition for 1 min: ECG Leads I/II/III (mV), core temperature and respiration rate. Data were acquired using the manufacturer's software (Figure 3.1b) in their native format (.iird) and exported as .csv files. Downstream data analysis was performed in MATLAB. ECGs were recorded for 45 secs and an average over 30 secs was analysed to extract wave amplitudes (P, Q, R, S, J, T) relative to the isoelectric line and the duration between waves

(e.g. RR, PR, QT) (Figure 3.1c). Whilst in the clinic, QT interval is defined as the start of the Q wave to the end of the T wave, it was not possible to reliably identify the end of the T wave in these recordings due to noise. Any recordings in animals with a core temperature below 35°C during the recording or traces without a clear R wave were excluded.

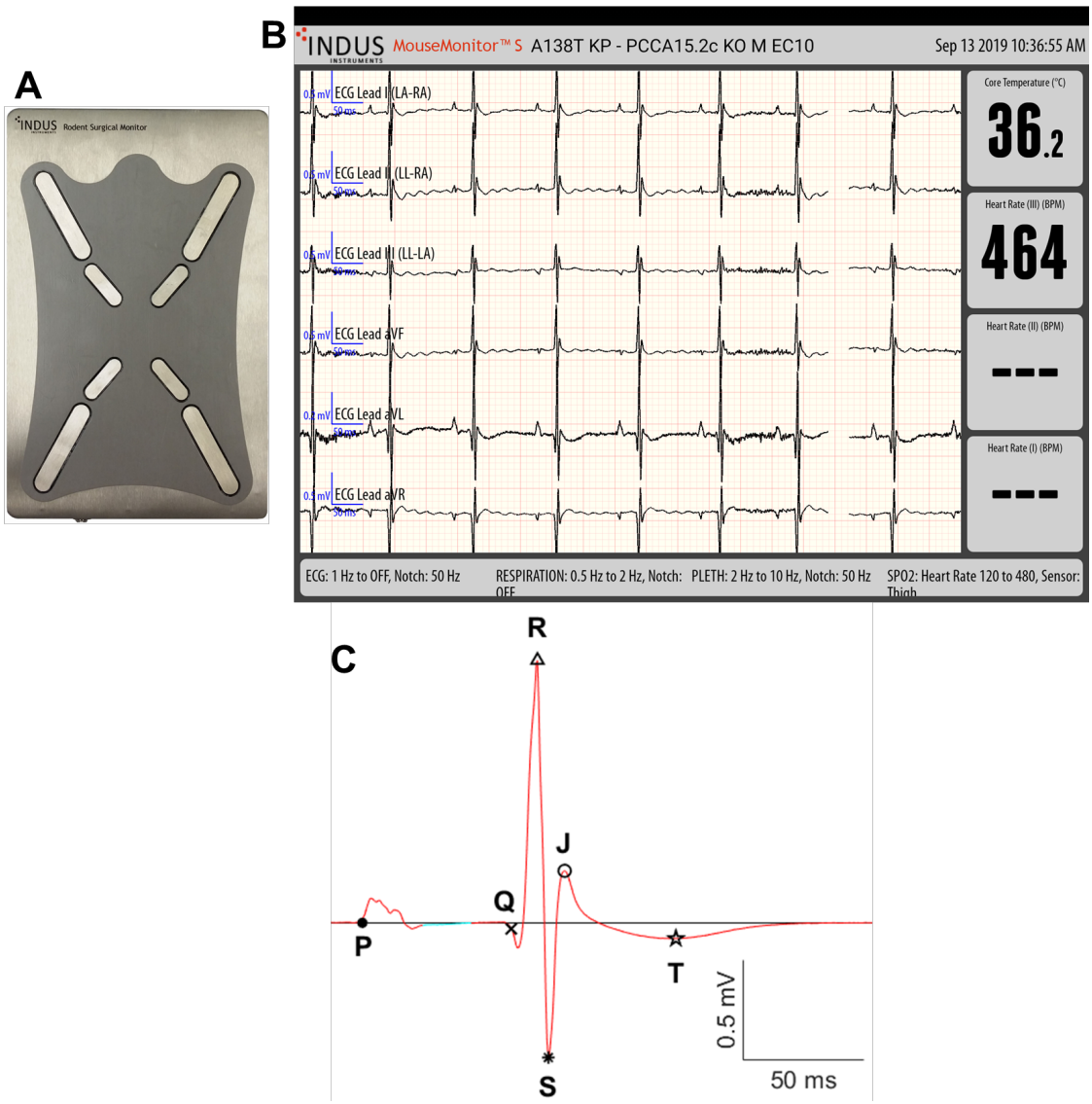


Figure 3.1. Recording of surface ECGs from isoflurane-anaesthetised adult mice. *(A)* Image of the Indus Instruments MouseMonitor⁺ recording platform. *(B)* Screenshot of the native recording software during an acquisition. *(C)* Representative lead I trace averaged over 30 secs. The waves (P/Q/R/S/J/T) are labelled appropriately. Wave amplitudes and intervals were defined in MATLAB as the points indicated by the symbols. E.g. QT interval was defined as the time between the cross (Q wave) and the star (T wave).

3.2.7 Cine-MRI

Setup. Cine-MRI was performed in the Department of Physiology, Anatomy & Physiology facility established by Professors Damien Tyler and Kieran Clarke. The cine-MRI setup is shown in Figure 3.2 and scanning was performed as previously described in the diurnal period (Tyler *et al.*, 2006; Seymour *et al.*, 2015). Experiments were performed in 8-week mice. Anaesthesia was induced in an anaesthetic chamber by 2.5% isoflurane in oxygen and nitrous oxide (O_2:N_2O 4:1, total of 2 L/min). After an adequate depth of anaesthesia was reached, as judged by lack of the pedal response, the mouse was transferred to the mouse cradle, positioned in the horizontal supine position, and anaesthesia was maintained using a nose cone at 1.8-2% for the experiment (O_2:N_2O 4:1, total of 2 L/min). The temperature of the cradle was maintained at 35°C via warm air-flow through an integrated heat-exchanger to maintain core temperature at 37°C. A bespoke ECG and respiratory gating device was used to monitor heart and respiration signals. ECG signals were obtained from electrodes inserted subcutaneously into the chest and respiratory signals were obtained from a wire loop positioned loosely at the level of the sternum. A custom-made $^{1}H/^{13}C$ butterfly surface coil (loop diameter, 20 mm) was also placed over the mouse chest to localise the signal from the heart.

Imaging. The cradle was inserted into a horizontal-bore 7 tesla MR scanner interfaced to a direct-drive console, with the animal's heart positioned at the isocentre of the scanner. Correct positioning of the mouse was confirming by acquiring cardiac-triggered and respiration-gated axial FLASH (proton fast low-angle shot) images. Long-axis scans were taken to orientate the

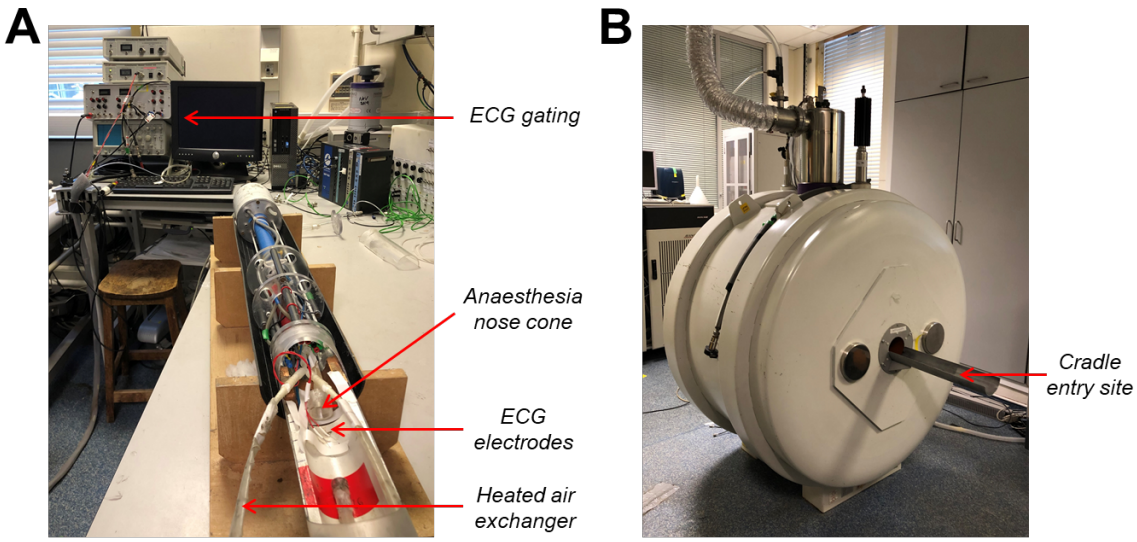


Figure 3.2. Cine-MRI setup. *(A)* Custom-made MR handling mouse cradle which includes integrated ECG electrodes and heat exchangers for the maintenance of body temperature. *(B)* 7-tesla horizontal bore MR system. The cradle entry site is indicated.

scanning angle and to set up true short-axis views. High-resolution cine-MR short-axis images were then acquired in 9-10 contiguous slices (1 mm thick) covering the entire heart. Each *in vivo* scanning protocol lasted ~45-50 mins. Animals were allowed to recover fully from anaesthesia.

Analysis. Images were analysed using Fiji ImageJ (Schneider *et al.*, 2012). For each 1 mm slice, end-diastolic and end-systolic frames were selected according to the size of the left-ventricular (LV) lumen. For each frame, the epicardial and endocardial border (drawing around any papillary muscles) were outlined using the free-hand tool in ImageJ using a Wacom CTL-4100K-N drawing tablet. The epicardial and endocardial area for each frame were summed across the Z-stack to cover the entire heart to render LV end-diastolic and end-systolic volumes

(EDV and ESV, respectively). Based on the measured LV EDV and ESV, other functional parameters were calculated as follows:

Stroke volume (SV): $SV\ (\mu L) = EDV\ (\mu L) - ESV\ (\mu L)$

Ejection fraction (EF): $EF\ (\%) = SV\ (\mu L) / EDV\ (\mu L)$

Cardiac output (CO): $CO\ (mL/min) = SV\ (\mu L) \times heart\ rate\ (bpm)$

3.3 Results

3.3.1 Effect of PCC disruption on the metabolome

The metabolic signature of PA patients is well-defined, whereby patients classically accumulate propionate metabolites such as 2-methylcitrate (MeCit), propionyl-glycine and 3-hydroxypropionate in physiological fluids (plasma and urine) (Baumgartner *et al.*, 2014). However, there is less information available on the effect of PCC disruption on the metabolic profile of the heart, or whether there are other 'non-classical' metabolites that are significantly accumulated. To determine the effect of disrupted PCC on cardiac metabolites, untargeted metabolomics was performed by anion-exchange chromatography coupled to high-resolution orbitrap mass spectrometry (IC-MS) in cardiac extracts and matching plasma samples from amPA animals.

The significantly altered metabolites in heart and plasma are shown in Figure 3.3. A total of 180 common metabolites were identified in heart and plasma by crosschecking m/z values with the Human Metabolome Database (HMDB) (Wishart *et al.*, 2018). In hearts, the most distinctive metabolites (both in terms of significance and abundance) that were increased in amPA were MeCit (~5-fold), methionine sulfone (~6-fold) and propionyl-glycine (~4-fold) (Figure 3.3a). Perhaps not surprisingly, the same metabolites were also increased in amPA vs amWT plasma (Figure 3.3b). However, these metabolites were detected at a strikingly higher abundance compared to hearts. For example, MeCit was ~25-fold higher in amPA plasma vs

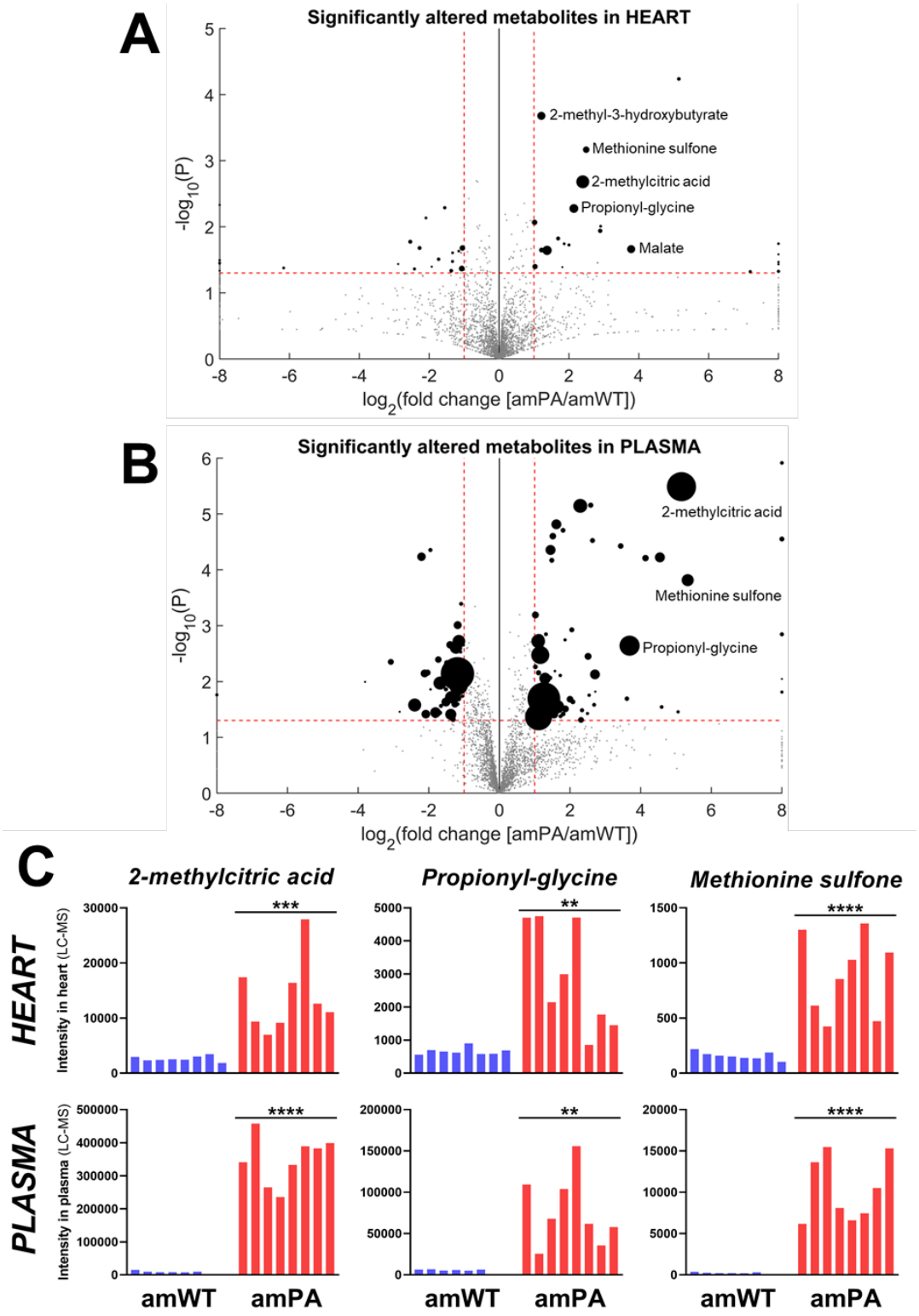


Figure 3.3. Metabolomic analyses of cardiac and plasma extracts. Samples were extracted from adult PA mice (amPA) and their wild-type litters (amWT). Volcano plots for significantly altered metabolites in *(A)* heart and *(B)* plasma. The size of circles represent abundance (note, same scale used for both graphs). *(C)* Histograms of 2-methylcitric acid (MeCit), propionyl-glycine and methionine sulfone, shown as MS intensity, in matching hearts (*top row*) and plasma (*bottom row*). Each bar represents a sample. N = 8 animals per group between 8-12 weeks of age. ** $P \leq 0.01$, *** $P \leq 0.001$ and **** $P \leq 0.0001$ on unpaired t-test.

amPA hearts, whilst propionyl-glycine was ~26-fold higher in amPA plasma compared to amPA hearts (Figure 3.3c).

Propionyl-carnitine (C3) has been recognised as the best plasma biomarker of PA and C3 is measured as part of PA newborn screening (Wikoff *et al.*, 2007). C3 was measured in 8-week amPA and amWT plasma by liquid-chromatography tandem mass-spectrometry (LC-MS/MS) (Figure 3.4). To control for variation in metabolite recovery, data were also normalised to acetyl-carnitine (C2) to obtain the C3:C2 ratio (Guenzel *et al.*, 2013). It should be noted that during the management of the amPA colony, it was recognised that there were frequent amPA that had to be culled short of their 8-week timepoint due to acute weight loss. Acute weight loss occurred in ~5% of all homozygotes. Of these homozygotes, ~70% were females. It was hypothesised that these mice were decompensating animals. Thus, to test this hypothesis, plasma acyl-carnitines were also measured in some of these mice ('amPA weight loss'; Figure 3.4).

Plasma C2 was detected in all groups (Figure 3.4a). In contrast, whilst C3 was negligible in amWT (0.45 ± 0.03 μM), it was ~19-fold higher in stable amPA (8.58 ± 0.70 μM; $P \leq 0.001$) and ~26-fold higher in amPA with weight loss (11.85 ± 1.2 μM; $P \leq 0.0001$), compared to amWT animals (Figure 3.4b). In keeping with these observations, the C3:C2 ratio was significantly increased by similar magnitudes (Figure 3.4c).

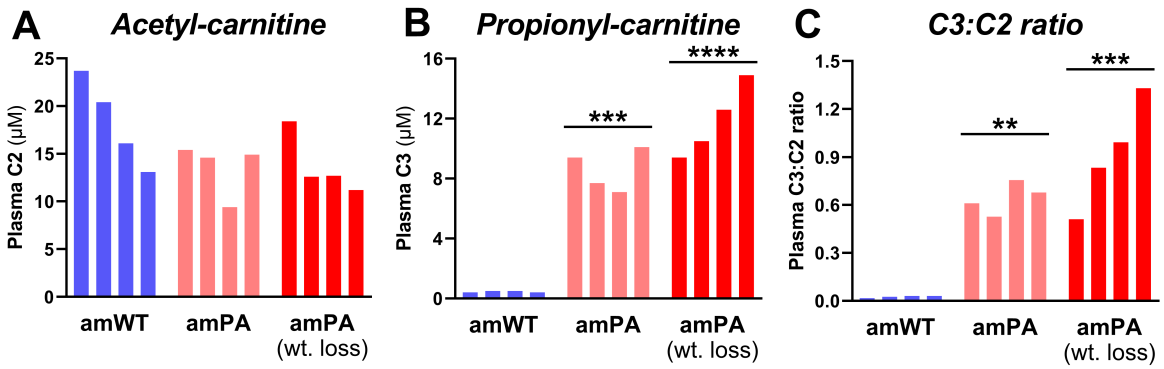


Figure 3.4. Measurement of plasma acyl-carnitines by LC-MS/MS. *(A)* Acetyl-carnitine (C2) and *(B)* propionyl-carnitine (C3) were measured in matching plasma samples from 8-week adult WT and PA mice (amPA and amWT), as well as in PA mice with acute weight loss ('amPA wt. loss'). *(C)* Data presented as C3:C2 ratio. Each bar represents a sample. $N = 4$ animals per group. ** $P \leq 0.01$, *** $P \leq 0.001$ and **** $P \leq 0.0001$ on one-way ANOVA with Dunnett's post-hoc test relative to amWT.

Collectively, these results demonstrate that PCC disruption results in a distinct metabolic signature in heart and plasma.

3.3.2 Effect of PCC disruption on organ weights

Given that there was indeed increased abundance of propionate metabolites in the PA mouse heart, a comprehensive appraisal of cardiac physiology was initiated for these mice. Organ weights were measured as a first-line assessment in sex-balanced cohorts (Figure 3.5). Body weights in age-matched amPA females were ~12% smaller than amWT females ($P \leq 0.01$). Although heart weight to body weight ratio (HW:BW) was significantly increased in female amPA vs amWT, heart weight to tibia length ratio (HW:TL) was unaffected. These results indicate that heart size is unaffected, but that the increased HW:BW ratio is attributable to the lower body weight in female amPA. There was no difference in lung weight in both sexes, thus excluding any overt pulmonary congestion.

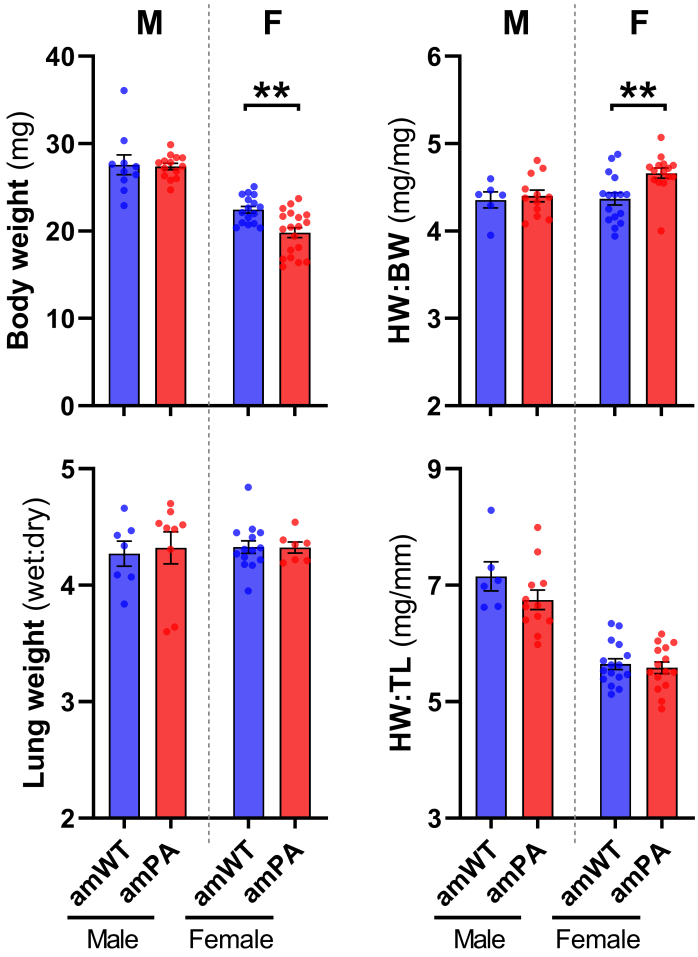


Figure 3.5. Body and organ weights of 8-week-old adult PA mice. BW, body weight; HW, heart weight; TL, tibia length. *N* = 10-19 animals per sex and per genotype. Two-way ANOVA for body weight: genotype, $P \leq 0.05$; sex, $P \leq 0.0001$; interaction, N.S (not significant). Two-way ANOVA for HW:BW ratio: genotype, $P \leq 0.05$; sex, N.S; interaction, N.S. ** $P \leq 0.01$ with Šídák's post-hoc multiple comparisons test. amPA, adult PA mouse; amWT, adult WT mouse.

3.3.3 Effect of PCC disruption and exogenous propionate on cardiomyocyte cell size

Since (i) HCM has been reported in PA patients and (ii) BNP expression has been shown to be increased in the hearts of PA mice (Guenzel *et al.*, 2013), the assessment for maladaptive cardiac hypertrophy was prioritised in the PA mouse. Despite an absence of difference in organ weights, this does not preclude cardiomyocyte hypertrophy. To determine whether there was any evidence for maladaptive cardiomyocyte hypertrophy in PA, experiments were carried out in (i) isolated AMVMs from amPA hearts, and (ii) cultured wild-type NRVMs that were treated with propionate.

3.3.3.1 Ventricular myocyte cell size in PCC-deficient hearts

Myocyte cell size was determined fluorescently by cSNARF-1 imaging in AMVMs isolated from 8-week amPA and amWT animals (Figure 3.6). There was no effect of PA on cell length, width, or area, providing evidence against maladaptive cardiomyocyte hypertrophy in PA.

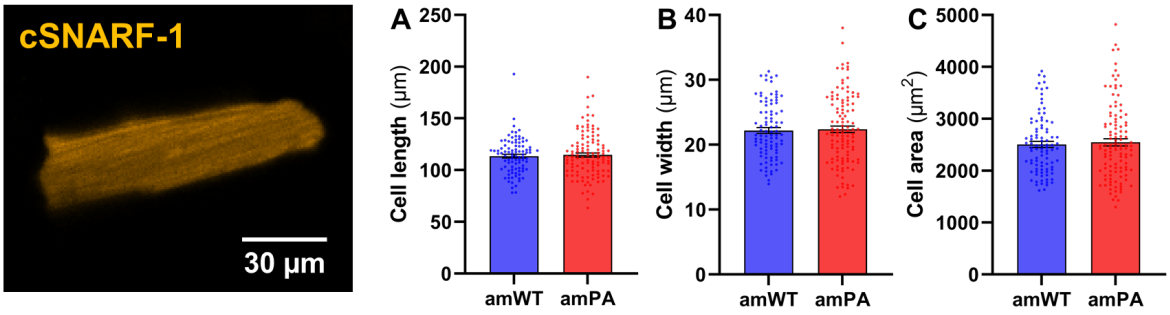


Figure 3.6. cSNARF-1 fluorescence imaging to determine cardiomyocyte cell size. Experiments were performed in myocytes isolated from 8-week-old adult PA mice (amPA) and their WT litters (amWT). An exemplar ventricular myocyte loaded with cSNARF-1 is shown; scale bar, 30 µm. Cell *(A)* length, *(B)* width and *(C)* area determined using the outline of the fluorescence signal. *N* = 93-113 cells from 4-5 animals per genotype. Unpaired t-test, not significant.

3.3.3.2 In vitro hypertrophic assay in cardiomyocytes treated with propionate

To further evaluate whether maladaptive hypertrophy occurs in PA, a quantitative *in vitro* assay was performed in wild-type NRVMs treated with propionate (Pr) in a concentration range reported in patient plasma. Cells were also treated with 3-hydroxypropionate (3-OH-Pr), the hydroxylated derivative of propionate that is commonly detected in PA patients (Chapter 1). Hypertrophy was assessed using the SRB protein biomass assay (Figure 3.7). The nuclear SRB signal (nSRB) has been shown to be independent of cell size. Therefore, normalising the cytoplasmic SRB signal ('extra-nuclear SRB', eSRB) to nSRB has been shown to be a reliable index of myocyte size (Loonat *et al.*, 2019). NRVMs treated for 48 hrs in propionate or 3-OH-Pr (both at pH 7.4) exhibited no difference in the eSRB/nSRB ratiometric index, with a significant change only observed with 10 μM phenylephrine (PE; α1 adrenoceptor agonist, positive control for hypertrophy).

In summary, the data from this sub-section indicate that maladaptive cardiac hypertrophy does not occur in the young PA mouse relative to time-matched WT controls, or in WT cardiomyocytes treated with propionate *in vitro*.

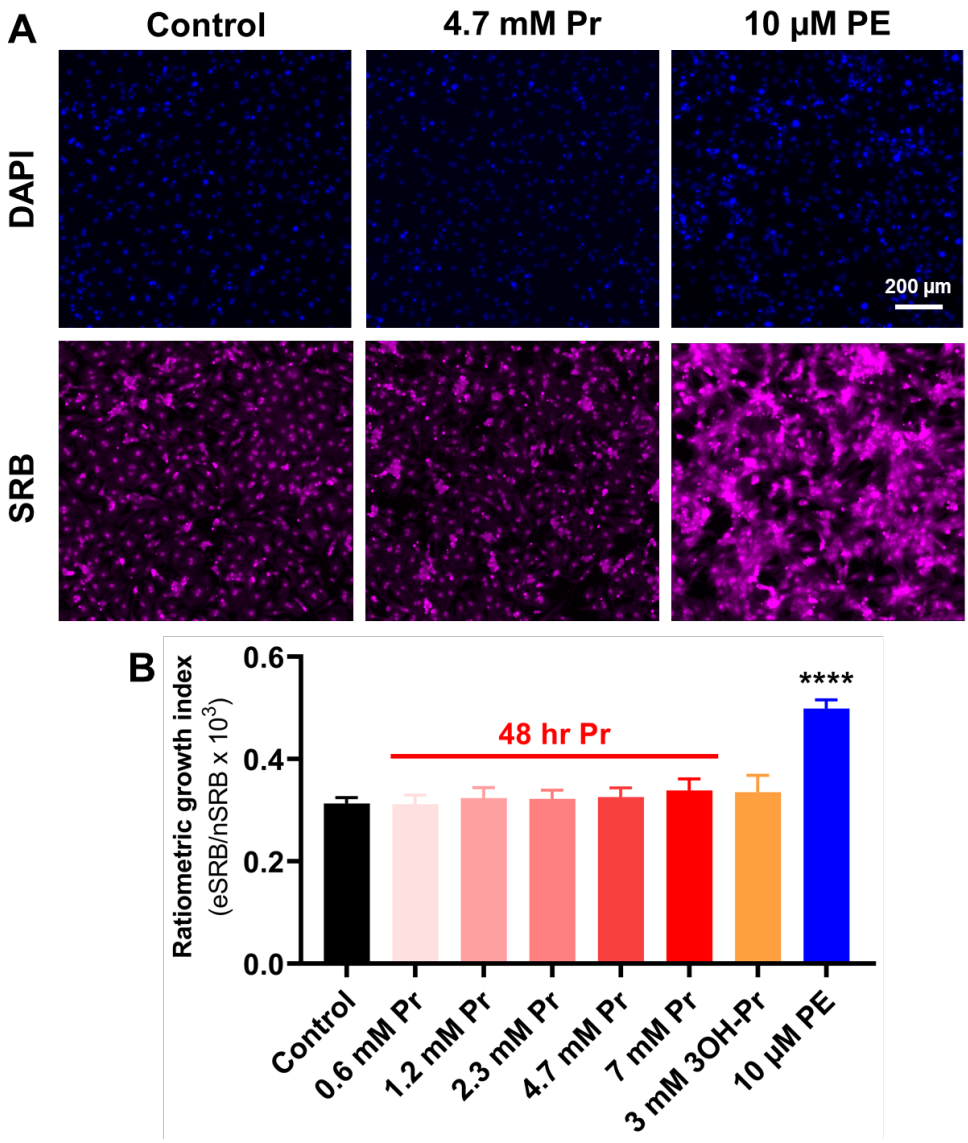


Figure 3.7. Sulforhodamine B (SRB) staining of NRVMs treated in propionate. Cells were treated under 8 conditions at pH 7.4 for 48 hrs: *control*, *0.6 – 7 mM propionate* (Pr), *3 mM 3-hydroxypropionate* (3-OH-Pr), *10 µM phenylephrine* (PE). ***(A)*** Exemplar images of DAPI and SRB co-staining in *control*, *4.7 mM Pr* and *PE*. ***(B)*** Effects of Pr, 3-OH-Pr and PE on ratiometric SRB growth index. eSRB, extra-nuclear SRB signal; nSRB, nuclear SRB signal. Data shown as mean ± SEM. **** $P \leq 0.0001$ on one-way ANOVA with Dunnett's post-hoc tests.

3.3.4 Effect of PCC disruption on the ECG

Prolonged QT intervals are a key cardiac complication observed in PA patients (Park *et al.*, 2020). To determine whether the ECG and QT interval are affected in amPA, non-invasive surface ECGs were recorded from sex-balanced cohorts of isoflurane-anaesthetised 8-week mice. Leads I, II and III were recorded for ~45 seconds from each animal and a 30-second average was analysed. It should be noted ECGs were recorded in the MRI facility room (air-conditioned). The measured core temperature (via rectal probe) during the ECG was typically ~35°C.

Example averaged traces and histograms for wave intervals (RR, PR, QT) and wave amplitudes (J, T) are shown for Leads I and II in Figure 3.8. The data are also presented in tabulated form in Table 3.1. Data obtained from lead III were similar and not shown for clarity. The RR interval, and thus HR, were unaffected. The best lead for measuring the QT interval is V3, followed by lead II (Davey, 2000). The data indicated shortening of the QT interval in lead II in amPA females (26.9 ± 1.1 ms in amWT vs 22.8 ± 0.9 ms in amPA). This result was significant in an unpaired t-test in a pairwise comparison between female animals only ($P \leq 0.01$). However, when statistical testing was performed by two-way ANOVA, the only significant effect was that of sex for J wave amplitude (lead I) and T wave interval (lead II). Post-hoc multiple comparisons tests with Šídák's correction found these variables as not being significant (Table 3.1). In summary, these data indicate that ECGs recorded from isoflurane-anaesthetised amPA animals are overall not statistically different from amWT animals.

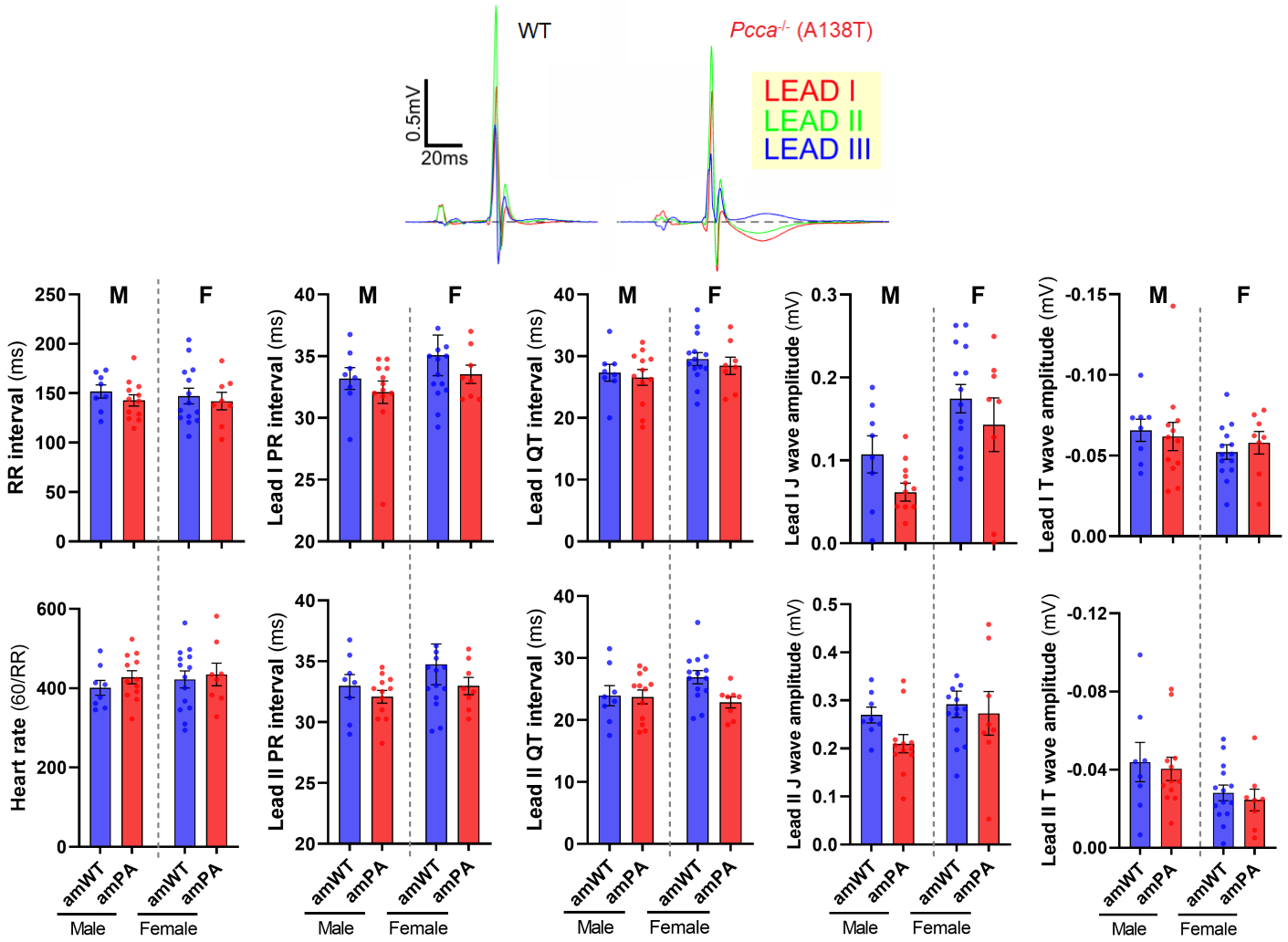


Figure 3.8. Summary of key ECG parameters determined from surface recordings of isoflurane-anaesthetised mice. Experiments were performed in 8-week-old adult PA mice (amPA) and their WT litters (amWT). ***(Top)*** Example lead I, lead II and lead III traces, averaged over a 30-second recording. ***(Bottom)*** Summary histograms for key wave intervals (RR, PR, QT) and wave amplitudes (J, T) from leads I and II. Data shown as mean ± SEM.

Table 3.1. ECG parameters determined from surface recordings in isoflurane-anaesthetised mice.

		Males		Females		Two-way ANOVA		
	Parameter	amWT (8) mean ± SEM	amPA (12) mean ± SEM	amWT (14) mean ± SEM	amPA (8) mean ± SEM	Genotype	Sex	Interaction
	Heart rate (bpm)	401 ± 20	428 ± 17	422 ± 22	435 ± 31	0.384	0.531	0.752
	RR interval (ms)	151.8 ± 7.2	142.7 ± 0.3	147.2 ± 8.2	142.0 ± 0.5	0.368	0.738	0.803
Lead I	**PR interval** (ms)	33.2 ± 0.9	32.1 ± 0.9	35.1 ± 1.7	33.5 ± 0.8	0.330	0.221	0.872
Lead I	**QT interval** (ms)	27.3 ± 1.5	26.6 ± 1.3	29.5 ± 1.1	28.4 ± 1.5	0.482	0.123	0.894
Lead I	**J wave amplitude** (mV)	0.11 ± 0.02	0.06 ± 0.01	0.17 ± 0.02	0.14 ± 0.03	0.067	**0.0008**	0.730
Lead I	**T wave amplitude** (mV)	-0.07 ± 0.01	-0.06 ± 0.01	-0.05 ± 0.00	-0.06 ± 0.01	0.895	0.230	0.502
Lead II	**PR interval** (ms)	33.0 ± 1.0	32.1 ± 0.5	34.8 ± 1.7	33.0 ± 0.8	0.308	0.308	0.730
Lead II	**QT interval** (ms)	23.9 ± 1.7	23.7 ± 1.2	26.9 ± 1.1	22.8 ± 0.9	0.090	0.400	0.124
Lead II	**J wave amplitude** (mV)	0.27 ± 0.02	0.21 ± 0.02	0.29 ± 0.03	0.27 ± 0.05	0.180	0.146	0.486
Lead II	**T wave amplitude** (mV)	-0.04 ± 0.01	-0.04 ± 0.01	-0.03 ± 0.00	-0.02 ± 0.01	0.574	**0.016**	0.986

Experiments were performed in 8-week-old adult PA mice (amPA) and their WT litters (amWT). Data shown as mean ± SEM. Number of animals scanned per cohort are indicated in parentheses. Heart rate is shown as beats per minute (bpm), calculated from the RR interval (HR = 60/RR). Data were first analysed by two-way ANOVA. Significant *P* values are in bold. Post-hoc multiple comparison tests with Sidak's correction were performed comparing amPA and amWT, for any parameters that showed a significant effect of genotype, sex, or an interaction between these factors. The result from these pairwise comparisons are shown under '*P* value'.

3.3.5 Effect of PCC disruption on contractile function

PA patients not only commonly exhibit a long QT syndrome, but also manifest a dilated cardiomyopathy (Park *et al.*, 2020). Therefore, to determine whether there was chamber dilatation or any changes to contractile function in amPA, cine-MRI was performed for sex-balanced cohorts of 8-week-old mice (Figure 3.9). Scanning was performed in isoflurane-anaesthetised mice in the horizontal supine position.

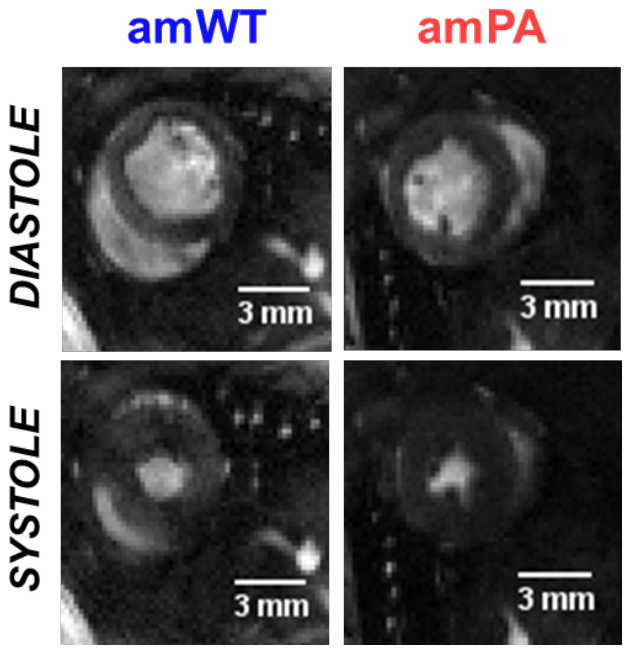


Figure 3.9. Assessment of *in vivo* contractile function and chamber morphology by cine-MRI. Example parasternal short-axis mid-ventricular scans at end-diastole and end-systole in 8-week adult PA mice (amPA) and their wild-type litters (amWT). Scale bar, 3 mm.

A technical challenge is delivering the same level of isoflurane to all animals, since size has a profound effect on the pharmacokinetic efficiency of anaesthetics. Because both the size of an animal and the level of anaesthesia has an impact on contractile function (Lindsey *et al.*, 2018), cine-MRI data were analysed by regression analysis including body weight as a factor (as opposed to two-way ANOVA for ECG data in Section 3.3.4). For this analysis, sex and genotype were treated as categorical factors, whilst body weight was treated as a continuous factor. The key cardiac functional indices are shown in Figure 3.9 and shown as the index values normalised to body weight where appropriate. The complete measured parameters determined by cine-MRI are shown in Table 3.2.

Despite established sex differences in haemodynamics (Murphy *et al.*, 2017), sex was not found to be a significant factor in these experiments. As expected from previous experiments assessing for cardiac hypertrophy, LV mass was unaffected. The structural dimensions of the LV (septal wall and free wall thickness) was also unaffected, arguing against any chamber dilatation. Interestingly, HR was significantly lower in male (~10%) and female amPA animals (~7%), independent of body weight. Should stroke volume (SV) be unaffected, it would be expected for cardiac output (CO) to be reduced. CO on its own appeared to be reduced by ~12% in amPA females. However, there was a significant effect of body weight on CO ($P = 0.039$; Table 3.2) and indeed, when normalised to body weight (cardiac index), the difference was abolished (Figure 3.10). Although LV end-diastolic volume (EDV) significantly correlated with body weight ($P \leq 0.01$), interestingly both LV EDV and end-systolic volume (ESV) were significantly

increased in amPA animals due to a genotype effect ($P \leq 0.01$), suggesting there is an element of contractile dysfunction in these mice (Figure 3.10 and Table 3.2). To help visualise the effect of genotype on parameters that were significantly associated with body weight (EDV, SV, CO), the data for these parameters were also plotted indexed to body weight. The result of this normalisation procedure is shown in Figure 3.10, clearly identifying EDV and ESV as increasing in both male and female amPA, relative to amWT of the respective sex, when adjusted for body weight. Finally, ejection fraction (EF), was not statistically different (Table 3.2).

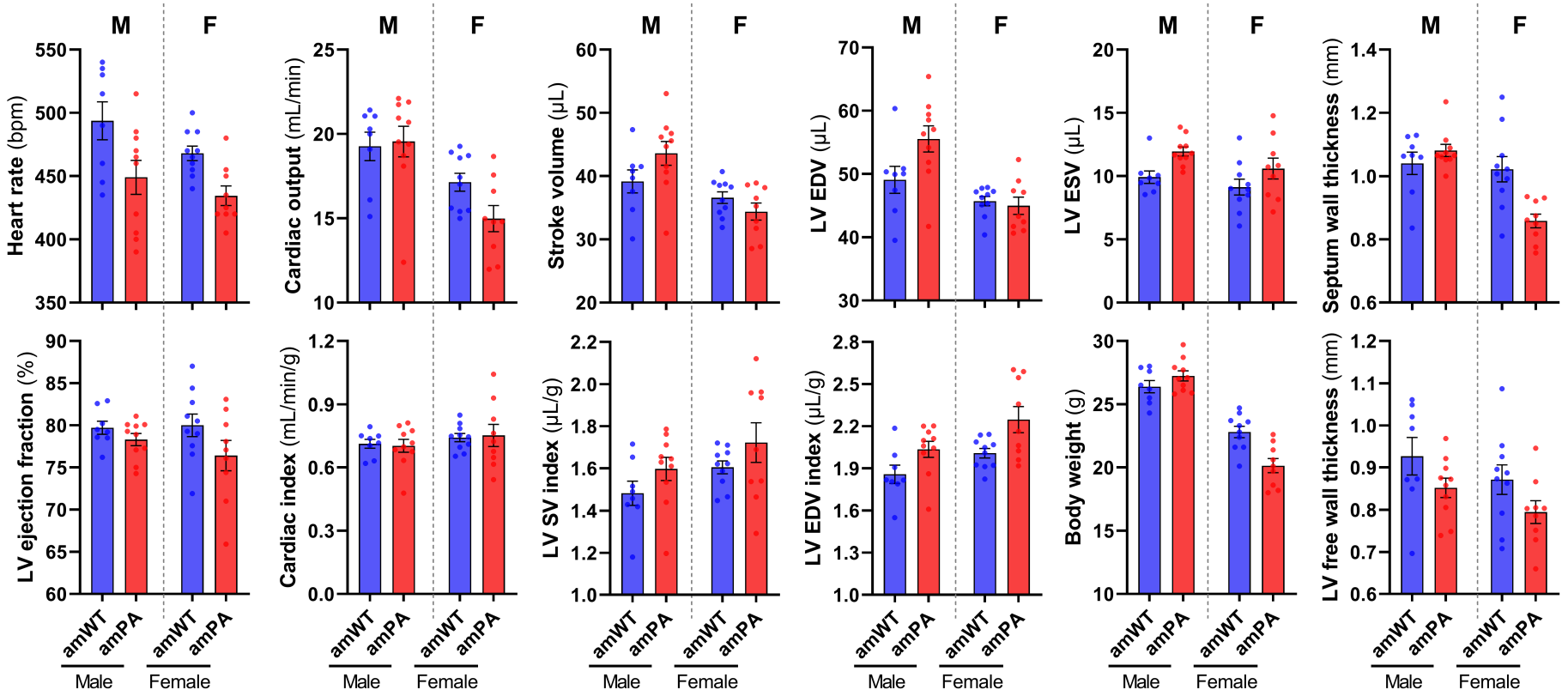


Figure 3.10. Summary histograms of key functional indices measured by cine-MRI. Experiments were performed in 8-week-old adult PA mice (amPA) and their WT litters (amWT). Parameters that were significantly associated with body weight (EDV, SV, CO) were also plotted indexed to body weight. End-diastolic volume, EDV; end-systolic volume, ESV; left ventricle, LV; SV, stroke volume. Data shown as mean ± SEM. *N* = 8-10 males per genotype and *n* = 9-10 females per genotype.

Table 3.2. *In vivo* cardiac function as measured by cine-MRI in isoflurane-anaesthetised mice.

	Males		Females		Regression analysis			
	amWT (8)	amPA (10)	amWT (10)	amPA (9)	Body weight	Genotype	Sex	Genotype:sex
Body weight (g)	26.4 ± 0.5	27.2 ± 0.4	22.8 ± 0.4	20.1 ± 0.6	0	0	0	0
LV mass (mg)	80.6 ± 2.6	86.4 ± 2.6	71.5 ± 2.2	67.3 ± 1.0	0.069	0.293	0.332	0.361
*LV EDV (µL)	49.1 ± 2.1	55.6 ± 2.1	45.7 ± 0.7	45.0 ± 1.4	**0.006**	**0.007***	0.436	0.656
*LV ESV (µL)	9.9 ± 0.5	12.0 ± 0.4	9.1 ± 0.6	10.6 ± 0.8	0.168	**0.003***	0.771	0.722
LV stroke volume (µL)	39.2 ± 1.8	43.6 ± 1.9	36.6 ± 0.9	34.4 ± 1.4	**0.019**	0.113	0.4911	0.543
LV EF (%)	79.7 ± 0.8	78.3 ± 0.7	80.0 ± 1.3	76.4 ± 1.8	0.942	0.091	0.908	0.497
*Heart rate (bpm)	494 ± 15	449 ± 13	468 ± 6	434 ± 8	0.942	**0.002***	0.274	0.645
Cardiac output (mL/min)	19.3 ± 0.8	19.6 ± 0.9	17.1 ± 0.5	15.0 ± 0.8	**0.039**	0.623	0.9589	0.820
Septum wall thickness in diastole (mm)	1.04 ± 0.04	1.08 ± 0.02	1.02 ± 0.04	0.86 ± 0.02	0.407	0.097	0.2589	**0.003**
LV free wall thickness in diastole (mm)	0.93 ± 0.04	0.85 ± 0.02	0.87 ± 0.03	0.79 ± 0.03	0.453	0.050	0.746	0.702

Experiments were performed in 8-week-old adult PA mice (amPA) and their WT litters (amWT). Data shown as mean ± SEM. Number of animals scanned per cohort are indicated in parentheses. Data were analysed by regression analysis. Significant *P* values are in bold and those significantly affected by genotype are also indicated by asterisks (*). EDV, end-diastolic volume; EF, ejection fraction; ESV, end-systolic volume; LV, left ventricle.

3.4 Discussion

The aim of this Chapter was to take the first steps into characterising the cardiac effects of PCC disruption and dysregulated propionate metabolism using the *Pcca*$^{-/-}$ A138T hypomorphic mouse model of PA. Experiments were performed to determine whether PCC disruption has an effect on cardiac metabolism, gross electrophysiology and contractile function *in vivo.* A key difference between this study and others was the experimental timepoint. Whereas other studies using this model have conducted experiments in 8-month-old mice, the experiments performed in this thesis used mice that were 8 weeks old. The rationale for this difference was an attempt to capture the changes that occur during the early stages of PA that precedes the development of other complex disease pathways (e.g. oxidative stress). Furthermore, all experiments in this thesis were sex-balanced to evaluate evidence for an effect of sex, which is in contrast to other studies using *Pcca*$^{-/-}$ A138T mice where typically only males are used.

The major findings from this Chapter were as follows. (i) PCC disruption results in a metabolic signature in the heart, as well as in plasma; (ii) dysregulated propionate metabolism has no pro-hypertrophic effect, as assessed by organ weights and cardiomyocyte cell size in 8-week-old amPA animals, or in *in vitro* hypertrophic assay; (iii) the surface ECG is unaffected in 8-week-old isoflurane-anaesthetised amPA animals; (iv) there is early evidence of contractile dysfunction in 8-week-old PCC-deficient mice.

3.4.1 PCC disruption has a metabolic signature in the heart

The PA mouse model ('amPA') used in this thesis was generated by Dr. Michael Barry (Mayo Clinic, US) (Guenzel *et al.*, 2013). In their study, the authors characterised the metabolic consequence of PCC disruption in plasma. Some of their key findings in plasma included increases in the C3:C2 ratio, MeCit, ammonia, as well as amino acids such as glycine and lysine. However, aside from assaying for brain-type natriuretic peptide (BNP, *Nppb*; RT-qPCR) and measuring HW:BW ratios, no other work was performed on the heart. Therefore, the first step in this thesis was to determine whether this model exhibits a metabolic profile in the heart. This was investigated in this Chapter by IC-MS in samples from 8-12-week-old mice, although it was underpowered for investigating a possible sex difference. Another purpose of the IC-MS was to profile the metabolome of the heart and determine whether there was an enrichment of other metabolites not routinely assayed for in PA patients, that may be of cardiac relevance.

A key finding from this experiment was that disrupting PCC indeed has a metabolic signature in the heart, but also that the signatures were highly consistent with little variation. Importantly, it was found that metabolites that were increased in plasma, also tended to be increased in the heart. This observation in itself is important in suggesting that the heart is not a 'closed compartment' and that it is sensitive to the extra-cardiac metabolic state (e.g. to defects in liver metabolism or the microbiome state); indeed, common treatments for PA include liver transplantation and broad-spectrum antibiotics to reduce propionate metabolites and to suppress the gut microbiome, respectively, to reduce widespread organ toxicity (Baumgartner

et al., 2014). Perhaps more interestingly, there appeared to be concentration gradient of significantly increased PA metabolites from amPA plasma to amPA heart (~20 fold more abundant in plasma vs heart), at least in the three highly significant metabolites MeCit, propionyl-glycine and methionine sulfone.

MeCit was one of the most abundant metabolites and significantly increased in amPA heart and plasma. MeCit is a classical PA metabolite utilised in the diagnosis of PA. Notably, it is generated from propionyl-CoA and has been shown to be metabolically toxic, by acting as an inhibitor of Krebs cycle enzymes (Cheema-Dhadli *et al.*, 1975). The concurrent increase in propionyl-glycine in heart and plasma was also expected, since glycine is one of the amino acids typically increased in PA; indeed, PA was historically first described as 'idiopathic hyperglycinaemia' (Childs *et al.*, 1961). Likewise, the C3:C2 ratio was also raised in amPA plasma, in agreement with Guenzel *et al.* (2013). Propionyl-glycine is considered as metabolic inert and the relevance of its increased abundance is mainly that there is more propionate in heart and plasma. This interpretation also applies to propionyl-carnitine. Indeed, carnitine supplementation is a treatment regime used in PA patients to reduce concentrations of the more toxic propionyl-CoA, by promoting the generation of propionyl-carnitine) (Baumgartner *et al.*, 2014). Although propionate was not directly measured, the increases in propionate metabolites such as MeCit, propionyl-glycine and propionyl-carnitine support that there is increased propionate in these mice.

A metabolite that was significantly enriched, but not routinely assayed for in PA was methionine sulfone. Methionine sulfone is the oxidised form of methionine, in which its sulphur group has undergone spontaneous oxidation, and is a direct readout of methionine. Since methionine is one of four amino acids that are metabolised to propionyl-CoA (the others being isoleucine, valine and threonine), presumably the excessive concentrations of propionyl-CoA are limiting the metabolism of upstream substrates. It may also reflect increased oxidative stress in these mice, which is considered one of the key processes contributing to organ dysfunction in PA (Richard *et al.*, 2015; Gallego-Villar *et al.*, 2016).

An important piece of information missing from these experiments is whether there are any sex differences in (1) the metabolic signature and (2) the abundance of the metabolites. Aside from general evidence in the field of there being sex differences in cardiometabolic diseases (Murphy *et al.*, 2017; Gerdts & Regitz-Zagrosek, 2019), there is evidence from Michael Barry's laboratory that there are sex differences in the PA mouse. In particular, the evidence suggests that the accumulation of propionate metabolites are greater in females (Guenzel *et al.*, 2015). The metabolomics experiment presented in this Chapter was not sex-balanced. Amino acids were also not measured, which is possible with IC-MS. Furthermore, the samples were from a wide age range (8-12 weeks), whereas almost every experiment in this thesis was conducted at 8 weeks of age. Collectively, it would be important to repeat the metabolomics with a larger, age-matched and sex-balanced cohort.

3.4.2 Maladaptive cardiac hypertrophy does not occur in PA

There is a risk that adverse cardiac hypertrophy can decompensate and eventually lead to complications such as heart failure. As such, assessing for hypertrophy in murine models of heart disease is common. Indeed, a standard first-line approach in cardiac phenotyping a model is histological and immunohistochemical staining for heart morphology (H&E), fibrosis (Masson's trichrome) and capillary density (endomucin) (Schiattarella *et al.*, 2019). However, in their description of the model, Guenzel *et al.* (2013) observed increased *Nppb* transcript in the heart (common hypertrophic gene) and increased HW:BW ratios, suggesting possible hypertrophy. Furthermore, HCM has been reported in PA, albeit in 1-2 patients (Park *et al.*, 2020). Therefore, the investigation for possible maladaptive hypertrophy in the PA mouse was prioritised.

In this thesis, the presence for cardiac hypertrophy in PCC-deficient mice was assessed by several methods. As a first-line assessment, hearts were weighed from the mice. Although HW:BW ratio was significantly increased in amPA females, there was no difference in HW:TL and BW alone was found to be significantly lower in amPA females. Ventricular myocytes isolated from these hearts showed no difference in cell size (cSNARF-1 imaging). Furthermore, LV mass determined from the rendering of short-axis z-stack scans from cine-MRI showed no difference.

Since in this thesis, propionate is hypothesised as a key driver of cardiac dysfunction in systems of dysregulated propionate metabolism (e.g. PA), its potential as a hypertrophic agonist was also

assessed by a quantitative *in vitro* assay utilising SRB staining. The binding of SRB to protein is stoichiometric, so the fluorescence exhibited from stained cells is directly proportional to cell mass (i.e. a hypertrophied cell would be expected to bind more SRB) (Vichai & Kirtikara, 2006; Loonat *et al.*, 2019). However, no change in biomass was detected following propionate treatment with this assay.

Collectively, the data from this Chapter indicate that maladaptive cardiac hypertrophy does not occur in the young PA mouse or in cardiomyocytes treated with propionate *in vitro*.

3.4.3 Assessment of cardiac electrophysiology in PCC-deficient mice by surface ECGs

QT prolongation is a major complication in PA patients (Park *et al.*, 2020). Thus, it was necessary to establish whether there is an effect on gross electrophysiology in PA mice, as well as investigating downstream processes such as cardiac contraction or Ca^{2+} handling. The work in this Chapter sought to determine whether the QT interval (and cardiac electrophysiology) was affected in PCC-deficient mice at the early timepoint of 8 weeks. Although there was a trend toward a shortening of the QT interval in amPA females, no significant differences were detected in the QT interval, or other key electrocardiographic readouts. However, given the evidence for early contractile dysfunction in 8-week-old mice (see Section 3.4.4), it may be that ECG differences would be resolvable at a later timepoint.

Studying the QT (and the ECG) is challenging in mice, particularly so in anaesthetised mice for several interrelated reasons. Pharmacological anaesthesia has been shown to introduce variability in the QT interval, compared to those recorded in conscious animals by telemetry, which had low variability in QT between animals (Mitchell *et al.*, 1998). In humans, the QT interval is commonly adjusted for heart rate (QTc). Since anaesthetics are known cardiorespiratory and autonomic depressants (Galletly *et al.*, 1994; Lindsey *et al.*, 2018), one would assume the anaesthesia-induced variability in QT could be corrected for by using common formulas (e.g. modified Bazett's, also referred to as Mitchell's). However, it has been found that modified Bazett's/Mitchell's formula can underestimate the QT interval and introduce a systematic measurement error (Boukens *et al.*, 2014). Another point to consider is that in humans, the QT interval is inversely related to heart rate. However, there is recent evidence demonstrating that there is significant variability of QT and RR, and that in both anaesthetised and non-anaesthetised mice, there is little correlation between these variables such that even with increased heart rate, QT did not shorten (Roussel *et al.*, 2016; Mulla *et al.*, 2018). The method of correcting the QT interval for heart rate and anaesthesia is not simple in mice and is still debated (Boukens *et al.*, 2014).

It was surprising that there were no significant differences in ECG parameters in PCC-deficient animals, even in the QT interval. However, given the high prevalence of affected QT intervals in PA patients, it is more likely that true differences are not being resolved because 8 weeks is an early timepoint, as well as due to the experimental approach. There are several technical

challenges in recording the ECG from anaesthetised mice, including (1) electrode contact efficiency, (2) anaesthesia depth and (3) temperature control. Pharmacological anaesthetics (e.g. isoflurane) are known to interfere with respiration depth, sinus rhythm and atrioventricular conduction (Galletly *et al.*, 1994). Hypothermia is known to reduce conduction velocity and prolong wave intervals, including the QT (Omar *et al.*, 2016), and it was technically challenging to maintain core temperature in the air-conditioned MRI facility where surface ECGs were recorded. Thus, the ideal method, and indeed the gold-standard, for studying mouse ECGs is by recording conscious ECGs via surgically implantable devices (telemetry) (Ho *et al.*, 2011; Mulla *et al.*, 2018). Doing so would also allow the reliable measurement of other important parameters such as heart rate variability (HRV; a clinically important biomarker of autonomic function), since recordings from surface electrodes in anaesthetised animals are ineffectual of *in vivo* physiology (Thireau *et al.*, 2008). However, since the ECG is ultimately the surface manifestation of cardiac electrical activity, determining whether action potential duration is affected in cardiomyocytes may be a more sensitive and direct approach to determine the effects of PCC deficiency on electrophysiology.

3.4.4 Evidence of early contractile dysfunction in the PA mouse

PA patients frequently manifest a DCM (Park *et al.*, 2020). Therefore, to determine whether there was chamber dilatation, or any changes to contractile function in amPA animals, *in vivo* cardiac function was assessed by cine-MRI in 8-week-old isoflurane-anaesthetised mice. The key findings from this experiment were that amPA had a lower HR, preserved EF, but raised LV

end-diastolic and end-systolic volumes. However, cardiac index was not different, and there was no evidence of gross chamber dilatation (LV free wall and septal wall thicknesses) or pulmonary congestion (lung weights; Figure 3.5). Collectively, these data indicate that young amPA animals (at 8 weeks old) have a mild perturbation of normal function.

Heart rate. There was a discrepancy between the recorded heart rates. That is, there was no difference in HR recorded on the ECG platform, yet a significantly reduced HR recorded during cine-MRI. This inconsistency is not simple to explain and is addressed separately in Section 3.4.5.

LV volumes. Both LV EDV and LV ESV were increased in amPA. The increased LV volumes would result in a rightward shifting of the pressure-volume loop, implicating changes to cardiac relaxation and contraction (Konstam & Abboud, 2017; Bastos *et al.*, 2020). LV EDV is determined by a variety of contributing factors: (1) LV ESV, which sets how much blood is present before diastolic filling, and is itself determined by factors such as contractility and Ca^{2+} transient size; (2) pressure and loading conditions (preload and afterload), which sets the rate of filling and also influences chamber stretch (and hence Frank-Starling effect); (3) kinetics of Ca^{2+} cycling in excitation-contraction coupling, determined by the activity of Ca^{2+} handling proteins as well as Ca^{2+} binding kinetics of troponin C; (4) wall-compliance, which influences the degree of chamber stretch and is determined by various factors, such as titin phosphorylation status; (5) HR, which influences filling time; (6) atrial contraction (Herring & Paterson, 2018).

Due to the variety of possible mechanisms by which LV EDV could be increased in amPA, it is difficult to pinpoint why EDV is increased in these animals without further study. Since cardiac contraction is driven at the cellular level by Ca^{2+} signalling, this would be an informative area of further investigation. Indeed, one explanation for a rightward shift in the pressure-volume loop would be a reduction in HR, as observed during cine-MRI in amPA. Reduced HR would increase filling time and would be expected to raise LV EDV, and LV ESV in parallel. Since the magnitude of changes in HR and volumes were similar (in terms of percentage changes), the possibility of these changes being driven by HR, cannot be excluded.

Ejection fraction. EF represents the proportion of blood ejected from the ventricle (SV/EDV) and is often referred to as a measure of ventricular contractility (Konstam & Abboud, 2017). Despite the changes in LV volumes, there was no statistical difference in EF. However, the error and variation in EFs suggest that there may be a biological change that is not being resolved at the early timepoint of 8 weeks. Regardless, there are caveats to interpreting this parameter and its meaningfulness. Any changes to LV EDV (e.g. due to structural changes) will powerfully influence EF at a given level of contractility and SV. Moreover, taking LV volumes aside, EF is highly dependent on loading conditions (preload or afterload; diastolic and systolic wall stress respectively, determined by volume and pressure) (Konstam & Abboud, 2017; Lindsey *et al.*, 2018). Finally, whilst the EFs seen in this study may appear high (~70-80%), a comparative study assessing cine-MRI vs echocardiography found that MRI can overestimate EF by ~12% due to the higher temporal resolution (Stuckey *et al.*, 2008).

Interpretation of findings. It is difficult to give an interpretation from the data presented in this Chapter alone. However, in combination with the findings in the remainder of this thesis, the changes observed in amPA mice may reflect the early phases of remodelling associated with a diastolic dysfunction and/or the development of DCM. This is explained in the final integrative discussion in Chapter 6.

It should be noted that cine-MRI assessment of cardiac function of amPA mice was performed in a cohort of 8-month-old male mice by Tamayo *et al.* (2020). However, the findings from this Chapter disagreed with their findings. Tamayo *et al.* (2020) claim reduced EF by ~10%, driven by increased ESV but unchanged EDV (i.e. reduction in SV), however it is unclear whether these findings are conclusive based on the presented data. There are some clear differences between our datasets which are difficult to explain. For example, the observed SV in 8-week-old WT males in this thesis were ~39 µL, which is considerably higher than the SV of ~31 µL reported in larger 8-month-old WT males. Comparing WT males again, CO was substantially lower in their mice (~19 mL/min in this thesis vs ~12 mL/min in the Tamayo *et al*. study), and this appears to be largely related to a lower baseline HR (~390 bpm).

3.4.5 Discrepancy in heart rates recorded in ECG platform vs cine-MRI experiments

A key aim from this Chapter was to examine for any potential differences in the QT interval. However, the ECG recordings from the MR setup lacked the resolution to resolve T waves; the priority during cine-MRI was to detect the R wave for the purposes of gating. Therefore, a more purpose-built platform was required. One major inconsistency between the ECG (Section 3.3.4) and the cine-MRI (Section 3.3.5) datasets was in the recorded HR. This was odd, especially given that for most experiments, surface ECGs and MRI were performed on the same mice (after induction of anaesthesia, the ECG was recorded, followed by MRI). This inconsistency is most likely due to the combined effects of anaesthesia and external temperature control (or lack thereof during the ECG recordings). The mouse HR is known to be highly sensitive to temperature (Cingolani & Kass, 2011).

Arguably, animals in the cine-MRI setup were more in a 'steady-state', due to optimised temperature control and the length of the experiment (i.e. ~30-45 secs on ECG platform, vs 40-50 mins in MR scanner). Whilst there was no significant difference in HR recorded from the ECG platform, HR recorded during cine-MRI was significantly lower in male (~10%) and female amPA animals (~7%), independent of body weight, suggesting that this may not be an isoflurane-effect. Speculatively, amPA animals may have basally raised blood pressure and activation of the baroreflex to reduce HR. However, in order to be fully confident that basal HR is different in amPA, long-term ECG monitoring by telemetry in conscious mice would be

required. This would alleviate confounding factors such as anaesthesia, thermoregulation and the diurnal cycle. Basal HR is dependent on a plethora of factors, including the expression and conductance of pacemaker currents (I_f), as well as autonomic tone and signalling by the autonomic nervous system. A truly lower basal HR in amPA would open a variety of interesting experimental avenues. Like humans, basal HR is dominated by vagal tone in mice (Swoap *et al.*, 2008), thus a first step could be to investigate whether cholinergic signalling is changed.

3.5 Summary

There were several key findings presented in this Chapter. Already at 8 weeks of age, mice with PCC-deficiency have a metabolic signature in the heart and significantly accumulate propionate metabolites. At this timepoint however, mice do not have evidence of maladaptive hypertrophy. There were no significant differences resolved in surface ECGs recorded from 8-week-old isoflurane-anaesthetised amPA animals. In contrast, 8-week-old amPA animals had evidence of early contractile dysfunction in the form of raised left-ventricular EDV and ESV, whilst SV, EF and CO were unchanged.

The cause for the increases in EDV and ESV is unknown. However, since cardiac contraction is driven by cardiomyocyte excitation-contraction (E-C) coupling, the experiments in the next Chapter sought to determine whether any changes to cardiac Ca^{2+} handling could explain the contractile dysfunction observed in amPA mice.

Chapter 4. Effects of propionate on cardiomyocyte excitation-contraction coupling

In Chapter 3, mice with PCC deficiency were found to have significantly increased propionate metabolites in heart and plasma, as well as evidence of early contractile dysfunction (cine-MRI) at 8 weeks of age. Therefore, the purpose of the work in this Chapter was to determine whether there was any change in excitation-contraction coupling that may explain the contractile phenotype observed in PA. A related aim was to determine whether any remodelling observed in PCC-deficient mice, could be attributed to an acute or slower-onset response of propionate. To address these questions, a comprehensive assessment of cardiomyocyte Ca^{2+} handling was carried out in isolated ventricular myocytes from PCC-deficient mice at 8 weeks and 20 weeks of age. The effect of propionate was appraised by repeating these studies in wild-type cardiomyocytes treated with high concentrations of propionate *in vitro*.

4.1 Introduction

4.1.1 Cardiac excitation-contraction coupling

Cardiac excitation-contraction (E-C) coupling is the process by which electrical excitation of the surface membrane is linked to mechanical contraction. E-C coupling involves the orchestration of numerous channels and proteins, acting in tandem to facilitate contraction and relaxation of the heart on a beat-to-beat basis. First demonstrated by Sydney Ringer in the early 1880s, the key factor that controls cardiac contraction is Ca^{2+} and the level of cytoplasmic Ca^{2+} ($[Ca^{2+}]_i$). Therefore, the precise regulation of $[Ca^{2+}]_i$ is a homeostatic priority in the heart, and often, processes that modulate E-C coupling involve targeting the properties of Ca^{2+} handling proteins.

4.1.1.1 The ventricular action potential

The cardiac action potential (AP) is the change in membrane voltage over a cardiac cycle, caused by different transmembrane ionic currents from the dynamic opening and closing of various ion channels. The ionic currents are activated in series, such that the AP can be divided into distinct phases (phases 0-4) (Varró *et al.*, 2020). The shape of the AP varies based on the region of the heart. Only the ventricular AP will be described here.

Since the sino-atrial node has the fastest intrinsic pacemaker activity, APs in the ventricular myocyte are normally triggered by an AP in the conduction system or an adjacent myocyte (Bers, 2002b). When the membrane potential reaches threshold, there is rapid activation of the fast-inward sodium current (I_{Na}) conducted by voltage-gated Na^+ channels ($Na_v1.5$). The

resultant Na^+ influx depolarises the cell, causing the upstroke and overshoot of the AP (phase 0). This depolarisation triggers the inactivation of I_{Na} and the transient opening of voltage-gated K^+ channels (I_{to}; transient outward K^+ current; $K_v4.3/K_v1.4$) which contributes to partial early repolarisation (phase 1). The ensuing electrochemical gradient causes the opening of voltage-gated L-type Ca^{2+} channels (LTCC; $Ca_v1.2$) which conduct an inward Ca^{2+} current ($I_{Ca,L}$). The Ca^{2+} influx from $I_{Ca,L}$ (which initiates the Ca^{2+} transient, described next) causes the plateau of the AP (phase 2) and maintains myocyte depolarisation. The later part of the AP plateau is maintained by an inward Na^+ current carried by the Na^+/Ca^{2+}-exchanger (I_{NCX}). Repolarisation of the AP during phase 3 is carried by the delayed rectifier outward K^+ current (I_K), which activates gradually and has a distinct rapid (I_{Kr}; $K_v11.1$, hERG) and slow (I_{Ks}; $K_v7.1$) component. The terminal phase of AP repolarisation is shaped by the inward rectifier potassium current (I_{K1}), and this current also serves as the primary determinant of the resting membrane potential (phase 4). The dissipated transmembrane Na^+ and K^+ gradients as a result of fluxes throughout the AP, are re-established and maintained by the constant activity of Na^+/K^+-ATPase, thus this pump also contributes to the setting of the resting membrane potential (Varró *et al.*, 2020).

Whilst the ventricular AP in rabbits and guinea pig are similar to the human, rat and mouse have a very short spike-like AP (Bers, 2002a). Mathematical models of the murine and rat AP have aided in gaining insight into the underlying mechanisms accounting for the species differences to human (Pandit *et al.*, 2001; Bondarenko *et al.*, 2004). A major difference from the human AP is that, in mouse and rat, $I_{Ca,L}$, carried by LTCC, contributes less to the ventricular

AP. Thus, their APs show a gradual repolarisation versus a distinct plateau (Kaese & Verheule, 2012). However, repolarisation itself is also different and, rather, differences in outward K^+ currents (due to variations in channel/accessory subunit expression) are understood as the primary determinant for variation of AP morphology between species and region of myocardium (Sah *et al.*, 2003). I_K has a minor, or even negligible, contribution to repolarisation in mouse and rat (Nerbonne, 2004). Instead, they have a much faster repolarisation phase predominantly mediated by fast and slow components of I_{to} ($I_{to,f}$ and $I_{to,s}$) (Kaese & Verheule, 2012). In fact, due to a relatively large I_{to} in small rodent myocytes, I_{to} overpowers the depolarising effect of $I_{Ca,L}$ and thereby minimises the plateau in these species (Sah *et al.*, 2003).

4.1.1.2 The Ca^{2+} transient and myofilament activation

Transverse tubules (t-tubules) are deep invaginations of the sarcolemma, which occur at the junction of each sarcomere (z-line) and aid in ensuring a synchronous rise of $[Ca^{2+}]_i$ during systole (Eisner *et al.*, 2017). LTCCs are concentrated in the t-tubule, such that LTCCs are in close proximity to clusters of ryanodine receptors (RyR2, herein referred to as 'RyR') on the junctional membrane of the myocyte's intracellular Ca^{2+} store, the sarcoplasmic reticulum (SR). Together, they form a calcium releasing microdomain, the dyad, and a functional couplon (Hong & Shaw, 2017).

The depolarisation of the myocyte during an AP opens LTCCs, causing Ca^{2+} influx into the cell. This 'trigger Ca^{2+}' causes RyR Ca^{2+} release channels to produce small localised local increases in $[Ca^{2+}]_i$ referred to as Ca^{2+} sparks (Cheng *et al.*, 1993) in a process termed Ca^{2+}-induced Ca^{2+}-

release (Fabiato, 1983). Thus, the bulk of Ca^{2+} required to activate the myofilaments originates from the SR, with Ca^{2+} influx through LTCC making a minor contribution. During the AP, the synchronous production of several thousand Ca^{2+} sparks cause a graded release of Ca^{2+} from the SR, resulting in an abrupt rise in $[Ca^{2+}]_i$ and the upstroke of the Ca^{2+} transient (CaT). This rise in $[Ca^{2+}]_i$ serves to trigger contraction. Ca^{2+} first binds to troponin C on the thin filament, increasing its affinity for troponin I. A conformational change in the troponin complex is then induced, promoting cross-bridge formation (Park *et al.*, 2017).

The 'activator Ca^{2+}' must then be removed from the cytoplasm to reduce $[Ca^{2+}]_i$ and allow relaxation. This is primarily achieved by Ca^{2+} being pumped back into the SR by the SR-Ca^{2+}-ATPase (SERCA2a, herein referred to as 'SERCA') and through cytoplasmic Ca^{2+} extrusion by Na^+/Ca^{2+}-exchange (NCX1, herein referred to as 'NCX'). However, the relative contribution of these processes varies between species. The quantitative Ca^{2+} fluxes in human ventricle and others such as guinea-pig are similar to the rabbit. In rabbit ventricular myocytes, SERCA removes 70% of activator Ca^{2+}, NCX removes 28% and the remaining 2% is removed by the so-called 'slow systems': 1% removed each by the plasma membrane Ca^{2+}-ATPase (PMCA) and the mitochondrial uniporter (Bers, 2002a). In contrast, rat and mouse ventricles poorly mimic the human in terms of quantitative Ca^{2+} flux balance. SERCA is quantitatively more important in mouse and rat due to a higher concentration of pump molecules and the removal of Ca^{2+} by NCX is proportionally less. The resultant balance is 92% of activator Ca^{2+} being removed by SERCA, 7% by NCX and 1% by the slow systems in rat and mouse ventricle (Bers, 2002a). In

regards to PMCA flux, although the involvement of PMCA to bulk cytoplasmic Ca^{2+} flux is traditionally considered small, it is possible PMCA's contribution is in fact higher. For example, whilst PMCA flux is found to be ~10% of the NCX flux by Donald Bers, a larger contribution of ~25-33% is found by David Eisner (Eisner *et al.*, 2020).

4.1.2 Control of cardiomyocyte Ca^{2+} handling

The heart has a remarkable capacity to fine-tune cardiac output according to physiological demand by adjusting various aspects of its function, including its contractile strength (inotropy) relaxation rate (lusitropy) and rhythmicity (chronotropy). These functional properties can be adjusted by modulating the multiple interacting proteins involved in E-C coupling. Specifically, cardiomyocyte Ca^{2+} handling has an important influence on cardiac inotropy and lusitropy. The regulation of cardiomyocyte Ca^{2+} handling and its modulation by the sympathetic nervous system are described below.

The activity of the key Ca^{2+} handling proteins (LTCC, RyR, SERCA and NCX) can be directed modulated by post-translational modifications (PTM) and their relative contribution to the Ca^{2+} handling ensemble can also be changed through their individual expression levels.

Kinase signalling. During acute physiological stimulation (e.g. exercise) or pathological stress (e.g. heart failure), the release of catecholamines results in the activation of G_s-coupled β-adrenergic receptors (β-ARs). In turn, the G-protein dissociates and the α_s subunit activates adenylyl cyclase, generating cAMP (3'-5'-cyclic adenosine monophosphate) from ATP.

Elevations in cAMP subsequently activate its main downstream effector, protein kinase A (PKA), which phosphorylates multiple key targets in the cardiomyocyte (Zaccolo & Movsesian, 2007). Ca^{2+}/calmodulin-dependent protein kinase II (CaMKII) shares similar phosphorylation targets with PKA and is also activated during sympathetic stimulation (Dewenter *et al.*, 2017).

Trigger Ca^{2+}: LTCC. The major entry pathway for Ca^{2+} into cardiomyocytes is the LTCC. The amount of Ca^{2+} released during systole is a function of 'trigger size', and the amount of Ca^{2+} stored in the SR, determined by the balance of Ca^{2+} fluxes. The key mechanism by which positive inotropy is achieved by PKA activation is through LTCC phosphorylation (leading to increased $I_{Ca,L}$) and/or greater SR Ca^{2+} availability (Bers, 2002a). Intracellular Ca^{2+} can also enhance $I_{Ca,L}$ via CaMKII-mediated phosphorylation of LTCCs (Varró *et al.*, 2020). Finally, LTCC is known to autoregulate its transcription through interaction of its carboxyl terminus with key cardiac promoters, such as Nkx2.5/Mef2 (Schroder *et al.*, 2009; Naranjo & Mellström, 2012).

SR function: RyR. Ca^{2+} release from the SR is tightly linked to LTCC through the couplon and is graded with the amplitude of LTCC, with the SR typically releasing only ~50% of its Ca^{2+} during the CaT (Eisner *et al.*, 2017). RyRs are arranged in clusters ('Ca^{2+} release unit'; CRU) and distributed evenly over the SR to ensure a homogenous propagation of Ca^{2+} sparks (i.e. CICR) and a synchronised global rise in $[Ca^{2+}]_i$ (Chen-Izu *et al.*, 2006; Cheng & Lederer, 2008). Indeed, this distribution can also become disordered and remodel in disease (Hiess *et al.*, 2018). The

propagation velocity of the Ca^{2+} signal is determined by several factors, including RyR spacing, SR Ca^{2+} load and SERCA activity (Swietach *et al.*, 2010; Landstrom *et al.*, 2017).

The open probability of RyR can also be regulated by its phosphorylation state, through balanced actions of PKA, CaMKII and protein phosphatases (PP1 and PP2A) (Landstrom *et al.*, 2017). RyR does not exist in isolation in the SR membrane. Instead, it is part of a macromolecular complex with a plethora of interacting proteins that directly regulate its function (Eisner *et al.*, 2017). RyR mainly forms a complex with triadin, junctin, and calsequestrin (the major Ca^{2+} buffer of the SR). As well as CICR and its sensitivity to dyadic Ca^{2+}, RyR is known to strongly be regulated by SR luminal Ca^{2+}, either through direct binding of Ca^{2+} to RyR, or luminal Ca^{2+} interacting with calsequestrin, triadin and junctin (Landstrom *et al.*, 2017). As such, Ca^{2+} overload of the SR can be pro-arrhythmic by initiating spontaneous Ca^{2+} release from RyRs (i.e. diastolic Ca^{2+} leak from leaky RyRs), which can trigger Ca^{2+} release from adjacent RyR clusters and propagate throughout a myocyte as arrhythmogenic Ca^{2+} waves (MacQuaide *et al.*, 2007; Cheng & Lederer, 2008). That is, these waves can induce Ca^{2+}-induced arrhythmias by activating inward currents such as I_{NCX} and triggering delayed afterdepolarisations (Landstrom *et al.*, 2017).

SR function: SERCA. Increased SR Ca^{2+} load through faster Ca^{2+} reuptake by SERCA is an important mechanism by which positive inotropy is achieved during β-AR stimulation (Bers, 2002a). Under basal conditions, the activity of SERCA is tonically suppressed by phospholamban (PLN), a small transmembrane protein located on the SR and an accessory

protein to SERCA. PLN exists in a dynamic equilibrium between monomeric and pentameric states. It is understood that the monomer is the active form that binds and inhibits SERCA, whilst the pentameric form is inactive, or at the least, less active than the monomer (Kranias & Hajjar, 2012).

The inhibitory mechanism of PLN on SERCA is to diminish its affinity for Ca^{2+}, rather than affecting its V_{max} (MacLennan & Kranias, 2003). Phosphorylation of PLN on serine 16 (PLN_{pSer16}) by PKA, or threonine 17 (PLN_{pThr17}) by CaMKII, relieves PLN inhibition of SERCA and increases its activity by two- to three-fold (MacLennan & Kranias, 2003). β-AR stimulation is positively lusitropic due to acceleration of the decline in $[Ca^{2+}]_i$ following systolic Ca^{2+} release. This effect is primarily achieved through dual-site PLN phosphorylation, and in addition, this faster SR Ca^{2+} reuptake also contributes to increasing SR Ca^{2+} load (Bers, 2002a).

Finally, like in the case of LTCCs, the expression of SERCA itself can also be regulated by Ca^{2+}, through the calcineurin/NFAT pathway (Naranjo & Mellström, 2012).

SR Ca^{2+} content. SR Ca^{2+} content is determined by the balance of Ca^{2+} fluxes. Increasing SERCA activity or decreasing RyR opening will act to increase SR Ca^{2+}. Therefore, increasing Ca^{2+} efflux through NCX will decrease SR Ca^{2+}. Counter-intuitively, increasing LTCC does not simply increase SR content. This is because, whilst the peak $I_{Ca,L}$ amplitude determines SR Ca^{2+} release (i.e. increase in current decreases SR content), the rest of the current loads the cell and the SR with Ca^{2+}. At steady-state, these two opposing effects are matched (Eisner *et al.*, 2017).

Ca^{2+} extrusion: NCX. NCX is electrogenic and by having a stoichiometry of 3 Na^+ for 1 Ca^{2+}, its activity produces an ionic current (I_{NCX}) (Eisner *et al.*, 2017). NCX activity is driven thermodynamically and uses the energy from the electrochemical gradients of Na^+ and Ca^{2+} (Blaustein & Lederer, 1999). NCX can operate in forward mode generating an inward depolarising current (inward I_{NCX}) by extruding 1 Ca^{2+} in exchange for the influx of 3 Na^+. However, NCX can also operate in reverse mode to bring Ca^{2+} into the cell, generating an outward depolarising current (outward I_{NCX}).

The activity of NCX is sensitive to the concentration gradients of Na^+ and Ca^{2+}, but also to the prevailing membrane potential (Eisner *et al.*, 2017). For example, high $[Ca^{2+}]_i$ favours Ca^{2+} efflux (inward I_{NCX}), whereas positive membrane potentials or high $[Na^+]_i$ favours Ca^{2+} influx (outward I_{NCX}) or simply reduces Ca^{2+} efflux (reduced inward I_{NCX}) (Bers, 2002a; Eisner *et al.*, 2020). Under normal physiological conditions, NCX predominantly operates by extruding Ca^{2+}, driven mostly by the CaT. However, the amount of Ca^{2+} influx through NCX can increase greatly if $[Na^+]_i$ is elevated (e.g. as in heart failure), SR Ca^{2+} release is inhibited, or AP duration is prolonged (Bers, 2002a).

Role of AP duration in influencing the CaT. As alluded to, the activity of LTCC and NCX are influenced by the membrane potential. As such, the CaT can shape the AP, and vice-versa, the shape of the AP can influence the time-course of the CaT (Santana *et al.*, 2010). For example, the positive membrane potential of the AP plateau limits Ca^{2+} extrusion by NCX (slowing CaT recovery). Similarly, a long AP with a prolonged plateau phase prolongs the open

time of LTCCs, resulting in greater Ca^{2+} entry (extending CaT duration). I_{to} is thought to play a modulatory role and influence $I_{Ca,L}$ (and possibly I_{NCX}) during E-C coupling (Sah *et al.*, 2003).

Ca^{2+} buffering. Most cytoplasmic Ca^{2+} in cardiomyocytes is bound to cytoplasmic buffers and only ~1% of Ca^{2+} is free and ionised (Smith & Eisner, 2019). Thus, even minor changes in cytoplasmic buffering capacity can have a profound effect on calcium signalling. Buffering capacity is dependent on numerous factors, including the amount of buffer, the prevailing $[Ca^{2+}]_i$ (buffering power is inversely proportional to $[Ca^{2+}]_i$), as well as Ca^{2+} binding kinetics (Eisner *et al.*, 2017). The major cytoplasmic buffers in cardiomyocytes are troponin C and SERCA, and the buffering capacities of these two proteins are regulated by the phosphorylation of troponin I and PLN, respectively (Smith & Eisner, 2019). The mitochondria contain a Ca^{2+} channel (mitochondrial Ca^{2+} uniporter, MCU), as well as a Na^+/Ca^{2+}-exchanger, which can influence myocardial energetics (Kohlhaas *et al.*, 2017). Although the evidence is mixed, the mitochondria have been suggested as a significant sink for Ca^{2+} (Eisner *et al.*, 2017).

Ca^{2+} flux balance. In the steady-state, the amount of Ca^{2+} entering the cell must equal that extruded during each cardiac cycle. Any imbalance between influx and efflux would result in a net gain or loss of Ca^{2+} from the cell, causing the cell to be no longer in steady-state. The myocyte therefore employs various mechanisms in order to achieve a homeostasis of Ca^{2+} levels and balance Ca^{2+} influx and efflux (Eisner *et al.*, 2020). Mechanisms of maintaining flux balance include altering sarcolemmal Ca^{2+} fluxes (e.g. NCX) and altering intracellular Ca^{2+} fluxes (e.g.

RyR), as well as changing expression levels of the major Ca^{2+} handling proteins (Naranjo & Mellström, 2012; Eisner *et al.*, 2017).

Summary of factors affecting Ca^{2+} handling protein biophysical properties. The key factors that influence the specified biophysical property of the four major Ca^{2+} handling proteins are summarised below (Bers, 2002a; Eisner *et al.*, 2017; Landstrom *et al.*, 2017; Varró *et al.*, 2020):

- $I_{Ca,L}$ carried by LTCC, depends on:
    - channel expression level;
    - recruited channel number (modulated by kinase signalling);
    - membrane potential (determined by stage of AP);
    - single channel conductance;
    - open probability (modulated by kinase signalling);
    - inactivation kinetics (influenced by voltage and prevailing $[Ca^{2+}]$).
- Ca^{2+} release by RyR, depends on:
    - channel expression level;
    - size of Ca^{2+} release unit (determined by number of RyR per cluster);
    - single channel conductance;
    - open probability (modulated by kinase signalling);
    - LTCC coupling;
    - SR Ca^{2+} load.
- Ca^{2+} reuptake by SERCA, depends on:
    - pump expression level;
    - Ca^{2+} affinity (determined by PLN status)
    - ATP/ADP ratio (drives ATPase activity);
- Ca^{2+} transport by NCX, depends on:
    - exchanger expression level;
    - membrane potential (determined by stage of AP);
    - prevailing $[Na^+]_i$ and $[Ca^{2+}]_i$.

4.1.3 Ca^{2+} handling in propionic acidaemia

Cardiomyocyte Ca^{2+} handling and E-C coupling frequently becomes dysregulated in a number cardiac pathologies, including cardiomyopathy and arrhythmia (Watkins *et al.*, 2011; Eisner *et al.*, 2017). However, the consequence of propionic acidaemia on Ca^{2+} handling is largely unknown. Only one study has been published to date. Tamayo *et al.* (2020) performed Ca^{2+} imaging on isolated ventricular myocytes also from the *Pcca*$^{-/-}$ A138T (amPA) mouse model, as done in this thesis. Their findings were indicative of reduced CaT amplitude, reduced SERCA activity and possibly increased diastolic Ca^{2+}. However, there are several technical differences from the study by Tamayo *et al.* (2020) that are notable. The experiments appear to be underpowered and also used conventional statistical methods (i.e. parametric tests), which have been recognised to overestimate significance in cardiomyocyte studies (Sikkel *et al.*, 2017). Cardiomyocyte imaging was also conducted at room temperature and using Fluo-3 (single-wavelength Ca^{2+} dye). E-C coupling is known to be temperature-sensitive and ratiometric (dual-wavelength) Ca^{2+} dyes are required to measure diastolic Ca^{2+}, since single-wavelength dyes require normalisation to the baseline fluorescence intensity (F/F_0) (Eisner *et al.*, 2020). Critically, experiments were performed in animals that were 8 months old, which are known to experience age-exacerbated oxidative stress and mitochondrial oxidative damage in this mouse model (Gallego-Villar *et al.*, 2016). Given that mitochondrial damage is progressive, we can more confidently attribute any changes in Ca^{2+} handling to a propionate-specific effect in the younger animals (8-week) where less oxidative damage is expected (Kujoth *et al.*, 2005; Peoples *et al.*,

2019). Indeed, Tamayo *et al.* (2020) found increased levels of reactive oxygen species in amPA cardiomyocytes and suggested oxidation of SERCA, which they attributed as a cause of reduced SERCA ATP hydrolysis found in their study.

Collectively, despite the study by Tamayo *et al.* (2020), the experiments performed in this Chapter were still warranted.

4.1.4 Aims of this Chapter

In vivo cardiac function assessed by cine-MRI in amPA animals demonstrated early evidence of contractile dysfunction (raised EDV and ESV; Chapter 3). These changes were observed even at the early timepoint of 8 weeks of age. Since cardiac contraction is driven by the cycling of Ca^{2+} during cardiomyocyte E-C coupling, it would be important to determine whether this process is affected in amPA, also at the 8-week timepoint. Moreover, it is unknown whether continued exposure of the heart to propionate metabolites, has an 'additive' effect to further drive dysfunction, or whether there would be a compensatory response instead to any observed remodelling to Ca^{2+} handling. Finally, the metabolomics experiment in amPA from Chapter 3 gave evidence for increased propionate in these hearts. However, it is unknown to what extent propionate contributes to remodelling in Ca^{2+} handling, or what kind of timescale is required for it to exert its actions. Therefore, the aims of this Chapter were to:

a) Appraise cardiomyocyte Ca^{2+} handling in ventricular myocytes freshly isolated from 8-week-old and 20-week-old amPA hearts;
b) Determine whether exogenously applied propionate to WT myocytes *in vitro* can phenocopy some of the responses observed in amPA.

4.2 Specific methods

4.2.1 Biological models

Myocytes from three biological models were used for the experiments described in this Chapter. The superfusion solutions are briefly mentioned here, but described in more detail in Section 4.2.3.

Pcca$^{-/-}$ *(A138T) AMVMs.* To determine the consequences of an *in vivo* accumulation of propionate and its metabolites on cardiomyocyte Ca^{2+} handling, adult mouse ventricular myocytes (AMVMs) were isolated from adult PA and wild-type animals (*amPA* and *amWT*, respectively) from the *Pcca*$^{-/-}$ (A138T) mouse line, at two timepoints: 8 weeks and 20 weeks of age. Measurements were made in regular Normal Tyrode's (NT) solution.

Wild-type ARVMs. To determine whether propionate alone has any acute effect on cardiomyocyte Ca^{2+} handling, experiments were performed in WT adult rat ventricular myocytes (ARVMs) acutely exposed (10-30 mins) to modified NT that contained propionate, either at a normal or modestly reduced extracellular pH (pH 7.4 and 7.3, respectively). Control experiments were performed in regular NT (pH 7.4) free of propionate.

Wild-type NRVMs. To determine whether propionate alone has any chronic effect on cardiomyocyte action potentials and Ca^{2+} handling, experiments were performed in WT neonatal rat ventricular myocytes (NRVMs) that were cultured (48 hrs) in various formulations

of culture media, which included propionate (Table 2.3, Section 2.2.4). Notably, measurements were made in regular NT after the washout of original treatment.

4.2.2 Primary cardiomyocyte isolation

Adult myocytes. Primary ventricular cardiomyocytes were isolated from adult mouse (AMVM) or adult rat (ARVM) as described in Section 2.2.2. After isolation, adult cardiomyocytes were stored in the original isolation solution containing 1 mM $CaCl_2$ and used for experiments the same day.

Neonatal myocytes. Primary ventricular cardiomyocytes were isolated from neonatal rat (NRVM) as described in Section 2.2.3. NRVMs were plated on fibronectin-coated 4-well chambered coverslips (Ibidi 4-well µ-slide, #80426) at ~60,000 cells/cm^2 in M1 media (10% HS, 5% NCS). On day-1 post-isolation, serum was reduced 10-fold (1% HS, 0.5% NCS) and on day-2 myocytes were serum-starved. On day-3, cells were treated for 48 hours and experiments were performed on day-5 post-isolation. Neonatal myocytes were kept in the cell culture incubator until they were loaded with fluorescent dyes for voltage and Ca^{2+} imaging (described in subsequent sub-sections).

4.2.3 Solutions

All cardiomyocyte superfusion experiments were performed using NT solution (NT) either buffered with bicarbonate (BC) or HEPES (NT-BC and NT-HEPES, respectively). Since CO_2/HCO_3^- is the physiological buffer *in vivo*, NT-BC was preferentially used, unless there was an experimental justification not to do so. The formulation for the standard solutions are shown in Table 4.1. NT-BC solutions as standard had 22 mM $NaHCO_3$, as when bubbled with 5% CO_2/air (5% of atmospheric pressure: 38 mmHg), this gives a physiological extracellular pH (7.39), as shown by the Henderson-Hasselbalch equation. Experiments in ARVMs to examine the acute effects of propionate used variations of NT-BC and NT-HEPES by, for example, including the sodium salt of propionate (NaPr), or having a reduced bicarbonate concentration. In such instances, osmolality was balanced by a proportional reduction in NaCl. Ca^{2+} experiments presented in this Chapter used the acetoxy-methyl ester (AM) form of fluorescent dyes to facilitate their permeation into the cell. Thus, to minimise dye extrusion during superfusion, the organic anion transport inhibitor probenecid was typically included in solutions (Di Virgilio *et al.*, 1990).

Table 4.1. Overview of experimental solutions used for superfusion studies.

STANDARD SOLUTIONS			
NT solution	Salts (in mmol/L)		
NT-BC	125 NaCl, 22 $NaHCO_3$, 4.5 KCl, 1 $MgCl_2$, 1 $CaCl_2$, 11 glucose, 1 probenecid (5% CO_2/air).		
NT-HEPES	135 NaCl, 20 HEPES, 4.5 KCl, 1 $MgCl_2$, 1 $CaCl_2$, 11 glucose, 1 probenecid; pH adjusted to 7.40 at 37°C with NaOH.		
EXPERIMENTAL SOLUTIONS			
Readout *Fluorophore* (relevant section no.)	Myocyte model	NT buffer	Specific modifications to the standard solutions (in mmol/L)
Ca^{2+} transients *Fura Red/Fluo-3* (4.2.6)	AMVM	BC	For caffeine-evoked Ca^{2+} release: NT-BC with 10 caffeine.
	ARVM	BC	Three experimental groups: • *Control:* standard NT-BC • *6 cPA:* 6 NaPr, 119 NaCl • *6 uPA*: 6 NaPr, 16 $NaHCO_3$, 0.2 NH_4Cl For caffeine-evoked Ca^{2+} release: standard/modified NT-BC solution with 10 caffeine.
	NRVM	HEPES	None.
Membrane potential *FluoVolt* (4.2.7)	NRVM	HEPES	None.

All experimental solutions were based on 'standard' Normal Tyrode's (NT) solutions shown at the beginning of the Table. Modifications made to NT are indicated according to the experiment performed. AMVM, adult mouse ventricular myocyte; ARVM, adult rat ventricular myocyte; cPA, compensated propionic acidaemia, NaPr, sodium propionate; NRVM, neonatal rat ventricular myocyte; NT-BC, bicarbonate-buffered Normal Tyrode's; NT-HEPES, HEPES-buffered Normal Tyrode's; uPA, uncompensated propionic acidaemia.

4.2.4 Myocyte superfusion

Adult and neonatal myocytes were superfused in a custom-made Perspex chamber and platform, respectively (Figure 4.1). They were designed to facilitate superfusion at high flow-rates in order to maintain temperature and target pH in CO_2/HCO_3^--buffered solutions. Solutions were also delivered through platinum-cured silicone tubing to minimise the escaping of CO_2.

Adult myocytes were plated on the chamber pre-coated with poly-L-lysine (Sigma-Aldrich/Merck, P4707) to enable myocyte adhesion and superfused at 3 mL/min (pump set to 12 RPM, Gilson MINIPULS 3). Caffeine pulses were delivered through a filamented borosilicate glass patch pipette manoeuvred with a micromanipulator (Narishige).

Neonatal myocytes were cultured and imaged in 4-well chambered coverslips (Ibidi 4-well µ-slide, #80426) positioned on a bespoke coverslip platform. Myocytes were superfused at 2.5 mL/min (pump set to 11 RPM, Gilson MINIPULS 3). Myocytes in the coverslip awaiting imaging were kept in NT-HEPES rather than the original treatment media (CO_2/HCO_3^--buffered).

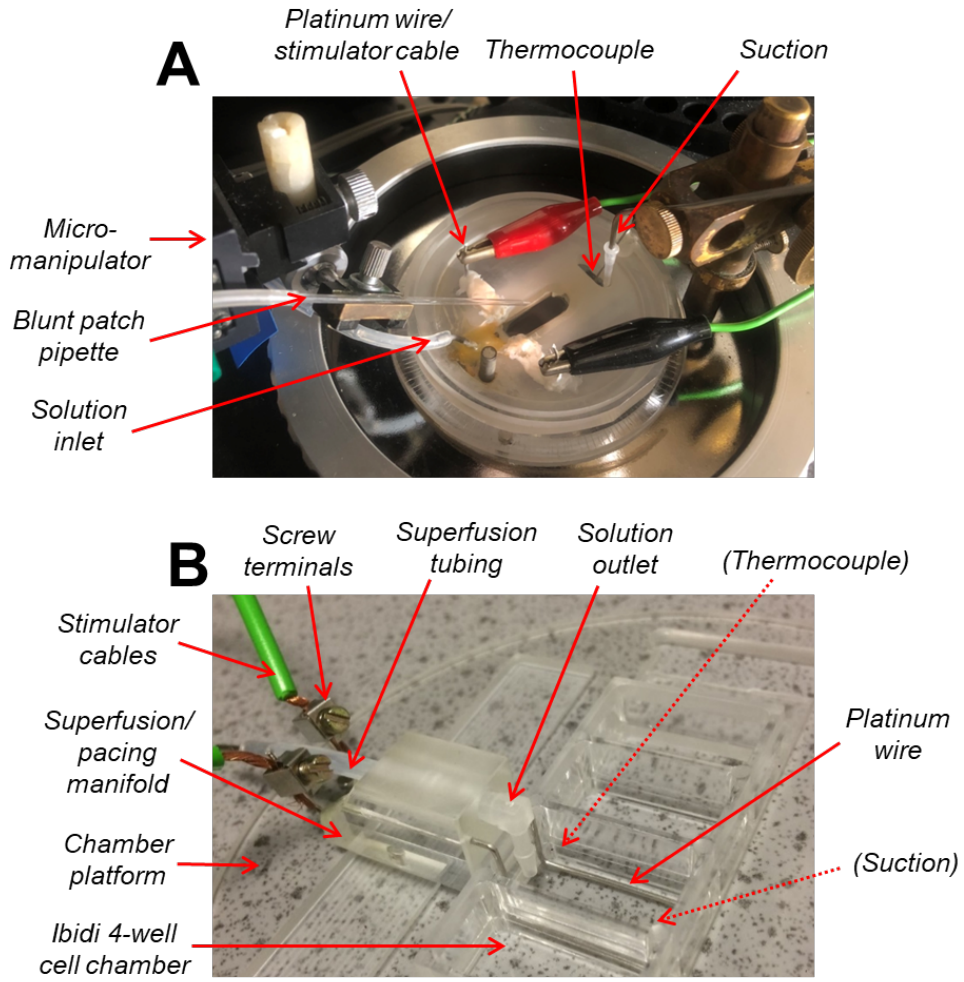


Figure 4.1. Superfusion setup for adult and neonatal myocytes. In both setups, field-stimulation (pacing) of myocytes was delivered through platinum wires and temperature was constantly monitored using a K-type thermocouple connected to a bath temperature controller. *(A)* Setup for adult myocytes. Caffeine pulses were delivered through the patch pipette manoeuvred with a micromanipulator. *(B)* Setup for neonatal myocytes. Myocytes were imaged in 4-well chambered coverslips under superfusion via a custom manifold.

4.2.5 Whole-cell epifluorescence microscopy

Epifluorescent imaging was conducted using an sCMOS camera (optiMOS, QImaging) and an LED light source (CoolLED pE-4000; firmware v 2.0.6) through a 40x dry objective. The appropriate filters (Chroma) were used for each fluorescent dye to achieve the desired excitation wavelength and capture its emission. The light source was synchronised to the camera using a

multichannel streaming device (MultiStream Pro, Cairn Research) and wavelength excitation was triggered by the sCMOS camera. MicroManager (version 1.4.23) was used to operate the camera. The exposure time and pixel binning used was optimised per dye and specified in relevant sections. Images were saved as stacks and analysed with Fiji ImageJ (Schneider *et al.*, 2012) using custom macros. Typically, a region of background clear of any cellular debris was first selected and its time-average was subtracted from the stack. The polygon tool was then used to draw around the region of interest and the fluorescent signal (F) was measured. Downstream data analysis was performed with MATLAB using custom scripts.

4.2.6 Ca^{2+} imaging

4.2.6.1 Ca^{2+} transients in adult myocytes

Fura Red. To record Ca^{2+} transients (CaTs), AMVMs and ARVMs were AM-loaded with Fura Red (FR; Invitrogen, F3021), a ratiometric (dual-wavelength) Ca^{2+} dye. Whilst single-wavelength dyes are more commonly used for qualitative data, ratiometric dyes are preferred for quantitative measurements (e.g. concentration) (Bootman *et al.*, 2013). The ratio of the two wavelengths, pre-calibrated to a known Ca^{2+} concentration (determined experimentally), is not affected by inter-cell differences such as loading efficiency. Thus, ratiometric dyes offer less cell-to-cell variability and are essential in the measurement of important cardiac parameters, such as diastolic Ca^{2+} (Eisner *et al.*, 2020). Indeed, it is known that Ca^{2+} indicators used in the measurement of $[Ca^{2+}]_i$ to some extent buffer Ca^{2+} (Bootman *et al.*, 2013). Therefore, the loading

conditions and the concentration of FR was kept consistent for every measurement made in this thesis, allowing any changes in $[Ca^{2+}]_i$ being attributed to true biological changes.

FR was prepared by reconstituting 50 µg dye with 50 µL of DMSO containing 10% w/v Pluronic F-127. Pluronic F-127 (Invitrogen, P6867) was solubilised in DMSO by heating at 40°C for 30 mins whilst vortexing at 1,000 RPM (ThermoMixer C). Myocytes were AM-loaded for 10 mins at room temperature at 1:100 v/v, to give a final concentration of 9.2 µM FR and 0.1% Pluronic. Cells were loaded and plated onto the bespoke Perspex superfusion chamber coated with poly-L-lysine mounted on an Olympus IX73 inverted microscope.

Execution. All adult myocyte CaT experiments were conducted in NT-BC (Table 4.1). When a myocyte is initially superfused, it is exposed to numerous physiological stresses, including physical shear forces and increased temperature. Additionally, superfusing in NT-BC initially acidifies the cell (as CO_2 enters). Therefore, to minimise abrupt disturbances to the cell, myocytes were superfused initially in NT-HEPES. After ~1 min when the experimental temperature (37°C) was reached, superfusion was switched to the appropriate NT-BC solution (Table 4.1) and recordings were made at least 5 mins after the switch to NT-BC, to allow pH_i to recover and myocytes to reach a steady-state.

The protocol used to interrogate Ca^{2+} handling is shown in Figure 4.2. To record electrically-evoked CaTs, myocytes were field-stimulated using a constant voltage isolated stimulator (Digitimer, model DS2A-Mk.II) triggered by an external stimulator. Cells were stimulated at 2

Hz with a 5 ms pulse duration at the lowest voltage that paced myocytes. After recording a train of ~10 steady-state electrically-evoked CaTs, the stimulator was turned off for 2-3 secs, and caffeine-evoked Ca^{2+} release was recorded by rapidly exposing the cell to test solution containing 10 mM caffeine, delivered via a filamented borosilicate glass patch pipette (Harvard Apparatus, GC150TF-10, #30-0066).

Ratiometric imaging. FR imaging was executed in dual-excitation mode (excitation alternating between 490 nm and 435 nm/emission 645 ± 37.5 nm) and imaging was conducted at 2 ms exposure time at each wavelength (490 nm and 435 nm) with 8 x 8 pixel binning (120 x 67 pixels, 150 fps). Calibration of FR ratio to true [Ca^{2+}] was done in separate experiments by dissolving the free FR acid in 10 mM BAPTA solutions over a range of free [Ca^{2+}]. The intensities of the LEDs were set at the beginning of the experimental series so that the resting fluorescence in wild-type myocytes was close to 1.0.

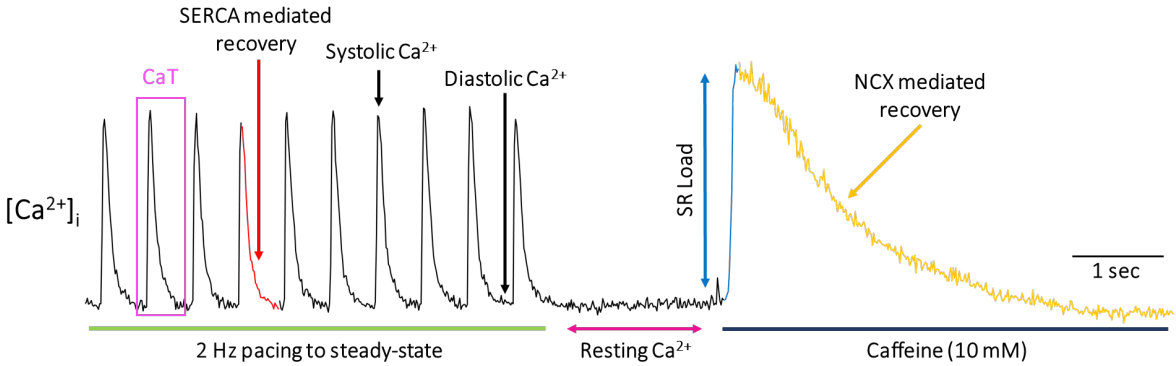


Figure 4.2. Protocol for the recording of electrically-evoked CaTs and caffeine-evoked Ca^{2+} release. An annotated representative trace is shown. A train of steady-state Ca^{2+} transients (CaTs) from electrical pacing (2 Hz) was recorded. The recovery kinetics from electrically-evoked CaTs was used to determine SR Ca^{2+}-ATPase (SERCA) activity. 2-3 secs after the cessation of pacing, the myocyte was rapidly exposed to superfusate containing 10 mM caffeine. The recovery kinetics of caffeine-evoked Ca^{2+} release was used to primarily determine Na^{+}/Ca^{2+}-exchanger (NCX) activity.

Analysis. Images were analysed to measure the fluorescent signal at 490 nm (F_{490}) and 435 nm (F_{435}). The data were ratioed ($F_{490/435}$) in MATLAB and a time-course was created for each cell (Figure 4.2). The following parameters were extracted from the averaged CaT (generated by averaging > 3 consecutive steady-state CaTs) and the time-course of caffeine-evoked Ca^{2+} release:

- ***Systolic and diastolic [Ca^{2+}]:*** quantified by the peak and trough of the averaged CaT;
- ***Time-averaged [Ca^{2+}]:*** Average [Ca^{2+}] throughout the CaT;
- ***Released [Ca^{2+}]:*** total [Ca^{2+}] released during the CaT, quantified by multiplying CaT amplitude (systolic – diastolic) by buffering capacity (characterised with the values B_{max} 109 μM and K_d 0.60 μM; Trafford *et al.* (1999) and Li *et al.* (2011));
- ***SERCA rate:*** shown as the inverse of the time-constant, quantified from the slope of the recovery phase of electrically-evoked CaTs, by plotting [Ca^{2+}] against flux (slope of recovery curve x buffering capacity);
- ***Backflux constant:*** the flux required to balance SR Ca^{2+} uptake by SERCA (mainly diastolic Ca^{2+} leak from RyRs);
- ***Resting [Ca^{2+}]:*** quantified from the interval between the last electrically-evoked CaT and caffeine-evoked Ca^{2+} release;
- ***Peak caffeine [Ca^{2+}] and SR Ca^{2+} load:*** [Ca^{2+}] at the peak of the caffeine-evoked Ca^{2+} release, and an estimation of SR load (buffering capacity was assumed as unchanged);
- ***Release fraction:*** fraction of total SR Ca^{2+} released during the CaT event (released [Ca^{2+}]/SR Ca^{2+} load);
- ***NCX rate:*** shown as the inverse of the time-constant, quantified from the slope of the recovery phase of caffeine-evoked Ca^{2+} release, by plotting [Ca^{2+}] against flux (slope of recovery curve x buffering capacity);
- ***Influx constant:*** the flux required to balance Ca^{2+} extrusion by NCX (the identity of this influx is unknown; Eisner *et al.* (2020)).

4.2.6.2 Ca^{2+} transients in neonatal myocytes

Fluo-3. CaTs were imaged in NRVM monolayers cultured in chambered coverslips (Ibidi, 4-well ibiTreat μ-Slide, #80426) using a bespoke superfusion setup. Myocytes were seeded on fibronectin-coated surfaces at ~60,000 cells/cm^2 in *M1* media. NRVMs were cultured as described in Section 2.2.3, and 72 hrs after isolation, were cultured for 48 hrs in the respective treatment media (Table 2.3). Myocytes were AM-loaded with Fluo-3 (Invitrogen, F1242), a single-wavelength (non-ratiometric) Ca^{2+} dye. Although a ratiometric dye (e.g. Fura Red) was preferred, neonatal myocytes were found not to uptake FR. Fluo-3 was prepared by reconstituting 50 μg dye with 37.5 μL of DMSO containing 7% w/v Pluronic. After washing out the treatment media with NT-HEPES, myocytes were loaded (in NT-HEPES) for 10 mins at room temperature at 3:100 v/v, to give a final concentration of 35.4 μM Fluo-3 and 0.07% Pluronic.

Execution. Due to the structure and dimensions of the chamber coverslip that the NRVMs were cultured in, a suitable caffeine delivery system was not available, and thus only electrically-evoked CaTs were recorded. Furthermore, due to the slower superfusion rate used in neonatal myocytes (consequent to the shape of the chamber), experiments were conducted in NT-HEPES as opposed to NT-BC, since CO_2 diffuses out of solution, affecting the CO_2-HCO_3 equilibrium, and thus pH. NRVMs were stimulated at 2 Hz with a 5 ms pulse duration as per the FR protocol. Recordings were made under steady-state conditions from a train of at least 10 CaTs under superfusion in NT-HEPES at 37°C.

Imaging. Fluo-3 imaging was executed in single-excitation mode (excitation 488 nm/emission >510 nm). Imaging was conducted at 3 ms exposure with 4 x 4 pixel binning (120 x 67 pixels, 333 fps).

Analysis. Images were analysed as stacks in ImageJ. After subtracting the background signal, fluorescence emission was measured in cells and expressed as fluorescence intensity normalised to baseline (F/F_0). The data was analysed in MATLAB and the following information was extracted per cell (averaged from at least 6 steady-state CaTs):

- ***Time-to-peak:*** quantified as the duration from baseline to peak $[Ca^{2+}]_i$, a readout of CICR coupling;
- ***Amplitude:*** difference between the peak and baseline fluorescence;
- ***CaT_{90}:*** Time to 90% CaT recovery (CaT_{90}), an approximation of SERCA activity.

4.2.7 Membrane potential imaging

FluoVolt. Action potentials (APs) were imaged in NRVM monolayers using FluoVolt, a fast-response, high-sensitivity membrane potential fluorescent probe (Invitrogen, F10488). Myocytes were loaded for 30 mins at room temperature with FluoVolt (1:1,000 v/v; supplemented with PowerLoad at 1:100 v/v) in NT-HEPES. Recordings were made under steady-state conditions from a train of at least 10 APs under superfusion in NT-HEPES at 37°C. APs were imaged in NRVMs paced at 2 Hz and FluoVolt imaging was executed in single-excitation mode (excitation 488 nm/emission >510 nm). Imaging was conducted at 3 ms exposure with 4 x 4 pixel binning (120 x 67 pixels, 333 fps). Images were analysed in ImageJ and

fluorescence data analysed as F/F_0. Time-courses were processed in MATLAB to quantify action potential duration (APD) at 90% repolarisation (APD_{90}).

It should be noted that during the analysis of APDs, it was observed that within a treatment group, there were on occasion two clear populations of APD. Fibroblast contamination is an inherent problem with NRVM culture. Whilst myocytes discharge an action potential upon depolarisation, it is known that there is electrical coupling between myocytes and fibroblasts (Ongstad & Kohl, 2016). As such, APs with a slow and curved upstroke were excluded from analysis.

4.2.8 Ca^{2+}-handling proteins western blot

Total lysates were prepared from ventricular tissue using RIPA buffer containing protease and phosphatase inhibitors, as described in Section 2.2.6. Lysates were subjected to western blotting as described in Section 2.2.8, with minor technical differences as noted below for probing PLN. PLN blots were transferred for 60 mins at 90 V, instead of 90 mins, and developed using a commercial ECL (Li-Cor, WesternSure Premium Chemiluminescent Substrate, #926-95010). Band sharpness for PLN blots was not found to be improved with Tris-Tricine, thus all samples were prepared (and blotting performed) with Tris-Glycine buffer. Antibodies used for probing ventricular lysates are shown in Table 4.2.

Table 4.2. Antibodies used for Ca^{2+} handling western blot experiments.

Primary antibody	Manufacturer Product code	Primary Ab concentration	Secondary antibody conc. (Manufacturer/code)	Resolving gel %	[Protein] loaded
PLN Ms mAb	Badrilla A010-14	1:2,000	1:20,000 HRP-conjugated Dk α-Ms IgG (Novus, NB120-7061)	15%	10 µg
PLN_{pSer16} Rb pAb	Badrilla A010-12AP	1:2,000	1:20,000 HRP-conjugated Dk α-Rb IgG (Novus, NB7185)	15%	10 µg
PLN_{pThr17} Rb pAb	Badrilla A010-13AP	1:2,000	1:20,000 HRP-conjugated Dk α-Rb IgG (Novus, NB7185)	15%	10 µg
SERCA Rb pAb	Alomone ACP-012	1:2,000	1:10,000 HRP-conjugated Dk α-Rb IgG (Novus, NB7185)	10%	20 µg
NCX Rb mAb	Abcam EPR12739	1:1,000	1:10,000 HRP-conjugated Dk α-Rb IgG (Novus, NB7185)	7.5%	20 µg

All primary antibodies were prepared in TBS-0.1% Tween 20 with 1% BSA, whilst all secondary antibodies were prepared in TBS-0.1% Tween 20. The percentage of the resolving gel used for each antibody and the amount of protein loaded per well is shown at the end of the table. Dk, donkey; mAb, monoclonal antibody; Ms, mouse; NCX, Na^+/Ca^{2+}-exchanger; pAb, polyclonal antibody; PLN, phospholamban; PLN_{pSer16}, phospholamban serine 16 phosphorylation; PLN_{pThr17}, phospholamban threonine 17 phosphorylation; Rb, rabbit; SERCA, sarcoplasmic reticulum Ca^{2+}-ATPase.

4.3 Results

4.3.1 Effects of PCC disruption on cardiomyocyte physiology

To interrogate Ca^{2+} handling, CaTs were recorded in freshly-isolated ventricular myocytes from adult PA mice (amPA) and their WT littermates (amWT). Due to evidence of a sex effect in cardiometabolic disorders (Gerdts & Regitz-Zagrosek, 2019) which may be an observation in PA mice (Guenzel *et al.*, 2015), all experiments were sex-balanced and the data analysed for any effect of sex.

4.3.1.1 Effect of PCC disruption on Ca^{2+} handling in 8-week-old animals

Figure 4.3 shows the averaged time-courses for electrically-evoked CaTs and caffeine-evoked Ca^{2+} release in amPA and amWT male and female mice that were 8 weeks old. To avoid confounding effects of pseudo-replication, all cardiomyocyte data were analysed by hierarchical statistical analysis (Sikkel *et al.*, 2017). Whilst there was no statistically significant effect of PCC disruption on Ca^{2+} handling in male mice, there was a significant effect in females, as described below. Figure 4.4 shows the key summary parameters derived from the time-courses. The analysis for clustering, and the results from standard vs hierarchical testing is shown in Table 4.3.

Despite an apparent reduction of systolic Ca^{2+} in amPA males, this was not significant due to clustering, and systolic Ca^{2+} was unchanged between the genotypes and sexes. Diastolic Ca^{2+} however was significantly raised in amPA females (vs. amWT females) by ~25 % (from 0.0473 to 0.0590 μM; $P \leq 0.05$). Since systolic Ca^{2+} was unchanged but there was an increase in diastolic Ca^{2+} in female amPA, it would be expected that CaT amplitude would be reduced. However, the apparent reduction in released [Ca^{2+}] was not significant due to clustering of data. This was also the case for SR Ca^{2+} load. The backflux constant, which represents the flux that balances SR Ca^{2+} influx (i.e. RyR diastolic Ca^{2+} leak), was unchanged in amPA in both sexes. Although SERCA rate was highly clustered, two-way ANOVA using the hierarchical model showed a significant effect of genotype on SERCA rate ($P \leq 0.05$), indicating a slowing of SERCA (Figure 4.4 and Table 4.3). In keeping with the observation of increased diastolic Ca^{2+}

in female amPA, resting Ca^{2+} was also significantly raised, by ~29 % (from 0.0454 to 0.0585 µM; $P \leq 0.05$). However, NCX rate, and the influx constant, which represents the flux that balances cellular Ca^{2+} efflux (i.e. LTCC Ca^{2+} entry), was unchanged.

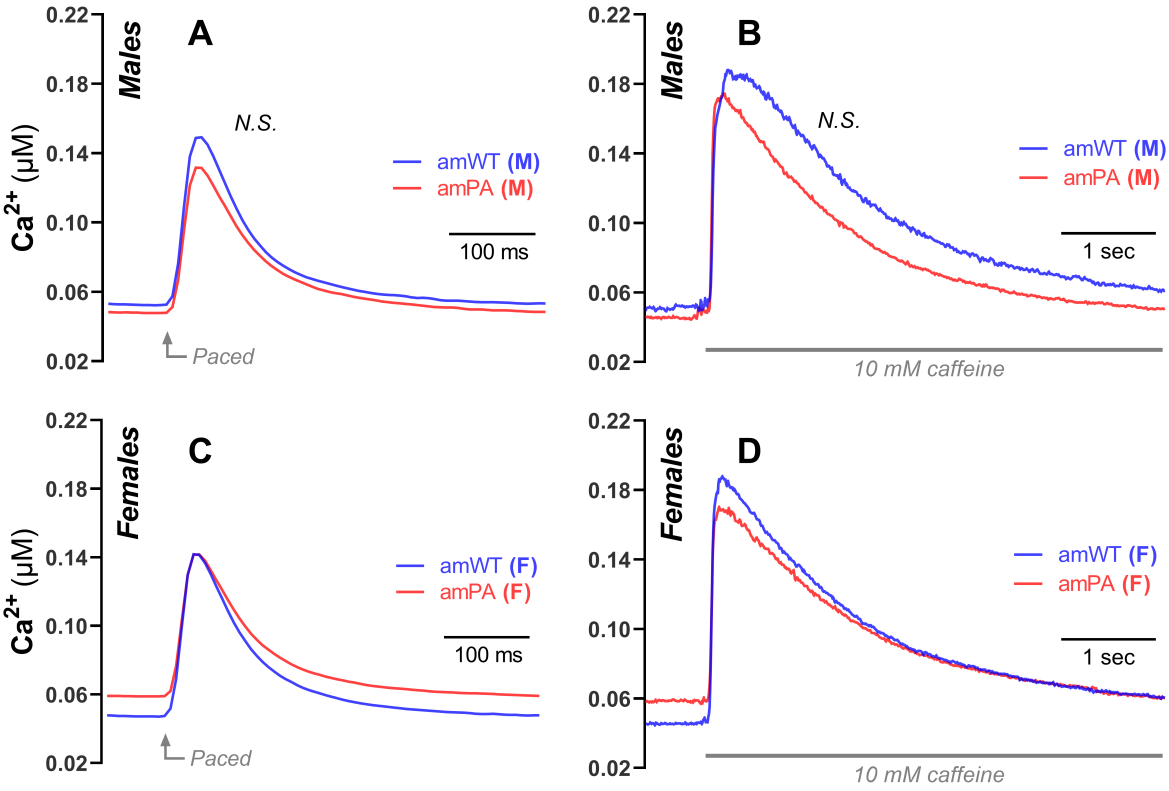


Figure 4.3. Averaged time-courses of electrically-evoked CaTs and caffeine-evoked Ca^{2+} release in 8-week-old mouse myocytes. Experiments were performed in adult PA mice (amPA) and their WT litters (amWT). Experiments were sex-balanced and performed separately for male (M) and female (F) mice. Recordings were made in NT-BC (pH 7.4) in steady-state. Ca^{2+} was measured by Fura Red and expressed as calibrated [Ca^{2+}]. ***(A and C)*** Averaged time-courses of electrically-evoked CaTs with 2 Hz field stimulation in male and female mice. ***(B and D)*** Averaged time-courses of paired caffeine-evoked Ca^{2+} release in male and female mice. Data shown as mean; *n* = 49-56 cells from 4 animals per genotype in male mice; *n* = 76-90 cells from 4-5 animals per genotype in female mice. No significance (N.S.) in summary parameters in males but significant changes were seen in females with hierarchical statistics (described in-text).

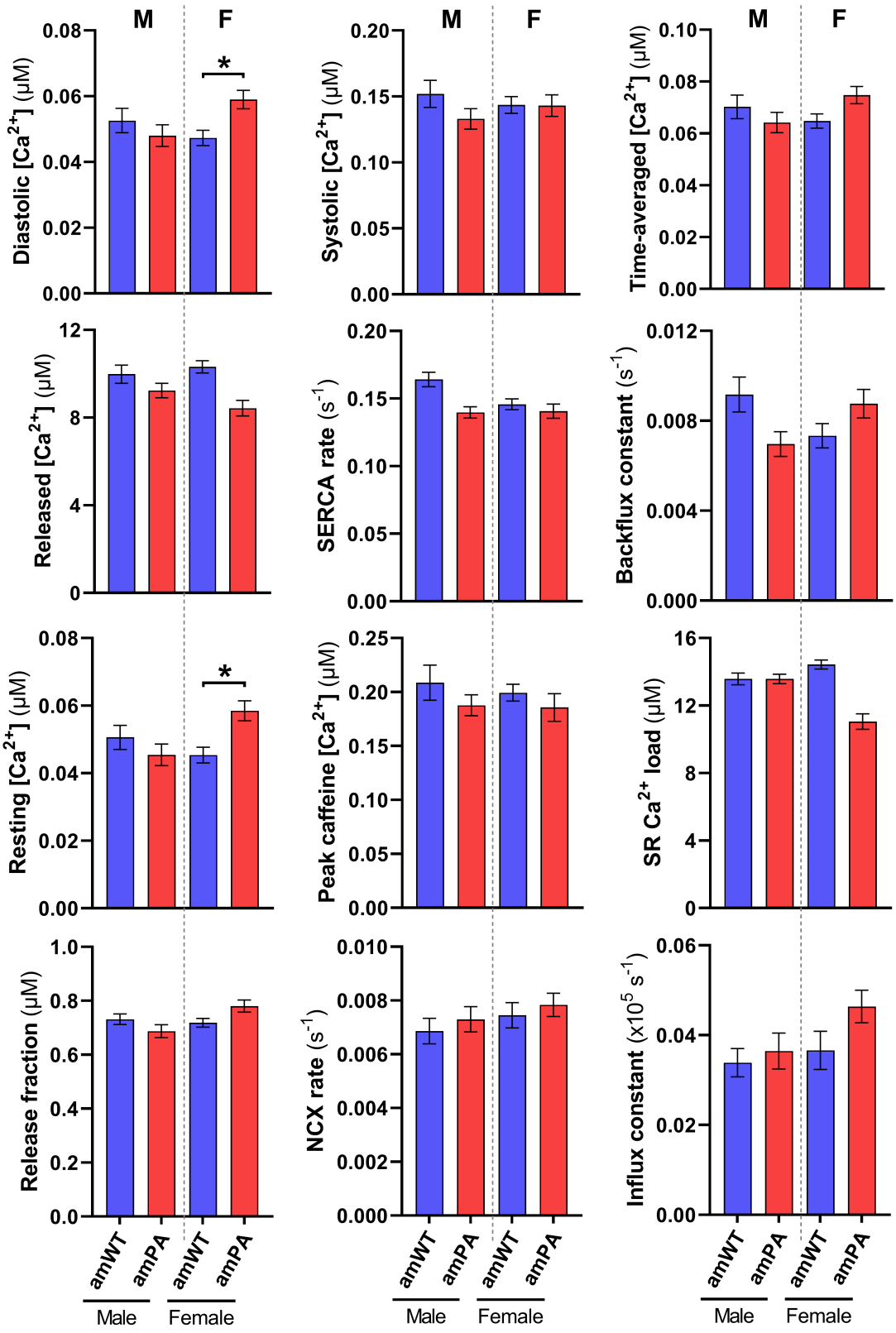


Figure 4.4. Ca^{2+} handling summary parameters from 8-week-old mouse myocytes. Recordings were made in NT-BC (pH 7.4) in steady-state. Ca^{2+} was measured by Fura Red and expressed as calibrated [Ca^{2+}]. Data shown as mean ± SEM; *n* = 49-56 cells from 4 animals per genotype in male mice; *n* = 76-90 cells from 4-5 animals per genotype in female mice. All data were analysed by hierarchical statistical analysis. * $P \leq 0.05$.

Table 4.3. Analysis of Ca^{2+} transient parameters in 8-week-old mice using standard vs. hierarchical statistical tests.

CaT parameters	Standard two-way ANOVA			Clustering of data (ICC)	Hierarchical two-way ANOVA			Comparison of goodness of fit (common vs hierarchical)
	Genotype	Sex	Interaction		Genotype	Sex	Interaction	
Diastolic [Ca^{2+}]	0.3136	0.2120	**0.0072**	0%	0.3096	0.2082	**0.0067**	N (1)
Systolic [Ca^{2+}]	0.1220	0.4555	0.2495	**9.9%**	0.4887	0.8341	0.3453	**Y (0.0207)**
Time-averaged [Ca^{2+}]	0.2677	0.2803	**0.0263**	0%	0.2637	0.2763	**0.0251**	N (1)
Released [Ca^{2+}]	0.1577	0.4956	0.0996	**24.0%**	0.5146	0.5374	0.7755	**Y (< 0.0001)**
SERCA rate	**0.0008**	**0.0064**	**0.0420**	**32.4%**	**0.0465**	0.0667	0.1374	**Y (< 0.0001)**
Backflux constant	**0.0214**	**0.0386**	**0.0041**	5.9%	0.1293	0.1423	0.0559	N (0.209)
Resting [Ca^{2+}]	0.2578	0.2130	**0.0025**	0%	0.2538	0.2092	**0.0023**	N (1)
Peak caffeine [Ca^{2+}]	0.2264	0.5616	0.7487	**17.4%**	0.9141	0.9253	0.6968	**Y (< 0.0001)**
SR Ca^{2+} load	0.9921	0.0832	**0.0001**	**31.7%**	0.6222	0.2180	0.0983	**Y (< 0.0001)**
Release fraction	0.1620	0.6565	**0.0111**	0%	0.1585	0.6538	**0.0104**	N (1)
NCX rate	0.5519	0.3864	0.9582	0.5%	0.5393	0.4185	0.9347	N (0.868)
Influx constant	0.6774	0.6351	0.3806	0%	0.6749	0.6322	0.3766	N (1)

Elements of the analysis of each variable are shown. A standard non-hierarchical two-way ANOVA is first shown. The clustering of data was then calculated by the intraclass correlation (ICC) for each variable. ICC varies between 0% for data showing no clustering, and 100% for intensely clustered data (i.e. each cluster contains multiple identical values, but the different clusters have different values). The results of a hierarchical testing two-way ANOVA is then shown. The comparison of the goodness-of-fit determined whether a common or hierarchical approach was more suited for the data. The results from the hierarchical model was used for those parameters that were shown to be have a better fit with hierarchical testing. Significant *P*-values are shown in bold. *N* = 49-56 cells from 4 animals per genotype in male mice; *n* = 76-90 cells from 4-5 animals per genotype in female mice.

4.3.1.2 Effect of PCC disruption on Ca^{2+} handling in 20-week-old animals

If the accumulation of propionate and/or propionate metabolites are indeed the cause of remodelling in Ca^{2+} handling, it would be reasonable to expect that a longer exposure to these metabolites may further drive disease remodelling. To test whether Ca^{2+} handling is further dysregulated in these mice due to an 'additive' effect of toxic metabolites, CaTs were recorded from mice that were 20 weeks old. Figure 4.5 shows the averaged time-courses for electrically-evoked CaTs and caffeine-evoked Ca^{2+} release in sex-balanced cohorts of amPA and amWT animals. As in 8-week-old mice, there was no significant effect in males. However, there was a major remodelling of Ca^{2+} handling in female mice (Figure 4.5c/d). Interestingly, there was a normalisation of diastolic and resting Ca^{2+} and these parameters were no longer increased in female amPA mice. Instead, there was a significant increase by ~26% in released $[Ca^{2+}]$ during the CaT (from 8.8 to 11.1 μM; $P \leq 0.05$) and in SR Ca^{2+} load (~27%; from 12.0 to 15.2 μM; $P \leq 0.05$) (Figure 4.6). However, NCX rate and influx constant were still unchanged in female amPA. The analysis for data clustering and the results from the standard vs hierarchical statistical testing is shown in Table 4.4.

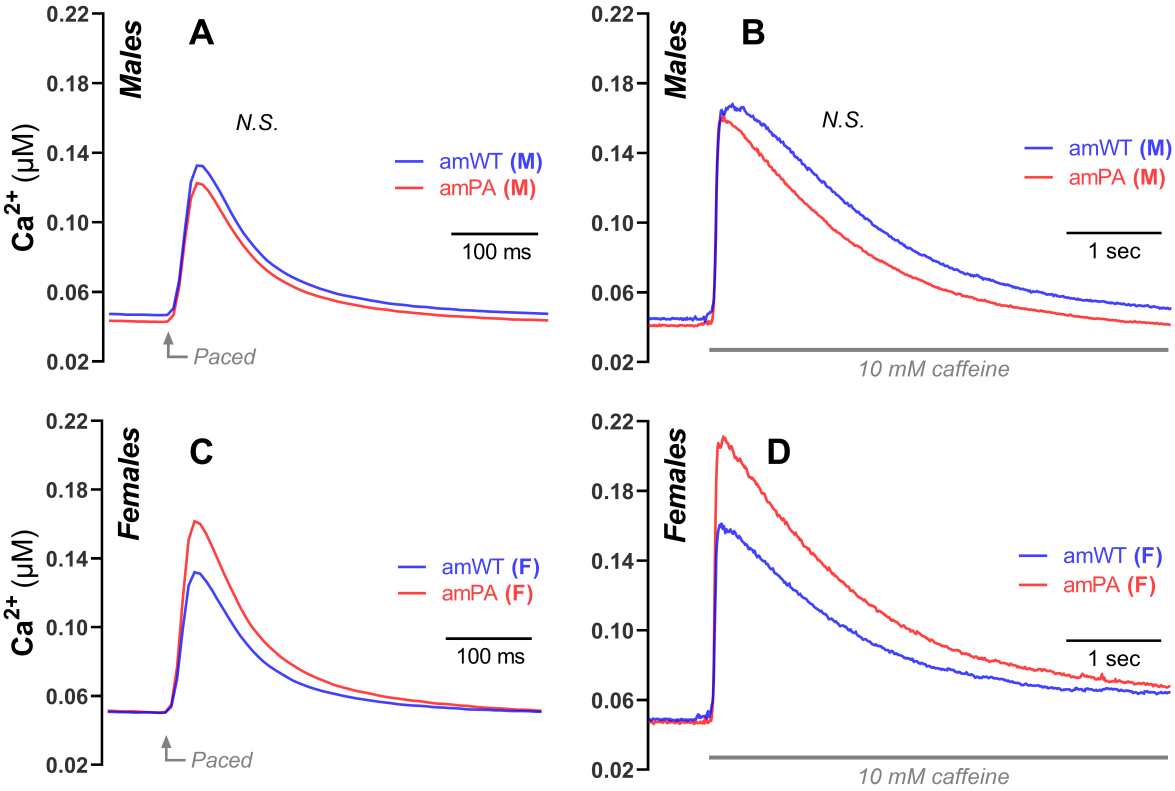


Figure 4.5. Averaged time-courses of electrically-evoked CaTs and caffeine-evoked Ca^{2+} release in 20-week-old mouse myocytes. Experiments were performed in adult PA mice (amPA) and their WT litters (amWT). Experiments were sex-balanced and performed separately for male (M) and female (F) mice. Recordings were made in NT-BC (pH 7.4) in steady-state. Ca^{2+} was measured by Fura Red and expressed as calibrated [Ca^{2+}]. ***(A and C)*** Averaged time-courses of electrically-evoked CaTs with 2 Hz field stimulation in male and female mice. ***(B and D)*** Averaged time-courses of paired caffeine-evoked CaTs in male and female mice. Data shown as mean; *n* = 64-83 cells from 3-4 animals per genotype in male mice; *n* = 47 cells from 4 animals per genotype in female mice. No significance (N.S.) in summary parameters in males but significant changes were seen in females with hierarchical statistics (described in-text).

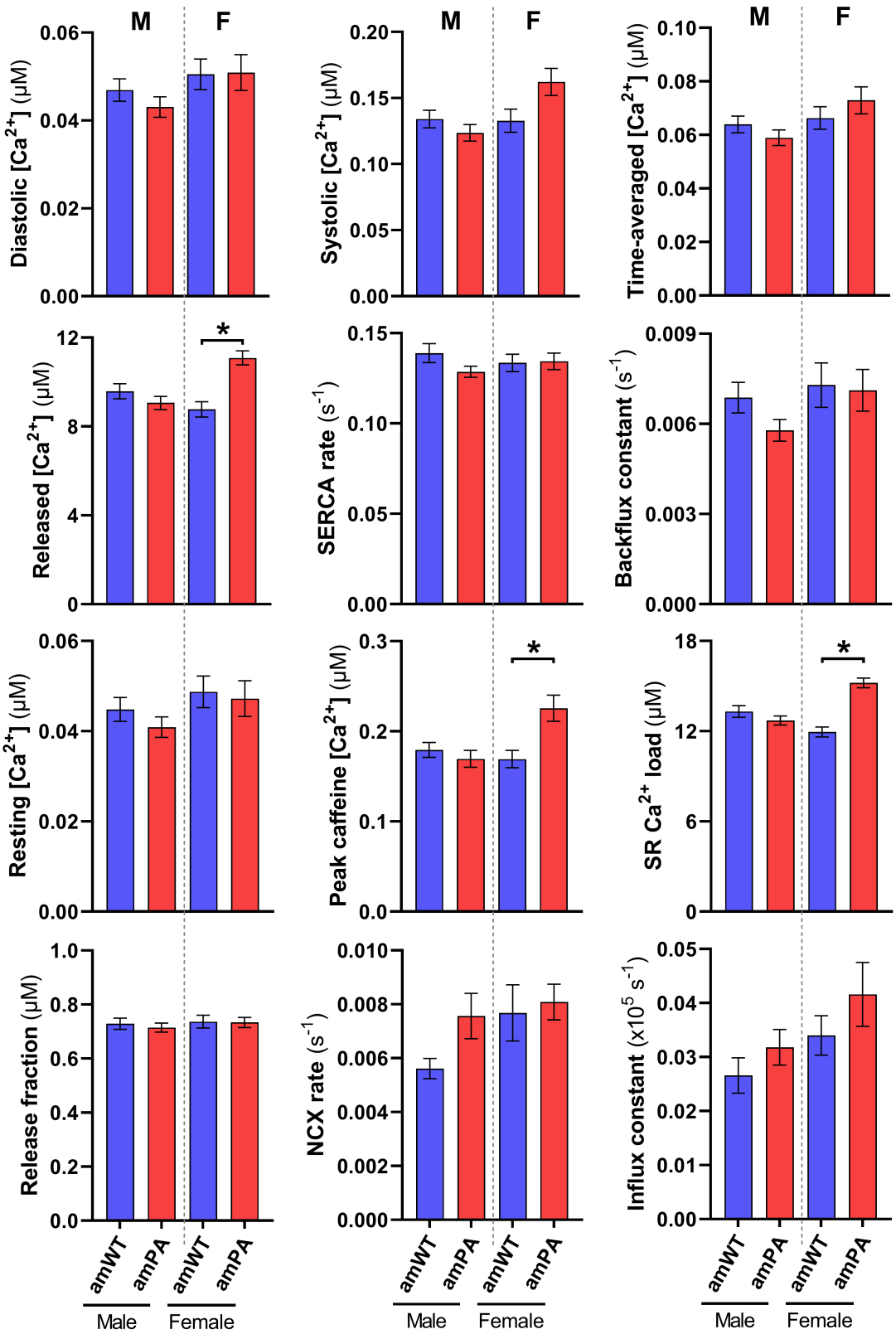


Figure 4.6. Ca^{2+} handling summary parameters from 20-week-old mouse myocytes. Recordings were made in NT-BC (pH 7.4) in steady-state. Ca^{2+} was measured by Fura Red and expressed as calibrated [Ca^{2+}]. Data shown as mean ± SEM; *n* = 64-83 cells from 3-4 animals per genotype in male mice; *n* = 47 cells from 4 animals per genotype in female mice. All data were analysed by hierarchical statistical analysis. * $P \leq 0.05$.

Table 4.4. Analysis of Ca^{2+} transient parameters in 20-week-old mice using standard vs. hierarchical statistical tests.

CaT parameters	Standard two-way ANOVA			Clustering of data (ICC)	Hierarchical two-way ANOVA			Comparison of goodness of fit (common vs hierarchical)
	Genotype	Sex	Interaction		Genotype	Sex	Interaction	
Diastolic [Ca^{2+}]	0.3320	0.4327	0.4909	0%	0.3278	0.4287	0.4871	N (1)
Systolic [Ca^{2+}]	0.3132	0.9126	**0.0131**	3.3%	0.4488	0.9884	0.0536	N (0.229)
Time-averaged [Ca^{2+}]	0.3112	0.6717	0.1277	0%	0.3069	0.6690	0.1244	N (1)
Released [Ca^{2+}]	0.2235	0.1003	**0.0001**	**5.9%**	0.4061	0.3103	**0.0055**	**Y (0.0231)**
SERCA rate	0.0670	0.3974	0.1986	**10.1%**	0.2897	0.7371	0.4508	**Y (0.0004)**
Backflux constant	0.1323	0.6108	0.4131	3%	0.2682	0.6077	0.5024	N (0.323)
Resting [Ca^{2+}]	0.3172	0.3871	0.6889	0%	0.3130	0.3829	0.6864	N (1)
Peak caffeine [Ca^{2+}]	0.4778	0.5207	**0.0024**	**5.5%**	0.6425	0.7290	**0.0375**	**Y (0.0301)**
SR Ca^{2+} load	0.1877	**0.0092**	**0.0001**	**15.5%**	0.5517	0.2244	**0.0095**	**Y (< 0.0001)**
Release fraction	0.5897	0.7895	0.7856	2.3%	0.6369	0.8053	0.7497	N (0.407)
NCX rate	0.0693	0.0918	0.3507	0%	0.0668	0.0890	0.3465	N (1)
Influx constant	0.3254	0.2213	0.7727	0%	0.3211	0.2172	0.7707	N (1)

Elements of the analysis of each variable are shown. A standard non-hierarchical two-way ANOVA is first shown. The clustering of data was then calculated by the intraclass correlation (ICC) for each variable. ICC varies between 0% for data showing no clustering, and 100% for intensely clustered data (i.e. each cluster contains multiple identical values, but the different clusters have different values). The results of a hierarchical testing two-way ANOVA is then shown. The comparison of the goodness-of-fit determined whether a common or hierarchical approach was more suited for the data. The results from the hierarchical model was used for those parameters that were shown to be have a better fit with hierarchical testing. Significant *P*-values are shown in bold. *N* = 64-83 cells from 3-4 animals per genotype in male mice; *n* = 47 cells from 4 animals per genotype in female mice.

4.3.1.3 Effect of PCC disruption on Ca^{2+} handling protein expression

To determine whether the remodelling of CaTs in female amPA involved a change in the expression of key Ca^{2+} handling proteins, western blotting was performed in ventricular lysates from 8-week-old animals. No significant changes were observed in SERCA, NCX or PLN (pentamer and monomer) expression (Figure 4.7). Moreover, the phosphorylation status of PLN (PLN_{pSer16} or PLN_{pThr17}) was unchanged.

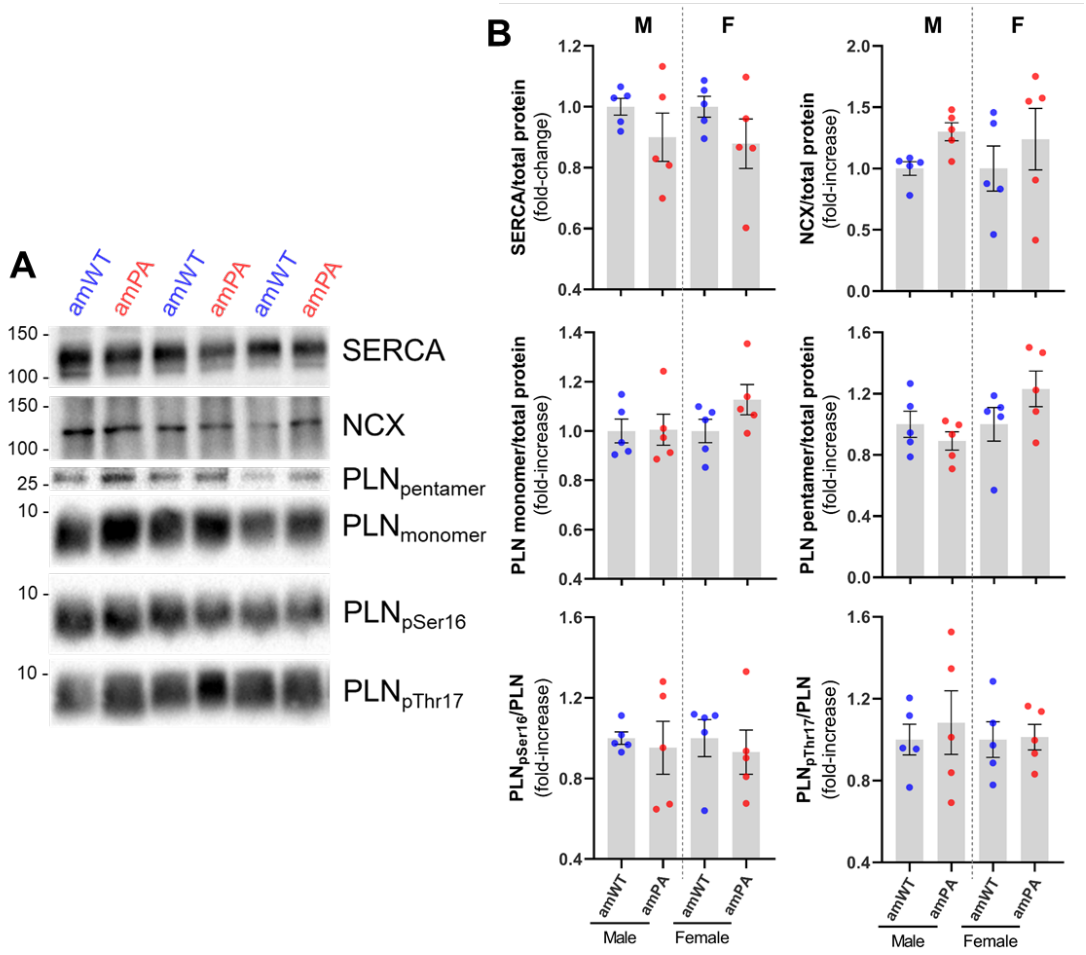


Figure 4.7. Western blotting of key Ca^{2+} handling proteins in ventricular lysates. *(A)* Representative blots of SERCA, NCX, total PLN expression (pentamer and monomer) and phosphorylated PLN (PLN_{pSer16} and PLN_{pThr17}). *(B)* Summary histograms for total band volume normalised to total protein (Coomassie). Data shown as mean ± SEM; *n* = 5 hearts per sex and per genotype. Two-way ANOVA, no significance.

The data shown thus far demonstrate a remodelling of Ca^{2+} handling in amPA mice and that interestingly, this effect is unique to female mice. Since there was a significant increase in propionate metabolites in heart and plasma of both male and female amPA mice, further cardiomyocyte experiments were performed to establish whether propionate is a bioactive molecule capable of remodelling Ca^{2+} handling. These experiments were conducted in WT myocytes exposed to a pre-defined concentration of propionate.

4.3.2 Effects of *in vitro* application of propionate on cardiomyocyte physiology

Since there was a remodelling of CaTs in PCC-deficient mice, the next set of experiments sought to determine whether propionate can remodel Ca^{2+} handling in a manner consistent with the mouse phenotype.

4.3.2.1 Effect of acute propionate exposure on Ca^{2+} handling

CaTs were measured first in wild-type ARVMs acutely superfused in *6 mM cPA* (pH 7.4) or with experimental solutions designed to mimic an uncompensated propionic acidaemia (*6 mM uPA*; 6 mM propionate at pH 7.3). Recordings were made in myocytes exposed to treatment (propionate) for 10-30 mins.

Strikingly, no significant effect was found on the electrically-evoked CaTs and caffeine-evoked Ca^{2+} release (Figure 4.8a/b). Systolic Ca^{2+}, diastolic Ca^{2+}, CaT amplitude, resting Ca^{2+} and SR load, determined from the averaged time-courses, were all unaffected by acute exposure to propionate, with or without acidosis (Figure 4.8c-g). The time constants of SERCA and NCX were on average higher in *6 mM cPA* and *6 mM uPA* when analysed by one-way ANOVA; indeed, on the averaged time-courses for caffeine-evoked Ca^{2+} release, it appears as though NCX is slower in propionate. However, upon hierarchical statistical analysis, the time constants were found to be highly clustered, thus not statistically significant and not shown.

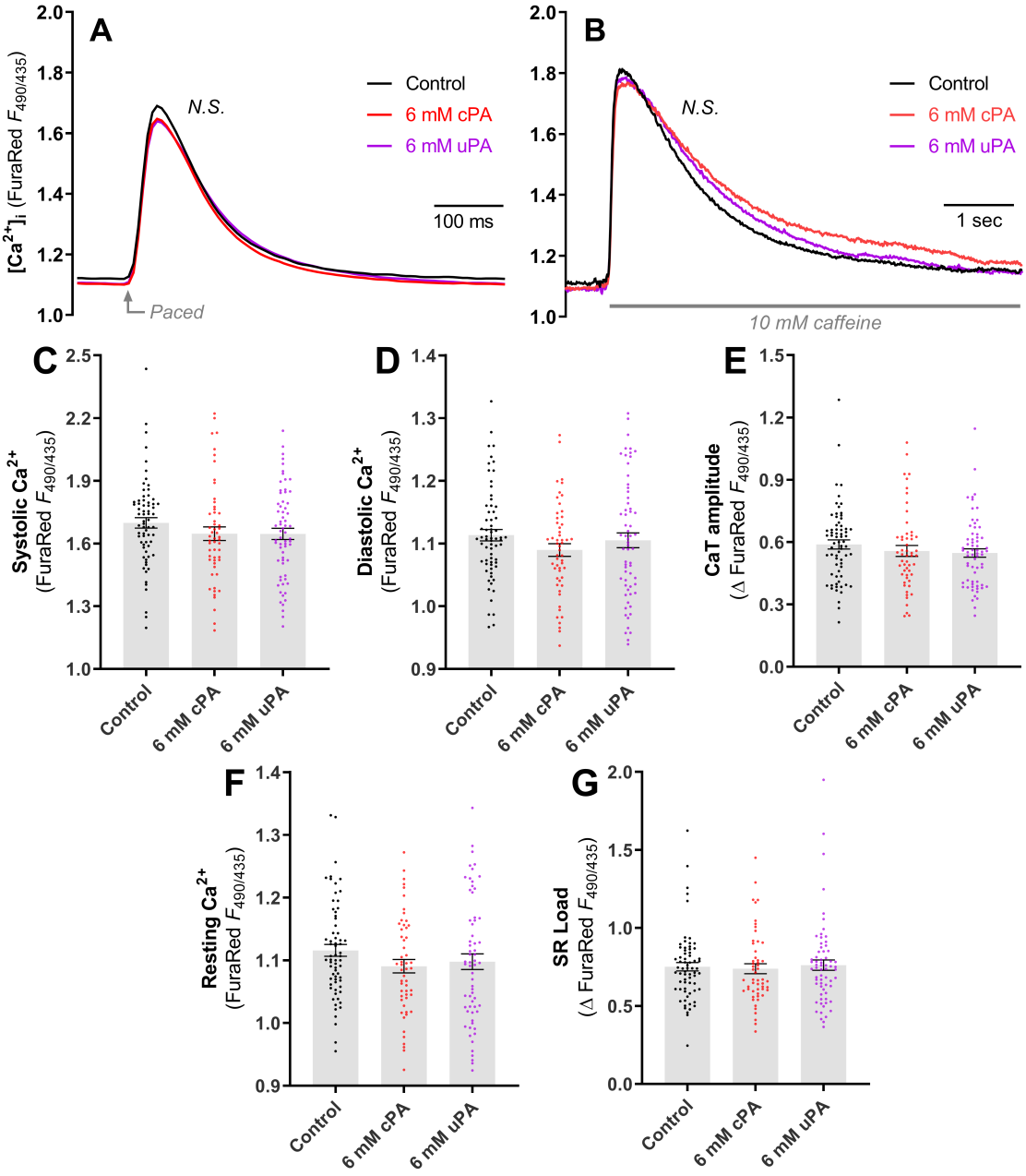


Figure 4.8. Electrically-evoked CaTs and caffeine-evoked Ca^{2+} release in wild-type myocytes acutely exposed to propionate. Recordings were made in NT-BC in ARVMs exposed for 10-30 mins to a compensated propionic acidaemia (cPA: 6 mM propionate; pH 7.4) or an uncompensated propionic acidaemia (uPA: 6 mM propionate, 0.2 NH_4Cl; pH 7.3). Ca^{2+} was measured by Fura Red and expressed as the 490/435 nm fluorescence ratio ($F_{490/435}$). Cells were paced at 2 Hz. ***(A)*** Averaged time-courses of electrically-evoked CaTs with 2 Hz field stimulation (shown as mean only). ***(B)*** Averaged time-courses of caffeine-evoked Ca^{2+} release. ***(C-D)*** Systolic and diastolic Ca^{2+}. ***(E)*** CaT amplitude (systolic Ca^{2+} – diastolic Ca^{2+}). ***(F)*** Resting Ca^{2+} determined as the Ca^{2+} level prior to the caffeine pulse. ***(G)*** Approximation of sarcoplasmic reticulum (SR) Ca^{2+} load (peak caffeine Ca^{2+} – resting Ca^{2+}). Data shown as mean ± SEM; *n* = 54-67 cells per group from 5 animals. Hierarchical statistical analysis showed no significance (N.S.) across all parameters.

4.3.2.2 Effect of chronic propionate exposure on AP-CaT coupling

The results from this Chapter have thus far shown that Ca^{2+} handling is remodelled when PCC is disrupted *in vivo* and till this stage, it was assumed that propionate is a key mediator of this response. However, acutely exposing wild-type cardiomyocytes to propionate (10-30 mins) had no effect on Ca^{2+} handling, suggesting that propionate may require a longer time to exert its actions. Therefore, experiments were repeated on wild-type cardiomyocytes treated with propionate for an extended 'chronic' duration (48 hrs).

Since adult myocytes detubulate when cultured for extended periods (thus affecting their E-C coupling physiology) (Pavlović *et al.*, 2010), the following experiments were conducted using wild-type NRVMs. To ensure any changes being detected are attributable to a 'remodelling' process, NRVMs were cultured in their respective treatment condition, but in contrast to the data from ARVMs (Section 4.3.2.1), all measurements were made in NT, after the washout of treatment.

APs and CaTs were recorded in electrically-paced (2 Hz) wild-type NRVMs cultured for 48 hrs under five experimental conditions: *control*; *acidosis* (pH 7.3); 3 mM compensated PA (*3 mM cPA*); *6 mM cPA*; *6 mM uPA*. Figure 4.9 shows the averaged time-courses of APs and CaTs. Normal coupling can be seen between these two processes under control conditions. CaT duration was unaffected in acidosis only. However, the CaT is prolonged and elongated relative to the AP under treatment with propionate at pH 7.4 (*3 mM cPA, 6 mM cPA*) and pH 7.3 (*6 mM*

uPA). Quantification of AP duration and CaT parameters are shown in subsequent sub-sections (4.3.2.3 and 4.3.2.4, respectively).

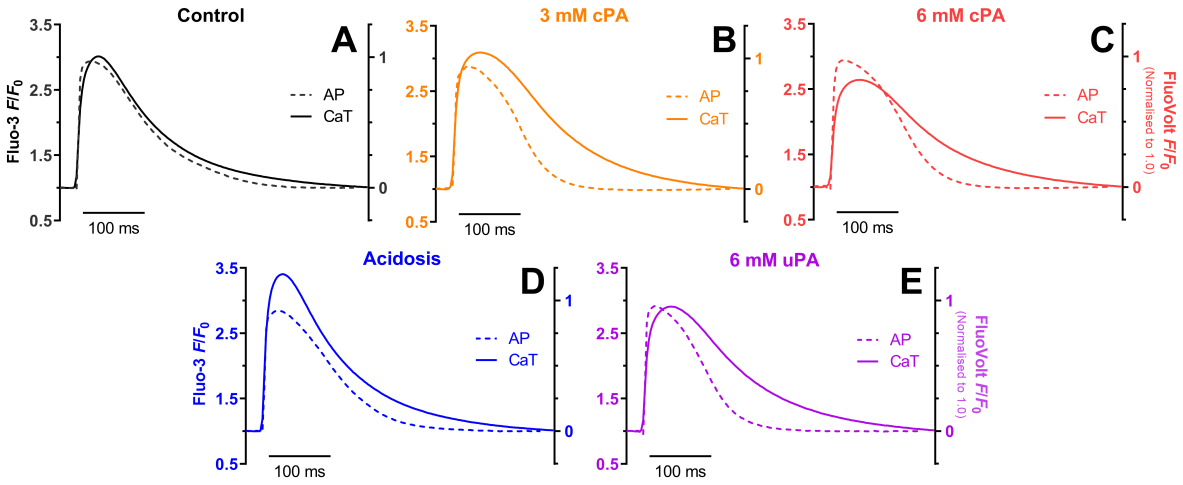


Figure 4.9. APs and CaTs recorded in electrically-paced NRVMs cultured for an extended period in propionate. Cells were treated under six conditions: ***(A)*** *control*; ***(E)*** *acidosis*; ***(B)*** 3 mM compensated PA (*3 mM cPA*); ***(C)*** 6 mM compensated PA (*6 mM uPA*); ***(E)*** 6 mM uncompensated PA (*6 mM uPA*). Cells were paced at 2 Hz. Data presented are averaged time-courses of action potentials (APs; FluoVolt F/F_0 normalised to 1.0) and Ca^{2+} transients (CaTs; Fluo-3 F/F_0). Data shown as mean; FluoVolt, n = 28-55 cells per group from 3-7 isolations per condition; Fluo-3, n = 81-109 cells from 5-9 isolations per condition.

4.3.2.3 *Effect of chronic propionate exposure on APD*

The AP recordings presented in Section 4.3.2.2 were analysed to quantify action potential duration at 90% repolarisation (APD_{90}). The superimposed averaged time-courses are shown in Figure 4.10a. APD_{90} was significantly reduced in all treatment conditions (Figure 4.10b). APD was shortened, by at least 20%, under treatment with propionate at pH 7.4 (*3 mM cPA, 6 mM cPA*) and pH 7.3 (*6 mM uPA*). Acidosis alone (pH 7.3) caused a milder shortening of APD (14%).

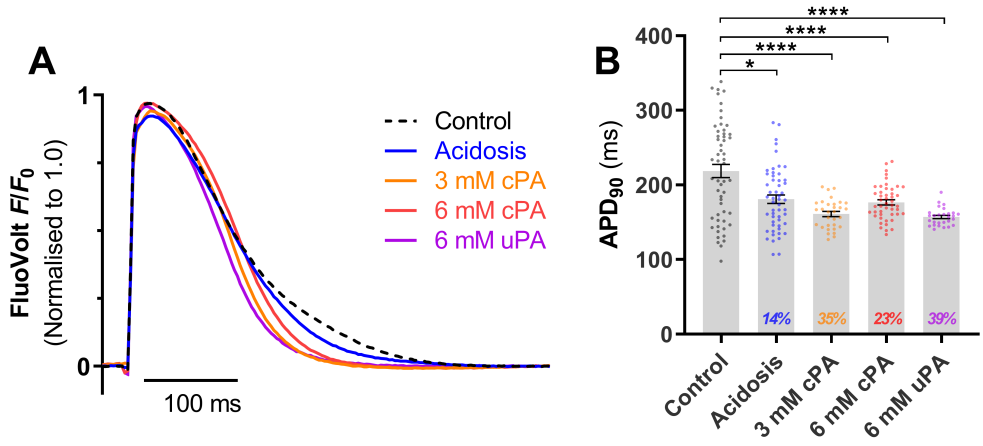


Figure 4.10. APD_{90} in NRVMs cultured for an extended period in propionate. Cells were treated (48 hrs) under five conditions: *control* (pH 7.4); *acidosis* (pH 7.3); *3 mM cPA* (pH 7.4); *6 mM cPA* (pH 7.4); *6 mM uPA* (pH 7.3). Recordings were made under steady-state pacing at 2 Hz. ***(A)*** averaged time-courses for all conditions shown as mean only. ***(B)*** Action potential duration at 90% repolarisation (APD_{90}) with percentage changes relative to *control*. Data shown as mean for time-courses and mean ± SEM for histograms; *n* = 28-55 cells per group from 3-7 isolations per condition. * $P \leq 0.05$ and **** $P \leq 0.0001$ on hierarchical statistical analysis and pairwise comparisons with Bonferroni correction.

4.3.2.4 Effect of chronic propionate exposure on electrically-evoked CaTs

The CaT recordings presented in Section 4.3.2.2 were analysed to quantify several CaT parameters. The superimposed averaged time-courses are shown in Figure 4.11a. The rising phase of the CaT (CaT time-to-peak) was significantly slower in myocytes treated with propionate, at both pH 7.4 (*3 mM cPA*, *6 mM cPA*) and pH 7.3 (*6 mM uPA*); the presence of an acidosis with propionate had no additive effect on CaT time-to-peak (Figure 4.11b). CaT amplitude was only significantly increased by acidosis (pH 7.3) (Figure 4.11c). In contrast, CaT_{90} (time to 90% CaT recovery) was only significantly affected by propionate, whereby duration was prolonged by treatment with propionate at both pH 7.4 (*3 mM cPA, 6 mM cPA*) and pH 7.3 (*6 mM uPA*) by ~11-12% (Figure 4.11d).

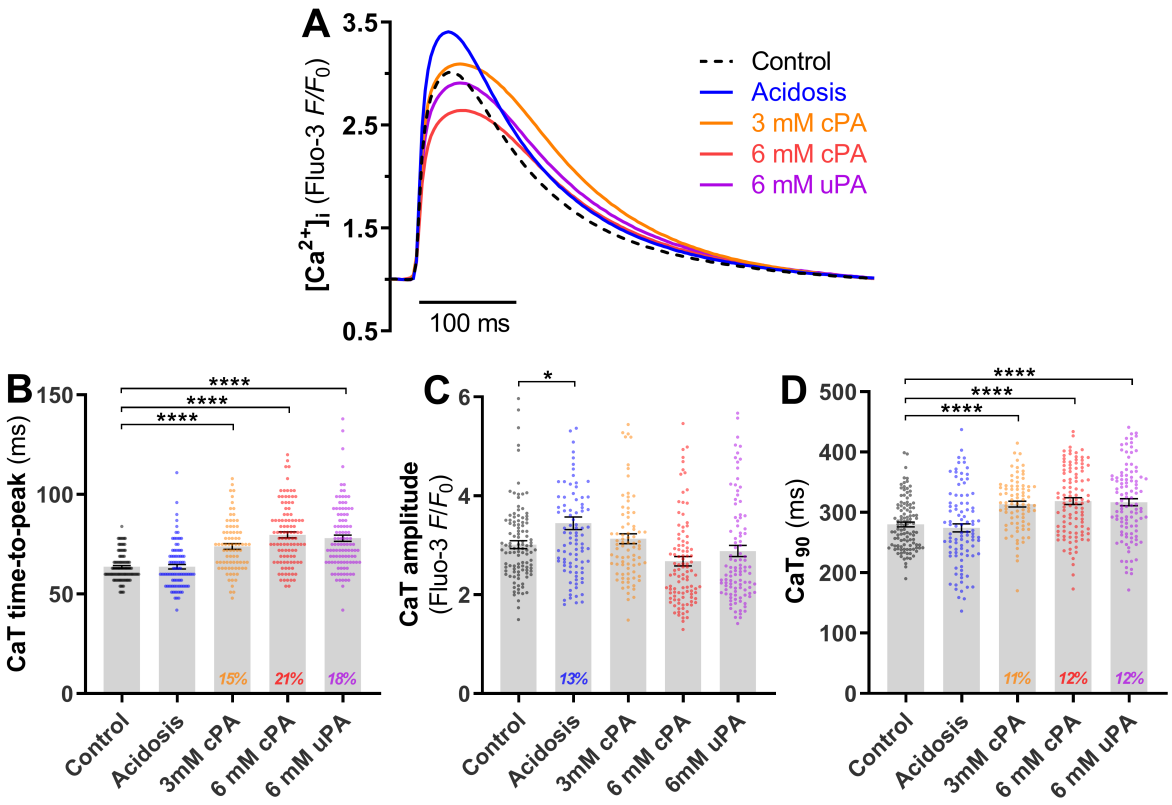


Figure 4.11. CaTs in NRVMs cultured for an extended period in propionate. Cells were treated (48 hrs) under six conditions: *control* (pH 7.4); *acidosis* (pH 7.3); *3 mM cPA* (pH 7.4); *6 mM cPA* (pH 7.4); *6 mM uPA* (pH 7.3). Recordings were made under steady-state pacing at 2 Hz. ***(A)*** Averaged time-courses for all conditions shown as mean only. ***(B)*** Time for CaT to reach its peak. ***(C)*** CaT amplitude (F/F_0). ***(D)*** Time to 90% CaT recovery (CaT_{90}). All percentages shown in histograms are changes relative to *control*. Data shown as mean for time-courses and mean ± SEM for histograms; n = 81-109 cells from 5-9 isolations per condition. * $P \leq 0.05$, *** $P \leq 0.001$, **** $P \leq 0.0001$ on hierarchical statistical analysis and pairwise comparisons with Bonferroni correction.

4.4 Discussion

The aims of this Chapter were to characterise how E-C coupling is affected in PA and to determine whether propionate is responsible for this process. Cardiomyocyte experiments in PA mice were performed in 8-week-old animals (as with the majority of experiments presented in this thesis), but also in 20-week-old mice, to determine whether cardiomyocyte function remodels further with prolonged exposure to propionate and its metabolites. Experiments where myocytes were treated with propionate *in vitro* were performed to determine whether propionate *per se* can remodel E-C coupling in a manner consistent with the mouse phenotype.

The major findings from this Chapter were as follows. (i) PCC disruption *in vivo* results in dysregulated cardiac Ca^{2+} handling at an early timepoint (8 weeks; young-adult), but appears to undergo a degree of further remodelling with ageing (probed at 20 weeks); (ii) remodelled Ca^{2+} handling in amPA is sex-dependent and only significant in female mice; (iii) propionate applied acutely to WT cardiomyocytes *in vitro* has no effect on Ca^{2+} handling; (iv) however, significant changes occur to E-C coupling when propionate is applied *in vitro* on a more 'chronic' timescale.

Prior to the discussion of data, it should be noted that there were several parameters, that with a common statistical approach, would have been considered significantly different (apparent when viewing the mean ± SEM of the histograms, e.g. Figures 4.4 and 4.6). Although cardiomyocyte studies typically report '*n*' cells from '*m*' animals, each cell is still considered as

an independent point during conventional statistical analysis (*n* x *m*), without due consideration to a potential effect of clustering (i.e. an effect of animal and isolation). Consequently, there is a potential for overestimation of statistical significance and a risk of 'pseudo-replication' (Sikkel *et al.*, 2017; Eisner, 2021). As such, a more stringent method was applied in the analysis of data presented in this Chapter, where the data were also analysed for any clustering. This method has superior power to eliminate false-positives arising from a 'batch-effect'. High clustering of data would attenuate the power to resolve true-positives, which was particularly problematic for parameters, such as systolic [Ca^{2+}] and SR Ca^{2+} load. That said, it should be recognised that a caveat to the hierarchical approach is that it assumes all myocytes from a heart are the same, despite it being recognised that there can be heterogeneity in Ca^{2+} handling and contractility within the ventricular myocardium, between endocardial and epicardial cardiomyocytes (Pan *et al.*, 2018).

4.4.1 Ca^{2+} handling is remodelled following PCC disruption

Ca^{2+} handling in the heart involves an ensemble of mechanisms working in tandem to generate the fluxes in cytoplasmic Ca^{2+} that mediate cardiac contraction and relaxation. To appraise Ca^{2+} handling, Donald Bers' approach was used of pairing an electrically-evoked CaT, with a caffeine-evoked response, to measure SERCA and NCX in the same cell (Bassani *et al.*, 1994). The major change in amPA was that in younger 8-week animals, the levels of diastolic Ca^{2+} and resting Ca^{2+} were significantly higher compared to amWT. However, in older 20-week animals, there was normalisation of diastolic and resting Ca^{2+}, and instead, released [Ca^{2+}] (i.e. CaT

amplitude) and SR Ca^{2+} load was significantly greater. Perhaps what was most striking was that the remodelling in Ca^{2+} handling was sex-dependent and observed only in females, across the two experimental timepoints.

4.4.2 Diastolic and resting [Ca^{2+}] are raised in 8-week amPA females

In comparison to systolic Ca^{2+}, little is known about the control and regulation of diastolic Ca^{2+}. There are several reasons for this: (1) it is easier to measure relative changes, vs absolute levels of [Ca^{2+}], due to requirement for indicator calibration; (2) non-ratiometric fluorescent indicators are typically used since ratiometric imaging requires more specialised equipment, and this data is typically normalised to diastolic or resting fluorescence (F/F_0); (3) pacing rate has a major effect on diastolic Ca^{2+} and although measuring steady-state CaTs help dissect the contribution of fluxes, it is by definition, artificial (Eisner *et al.*, 2020).

Although they are indeed interrelated, it is important to acknowledge that diastolic and resting Ca^{2+} are not the same thing. Whilst diastolic [Ca^{2+}] is established by a balance between many Ca^{2+}-handling mechanisms, in a quiescent myocyte, the resting Ca^{2+} level is determined entirely by fluxes across the sarcolemma (Eisner *et al.*, 2020).

4.4.2.1 Resting Ca^{2+}

Resting [Ca^{2+}] was significantly higher in amPA. Such a change could be due to (1) a reduction in Ca^{2+} efflux and/or (2) an increase in Ca^{2+} influx.

The primary sarcolemmal Ca^{2+} extrusion pathway for the cell is through NCX, thus a reduction in NCX activity can result in reduced Ca^{2+} efflux. As NCX is the only Ca^{2+} transporter coupled to Na^{+} ions, a change in NCX activity can arise from changes in Na^{+} handling. Under circumstances such as Na^{+} overload, the driving force for Ca^{2+} extrusion is reduced and NCX activity can slow, or even operate in 'reverse mode' to ultimately Ca^{2+}-load the cell (Shattock *et al.*, 2015). However, the activity of NCX (probed from caffeine-evoked Ca^{2+} release) was unchanged in amPA, with little evidence for clustering. Thus, it is also unlikely that amPA cells have raised Na^{+}, although this would require definitive testing, for example though fluorescence measurements, such as SBFI imaging.

Since there was no change in NCX activity, reduced Ca^{2+} efflux is unlikely to be the cause of raised resting Ca^{2+} in amPA. Raised resting [Ca^{2+}] in amPA could be instead due to increased 'background' Ca^{2+} influx. Indeed, there was no significant change in influx constant, due to a high degree of clustering. However, there was a trend toward increased influx in amPA (Figure 4.5). Whilst background influx is known to be sensitive to Gd^{3+} (Kupittayanant *et al.*, 2006), the exact pathway and identity of the background Ca^{2+} influx is currently unknown. The best available evidence suggests contribution from connexin hemichannels and transient receptor

potential (TRP) channels (Eisner *et al.*, 2020). Thus, a higher influx may also relate to a more depolarised resting membrane potential, although this has not been measured in this thesis.

4.4.2.2 Diastolic Ca^{2+}

In comparison, more is generally known about the control of diastolic Ca^{2+}, which was also significantly higher in 8-week amPA animals. Increases in diastolic Ca^{2+} could be due to: (1) increased sarcolemmal Ca^{2+} influx; (2) reduced sarcolemmal Ca^{2+} efflux; (3) incomplete reuptake of Ca^{2+} into the SR, at the end of an electrically-evoked CaT; (4) raised Ca^{2+} buffering, which would slow the process of re-sequestration.

Background Ca^{2+} influx and sarcolemmal Ca^{2+} efflux. These factors have been discussed above in Section 4.4.2.1.

Diastolic Ca^{2+} & SERCA. Here, SERCA activity was measured in terms of the rate constant, which was based on the best fit to the decay phase of the electrically-evoked CaT, with the assumption buffering was unchanged (see next). There was a significant decrease in SERCA rate in amPA (irrespective of sex). Reduced SERCA activity would be expected to leave end-diastolic $[Ca^{2+}]$ higher, by slowing the systolic Ca^{2+} decay. The expression of SERCA/PLN protein and PLN phosphorylation status, which are known to modulate SERCA activity, was unchanged in amPA hearts, however the large standard error in these measurements also suggest the western blotting was potentially underpowered.

Diastolic Ca^{2+} & buffering capacity. Assuming all other fluxes are at steady-state, an increased buffering capacity would slow the rate of change of $[Ca^{2+}]_i$, thus the CaT will not fully decay back to baseline in time before the next excitation, and consequently diastolic $[Ca^{2+}]$ would rise (Eisner *et al.*, 2020). The major cytoplasmic buffers in cardiomyocytes are troponin C and SERCA, but includes several other sites (e.g. histidyl-dipeptides) (Smith & Eisner, 2019). Based on the expression of SERCA being unchanged in amPA hearts, the analysis of CaT parameters had assumed constant buffering. Furthermore, there was no evidence to suggest an increase in protein 'mass' (i.e. maladaptive hypertrophy) in amPA cardiomyocytes that would increase cytoplasmic buffering capacity (cell size with cSNARF-1; Chapter 3). Collectively, altered (increased) cytoplasmic buffering capacity is unlikely to contribute to raised diastolic Ca^{2+} in amPA, but in the absence of direct measurements, it cannot be excluded.

4.4.2.3 Interpretation of Ca^{2+} handling in 8-week amPA females

The increased diastolic Ca^{2+} in 8-week-old animals is an important finding, as it may partially explain the cardiac contractile phenotype observed on cine-MRI in Chapter 3. The finding of raised diastolic Ca^{2+} may indicate these mice have diastolic dysfunction (Zile & Gaasch, 2011; Adeniran et al., 2015; Runte et al., 2017). Therefore, cell-shortening kinetics in the myocytes, or Doppler echocardiography of hearts *in vivo*, would have been useful to establish evidence for diastolic dysfunction.

It is worth considering here, the results of systolic Ca^{2+} and SR Ca^{2+} load. Systolic $[Ca^{2+}]$ is predominantly a function of the size of $I_{Ca,L}$ and SR Ca^{2+} load. It was interesting that systolic

[Ca^{2+}] was unchanged in amPA, in the context of the positive relationship between systolic and diastolic [Ca^{2+}] in normal cardiomyocytes (Eisner *et al.*, 2020). In the absence of a proportional change in systolic Ca^{2+}, the data suggest that SR Ca^{2+} loading was affected in amPA, as it did not respond in a way that normal cells would, when diastolic Ca^{2+} is raised.

Collectively, female amPA myocytes may have reduced E-C coupling gain and present with a state of negative inotropy (i.e. depression of the active length-tension curve) and negative lusitropy (i.e. uplift of the passive length-tension curve). There are three possibilities for this apparent reduction in E-C coupling gain in female amPA myocytes. First, there could be reduced SERCA activity in amPA. In support of this, there was a significant decrease in SERCA rate in amPA, irrespective of sex. Equally, a decrease in $I_{Ca,L}$ may contribute to the phenotype and apparent reduction in SR Ca^{2+} load, although this was not directly measured by electrophysiology. A third possibility is related to RyR dysfunction. Increased SR Ca^{2+} leak through leaky RyRs would increase diastolic Ca^{2+}, reduce SR Ca^{2+} content, and hence CaT amplitude (although in the long-term, feedback mechanisms would be expected to restore CaT size) (Eisner *et al.*, 2020). Since there was an 'apparent' increase in the backflux constant (the efflux that balances SERCA, i.e. RyR leak), and possibly reduced SR Ca^{2+} load, there would be merit in investigating if RyR function is changed in amPA, for which there are several possible experimental approaches: (i) measuring RyR protein expression in amPA hearts; (ii) measuring Ca^{2+} wave velocity in amPA cardiomyocytes (or Ca^{2+} spark frequency); (iii) determining RyRs

leakiness in amPA cardiomyocytes (e.g. with FR, by measuring SR Ca^{2+} content in an unstimulated cell after an extended rest period).

4.4.3 CaT amplitude and SR Ca^{2+} load are increased in 20-week amPA females

Interestingly, akin to 8-week amPA myocytes, significant changes in Ca^{2+} handling were only observed in female mice at 20 weeks of age. The summary of the key changes to Ca^{2+} handling in amPA myocytes is shown in Figure 4.12. Remarkably, diastolic and resting Ca^{2+} were no longer increased in 20-week amPA females. Instead, there was normalisation of these parameters, and by 20 weeks of age, there was significantly greater CaT amplitude (released $[Ca^{2+}]$) and SR Ca^{2+} load. This dramatic change may relate to compensatory mechanisms to restore Ca^{2+} flux balance and contractile function; for example, the rightward shift in EDV and ESV at 8 weeks (cine-MRI; Chapter 3), could be normalised for by an increase in inotropic state.

The increase in CaT amplitude and SR Ca^{2+} load may be a manifestation of several factors, including higher SERCA rate, greater $I_{Ca,L}$, reduced Ca^{2+} extrusion by NCX (e.g. due to increased $[Na^+]_i$), and to a lesser extent, reduced Ca^{2+} extrusion by PMCA. There was no clear indication of decreased NCX/PMCA activity from caffeine-evoked Ca^{2+} release, in both 8-week and 20-week amPA females. Thus, the observed changes at 20 weeks are most likely related to greater $I_{Ca,L}$, and/or higher SERCA rate.

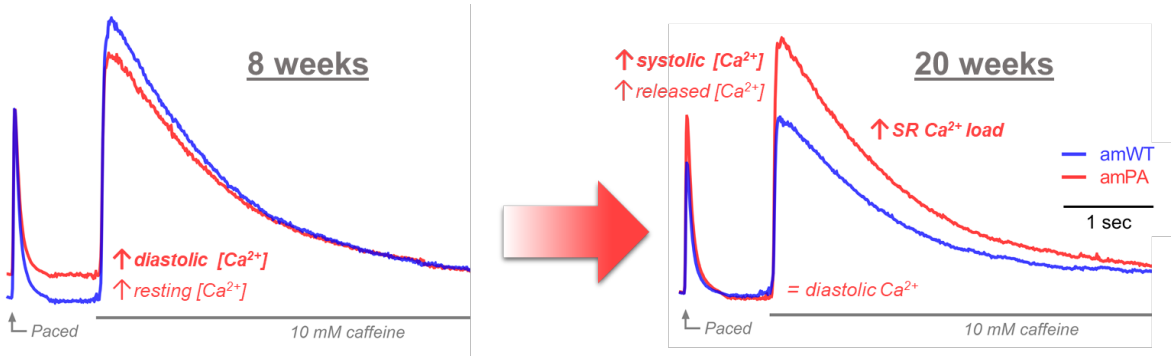


Figure 4.12. Summary of remodelling to Ca^{2+} handling in female amPA cardiomyocytes. Averaged time-courses of electrically-evoked CaTs and caffeine-evoked Ca^{2+} release in female wild-type (amWT; blue) and PA (amPA; red) mice, at 8 and 20 weeks of age.

4.4.4 Sex-specificity of the effect on Ca^{2+} handling in PCC-deficient animals

Perhaps the most intriguing observation was that the effect of PCC disruption on Ca^{2+} handling was observed in females only. Sex bias is known to be prevalent in preclinical biomedical research. Even in cardiovascular research, male animal models are typically used in laboratory research with gross underrepresentation of females (Ramirez *et al.*, 2017). This is problematic, given that there are well-established physiological differences in cardiovascular physiology and pathology between genders. For example, heart failure with preserved ejection fraction (HFpEF) is more common in females and women have a greater predisposition to diastolic dysfunction (Beale *et al.*, 2018). Of note is that there are known to be sex differences in myocardial substrate metabolism and in cardiometabolic disorders (Peterson *et al.*, 2008; Murphy *et al.*, 2017; Gerdts & Regitz-Zagrosek, 2019).

Although the underlying molecular and cellular mechanisms are not well understood, oestrogen appears to exert powerful effects in the cardiomyocyte. For example, there are marked sex differences in Ca^{2+} handling (Murphy *et al.*, 2017), which appears to involve changes in cyclic nucleotide signalling (Regitz-Zagrosek & Kararigas, 2017). Ovariectomised rats have increased Ca^{2+} fluxes through RyR and NCX that are reversed upon oestrogen replacement, an effect attributed to oestrogen downregulating PKA (Kravtsov *et al.*, 2007). Another study demonstrated smaller CaT amplitude and lower E-C coupling gain in female vs male cardiomyocytes, due to lower basal levels of cAMP from higher endogenous expression of phosphodiesterase 4B (Parks *et al.*, 2014).

Since the Ca^{2+} handling experiments were sex-balanced, comparing female wild-type and female PA mice, it is unlikely that background sex differences in Ca^{2+} handling *per se* is the contributing factor for the observed remodelling. Instead, it is more likely that there is a sex effect related to the PCC lesion itself, tested statistically as the interaction between genotype and sex. To further investigate the sex effect in PA, the next logical experiment would be to perform untargeted metabolomics in sex-balanced heart and plasma cohorts, as discussed in Chapter 3. There is a good possibility that there is an effect of sex on the accumulation of propionate and its metabolites, since the classical plasma PA metabolites propionyl-carnitine and MeCit have been shown as being higher in amPA females vs males (Guenzel *et al.*, 2015).

Regardless, since it is clear that disrupting PCC results in remodelled Ca^{2+} handling, the other set of experiments presented in this Chapter tested the hypothesis that propionate is a bioactive

molecule capable of remodelling this process. The experiments in the remainder of this Chapter tested the effects of exogenously applied propionate on the physiology of WT cardiomyocytes.

4.4.5 *In vitro* application of propionate on WT cardiomyocytes

To determine whether propionate *per se* can remodel E-C coupling in a manner consistent with the mouse phenotype, experiments were performed in WT cardiomyocytes exposed to propionate *in vitro*. The experiments were performed at two timescales of exposure to establish whether the responses to propionate are acute or slower-onset.

4.4.5.1 Acute exposure to propionate

First, CaTs were recorded in myocytes acutely superfused with propionate (10-30 mins) at pH 7.4 (to mimic a compensated PA) and pH 7.3 (to mimic uncompensated PA), to distinguish the effect of propionate, vs metabolic acidosis (pH). Propionate was used at 6 mM, a very high concentration observed in acutely decompensated patients. Surprisingly, both compensated and uncompensated PA had no effect, on either the electrically-evoked CaT, or caffeine-evoked Ca^{2+} release. This argues against acute (e.g. allosteric) actions of propionate on the remodelled Ca^{2+} handling in amPA.

4.4.5.2 Chronic exposure to propionate

Given the changes to Ca^{2+} handling in PCC-deficient animals, it was unusual that acutely applying propionate had categorically no effect on cardiomyocyte Ca^{2+} handling. These two observations suggest that propionate must be exerting its actions on a more chronic timescale.

To test this hypothesis, NRVMs were cultured for 48 hrs in propionate, and field-stimulated APs and CaTs were recorded, after the washout of treatment. Thus, any observed changes could be attributed to 'persistent' changes.

Since adult myocytes are terminally differentiated and abnormally change in function (detubulate) over a relatively short timescale, neonatal myocytes are a popular model for the study of long-term remodelling processes (Korhonen *et al.*, 2009). E-C coupling in neonatal myocytes has been well-defined (Bers, 2002b; Korhonen *et al.*, 2009). Indeed, a unique feature of the neonatal myocyte is that they lack the T-tubule system, leading to them having a more heterogenous cytosolic Ca^{2+} signal (versus the rapid three-dimensionally uniform CICR typical in adult myocytes) (Korhonen *et al.*, 2009).

The *in vitro* application of propionate was found to significantly remodel the AP and CaT after a more chronic exposure, suggesting that propionate exerts its actions through longer-term changes. Given the evidence for propionate being able to act as an epigenetic modifier (Koh *et al.*, 2016), these actions could be related to gene expression (tested in Chapter 5). The changes to the CaT in NRVMs with long-term propionate exposure *in vitro*, may correlate with the changes seen in female amPA myocytes. That is, CaT duration was longer (consistent with slower SERCA rate) and amplitude was reduced. These observations suggest that propionate may be what remodels E-C coupling in the PA mouse. In any case, the important finding from this experiment was the finding that propionate itself can remodel E-C coupling, but it does so

through longer-term actions. The propionate-evoked remodelling of the AP and CaT *in vitro*, are discussed separately, below.

Propionate and the action potential. APD was significantly shorter in NRVMs treated with propionate. This effect was seen irrespective of whether there was a concurrent extracellular acidosis, indicating that propionate itself can cause remodelling.

There is only one study to date examining the effects of propionate and propionate metabolites on electrophysiology using human embryonic kidney cells and human induced pluripotent stem cell-derived cardiomyocytes. Bodi *et al.* (2016) examined the acute and chronic effects of various propionate metabolites (propionic acid, propionyl-carnitine and MeCit) on I_{Kr} and I_{Ks} (*KCNQ1*). Although I_{Kr} was largely unaffected, acute application of propionate metabolites significantly decreased I_{Ks} current densities (tail and end-pulse currents). Propionic acid (10 mM significantly prolonged APD in human induced pluripotent stem cell-derived cardiomyocytes, but not in KCNQ1-deficient rabbits lacking I_{Ks}. Collectively, their results suggested a reduction of I_{Ks} may account for the observed prolongations in APD and QT interval in PA patients.

Indeed, it is unclear why the remodelling of APs occurred in opposite directions. That is, why in PA patients and in the study by Bodi *et al.* (2016), there was prolongation of APD, versus shortening of APD in this thesis. It may be related to species differences and the relative importance of different repolarising currents, since APD is determined by the rate of repolarisation (Winter & Shattock, 2016). Although I_K has an important role in repolarisation

in the human ventricle, in mouse and rat, I_K has a minor, or even negligible contribution to repolarisation. Instead, they have a faster repolarisation mediated by I_{to} (Kaese & Verheule, 2012). A possible explanation is that in both human and rodent ventricle, propionate reduces I_K, whilst increasing I_{to}. In human ventricle, the reduction in I_K offsets the increase in I_{to}, overall resulting in APD prolongation. However, in rat and mouse, since I_K is largely absent, I_{to} contributes to the phenotype and shortens APD. Indeed, the measurements in this thesis were done in ventricular myocytes and $I_{to,f}$ is expressed throughout the left and right ventricle in mouse and rat (vs. mainly epicardium in humans) (Nerbonne, 2004; Kaese & Verheule, 2012).

A future experiment would be to measure APD in amPA myocytes, which can be performed for example, using current-clamp in whole-cell mode (Shattock *et al.*, 2017) or optical mapping (Varró *et al.*, 2020). Should APD also be reduced in amPA cardiomyocytes, the next step would be to identify the contribution of different repolarising currents by voltage-clamp.

Propionate and the Ca^{2+} transient. The interpretation of the CaT data is simpler. An increase in amplitude in *acidosis* can be explained as effects mediated by Na^+ (Na^+ loading via NHE, thus reduced Ca^{2+} extrusion by NCX and greater SR Ca^{2+} load) (Vaughan-Jones *et al.*, 2009). Interestingly, *acidosis* had no effect on temporal kinetics and instead, such changes were only induced by propionate.

Time-to-peak, was significantly slower in propionate-treated neonatal myocytes. In adult myocytes, time-to-peak is a readout of LTCC-RyR coupling, which for example, can be

regulated by junctophilin-2 (Landstrom *et al.*, 2017). However, NRVMs lack spatial coupling between the LTCC and RyR since they lack T-tubules. Rather, the CaT upstroke in neonatal myocytes have two distinct components: (1) diffusion of Ca from the sarcolemma (i.e. LTCCs) to the SR (i.e. RyRs) located in the perinuclear region; (2) propagation of local CICR at the level of the SR (Korhonen *et al.*, 2009). Indeed, there was no evidence of hypertrophy in propionate-treated NRVMs (SRB assay, Chapter 3), which would affect diffusion distance. Thus, the slower time-to-peak in propionate-treated neonatal myocytes could be due to a combination of reduced buffering capacity and irregular/reduced distribution of RyR clusters, which for example has been observed in failing hearts (Hiess *et al.*, 2018).

Compared to ARVMs, NRVMs have weaker SR Ca^{2+} handling and instead, sarcolemmal Ca^{2+} handling is more important, with a significant contribution by NCX (Korhonen *et al.*, 2009). CaT duration was also significantly longer in propionate-treated neonatal myocytes. Since caffeine-evoked Ca^{2+} release was not measured here, the relative contributions of SERCA and NCX are unknown.

4.5 Summary

The key findings from this Chapter were that Ca^{2+} handling was affected by PCC-deficiency, in the form of raised diastolic $[Ca^{2+}]$ but unaltered systolic $[Ca^{2+}]$ in younger 8-week-old animals, which can be explained by a greater influx and/or reduced efflux across the sarcolemma. The changes suggest a decrease in E-C coupling gain, which could be attributed to reduced SERCA

activity, reduced $I_{Ca,L}$, and/or higher RyR leak. By 20 weeks of age, there was normalisation of diastolic and resting [Ca^{2+}], but myocytes manifested increases in systolic [Ca^{2+}], SR Ca^{2+} load and released Ca^{2+}. This dramatic change may relate to compensatory mechanisms to restore Ca^{2+} flux balance and contractile function (increased contractility). Interestingly, the remodelling of Ca^{2+} handling was only significant in females.

To determine whether propionate can contribute to this remodelling, experiments were repeated in WT myocytes treated with propionate. Surprisingly, there was unequivocally no acute effect of propionate on Ca^{2+} handling, but a substantial remodelling of E-C coupling when applied chronically. The observed changes to E-C coupling *in vitro* may relate to those observed in the adult PA mouse. In any case, the important finding from the *in vitro* studies was the fact that propionate can remodel E-C coupling, but only through longer-term actions. Therefore, the remodelling to Ca^{2+} handling observed in PCC-deficient mice, could be attributed to slower-onset actions of propionate. Since long-term exposures to propionate and propionate metabolites (*in vivo* and *in vitro*) clearly remodel E-C coupling, the remaining question was why this remodelling only occurs on a chronic timescale. Since propionate is known to be an epigenetic modifier, it would be intuitive to assume that the remodelled E-C coupling is due to changes in expression of key cardiac genes. The effect of propionate on epigenetics and gene expression is addressed in the next Chapter.

Chapter 5. Effects of propionate on cardiac epigenetics and gene expression

In Chapter 4, changes to Ca^{2+} handling were observed in cardiomyocytes from the PA mouse model. To determine whether propionate is involved in the remodelling of Ca^{2+} handling, these experiments were repeated in WT cardiomyocytes treated with propionate *in vitro*. Whilst propionate did indeed remodel the Ca^{2+} transient, surprisingly, it only had an effect when applied chronically. There is a large evidence-base for propionate affecting gene expression. Propionate has been established as a histone deacetylase inhibitor in studies of the gut microbiome and has also been shown to act as a substrate for lysine acetyltransferases. Therefore, the purpose of the work in this Chapter was to test the hypothesis that cardiac dysfunction in PA involves a change in cardiac gene expression. To address this, whole-exome transcriptomic analysis and an assessment of histone modifications were performed in wild-type cardiomyocytes treated with propionate *in vitro*. Having determined that propionate had an effect on gene expression and histone marks, transcriptomic analysis was repeated in ventricular

tissue of 8-week-old PCC-deficient mice. The transcriptomic datasets from propionate-treated cardiomyocytes and the mouse model were then compared to establish propionate-sensitive genes, and to also determine which of these genes were affected by the canonical mechanism of HDAC inhibition, vs a non-canonical mechanism of, putatively, propionylation.

5.1 Introduction

5.1.1 Gene expression: structural considerations

5.1.1.1 Histones and the epigenome

The nucleus of every eukaryotic cell contains the genetic material (DNA) required for the translation of proteins necessary for biological function. Approximately 1.7 metres of DNA is packaged into every nucleus of ~6 microns in diameter (Han *et al.*, 2011). This remarkable feat is achieved by the packaging of DNA into a protein-DNA macromolecular complex known as chromatin. The fundamental structural unit of chromatin is the nucleosome, which consists of ~147 bp of DNA wrapped around an octameric core of histone proteins (two copies each of H2A, H2B, H3 and H4), which is then further assembled into the chromatin fibre with the linker histone H1 (Shechter *et al.*, 2007; Haws *et al.*, 2020).

Epigenetics is the field of study that examines the epigenome, which refers to the chemical modifications on DNA and histones that allow for the regulation of chromatin structure and function, without altering genomic sequences (Haws *et al.*, 2020). There are several processes that have been shown to control chromatin structure, including DNA methylation and ATP-dependent chromatin remodelling (Han *et al.*, 2011). However, an important process is the covalent modifications of histone proteins. Histones are small, positively-charged basic proteins that are among the most highly conserved eukaryotic proteins (Shechter *et al.*, 2007). They are, however, susceptible to a plethora of post-translational modifications (PTMs). Such PTMs affect

chromatin electrostatic interactions and contribute to the formation of higher-order chromatin structures: heterochromatin, which is physically compact and euchromatin which is physically open (Haws *et al.*, 2020). The chromatin state, and thus the accessibility of DNA, therefore influences gene transcription by modulating access by DNA-binding proteins (e.g. transcription factors, polymerases) or modifying the nucleosome surface to modulate the recruitment of effector protein complexes that 'read' histone PTMs (e.g. bromodomain) (Taverna *et al.*, 2007; Park, 2009). PTMs on histones can have a profound effect on gene expression by directly affecting the chromatin state, and these PTMs are known to be directly linked to the metabolic state of the cell. This is discussed further in Section 5.1.2.

5.1.1.2 Nuclear organisation

The organisation of the genome in the nucleus is not random and the conformation of chromatin in the three-dimensional space is hierarchical and highly complex (Zheng & Xie, 2019). This principle is important because there is considered to be interplay between the spatial organisation of the genome and transcriptional machinery, thus having functional effects on gene expression in many cell types (van Steensel & Furlong, 2019), including cardiomyocytes (Papait *et al.*, 2020; Bertero & Rosa-Garrido, 2021).

As aforementioned, generally transcriptionally inactive or repressed genomic regions are heterochromatic, whereas transcribed or active regions are euchromatic (van Steensel & Furlong, 2019). These regions are usually marked by the same histone modifications, hence the referral to some histone marks as transcriptionally 'active' or 'inactive'. For example,

euchromatic regions are densely populated by active genes and enhancers, as well as a panel of typical histone marks such as H3K27ac (van Steensel & Furlong, 2019; Bertero & Rosa-Garrido, 2021). Ultimately, the physical compaction or openness of chromatin (heterochromatin and euchromatin, respectively) either prohibits or permits the access of transcriptional machinery necessary for gene transcription (Haws *et al.*, 2020).

In the majority of cell types, euchromatin is generally located in the nuclear interior, with heterochromatin being in the nuclear periphery (van Steensel & Furlong, 2019). However, this is an over-generalisation and it is known that the relative location of these compartments can differ depending on both tissue type and developmental stage (Chapski *et al.*, 2018; van Steensel & Furlong, 2019). Chromosome conformation capture technologies such as Hi-C can be used to generate genome maps at the sub-chromosomal level, which can be used to reveal the segmentation of chromatin domains into two compartments at high-resolution: compartment A (active; euchromatic) and compartment B (inactive; heterochromatic) (Bonev & Cavalli, 2016). However, the mechanism responsible for the compartmentation of chromatin is under intense debate and largely unknown (Falk *et al.*, 2019).

5.1.2 Metabolic regulation of gene expression

It has become increasingly appreciated in recent years that gene expression and cellular metabolism are interrelated, and that perturbations in cellular metabolism can have substantial consequences on gene expression (Reid *et al.*, 2017; Sabari *et al.*, 2017; Li *et al.*, 2018). This is because metabolites serve directly as substrates and co-factors for histone PTMs. The level of an acyl-PTM is directly related to the abundance of that particular acyl-CoA and is increased by acyl-CoA in a dose-dependent manner (Simithy *et al.*, 2017). Lysines are the amino acids in histones modified by acylation. A variety of so-called 'short-chain lysine acylations' have been discovered involving different metabolites, including lysine propionylation (Kpr), butyrylation (Kbu), succinylation (Ksucc), malonylation (Kma) and crotonylation (Kcr) (Sabari *et al.*, 2017), with the most recently discovered being lactylation (Klac) (Zhang *et al.*, 2019).

Short-chain fatty acids (SCFAs) such as acetate, propionate and butyrate are produced directly by the gut microbiome from the fermentation of dietary fibre. As alluded to, SCFAs are a common metabolic substrate for histone acylations. SCFAs can also act as direct agonists for G-protein coupled receptors and, as such, microbiome SCFA biology is an area of active research (Koh *et al.*, 2016). The most widely-studied short-chain lysine acylation is lysine acetylation (Kac), which uses the substrate acetyl-CoA, a central metabolic intermediate which is also recognised to function as a second messenger for a diverse range of biological processes (Pietrocola *et al.*, 2015).

During acetylation, an acetyl group from acetyl-CoA is used to modify a lysine on its ε-amine group (the amino group on the side chain of lysine; where most PTMs occur). This chemical change (lysine acetylation; Kac) has several effects, including the neutralisation of the positive charge of the amine group, increased hydrophobicity and increased size of the lysine side chain. Together, these changes compromise the lysine side chain's ability to chemically interact with other proteins and notably relax chromatin structure (Sabari *et al.*, 2017).

The different types of acylation (e.g. Kac, Ksucc, Kcr) can be classified based on the chemical properties of the acyl-moiety. Acetyl, propionyl and butyryl groups are all hydrophobic, thus Kac (2-carbon), Kpr (3-carbon) and Kbu (4-carbon) are classified together as hydrophobic modifications and have chemically similar effects, differing mainly by the size and hydrophobicity of their modified lysine chain (determined by hydrocarbon length) (Sabari *et al.*, 2017).

5.1.2.1 Writers and erasers: KATs and HDACs

The acylation state of histones is regulated by a dynamic balance between the enzymatic activities of writers and erasers, which add and remove acyl moieties, respectively. The activity of these enzymes is regulated by the metabolic state of the cell (Reid *et al.*, 2017). Lysine acylations have been proposed to occur non-enzymatically in microenvironments that have alkaline pH and high acyl-CoA concentrations (thus thermodynamically favouring the reactions), such as in the mitochondrial matrix. However, the conditions in the nucleus are less

favourable and thus histone acylations are largely governed by the enzymatic activity of writers and erasers (Sabari *et al.*, 2017; Simithy *et al.*, 2017).

Writers: lysine acetyltransferases. Histone acetylation is catalysed by the lysine acetyltransferase family of enzymes (KATs), traditionally known as histone acetyltransferases (HATs). The KAT nomenclature was introduced by Allis *et al.* (2007) to simplify the identification and classification of new histone acetyltransferases. There are three major families of HATs, based on their sequence and structural features: (1) p300 family (e.g. CBP/KAT3A and p300/KAT3B); (2) GNAT family (e.g. Gcn5/KAT2 and PCAF/KAT2B); (3) MYST family; (Allis *et al.*, 2007; Sabari *et al.*, 2017). The activity of these enzymes are determined by substrate and co-factor availability, as well as their kinetic (K_m) and thermodynamic (K_d) properties (Reid *et al.*, 2017). Although writers specific for non-acetyl acyl groups have not been identified, the KATs identified thus far have been shown to have non-selective acyl-transferase activity, primarily driven by substrate availability (Sabari *et al.*, 2017).

Erasers: histone deacetylases. The HDAC superfamily comprises four major classes of HDAC enzymes: class I (HDACs 1/2/3/8; Zn^{2+}-dependent), class II (HDACs 4/5/6/7/9/10; Zn^{2+}-dependent), class III (sirtuins 1-7; NAD^{+}-dependent) and class IV (HDAC 11; Zn^{2+}-dependent). Class II has two further sub-classifications (IIa and IIb) and notably, class IIa HDACs (4/5/7/9) lack deacetylase activity due to a mutation within the catalytic domain (Bagchi & Weeks, 2019).

Whilst class I HDACs are primarily localised to the nucleus, class IIa/b HDACs have been shown to shuttle between the nucleus and cytoplasm (Steliou *et al.*, 2012). The most abundant HDACs in cardiomyocytes are HDAC2 (class I), HDAC3 (class I) and HDAC5 (class IIa) (Bagchi & Weeks, 2019). Interestingly, class IIa HDACs have large N-terminal extensions with conserved binding sites for transcription factors such as myocyte enhancer factor 2 (MEF2) (Haberland *et al.*, 2009). The activity of class IIa HDACs are phosphoregulated by kinases such as protein kinase D and CaMKII, thus, in the heart, are open to modulation by excitation-transcription coupling (Haberland *et al.*, 2009; Bers, 2011).

Inhibition of HDACs by SCFAs. There are several structurally distinct classes of HDAC inhibitors reported to date, including trichostatin A (TSA) and analogues, hybrid polar compounds (e.g. SAHA, suberoylanilide hydroxamic acid) and SCFAs (e.g. propionate, butyrate, valproate) (Lu *et al.*, 2004). Although there is a wealth of literature on SCFAs being used as HDAC inhibitors, primarily in studies of cancer and the microbiome (Koh *et al.*, 2016), their actual mechanism of action has not been fully elucidated. This is partially due to the carboxylic acid class having poor HDAC inhibition activity, compared to well-established inhibitors such as TSA, thus garnering less interest (Bora-Tatar *et al.*, 2009). SCFAs are the least potent inhibitors, with an IC_{50} approximately in the millimolar range, compared to micromolar, or even nanomolar, for other types of HDAC inhibitors (Lu *et al.*, 2004).

Insight into the mode-of-action of HDACs were largely borne from the study by Finnin *et al.* (1999), where the authors investigated the mechanistic basis of HDAC inhibition by TSA and

SAHA, through deacetylase–inhibitor interaction crystallography studies. It has become clearer in recent years that the structurally distinct classes of HDAC inhibitors share a common pharmacophore consisting of several components, including a metal-binding functional group that interact with Zn^{2+}, the essential ionic co-factor for class I and II HDAC catalytic activity (Miller *et al.*, 2003; Bora-Tatar *et al.*, 2009).

Between the SCFAs, there is mainly literature available on the possible mechanism of action by butyrate. Since trichostatin A, the gold-standard class I & II HDAC inhibitor, has been shown to occupy the hydrophobic pocket of HDAC (which contains the deacetylase core), butyrate has been suggested to act in a similar manner by occupying this pocket. However, this explanation is unlikely given that butyrate mainly displays non-competitive pharmacokinetic properties (Davie, 2003). Rather, based on structural studies, the most likely explanation is that the carboxyl groups of SCFAs act as metal-binding (Zn^{2+}) moieties and interacts with the Zn^{2+} in the active site of HDACs (Finnin *et al.*, 1999; Miller *et al.*, 2003).

5.1.2.2 Lysine propionylation: propionyl-CoA as a substrate for PTMs

Under normal physiological conditions, the intracellular concentration of acetyl-CoA is higher than propionyl-CoA (Palladino *et al.*, 2012). Thus, Kac is the primarily observed PTM. However, KATs are not specific for acetyl groups; their activity is driven by substrate availability, and the occurrence of a particular acyl-PTM is directly related to the concentration of the acyl-CoA (Sabari *et al.*, 2017). Thus, under metabolic conditions in which propionate and propionyl-CoA are increased (like in PA), it would be expected for more propionyl groups to be utilised as a substrate.

Histone propionylation. Lysine propionylation (Kpr) was first discovered as a PTM of H3 and H4 by Chen *et al.* (2007). Notably, H3K14pr has been characterised in the liver of PA (*Pcca*$^{-/-}$ A138T) mice as a mark associated with transcriptionally active chromatin (Kebede *et al.*, 2017). More recently, deficiency in H3K23pr was found to be critical in the development of neurodevelopmental disorders (Yan *et al.*, 2020). Like histone Kac, histone Kpr requires enzymatic catalysis by KATs and these enzymes show site-specificity. For example, H3K14pr requires KAT3B (p300), KAT2 (GCN5) or KAT2B (PCAF) (Kebede *et al.*, 2017). H3K23pr requires KAT6A and KAT6B forming a tetrameric complex with BRPF1 (bromodomain- and PHD finger–containing protein 1) (Yan *et al.*, 2020).

Non-histone protein propionylation. After the discovery of histone propionylation in 2007, a report was subsequently published by the same laboratory demonstrating propionylation of non-histone proteins (Cheng *et al.*, 2009). Although not related to gene expression, non-histone

protein acylations are regarded as important PTMs in regulating protein function (Narita *et al.*, 2019), including those important in cardiac function (Foster *et al.*, 2013). Interestingly, fibroblasts from PA patients have been shown to have increased protein Kpr (Pougovkina *et al.*, 2014).

5.1.2.3 Acyl-CoA accessibility and compartmentalisation

An important concept to consider is where the acyl-CoA (e.g. acetyl and propionyl) is sourced from to fuel histone PTMs in the nucleus. The mitochondrial membrane is impermeable to CoA-esters, thus acyl-CoAs either need to be generated in the cytosol or exported from the mitochondria by a specialised transport process.

Both acetyl-CoA and propionyl-CoA can be exported from the mitochondria by the carnitine shuttle. In contrast, acetyl-CoA and propionyl-CoA can also be enzymatically esterified in the cytosol from their respective SCFAs (acetate and propionate) by ACSS2 (Figure 1.2; Chapter 1) (Pietrocola *et al.*, 2015; Trefely *et al.*, 2020). In the case of PA, since the liver is the metabolically dominant organ (Wilson *et al.*, 2017), the majority of propionate is most likely to be sourced from outside the heart, thus requiring the action of ACSS2 to become a PTM substrate.

Interestingly, recent evidence suggests there are distinct nuclear and cytosolic pools of acetyl-CoA that are functionally distinct (Sivanand *et al.*, 2018). This is also presumably the case for propionyl-CoA. ACSS2 is known to be able to translocate to the nucleus to regulate gene expression (Li *et al.*, 2018). Small molecules (< 9 nm/< 40 kDa) can freely diffuse through nuclear

pore complexes and, as such, the nuclear pore is permeable to SCFAs and short-chain acyl-CoAs (Görlich & Kutay, 1999). Therefore, there is a possibility for both acetyl-CoA and propionyl-CoA being sourced from either the nucleus or the cytosol.

5.1.3 Histone modifications in cardiovascular disease

The epigenome is known to have an important role in cardiovascular diseases, whereby aberrant gene expression plays a central part in the pathophysiology (Gillette & Hill, 2015; Papait *et al.*, 2020). A classic example is heart failure, in which a biochemical signature of the failing heart is the re-expression of foetal genes (e.g. *Myh7*, *Nppb*) (Cui *et al.*, 2018).

Histone modifications are known as being important factors driving adverse cardiac remodelling (Liu & Tang, 2019; Li *et al.*, 2020). For example, in the seminal study by Papait *et al.* (2013), a comprehensive analysis of histone PTMs was performed cardiomyocytes from a pressure-overload model of murine heart failure (transverse aortic constriction, TAC). Papait *et al.* identified that the genomic distributions of H3K9ac and H3K27ac are altered in TAC-induced cardiac hypertrophy, and these histone marks contribute to the modulation of promoter and enhancer activities in heart failure.

5.1.4 Aims of this Chapter

Ca^{2+} handling was remodelled in ventricular myocytes isolated from 8-week-old PCC-deficient animals (Chapter 4). Ca^{2+} handling was also remodelled when propionate was applied to cardiomyocytes *in vitro*, but only over a chronic timescale, suggesting the mechanism by which propionate exerts its actions requires time. Propionate is established as an epigenetic modifier (HDAC inhibitor) from studies of the gut microbiome, albeit less potent than the commonly used SCFA HDAC inhibitor, butyrate. There is also emerging evidence that propionate, as propionyl-CoA, can act as a direct substrate for PTMs on histones (and non-histone proteins). Thus, these observations combined suggest that propionate-mediated changes in cardiac gene expression or protein function are important mechanisms by which cardiac dysfunction could occur. Therefore, the aims of this Chapter were to:

a) By whole-exome transcriptomic sequencing of WT cardiomyocytes treated with high concentrations of propionate *in vitro*, confirm whether propionate is capable of eliciting a change in cardiac gene expression, and determine which genes are related to the canonical mechanism of HDAC inhibition by identifying the genes that are commonly changed by propionate *and* butyrate (positive control for HDAC inhibition), vs the lesser-known non-canonical mechanism of, putatively, propionylation, from genes differentially expressed by propionate *only*;
b) Determine whether there is a change in cardiac gene expression *in vivo* from ventricular tissue of 8-week-old PCC-deficient mice that may explain the cardiac phenotype, also by whole-exome transcriptomic sequencing, and by comparing with the *in vitro* dataset,

confirm which differentially expressed genes are propionate-sensitive and affected by canonical vs non-canonical mechanisms;

c) By enrichment analysis, predict which histone marks are associated with the differentially expressed genes, and confirm whether these marks are increased in the heart by immuno-based methods;

d) Probe for any evidence of histone or non-histone propionylation in the heart.

5.2 Specific methods

5.2.1 Biological models

Wild-type NRVMs and ARVMs. To determine the effects of propionate on cardiomyocyte histone modifications and gene expression, myocytes isolated from wild-type neonatal and adult ventricular myocytes were cultured in various formulations of culture media, based on those described in Section 2.2.4 (Table 2.3).

$Pcca^{-/-}$ (A138T) hearts. To determine the consequences of an *in vivo* accumulation of propionate and its metabolites on cardiac histone modifications and gene expression, ventricular tissue was collected from 8-week-old PA and wild-type mice (amPA, amWT) as described in Sections 0 and 2.2.6.

5.2.2 Sample preparation

5.2.2.1 Total RIPA lysates

Total lysates were prepared with RIPA containing protease and phosphatase inhibitors as described in Section 2.2.6. Samples were prepared for SDS-PAGE in 2x Laemmli sample buffer under reducing conditions (β-mercaptoethanol) as described previously (Section 2.2.8).

5.2.2.2 Histone extraction

Since histone proteins are basic proteins, they are amenable to methods of chemical extraction from the cell, such as acid-, or high salt-based methods. These methods have been widely adopted and are effective in extracting histones, whilst conserving histone PTMs (Shechter *et al.*, 2007). Total histones were extracted from cultured NRVMs and snap-frozen mouse ventricular tissue using the EpiQuik Total Histone Extraction Kit (Epigentek, #OP-0006), a pre-optimised acid extraction method. For mouse hearts, tissue was first cryoground and homogenised, as described in Section 2.2.6, in the lysis buffer provided in the kit, prior to proceeding with the manufacturer's protocol. Extracted histones were quantified using BCA assay (Section 2.2.7) and stored in -80°C until use. Samples were prepared for SDS-PAGE in 4x Laemmli sample buffer under reducing conditions (β-mercaptoethanol) as described in Section 2.2.8.

5.2.2.3 RNA extraction

All procedures for RNA extraction were performed in DNase/RNase-free conditions.

For RT-qPCR. TRIzol reagent (Invitrogen) was used to extract total RNA from NRVMs for RT-qPCR experiments following the manufacturer's protocol. In brief, after treatment of NRVMs in their respective culture media, the media was rinsed away with ice-cold PBS and lysed in TRIzol reagent.

For RNA-seq. Ventricular tissue from 8-week mice was snap-frozen and cryoground as described in Section 2.2.6. Bulk RNA was extracted using the Zymo Quick-RNA Miniprep Plus Kit (R1057), following the manufacturer's protocol with some modifications, mainly in the tissue digestion stage. All centrifugation steps were performed at 16,000 RCF at 4°C and only DNA LoBind microcentrifuge tubes were used (Eppendorf #022431021). 20 mg of cryoground tissue was mechanically homogenised on ice with disposable probes (Qiagen TissueRuptor II) in 350 µL of DNA/RNA Shield. 45 µL of Proteinase K mix was added to 300 µL of sample, incubated for 30 mins at 55°C, and centrifuged for 2 mins after incubation. The supernatant was transferred to new microcentrifuge tubes and 300 µL RNA Lysis Buffer was added at 1:1 to the supernatant. Thereafter, the RNA purification procedure followed the manufacturer's protocol, with some differences: (1) ½ volume ethanol (300 µL) was added, in order to isolate RNAs ≥ 200 nt for poly(A) enrichment; (2) DNase I treatment was performed in-column; (3) RNA was eluted in non-DEPC-treated nuclease-free water (Invitrogen Ambion, #AM9937) as DEPC is known to interfere with sequencing.

5.2.3 Poly(A)+ RNA-sequencing

Library preparation and RNA-sequencing (RNA-seq) was performed by the Oxford Genomics Centre, Wellcome Centre for Human Genetics, University of Oxford. RNA sample preparation and submission were as described below. Sample preparation for NRVM RNA-seq was performed by Dr Kerrie Ford prior to the commencement of this DPhil project. Sample preparation for the mouse heart RNA-seq was performed by the Author, as described below.

5.2.3.1 Assessment of RNA sample quality

RNA integrity. The assessment of RNA integrity was performed using the Agilent RNA 6000 Nano Kit with the Agilent 2100 Bioanalyzer microfluidics-based automated electrophoresis system. The properties of the electropherograms, including the 18S to 28S ribosomal fragment band ratio can be used to compute the RNA Integrity Number (RIN). Shorter fragment sizes are observed with progressively degraded RNA. The Bioanalyzer algorithm classifies the RIN of total RNA between 1 to 10, with 1 being the most degraded and 10 being the most intact. For tissue samples, RIN > 7.0 is considered as having high integrity.

Sample purity. The absorbance ratio of 260 and 230 nm (A_{260}/A_{280}) was used to assess the purity of the extracted samples. Samples were loaded onto a specialised microplate (LVis Plate, BMG Labtech) and absorbance was read using a plate-reader platform (SECTROstar Nano, BMG Labtech).

5.2.3.2 Library preparation, sequencing and analysis pipeline

Library preparation and sequencing. Total RNA was submitted to the Oxford Genomics Centre (University of Oxford) for library preparation and next-generation sequencing. For library preparation, RNA was fractionated by enrichment for poly(A). Poly(A)+ RNA was converted to a library of cDNA fragments and adapter-ligated. Samples were sequenced on an Illumina NovaSeq 6000 System across 2 x 10-plex units, to achieve an approximate sequencing depth of 25 million reads per sample. Raw reads were 150 bp in length.

Analysis pipeline. The following analysis was performed on a UNIX platform via remote access to an account with the MRC WIMM Centre for Computational Biology (University of Oxford). Spliced Transcripts Alignment to a Reference (STAR) was used to align raw reads to the UCSC mouse reference genome *mm10* (or UCSC rat reference genome *rn6* for NRVM experiment) (Dobin *et al.*, 2013). PCR duplicates were removed using the sequence alignment/map (SAM) tools (Li *et al.*, 2009). featureCounts was used to generate the list of differentially expressed genes (DEGs) and their abundance in the samples, expressed as counts per million (cpm) (Liao *et al.*, 2014).

DEG analysis was performed using DESeq2 (Love *et al.*, 2014). DESeq2 is a statistical framework for testing differential expression with respect to user-defined thresholds of biological significance, and the ranking and visualisation of genes based on effect sizes (log fold-changes). Briefly, in DESeq2, the counts for a particular gene in each sample, is normalised by the geometric mean calculated for said gene, across every sample. The median of these ratios in a

sample is then the size factor for that sample. These steps act as an internal normalisation to correct for library size and RNA composition bias. Such biases can arise, if for example, a small number of genes are very highly expressed in one condition, but not in the other (Love *et al.*, 2014).

The following analysis was conducted using R (version 3.4.0). For genes with adequate expression (>1 cpm, already corrected for PCR duplicates and normalised to the library size), analysis for DEGs was performed using DESeq2 with an adjusted probability threshold of 5%. The formula for mouse was the Wilkinson formula genotype + sex + genotype:sex to assess the effect of genotype, sex, and their interaction. The formula for NRVM was treatment (3 levels; control + propionate + butyrate). After identifying the DEGs, the mouse and NRVM datasets were analysed and compared accordingly.

5.2.4 RT-qPCR

Reverse transcription quantitative real-time PCR (RT-qPCR) was performed in accordance with the MIQE guidelines (Bustin *et al.*, 2009). All procedures were performed in DNase/RNase-free conditions. Total RNA was extracted by the TRIzol method and reconstituted in nuclease-free water. Extracted RNA samples were stored at -80°C and kept on ice during the experiment. Freeze-thaw cycles were minimised. Nucleic acid quality-control (e.g. A_{260}/A_{280}) was performed using spectrophotometry. First-strand cDNA was synthesised using the GoScript Reverse Transcription System (Promega, A5000). RT-qPCR was performed on a ViiA 7 System (Life Technologies) using Fast SYBR Green (Fast SYBR Green 2X Master Mix; Applied Biosystems, #4385612). Each reaction used 4 ng of cDNA and the concentration of primers were 200 nM. Exon-spanning primers were designed whilst taking into account: primer length, BLAST specificity, amplicon size, GC content, melting temperature and predicted secondary structures. The sequences of the primers used are shown in Table 5.1. Three reference genes for normalisation were tested in samples: *Gapdh*, *Hprt1* and *Tbp*. *Gapdh* expression levels were found to be affected by the treatment groups and *Tbp*, although unchanged by treatment, had low levels of expression (not shown). Thus, *Hprt1* was selected as the reference gene for experiments. Whilst *Hprt1* is an X-linked gene, no effect was seen in control samples. Indeed, by random selection, it would be expected that the pups used for NRVM isolations would be approximately 50:50 males:females. Fold-changes were determined by the $2^{-\Delta\Delta Ct}$ method (Livak & Schmittgen, 2001).

Table 5.1. Primer sequences used for RT-qPCR experiments.

Gene	Primer sequence
Hprt1	F: 5' CCTGCTGGATTACATTAAAGCGC 3' R: 5' CTCCACCAATAACTTTTATGTCCC 3'
Myh6	F: 5' TGCCTGATGACAAGGAGGAG 3' R: 5' GAGGGTTCTGCTGCATCAC 3'
Atp1a2	F: 5' ATGGAGGACGAACCATCCAATG 3' R: 5' GTAGGAGAAGCAGCCAGTGACG 3'
Cacnb1	F: ACATCCAACAGCTTTGTCCGTC 3' R: 5' TTTCTCGAGCTGGGCTAAGGC 3'
Cox6b2	F: GCCTGCGACTACTATTTCCGTG 3' R: 5' CTGCTTGATCTGCTCATTCCAGC 3'
Plk1	F: CACCTTTTGAGACCTCATGCC 3' R: 5' TCTGTCTGAAGCATTTTCTGGATG 3'

F, forward; R, reverse.

5.2.5 Western blot

Samples were either prepared from NRVMs treated for 24 hrs or from 8-week-old mouse ventricular tissue as described in Section 5.2.2 and subjected to western blot as described in Section 2.2.8. SDS-PAGE was performed using pre-cast 4-20% gradient gels (Bio-Rad, Mini-PROTEAN TGX Precast Protein Gels, #4561096). Antibodies used for probing histone modifications are shown in Table 5.2. Total H3 and H4 were probed in stripped blots (30 mins, 0.2 M NaOH) originally probed for specific modifications (pan-Kpr and H3K9ac blots, respectively). Densitometry was performed as described in Section 2.2.8.

Table 5.2. Antibodies used for western blot experiments.

Primary antibody	Manufacturer Product code	Primary Ab concentration	Secondary antibody conc. (Manufacturer/code)	Resolving gel %	[Protein] loaded
H3K9ac Rb mAb	Cell Signalling Technology #C5B11	1:2,000	1:10,000 HRP-conjugated Dk α-Rb IgG (Novus, NB7185)	4-20%	Histone 4 µg
Pan-Kpr Rb pAb	PTM Biolabs #PTM-201	1:2,000	1:10,000 HRP-conjugated Dk α-Rb IgG (Novus, NB7185)	4-20%	Histone 4 µg RIPA 20 µg
Total H3 Ms mAb	Cell Signalling Technology #1B1B2	1:2,000	1:50 Polymeric HRP Gt α-Ms IgG (Abcam, #ab214879)	4-20%	Histone 4 µg
Total H4 Rb mAb	Cell Signalling Technology #D2X4V	1:1,000	1:10,000 HRP-conjugated Dk α-Rb IgG (Novus, NB7185)	4-20%	Histone 4 µg

All primary antibodies were prepared in TBS-0.1% Tween 20 with 1% BSA, whilst all secondary antibodies were prepared in TBS-0.1% Tween 20. The percentage of the resolving gel used for each antibody and the amount of protein loaded per well is shown at the end of the table. Dk, donkey; mAb, monoclonal antibody; Ms, mouse; pAb, polyclonal antibody; Rb, rabbit.

5.2.6 Whole-cell ELISA

Quantitative indirect ELISA was performed on fixed myocytes. NRVMs were seeded onto clear 96-well microplates at a density of 45,000 cells per well in culture media (Section 2.2.4). At day-2 post-isolation, myocytes were serum-starved and on day-3 were treated for 24 hrs. After 24 hrs, the myocytes were first rinsed twice with cold 1x PBS, fixed with ice-cold methanol (stored at -20°C) for 10 mins at 4°C, followed by a preliminary blocking stage with 0.3% H_2O_2 in PBS for 10 mins at room temperature. The myocytes were blocked in blocking buffer containing 10% FCS in PBS-T (0.05% Tween-20) for 1 hr at room temperature. Primary antibody was applied

for 2 hrs at room temperature in blocking buffer. Following incubation with the primary, the cells were washed four times with PBS-T (0.05% Tween-20) and incubated for 1 hour at room temperature with HRP-conjugated secondary antibody in blocking buffer (see Table 5.3 for antibodies used for ELISAs). The washing step with PBS-T was repeated after incubation with the secondary and the ELISA was developed as soon as possible. Development of the ELISA was based on McIlwain's solution, prepared in advance, containing 280 mM Na_2HPO_4 and 100 mM citric acid (pH 5.0 at room temperature). Immediately prior to use, H_2O_2 and o-phenylenediamine dihydrochloride (OPD) was added to McIlwain's solution as a substrate for HRP: in 10 mL McIlwain's, 10 mg OPD and 10 µL of H_2O_2 (30% stock). 50 µL of McIlwain's development solution was added to each well and the reaction was stopped by 100 µL of 2.0 M H_2SO_4 once the wells showed a good level of development (gold colour). Care was taken between all above solution changes to avoid wells drying out. Absorbance was read immediately at 490 nm using a plate-reader platform (Cytation 5, BioTek).

Table 5.3. Antibodies used for whole-cell indirect ELISA.

Antibody	Manufacturer Product code	Concentration	Secondary antibody
H3K9ac Rb mAb	Cell Signalling Technology #C5B11	1:300	1:4 polymeric HRP Gt α-Rb IgG (Abcam, #ab214880)
H3K27ac Rb mAb	Cell Signalling Technology #D5E4	1:100	1:4 polymeric HRP Gt α-Rb IgG (Abcam, #ab214880)
H3 Ms mAb	Cell Signalling Technology #1B1B2	1:300	1:4 polymeric HRP Gt α-Ms IgG (Abcam, #ab214879)

All antibodies were prepared in PBS-0.05% Tween 20 with 10% FCS. Gt, goat; pAb, polyclonal antibody; Rb, rabbit; mAb, monoclonal antibody; Ms, mouse.

5.2.7 Immunofluorescence

Immunofluorescence was performed for histone modifications in the nuclei of ARVMs and NRVMs. Myocytes were plated on 12-well chamber glass slides (Ibidi, #81201). Although the method was in principle the same between these two models, there were some technical differences (plating, treatment, etc.) which are outlined below. Myocytes were fixed with ice-cold methanol (stored at -20°C) for 10 mins at 4°C. The following steps were performed at room temperature. After fixation, cells were blocked in PBS containing 3% BSA for 1 hr. Primary antibodies were loaded in PBS/3% BSA for 90 mins. Cells were washed three times with PBS-0.05% Tween 20 then incubated with the secondary antibodies in PBS/3% BSA for 1 hr, protected from light. The secondary antibodies were briefly centrifuged prior to use. After secondary antibody incubation, the wash step was repeated and the slide fixed following application of anti-fade reagent (ProLong Gold antifade, Invitrogen, #P36934) with a 170 μm cover glass (Ibidi, #10811). Antibodies used for immunofluorescence experiments are listed in Table 5.4.

Immunofluorescence in ARVMs. ARVMs were plated on 12-well chamber slides (Ibidi) pre-coated with laminin (100 μg/mL in PBS) and allowed to settle for 1 hr at room temperature, prior to starting treatment with media (see below, 'treatment conditions'). Treatment medium was pre-equilibrated in a 5% CO_2 incubator and ARVMs were treated for up to 4 hrs. After methanol-fixation and prior to blocking, myocytes were pre-treated with TrueBlack lipofuscin autofluorescence quencher (Biotium, #23007) for 5 mins at room temperature. After incubation

with the secondary antibody, prior to fixation of the slide, the cells were briefly incubated with Hoechst-33342 (0.1% v/v in PBS), a DNA stain that emits blue fluorescence when excited at 405 nm (Invitrogen, H3570).

Immunofluorescence in NRVMs. NRVMs were also plated on 12-well chamber slides (Ibidi) but pre-coated with fibronectin. NRVMs were cultured as described in Section 2.2.3 and treated for 24 hrs. Instead of staining cells with Hoechst-33342, cells were co-stained for vimentin to allow identification fibroblasts (and their nuclei).

Imaging. Cells were imaged on a Zeiss LSM 700 confocal microscope with a 40x objective (*xy* mode, unidirectional scanning, pinhole 6.0 µm, 512 x 512 pixels) with sequential excitation of wavelengths 405, 488 and 555 nm. Laser intensity and gain was set appropriately to achieve optimal signal intensity whilst avoiding saturation or bleaching, and these settings were kept the same between experimental replicates. Images were analysed with MATLAB.

Table 5.4. Antibodies used for immunofluorescence experiments.

Antibody	Manufacturer Product code	Primary Ab. conc.	Secondary antibody
H3K9ac Rb mAb	Cell Signalling Tech. #C5B11	1:300	1:1,000 Alexa Fluor Plus 488 conjugated α-Rb IgG (Invitrogen, #A32731)
H3K27ac Rb mAb	Cell Signalling Tech. #D5E4	1:100	1:1,000 Alexa Fluor Plus 488 conjugated α-Rb IgG (Invitrogen, #A32731)
H3 Ms mAb	Cell Signalling Tech. #1B1B2	1:300	1:1,000 Alexa Fluor Plus 555 conjugated α-Ms IgG (Invitrogen, #A32727)
Vimentin Ck pAb	Abcam #ab24525	1:300	1:500 Alexa Fluor 405 conjugated α-Ck IgY (Abcam, #ab175675)
* Hoechst-33342	Invitrogen #H3570	1:1,000	-

*Hoescht is a nucleic acid stain, prepared at 1:1,000 in PBS (for 2 mins). All antibodies were prepared in PBS with 3% BSA. Ck, chicken; pAb, polyclonal antibody; Rb, rabbit; mAb, monoclonal antibody; Ms, mouse.

5.3 Results

5.3.1 Effect of propionate application *in vitro* on cardiac gene expression

To determine the effect of propionate on cardiac gene expression, transcriptomic profiling was performed by poly(A)+ RNA-sequencing (RNA-seq) of wild-type NRVMs treated for 24 hrs in propionate or butyrate (positive control for HDAC inhibition). Propionate and butyrate were found to have a profound effect on gene expression, with genes being differentially expressed commonly by both groups, or uniquely by one group.

Principle component analysis. Principle component analysis (PCA) is a mathematical method to reduce the dimensionality of complex data into a small number of variables, known as principle components (PCs), along which the variation in data is maximal (Ringnér, 2008). In doing so, it allows the experimenter to determine the greatest source of variability between samples. The PCA plot for the samples is shown in Figure 5.1. The PCA showed three distinct clusters, with each cluster representing the individual treatment groups: *control*, *6 mM propionate* and *6 mM butyrate.* The greatest source of variation was PC 1 (89% variance), which mainly represents the three treatment groups and their efficacy. However, *propionate* was not exactly in the midpoint between *control* and *butyrate*, suggesting there's a component of difference that may relate to propionate-specific actions not phenocopied by butyrate. Variance was little in PC 2 (7%) indicating there was minimal variation between biological replicates and demonstrating that the transcriptional profile was consistent for each treatment group.

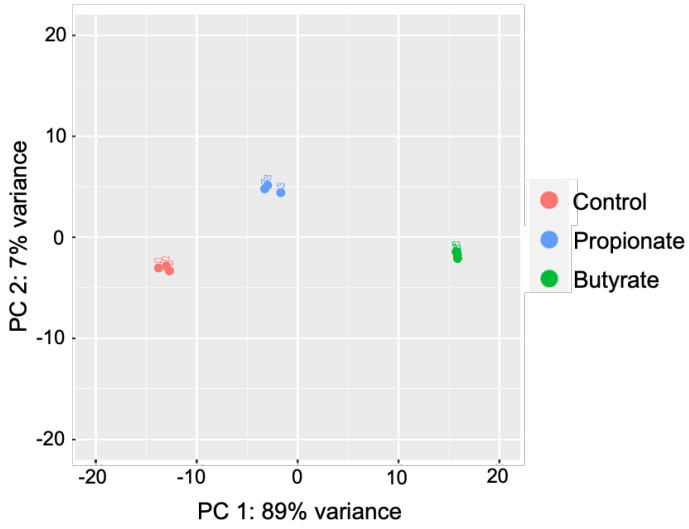


Figure 5.1. Principle component analysis of RNA-seq in NRVMs treated with propionate or butyrate *in vitro*. PC, principle component. *N* = 3 litters per group.

Heat map and DEG analysis. In propionate-treated cells, analysis for differentially expressed genes (DEGs) using DESeq2 found 2,776 DEGs which had an adjusted *P*-value < 0.05. A heat map visualising the differential expression across samples, relative to propionate, is shown in Figure 5.2a. Of the 2,776 DEGs in propionate, 1,363 (~49%) were upregulated whilst 1,413 (~51%) were downregulated (Figure 5.2b). Interestingly, there were DEGs that were common to both propionate and butyrate, and some DEGs that were uniquely changed in propionate only, or butyrate only. A linear regression performed on all the propionate-evoked DEGs (for their fold-changes in propionate versus butyrate) found that the majority of DEGs were co-ordinately upregulated in propionate and butyrate, giving a slope of correlation of 0.771, suggesting that the dose of propionate used had ~77% efficacy of that of butyrate (Figure 5.2c). Furthermore, the correlation was such that, for a gene that was co-ordinately differentially expressed between these groups, the effect of butyrate on fold-change was approximately double that of propionate (Figure 5.2c).

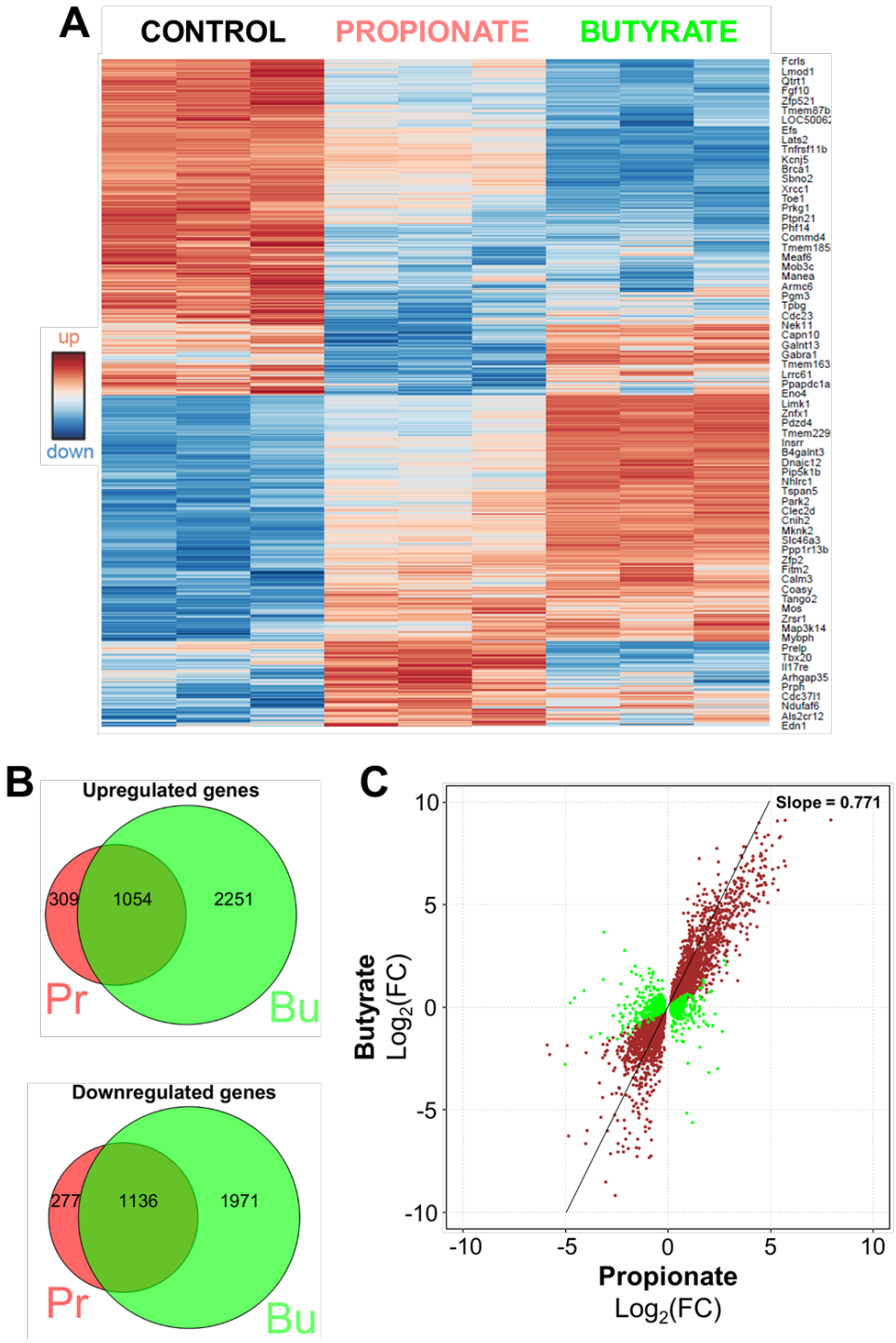


Figure 5.2. Analysis of differentially expressed genes (DEGs) determined by RNA-seq. Sequencing was performed on RNA extracted from NRVMs treated for 24 hrs in propionate or butyrate. ***(A)*** Heat map for DEGs in propionate-treated cells. ***(B)*** Venn diagram of upregulated and downregulated DEGs in propionate (Pr) or butyrate (Bu). The number of common differentially expressed genes are shown at the intersection. ***(C)*** Correlation of propionate-evoked DEGs for their log_2 fold-changes (FC) in propionate versus butyrate.

Volcano plots and DEGs. To better visualise the genes that were most significantly affected commonly by propionate and butyrate treatment, DEGs were plotted for fold-change vs adjusted probability in enhanced volcano plots (Figures 5.3 and 5.4). The volcano plot for propionate-evoked DEGs is shown in Figure 5.3a, with histograms produced for three highly significant DEGs, selected from the ten most significant DEGs (Figure 5.3b). Some prominent DEGs from the volcano plot included *Top2a* (DNA topoisomerase II alpha), *Smc2* (structural maintenance of chromosomes protein 2; also known as chromosome-associated protein E, CAP-E) and *Myh1* (myosin heavy chain 1) (Figure 5.3a). Genes involved in E-C coupling were also changed, for example *Cacnb1* (calcium voltage-gated channel auxiliary subunit β1) (Figure 5.3b).

The volcano plot for butyrate-evoked DEGs is shown in Figure 5.4a, with histograms for three genes selected from the top ten most significant DEGs (Figure 5.4b). There were DEGs that were significantly affected only in butyrate, e.g. *Pdgfrb* (platelet-derived growth factor receptor β), as well as DEGs affected both by propionate and butyrate treatment, including *Smc2* and *Mmp23* (matrix metalloproteinase 23) (Figure 5.4b). These results demonstrate that propionate can affect gene expression both by mechanisms that are common with butyrate (canonical mechanism of HDAC inhibition) and unique to itself (non-canonical mechanisms).

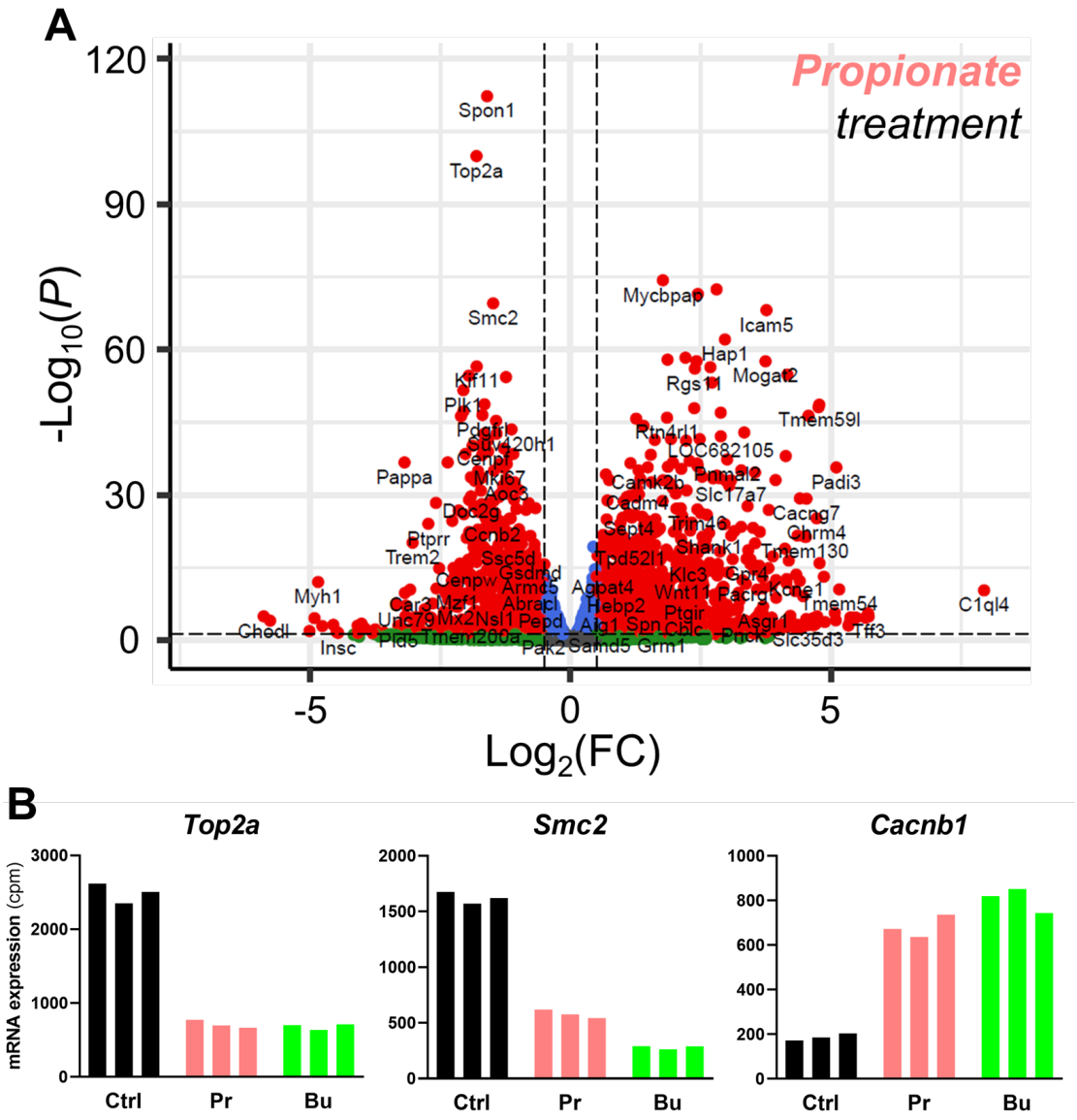


Figure 5.3. Genes differentially expressed in NRVMs by propionate treatment *in vitro*. *(A)* Enhanced volcano plot with $\log_2$ fold-change (FC) against $\log_{10}$ adjusted probability value (*P*). Grey dots, not significant; green dots, significant $\log_2$(FC) only (cut-off ± 0.1); blue dots, significant adjusted *P*-value only (cut-off $P \leq 0.05$); red dots, significant $\log_2$(FC) and adjusted *P*-value. *(B)* Histograms for three selected highly significant DEGs in propionate, shown as mRNA expression in counts per million (cpm).

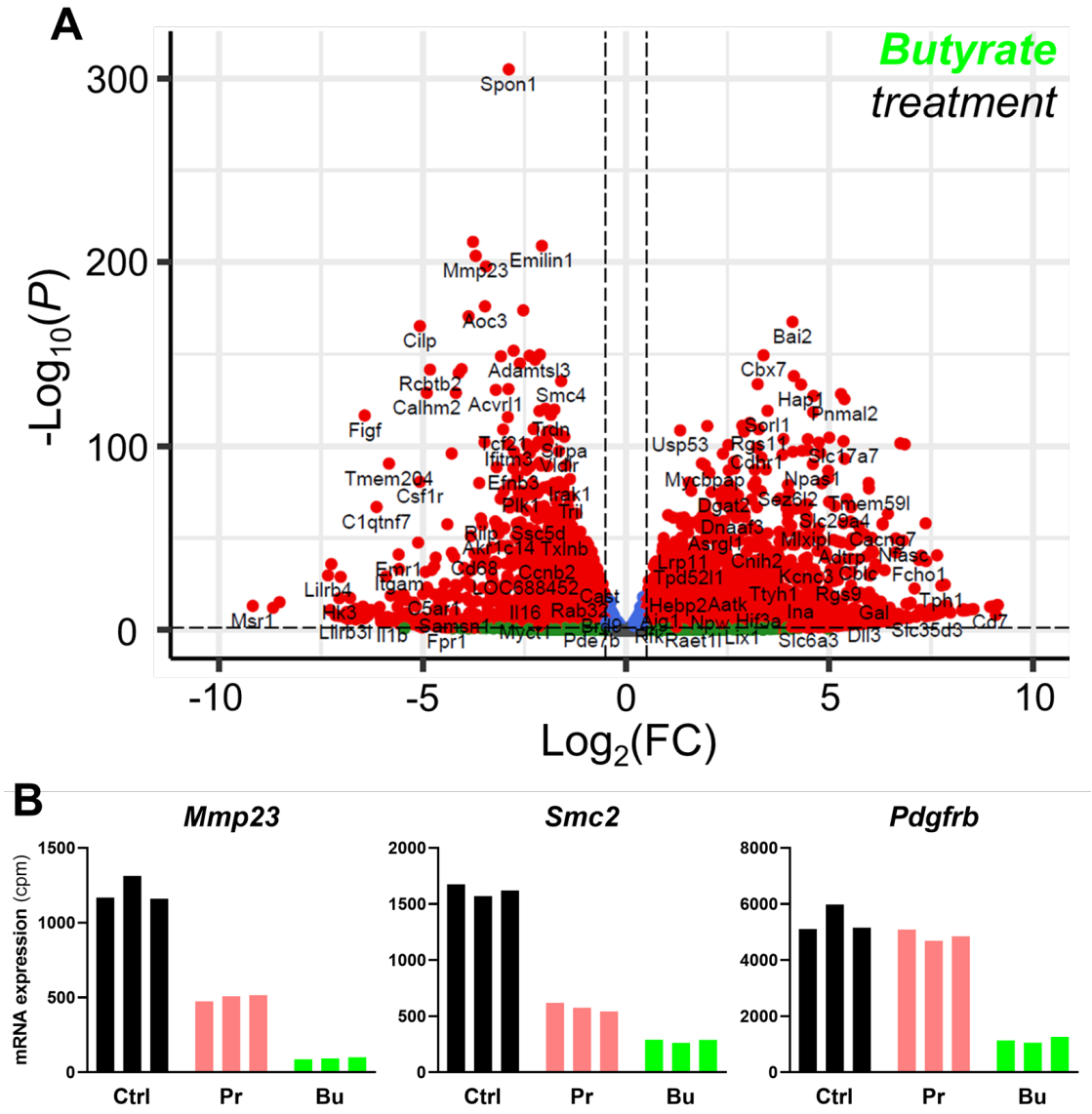


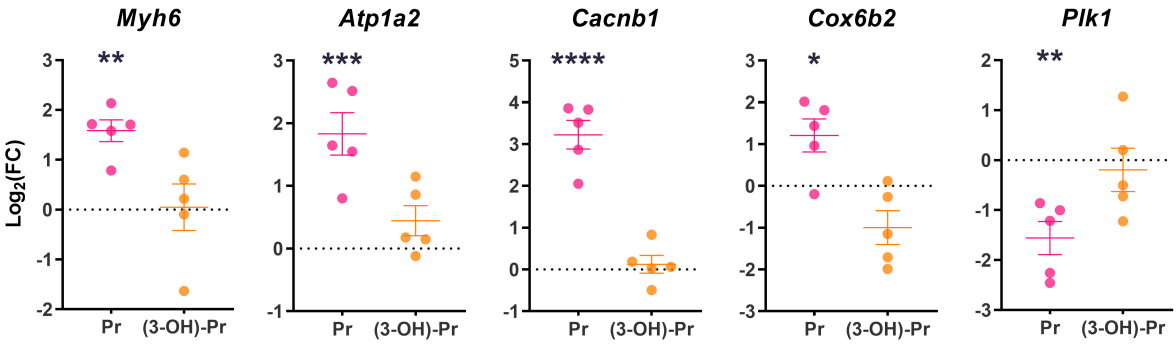
Figure 5.4. Genes differentially expressed in NRVMs by butyrate treatment *in vitro*. *(A)* Enhanced volcano plot with $\log_2$ fold-change (FC) against $\log_{10}$ adjusted probability value (*P*). Grey dots, not significant; green dots, significant $\log_2$(FC) only (cut-off ± 0.1); blue dots, significant adjusted *P*-value only (cut-off $P \leq 0.05$); red dots, significant $\log_2$(FC) and adjusted *P*-value. *(B)* Histograms for three selected highly significant DEGs in butyrate, shown as mRNA expression in counts per million (cpm).

Pathway analysis and validation of selected DEGs. The DEGs that were changed only in butyrate were not prioritised for current analysis. Only propionate-evoked DEGs were considered for interpretation, whether they were differentially expressed in propionate alone (non-canonical mechanisms), or differentially expressed by both propionate and butyrate treatment (canonical mechanism). The propionate-evoked DEGs were data-mined and put through gene-enrichment and functional annotation analysis using the database for annotation, visualization and integrated discovery (DAVID) bioinformatics resource (Huang *et al.*, 2009).

The aim of DAVID (and other bioinformatic tools) is to systemically map a large set of genes into lists of the associated biological annotation (e.g. gene ontology terms), and to then highlight the statistically overrepresented (enriched) biological annotations (Huang *et al.*, 2009). The analysis revealed several KEGG (Kyoto Encyclopedia of Genes and Genomes) pathways of interest as being enriched in propionate, including '*cardiac muscle contraction*' and '*MAPK signalling*'. The genes encoding some of the key Ca^{2+} handling proteins, such as *Cacna1c* (LTCC), *Ryr2* (RyR), *Atp2a2* (SERCA), *Pln* (PLN) and *Slc8a1* (NCX), were not affected by propionate.

To validate some of the hits from the RNA-seq, a selection of the DEGs involved in these pathways were confirmed by RT-qPCR: *Myh6* (myosin heavy chain 6), *Atp1a2* (α2-subunit of Na^{+}/K^{+}-ATPase), *Cacnb1* (β1-subunit of voltage-gated Ca^{2+} channel), *Cox6b2* (β2-subunit of cytochrome C oxidase) and *Plk1* (polo-like kinase 1) (Figure 5.5). In this experiment, NRVMs were either treated in 6 mM propionate or 6 mM 3-hydroxypropionate (3-OH-Pr), the hydroxylated derivative of propionate which is also commonly detected in PA patients. Due to

its chemical dissimilarity to propionate, it was expected for the hydroxylated form to be epigenetically inactive and serve as a negative control. Whilst all tested genes were differentially expressed by propionate, 3-OH-Pr had no effect on their expression levels (Figure 5.5).



Gene	*Myh6*	*Atp1a2*	*Cacnb1*	*Cox6b2*	*Plk1*
Name	Myosin heavy chain 6	Na^+/K^+-ATPase α2-subunit	Voltage-gated Ca^{2+} channel β1-subunit	Cytochrome C oxidase 6 β2-subunit	Polo-like kinase 1
RNA-seq log_2(FC)	0.96	1.12	3.69	1.64	-2.04
KEGG pathway	Cardiac muscle contraction				Cell cycle

Figure 5.5. Validation of DEGs by RT-qPCR. ***(Top)*** NRVMs were treated for 24 hrs in 6 mM propionate (Pr) or 6 mM 3-hydroxypropionate (3-OH-Pr). Data are $log_2(\Delta\Delta Ct)$ values normalised to *Hprt1* shown as the mean ± SEM. *N* = 5 litters; * $P \leq 0.05$, ** $P \leq 0.01$, *** $P \leq 0.001$, **** $P \leq 0.0001$ on one-way ANOVA. ***(Bottom)*** Table of the DEGs selected for validation with their fold-change (FC) from the RNA-seq and their associated KEGG pathway.

Histone mark enrichment analysis. Thus far, the RNA-seq in NRVMs showed that a major mechanism by which propionate affects gene expression was through a mechanism similar to butyrate. Short-chain fatty acids produced by the microbiome are known to inhibit HDACs (Waldecker *et al.*, 2008). Thus, to determine whether a change in histone marks may be implicated in propionate-evoked differential expression of genes, the list of DEGs were

compared to the gene enrichment dataset EnrichR (Kuleshov *et al.*, 2016). This analysis predicted two histone marks, associated with transcriptionally-active chromatin, as being associated with the propionate-sensitive DEGs: histone 3 lysine 9 acetylation (H3K9ac) and histone 3 lysine 27 acetylation (H3K27ac). Therefore, experiments were next performed to investigate whether these histone marks occur in response to propionate. Indeed, there were DEGs that were affected *only* by propionate. A possible mechanism for this could be histone propionylation, where propionyl-CoA is used as a substrate by HATs, instead of acetyl-CoA (like for acetylation) (Chen *et al.*, 2007). Therefore, the possibility of histone propionylation was also investigated in the experiments shown next.

5.3.2 Effect of propionate application *in vitro* on cardiomyocyte histone acetylation and propionylation

Since the DEGs from the RNA-seq in propionate-treated myocytes were predicted to be associated with histone 3 lysine 9 and histone 3 lysine 27 acetylation (H3K9ac, H3K27ac), the following experiments aimed to determine whether these histone marks occur in cardiomyocytes in response to propionate. Furthermore, the experiments sought to determine whether there was any possible change in histone lysine propionylation (Kpr).

Histone extracts were prepared from NRVMs treated for 24 hrs in propionate or butyrate (3 mM, pH 7.4) and subjected to western blotting (Figure 5.6). H3K9ac (normalised to total H3) was found to be increased by both propionate and butyrate, although a stronger acetylation response was evoked by butyrate. As expected, histone Kpr probed with a pan-propionyllysine

antibody, was mainly found to occur due to propionate treatment. Interestingly, bands were detected at ~17 kDa and ~11 kDa, corresponding to the molecular weights of H3 and H4 respectively. Kpr, normalised to total H3, was significantly increased by propionate treatment (Figure 5.6b).

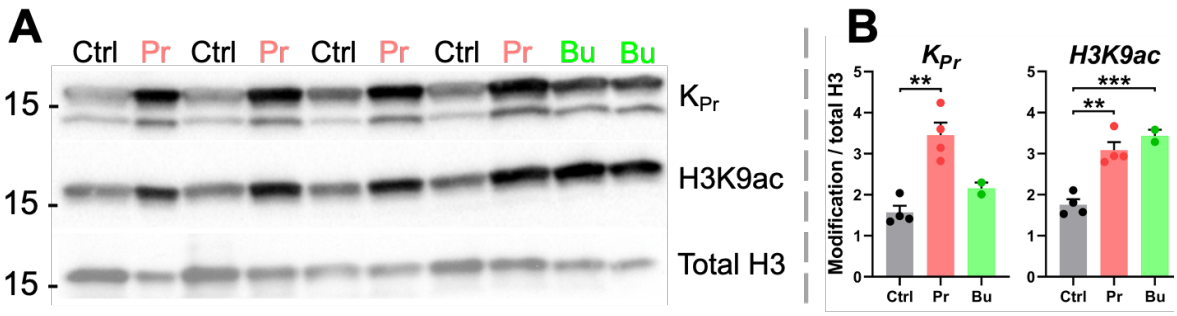


Figure 5.6. Western blotting for lysine propionylation and H3K9ac in histones extracted from NRVMs treated with propionate *in vitro*. Immunoblotting was performed for lysine propionylation (Kpr) and histone 3 lysine 9 acetylation (H3K9ac). Cells were treated under 3 conditions for 24 hrs at pH 7.4: *control*, *3 mM propionate* (Pr), *3 mM butyrate* (Bu). ***(A)*** Representative blot. ***(B)*** Summary histograms for total band volume of the modification (Kpr, H3K9ac) normalised to band volume of total H3. Note, for Kpr, the top band was quantified. Data shown as mean ± SEM; *n* = 4 litters for *control* and *propionate*; n = 2 litters for *butyrate.* ** $P \leq 0.01$ and *** $P \leq 0.001$ on one-way ANOVA with Dunnett's post-hoc test.

5.3.3 Concentration-dependence of propionate-evoked histone acetylation *in vitro*

The western blotting experiment provided evidence for H3K9ac and histone Kpr increasing in response to propionate *in vitro*. However, it would be important to determine whether there is an activation threshold for the histone marks to increase. Furthermore, the concentration of propionate is not 'static' *in vivo*, but rather changes dynamically, according to dietary intake and endogenous metabolism levels. Therefore, an ELISA was also performed for histone marks, which is more quantitative versus western blotting. Whole-cell ELISA for H3K9ac was

performed in NRVMs treated for 24 hrs within a range of propionate concentrations relevant to PA patients. Propionate-evoked H3K9ac was found to be concentration-dependent with an approximate EC_{50} of 0.62 mM (Figure 5.7a). Interestingly, fluoroacetate, a weed-killer compound known to cause PA-like cardiotoxicity and a structural mimetic of propionate (Goncharov *et al.*, 2006), had no effect on H3K9ac (Figure 5.7b).

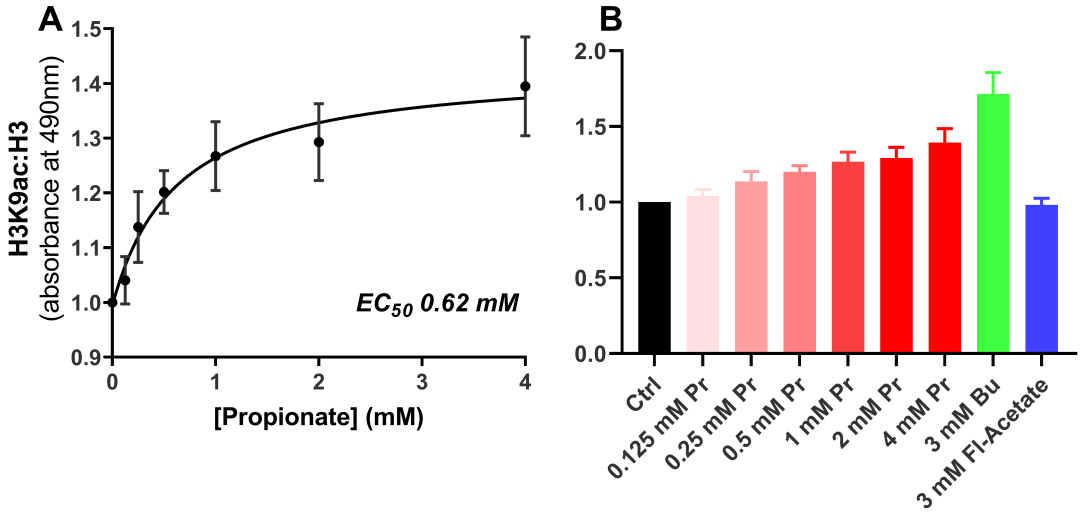


Figure 5.7. Whole-cell ELISA for H3K9ac in NRVMs treated for 24 hrs over a range of propionate concentrations. NRVMs were treated under eight conditions, all at pH 7.4: *control*; 0.125-4 mM propionate (*0.125-4 mM Pr*); 3 mM butyrate (*3 mM Bu*); 3 mM fluoroacetate (*3 mM Fl-Acetate*). Ratios presented were absorbance at 490nm for H3K9ac relative to H3 (H3K9ac:H3) per condition, normalised to the control group. ***(A)*** Data fitted to three-parameter Hill function giving a best-fit EC_{50} of 0.62 mM Pr (R^2 = 0.481). ***(B)*** Summary data for each treatment condition. Data shown as mean ± SEM from 6 litters, with 4 technical replicates per condition per litter.

5.3.4 Propionate induces a consistent spatial pattern of nuclear H3K9ac and H3K27ac

Thus far, data have been presented for H3K9ac (and histone Kpr) being induced by propionate. However, it was unclear whether there may be any functional consequence of these histone marks. It is known that nuclear organisation is not random, and that transcriptionally active chromatin is highly organised within the nucleus (van Steensel & Furlong, 2019). Thus, to begin investigating whether the propionate-evoked histone acetylation may have any functional consequence, immunofluorescence was performed in fixed cardiomyocytes to determine whether the acetylation occurs in an organised manner.

This experiment was performed in two models: NRVMs treated for 24 hrs (as with previous experiments), but also in ARVMs treated for a shorter period determined empirically (4 hrs). Since PA patients frequently decompensate and experience spikes in propionate-load (Chapman *et al.*, 2012; Baumgartner *et al.*, 2014), the rationale for the shorter treatment period in ARVMs was test whether 'acute' propionate loads could also evoke histone marks. Immunofluorescence images were taken by confocal microscopy and analysed in MATLAB as histone modification normalised to total histone (H3K9ac:H3 and H3K27ac:H3) (Figure 5.8a/b). The data were analysed in two ways: (1) total fluorescence intensity averaged over the entire nucleus ('global' signal); (2) fluorescence intensity quantified radially inwards, every 100 nm, relative to the nuclear outline ('spatial' signal) (Figure 5.8c/d).

Both H3K9ac and H3K27ac were significantly increased in response to propionate, irrespective of treatment duration (4 or 24 hrs) and developmental stage (adult or neonatal myocytes) (Figure 5.8c/d). Butyrate treatment was performed as a positive control for HDAC inhibition. Interestingly, the induction of H3K9ac/H3K27ac was spatially consistent. That is, in adult myocytes, the acetylation was consistently induced toward the core of the nucleus (Figure 5.8 c1/d1), whilst in neonatal myocytes the acetylation was induced toward the nuclear periphery (Figure 5.8 c2/d2). These results suggest that propionate-evoked H3K9ac/H3K27ac are unlikely to be an epiphenomenon, but rather to have some functional meaning.

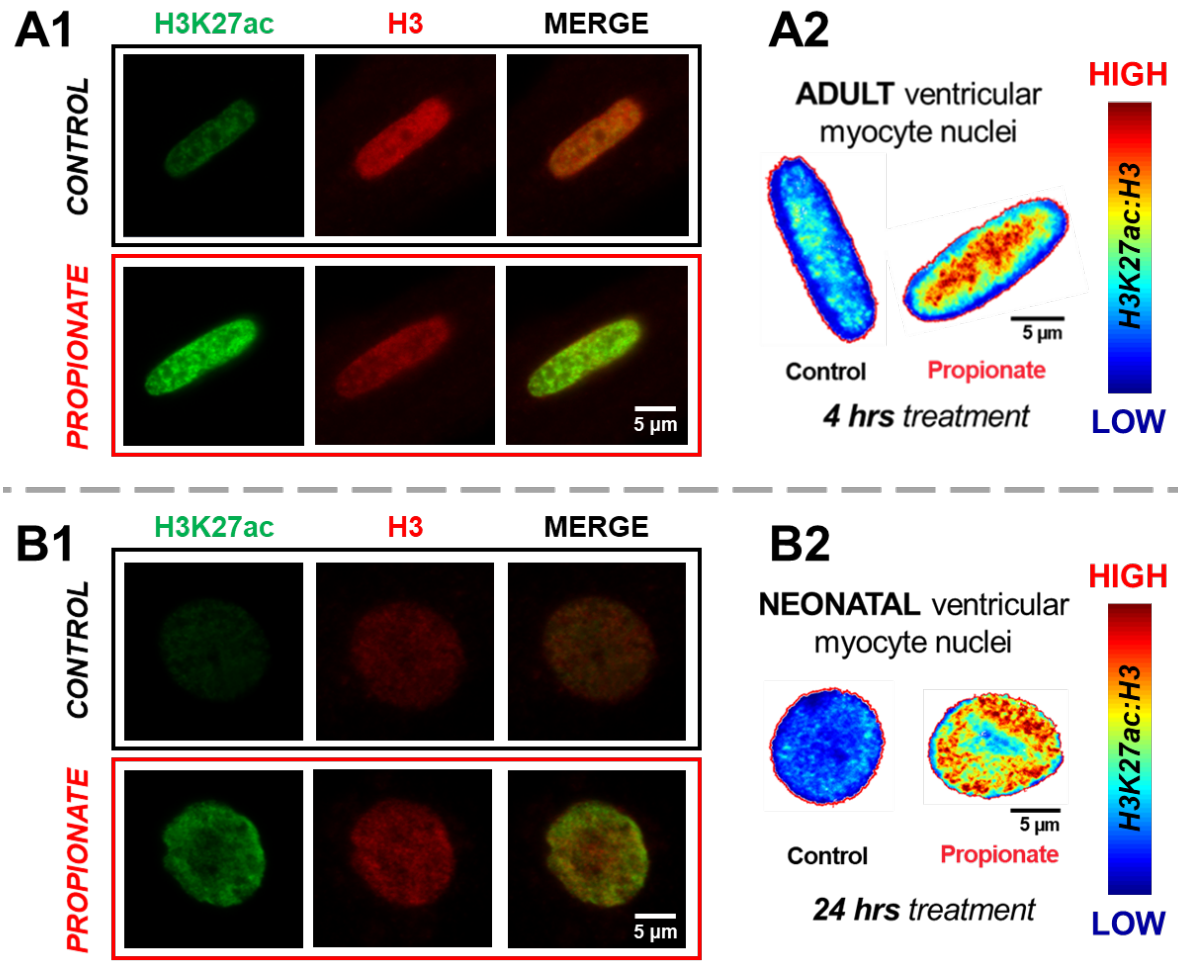


Figure 5.8. Immunofluorescence for H3K9ac and H3K27ac in the nuclei of adult and neonatal rat ventricular myocytes treated with propionate *in vitro*. Confocal imaging of methanol-fixed myocytes treated under three experimental groups at pH 7.4: *control*; 4.7 mM propionate (*Pr*); 4.7 mM butyrate (*Bu*). Adult and neonatal myocytes were treated for 4 and 24 hrs respectively. ***(A1)*** Representative immunofluorescence images of H3K27ac and H3 in adult myocyte nuclei from *control* and *propionate* groups. ***(A2)*** Exemplar MATLAB render of nuclei H3K27ac fluorescence normalised to H3 fluorescence (H3K27ac:H3), with signal intensity shown on a colour scale (blue, low; red, high). ***(B1)*** Representative immunofluorescence images of H3K27ac and H3 in neonatal myocyte nuclei from *control* and *propionate* groups. ***(B2)*** Exemplar MATLAB render of nuclei. ***(C, overleaf)*** Summary data for H3K9ac in ***(C1)*** adult and ***(C2)*** neonatal myocytes. Data shown as the average H3K9ac:H3 signal over the entire nucleus *(left)* and H3K9ac:H3 ratio plotted against distance from the nuclear outline (µm) *(right)*. ***(D, overleaf)*** Same experiment but for H3K27ac in ***(D1)*** adult and ***(D2)*** neonatal myocytes. Data shown as mean ± SEM. Adult myocytes, n = 80 nuclei (40 cells) from 4 animals per group, for each antibody. Neonatal myocytes, n = 80 nuclei (80 cells) from 4 litters per group, for each antibody. ** $P \leq 0.01$, *** $P \leq 0.001$ and **** $P \leq 0.0001$ on hierarchical statistical analysis and pairwise comparisons with Bonferroni correction.

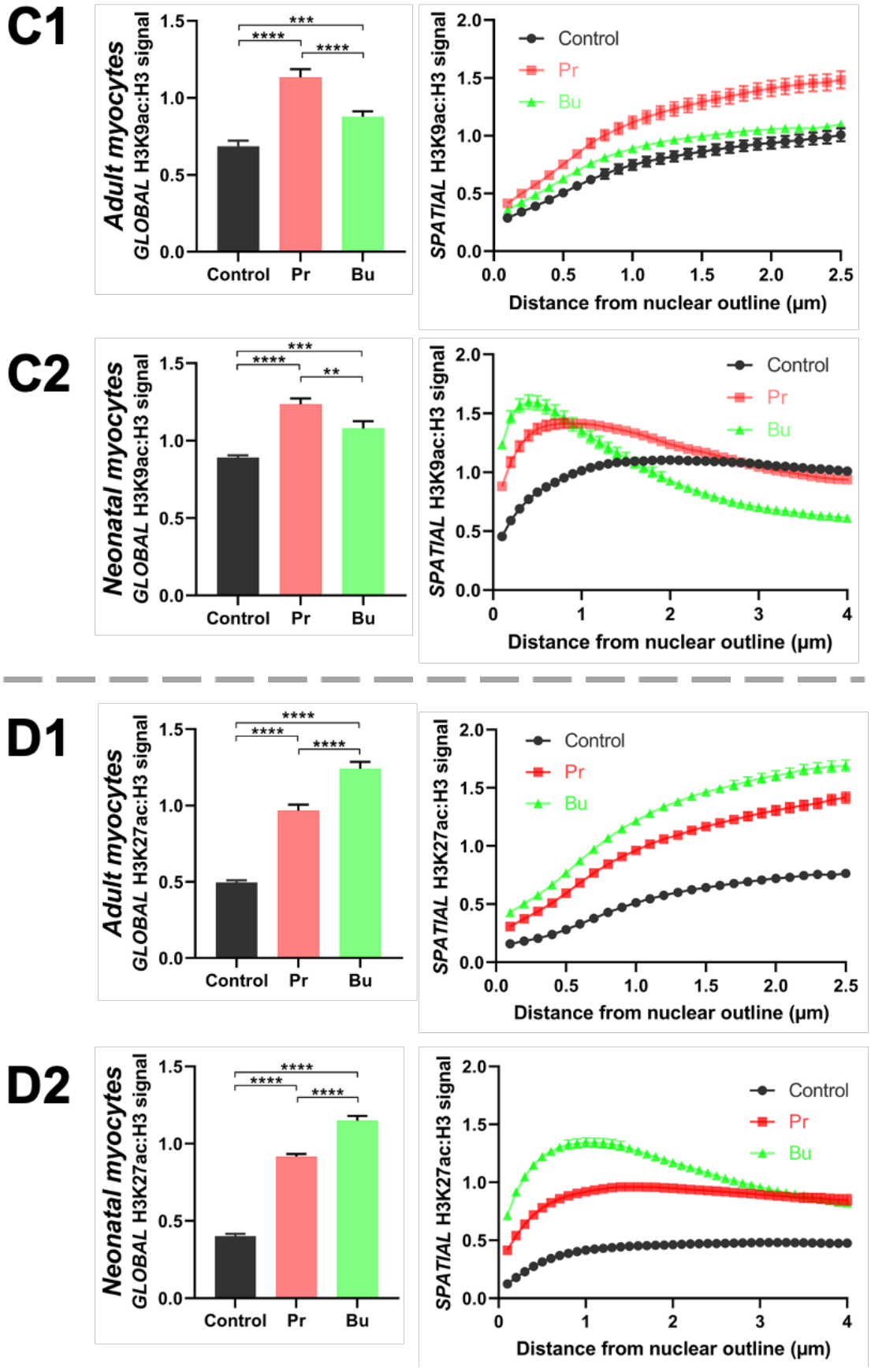


Figure 5.8 continued. Summary data for H3K9ac/H3K27ac. See previous page for legend.

5.3.5 Effect of PCC disruption on cardiac histone propionylation and H3K9ac

Collectively, the results from the experiments thus far demonstrated that the application of propionate to cardiomyocytes *in vitro* results in a large remodelling of the transcriptome, evokes histone modifications in a dose-dependent manner, which in the nucleus occurs in a regular spatial pattern. Whilst these *in vitro* experiments were important in characterising the functional properties of propionate, they do not fully recapitulate the *in vivo* metabolic milieu. Therefore, the remaining experiments in this Chapter were performed in hearts from the PA mouse model (*Pcca*$^{-/-}$ A138T; amPA).

Histone extracts were prepared from the hearts of 8-week-old amPA and amWT animals and subjected to western blotting (Figure 5.9). In contrast to the afore presented *in vitro* data, there was no resolvable difference in H3K9ac. The blot for Kpr was indicative of increased histone propionylation at H3 and H4 (9-sec and 45-sec exposure, respectively). However, the propionylation response was indeed modest and not as pronounced as the *in vitro* experiments.

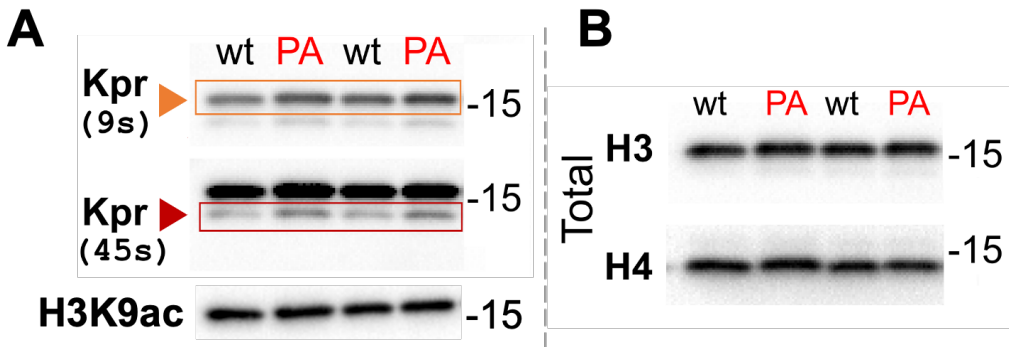


Figure 5.9. Western blotting for lysine propionylation and H3K9ac in cardiac histones extracted from 8-week-old mice. Histones were extracted from adult PA mice ('PA') and their wild-type litters ('wt'). ***(A)*** Representative blots of lysine propionylation (Kpr) and H3K9ac. Note, two exposure times for the Kpr blot is shown (9 seconds and 45 seconds). ***(B)*** Representative blots of total H3 and total H4, stripped and re-probed from the Kpr and H3K9ac blots, respectively. *n* = 3 hearts of mixed sexes per genotype.

5.3.6 Effect of PCC disruption on cardiac non-histone protein propionylation

Unlike the *in vitro* experiments, the induction of lysine propionylation was modest in cardiac histones from PA mice, and a change in H3K9ac was not resolvable by western blot. Indeed, there is considerable evidence for histone propionylation, including in the liver of *Pcca*$^{-/-}$ A138T mice (Kebede *et al.*, 2017). However, the possibility of Kpr of cytoplasmic proteins has not been addressed. Propionylation occurs by the promiscuity of KATs, and since these enzymes have been shown to acetylate cytoplasmic proteins in the heart (Foster *et al.*, 2013), it is plausible that KATs could mediate cytoplasmic propionylation. To test this, western blotting was performed using the same pan-propionyllysine antibody but on total RIPA lysates from the hearts of PA mice.

Figure 5.10 shows a representative blot for lysine propionylation in cardiac lysates from amPA and amWT mice. Interestingly, the blot was indicative of increased propionylation of cytoplasmic proteins in the heart. Coomassie Blue staining of the membrane indicated no overt differences in loaded protein concentration. There were two dominant bands detected at ~55 and ~70 kDa, although, the identity of these proteins was unclear and there was no striking difference in their level of propionylation. However, propionylation was more apparent in smaller proteins ~20-50 kDa with a longer exposure time (250 secs; Figure 5.10). Although, like histone Kpr *in vivo*, the apparent increase in propionylation of cytoplasmic proteins was modest

in PA mice. An interesting observation was that the level of propionylation was not consistent between animals and variation was apparent even between mice of the same sex and genotype.

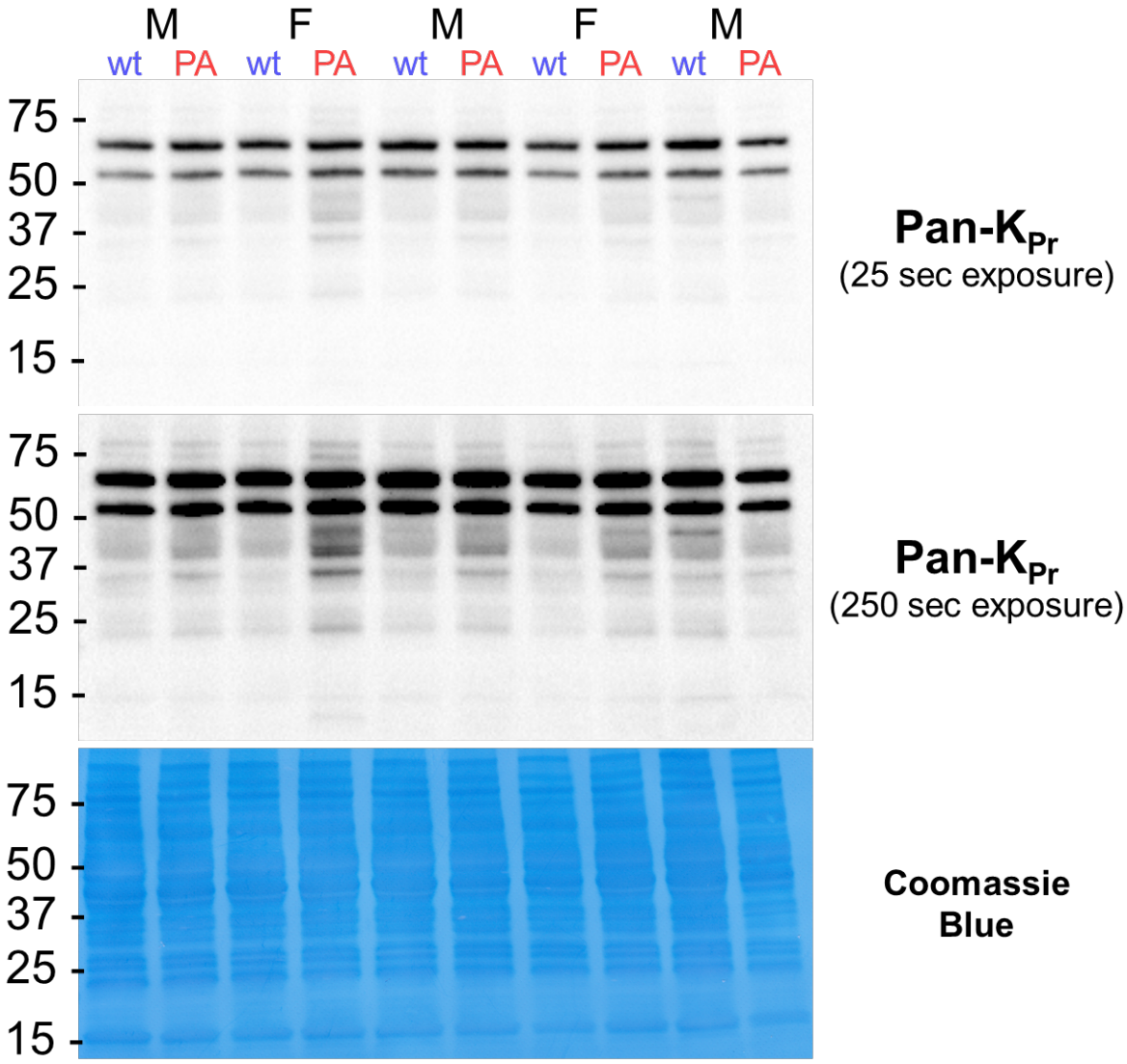


Figure 5.10. Western blotting for lysine propionylation in total RIPA lysates from 8-week-old mouse hearts. Ventricular lysates were prepared from adult PA mice ('PA') and their wild-type litters ('wt'). Shown, representative blot, probed for lysine propionylation (Kpr) with a pan-propionyllysine antibody. The developments shown are for the same membrane at 25 secs and 250 secs exposure. Note, the dominant bands at ~55 and ~70 kDa were fully saturated at 250 secs exposure. Coomassie Blue staining of the membrane was used to determine any variability in protein loading. Shown, *n* = 3 hearts per genotype for males and *n* = 2 hearts per genotype for females.

5.3.7 Effect of PCC disruption on cardiac gene expression

The western blots of PA mouse cardiac histones and lysates thus far indicated a modest increase in propionylation of histones and cytoplasmic proteins. Furthermore, no difference was resolvable by immunoblot in H3K9ac. However, given that these mice have a predominantly mild PA phenotype (Guenzel *et al.*, 2013), these results were not entirely surprising. There was sufficient evidence to suggest that a change in cardiac gene expression was occurring in amPA and that a more sensitive method was required to detect these changes. Therefore, RNA-seq was performed in ventricular tissue for a full sex-balanced cohort of amPA and amWT mice.

From the western blotting experiment for non-histone protein Kpr in the preceding section (Section 5.3.6), it was apparent that there was some variation in the captured level of propionylation between animals. Thus, to ensure consistency in the sequencing samples, hearts were screened by RIPA propionylation immunoblotting prior to downstream sequencing. The decision to use non-histone protein propionylation (Section 5.3.6) versus histone propionylation (Section 5.3.5) was due to the improved signal:noise ratio, as well as it being more amenable to medium-throughput sample preparation (RIPA lysis versus histone extraction).

Sample selection and quality control. A total of 40 hearts (snap-frozen ventricular tissue) were screened with immunoblot by quantifying the propionylation signal over the entire lane, normalised to the Coomassie Blue protein staining using ImageJ (*not shown*). Outliers were

excluded and total RNA was then extracted from a total of 24 hearts (6 per sex, per genotype). The quality of the extracted RNA was assessed by automated RNA electrophoresis (Bioanalyzer, Agilent) to determine the RNA Integrity Number (RIN), the standardised quality control method used to assess RNA quality (Figure 5.11). 5 hearts per sex and per genotype (20 total), were selected on the collective basis of the RIPA propionylation profile, RIN and A_{260}/A_{280} nm ratio, and subjected to poly-A(+) RNA-seq.

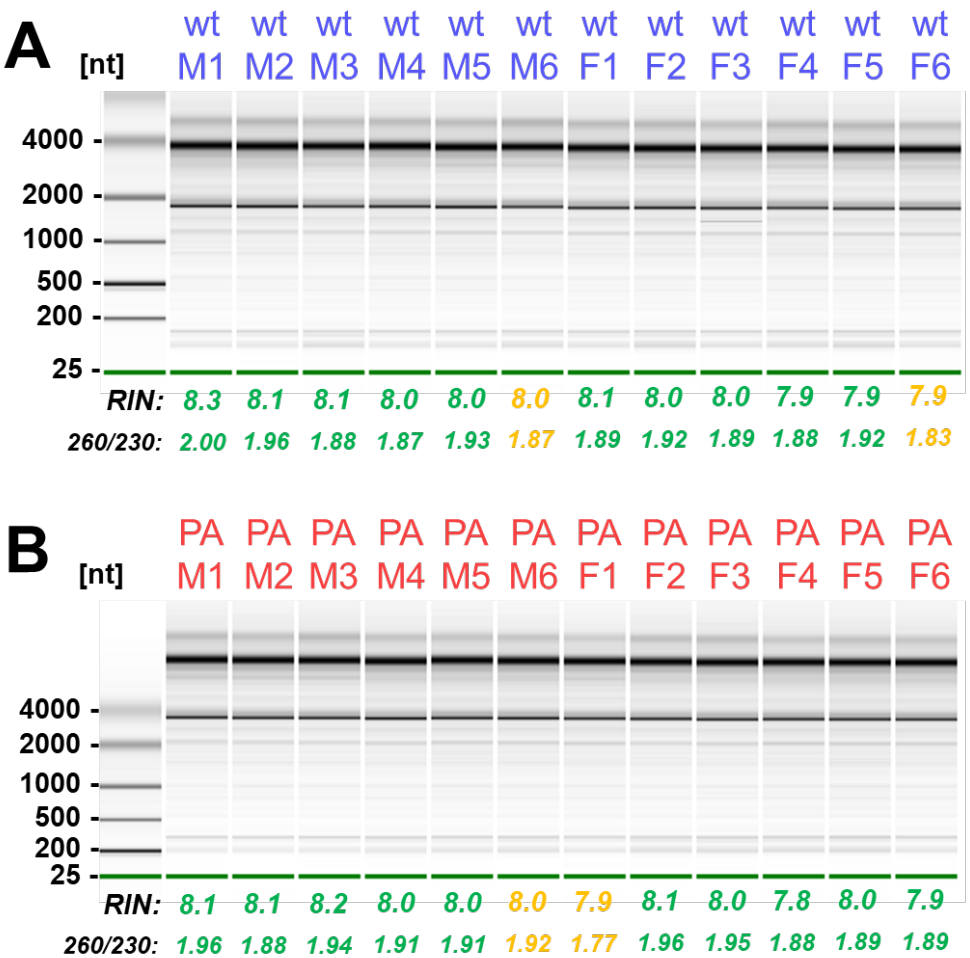


Figure 5.11. Converted Bioanalyzer electropherograms of total RNA samples extracted from 8-week-old mouse hearts. Sample were prepared from male ('M') and female ('F') adult PA mice ('PA') and their wild-type litters ('wt'). The computed RIN numbers, determined by the Bioanalyzer software algorithm, are shown for each sample. The A_{260}/A_{280} nm ratio is also shown, determined separately by spectrophotometry. Samples coloured in green indicates those taken forward for sequencing.

Principle Component Analysis. PCA was used to visualise variation between samples (Figure 5.12). The greatest source of variation was in fact due to sex, illustrated by the demarcation of male and female samples along PC 1 (40% variance). Along the other principle component (PC 2; 16%), samples from females were clustered by genotype (amPA vs amWT), demonstrating that the second greatest source of variation was genotype. However, the clustering of samples was less defined for male samples.

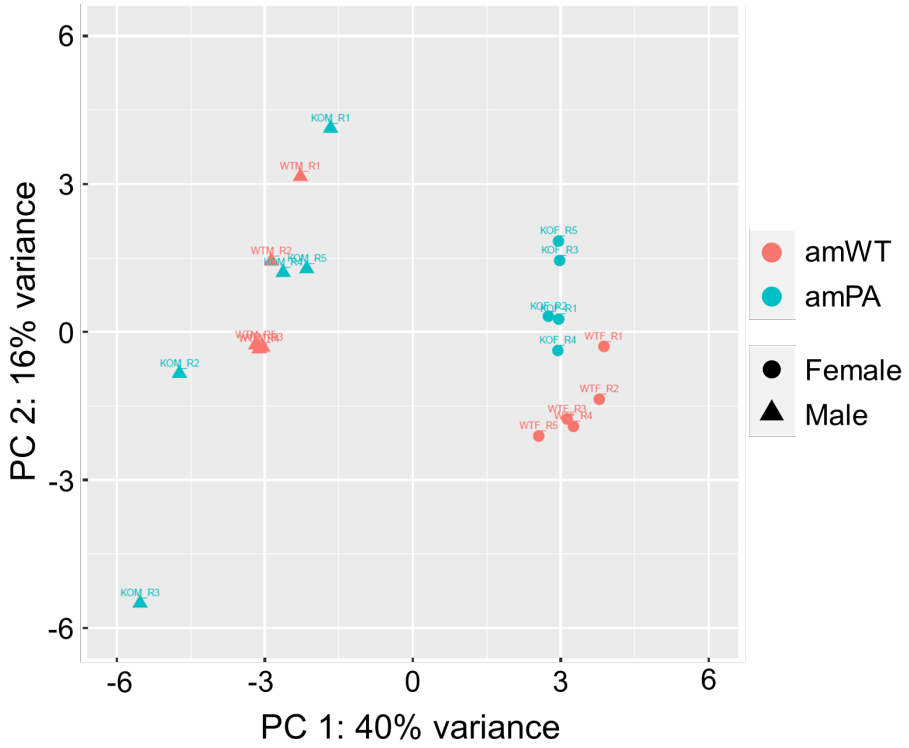


Figure 5.12. Principle component analysis of RNA-seq samples in 8-week-old mouse hearts. Samples were prepared from adult male and female PA (amPA) and wild-type (amWT) mouse hearts. PC, principle component. *N* = 5 hearts for each sex per genotype.

Heat map and DEG analysis. The analysis of the RNA-seq data for DEGs was conducted using the bioinformatic package DESeq2 as described for the RNA-seq in NRVMs (adjusted *P* value < 0.05) (Section 5.3.1). The heat maps of DEGs in females and males are shown in Figure 5.13.

The effect of sex was appreciable from the heat maps, with the differential expression of genes even differing within the same genotype (between males and females).

An important consideration when interpreting the amPA mouse RNA-seq data was that there are other known mechanisms that could contribute to cardiac dysfunction in PA. Indeed, another mechanism by which cardiac gene expression could be affected in PA is through dysregulated micro-RNAs, which has been demonstrated in a range of tissues in the PA mouse (Rivera-Barahona *et al.*, 2017b). Thus, to determine which DEGs *in vivo* were directly propionate-sensitive, the DEGs from the mouse model were analysed in conjunction with the DEGs from the RNA-seq in cardiomyocytes cultured in propionate *in vitro* (Section 5.3.1).

Venn diagrams were constructed showing the number of DEGs in amPA males and females, but also taking into account the DEGs that were commonly changed *in vitro* (Figure 5.14). The Venn diagrams were split by the mechanism by which propionate resulted in the differential expression of those genes *in vitro*. That is, Figure 5.14a shows the number DEGs in amPA that were also changed *in vitro* and commonly affected by both propionate *and* butyrate. Similarly, Figure 5.14b shows the number DEGs in amPA that were also changed *in vitro*, but genes that were *only* affected by propionate. Indeed, these Venn diagrams further illustrated the powerful effect of sex on gene expression, emphasised by the fact that there were more genes that were differentially expressed in females, versus males (Figure 5.14).

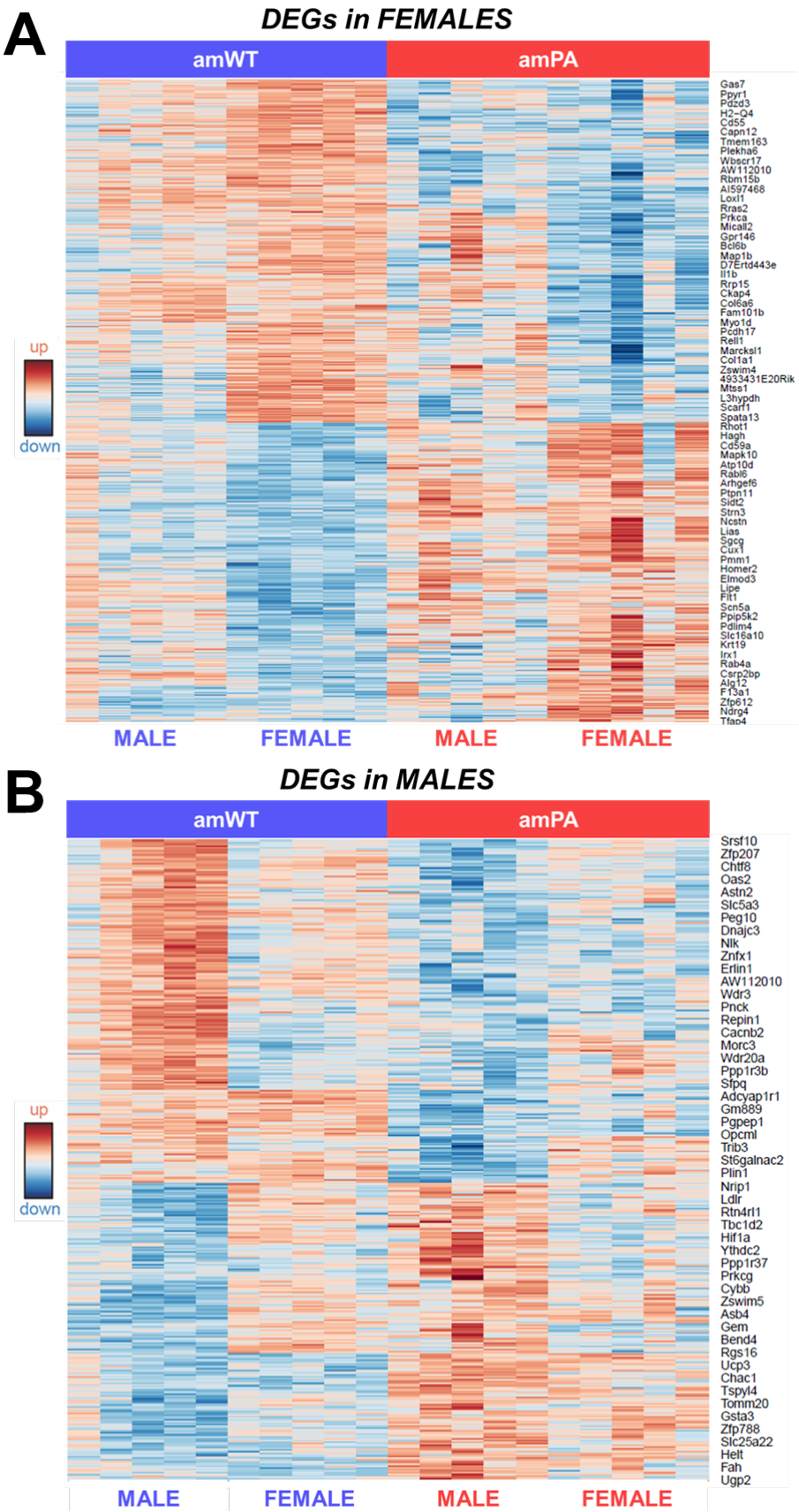


Figure 5.13. Heat map of DEGs in 8-week-old mouse hearts. ***(A)*** DEGs in females (female amPA vs female amWT). ***(B)*** DEGs in males (male amPA vs male amWT). *N = 5* hearts per sex and per genotype. Adult PA mice, amPA; adult WT mice, amWT.

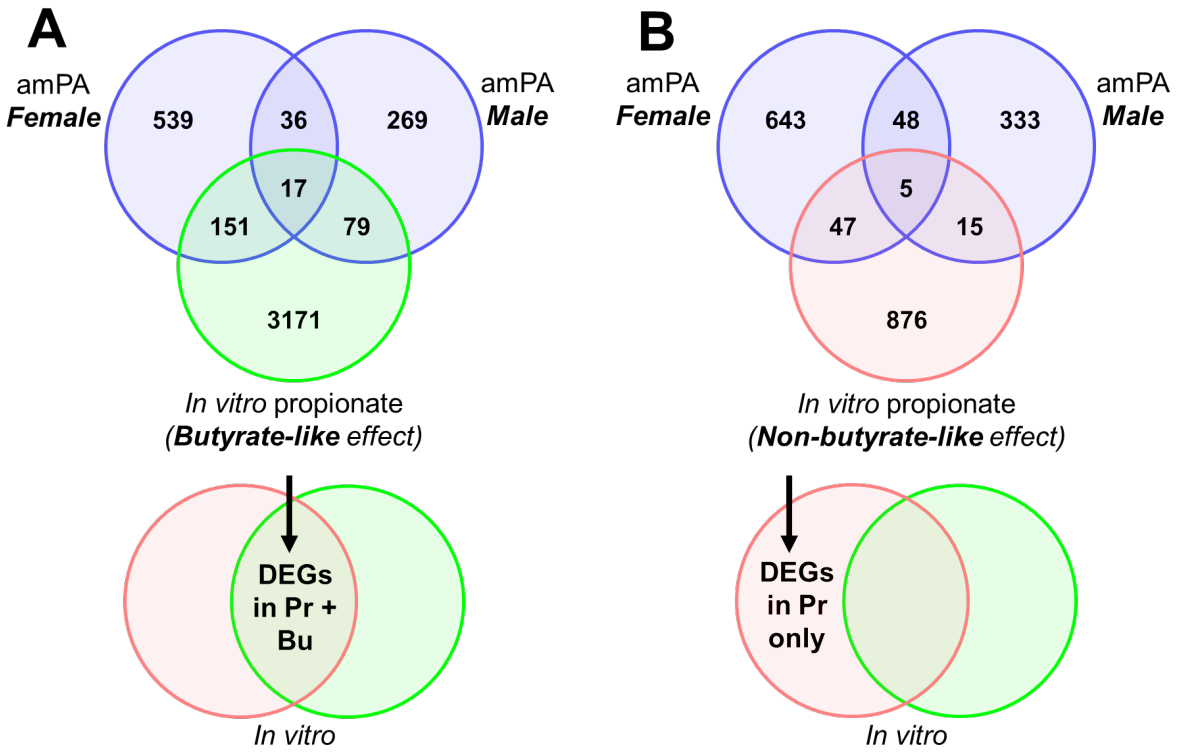


Figure 5.14. Venn diagram of the number of DEGs in amPA hearts and cardiomyocytes exposed to propionate *in vitro*. ***(A)*** Number of genes that were differentially expressed in both propionate- and butyrate-treated cells and changed *in vivo*. ***(B)*** Number of genes that were differentially expressed in propionate-treated cells and changed *in vivo*.

Enhanced volcano plots. To better visualise the genes that were most significantly affected by PA in females and males, these DEGs were also plotted for fold-change vs adjusted probability in enhanced volcano plots. Separate plots were generated for males and females, considering the different possible mechanisms from the *in vitro* experiments. In doing so, the total number of DEGs was reduced dramatically whilst highlighting genes of cardiac interest.

Every DEG in female and male amPA hearts is shown in Figure 5.15a/c. *Pde9a* (phosphodiesterase 9A) was the most significant DEG in females, after *Pcca*. Other DEGs that were very significantly changed in females included *Mettl21e* (protein-lysine methyltransferase-like 21e) and *Spp1* (secreted phosphoprotein 1). In males, the most significant DEG after *Pcca*

was *Banp* (BTG3 Associated Nuclear Protein). Those genes that were not affected by propionate (i.e. those not changed *in vitro*) are shown in Figure 5.15b/d for females and males respectively. Interestingly, several highly significant DEGs were not found *in vitro* (i.e. not propionate-sensitive), including *Mettl21e* and *Spp1* (females), and *Banp* (males).

Figure 5.16 shows the DEGs that were affected both *in vivo* (PCC disruption) and *in vitro* (propionate treatment), but those that were commonly changed with butyrate (canonical mechanism). In females, 168 genes were differentially expressed both *in vivo* and *in vitro* with a butyrate-like mechanism. From visual inspection of the plot, the most striking DEG was upregulated *Pde9a* (log_2FC +1.43; P = 2.01E-09). This was followed by *Mme* (membrane metalloendopeptidase) and *Gsta3* (glutathione S-transferase alpha 3) (Figure 5.16). In males, 96 genes were differentially expressed *in vivo* and butyrate-like *in vitro*, with some of the most significantly affected genes being *Angptl4* (angiopoietin-like 4) and *Zc3h6* (zinc finger CCCH domain-containing protein 6).

Interestingly, the number of genes that were differentially expressed *in vivo* and *in vitro* in propionate only (non-canonical mechanisms), was substantially smaller for both sexes. Other than *Pcca*, in females, significantly affected genes included *Adcyap1r1* (pituitary adenylate cyclase-activating polypeptide type I receptor) and *Dpy19l3* (probable C-mannosyltransferase DPY19L3), whereas *Ung* (uracil-DNA glycosylase) was changed in males (Figure 5.17).

Since the E-C coupling phenotype was seen only in cardiomyocytes from female mice (Chapter 4), DEGs of interest in cardiac physiology for females were selected and presented in Figure 5.18. Such DEGs included *Mme* (membrane metalloendopeptidase), a variety of adenylate cyclase isoforms (*Adcy3, Adcy7, Adcy9)*, *Trdn* (triadin), *Apln* (apelin) and *Plxnd1* (plexin D1).

Collectively, these results show that PCC disruption has a profound effect on cardiac gene expression, which appear to occur via mechanisms both dependent and independent of propionate.

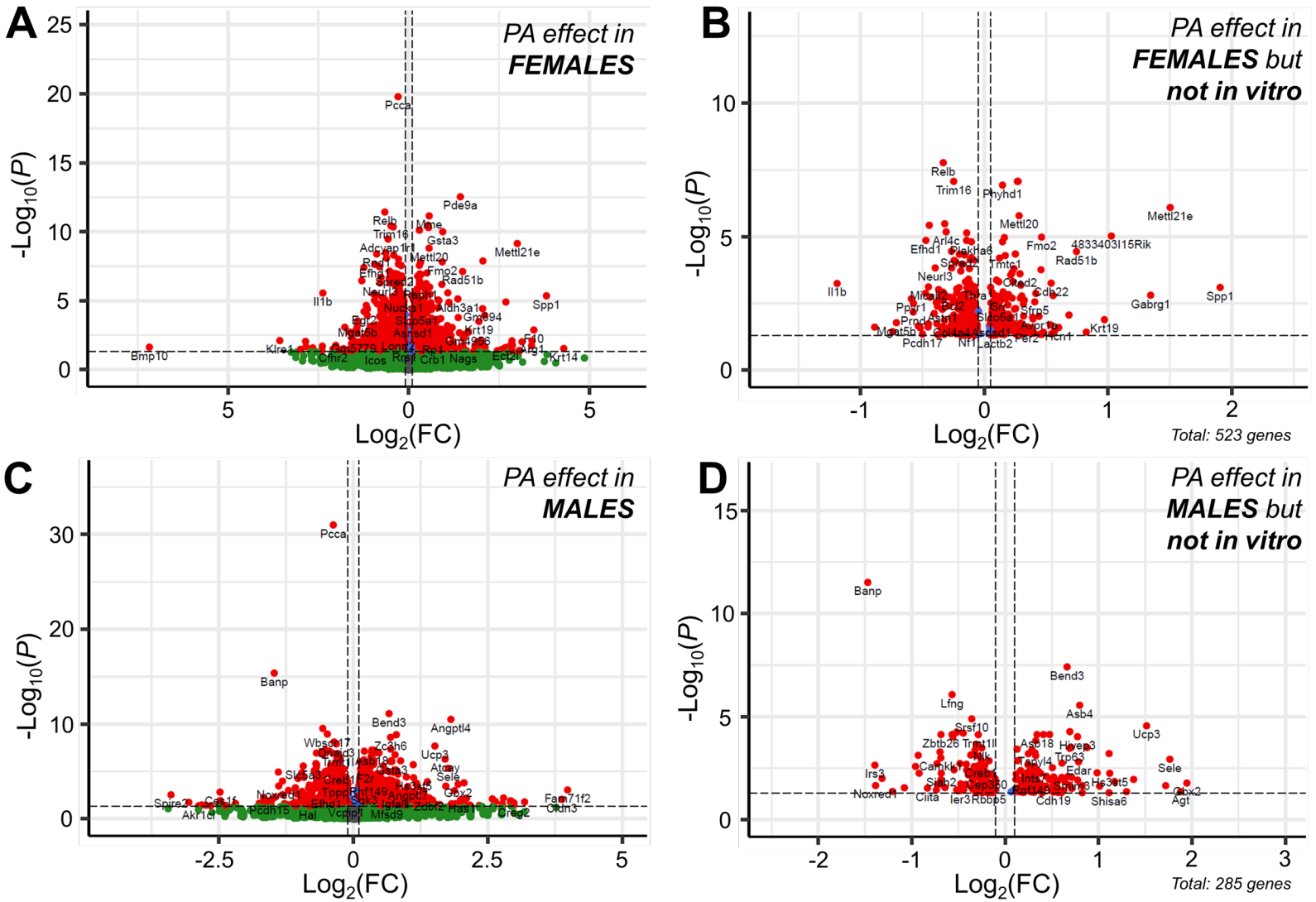


Figure 5.15. Enhanced volcano plots of DEGs in 8-week-old mouse hearts. ***(A)*** DEGs in amPA females. ***(B)*** DEGs in amPA females but not *in vitro*. ***(C)*** DEGs in amPA males. ***(D)*** DEGs in amPA males but not *in vitro*. Grey dots, not significant; green dots, significant $\log_2$(FC) only (cut-off ± 0.1); blue dots, significant adjusted *P*-value only (cut-off $P \leq 0.05$); red dots, significant $\log_2$(FC) and adjusted *P*-value.

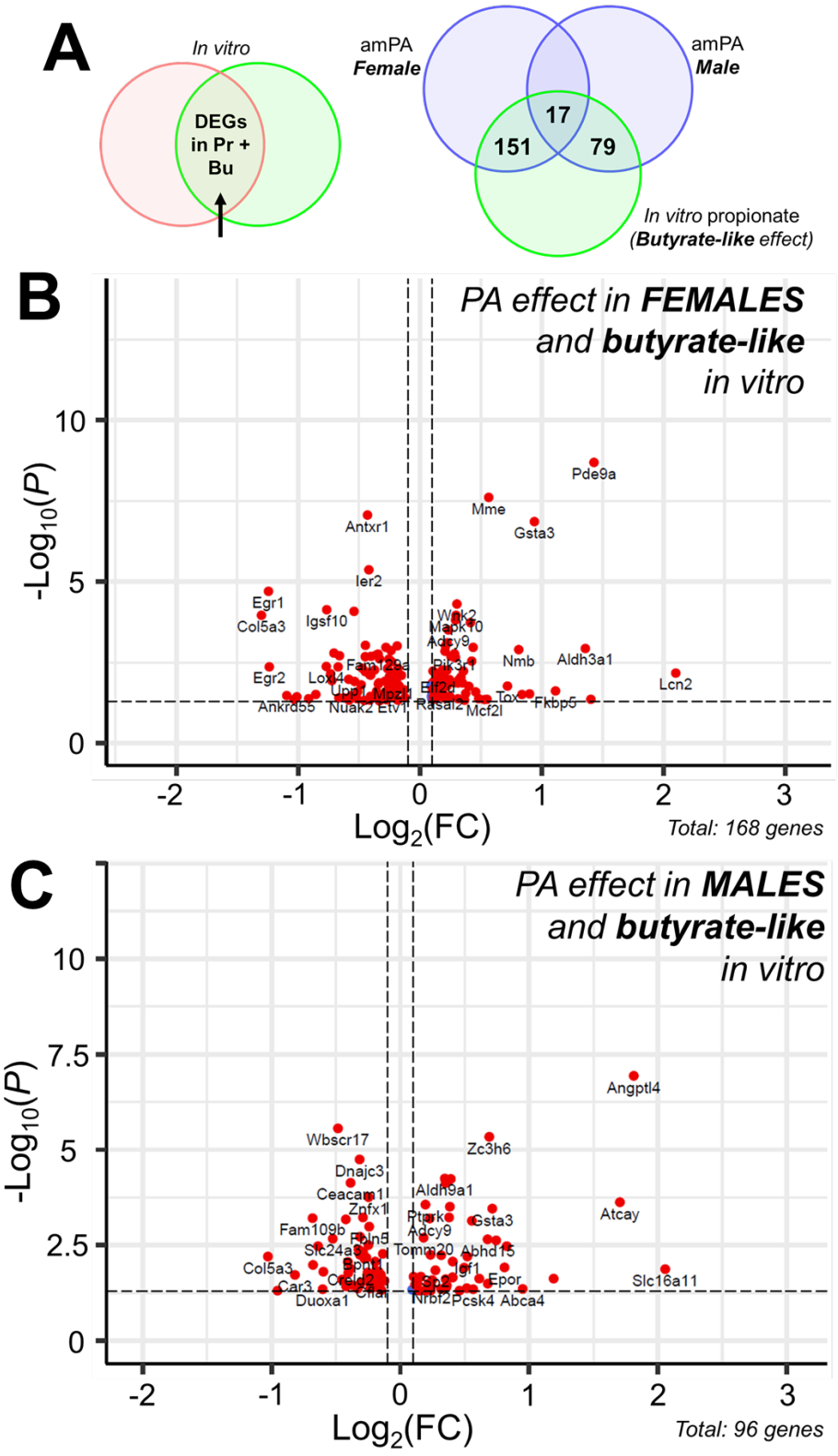


Figure 5.16. DEGs in 8-week-old mouse hearts also changed by propionate *in vitro* with a butyrate-like effect. ***(A)*** Venn diagram illustrating the DEGs shown in the volcano plots in this figure. ***(B)*** DEGs that were affected in females, but also changed by propionate *in vitro* with a butyrate-like effect. ***(C)*** Same plot as 'B' but for males. Dashed lines are relative to the DEGs with the lowest $\log_2$(FC) and $-\log_{10}$ adjusted *P* values.

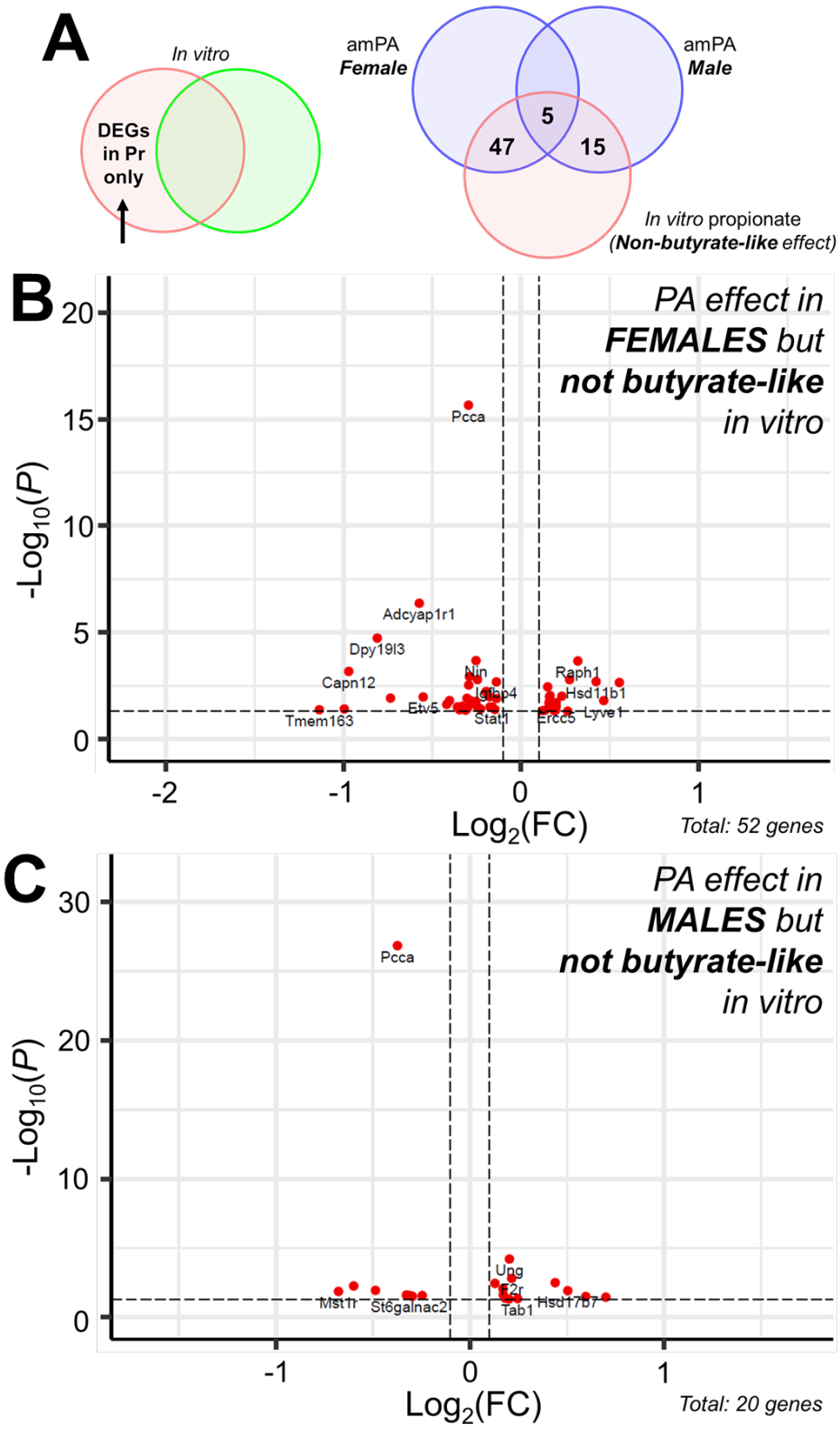
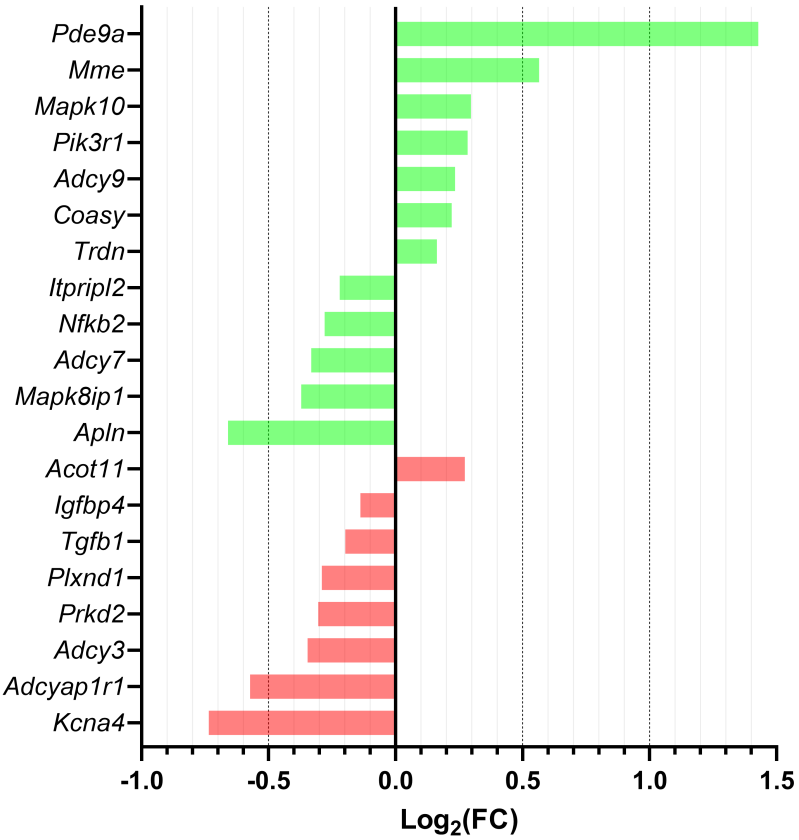


Figure 5.17. DEGs in 8-week-old mouse hearts also changed by propionate *in vitro* but not butyrate-like. ***(A)*** Venn diagram illustrating the DEGs shown in the volcano plots in this figure. ***(B)*** DEGs that were affected in females, but also changed *only* by propionate *in vitro* (i.e. not butyrate-like). ***(C)*** Same plot as 'B' but for males. Dashed lines are relative to the DEGs with the lowest $\log_2$(FC) and $-\log_{10}$ adjusted *P* values.



PA effect and butyrate-like *in vitro* *(green)*			PA effect but not butyrate-like *in vitro* *(red)*		
Gene	Full name	*Adjusted P* value	Gene	Full name	*Adjusted P* value
Pde9a	Phosphodiesterase 9A	2.01E-09	*Acot11*	Acyl-CoA thioesterase 11	0.0016
Mme	Membrane metallo-endopeptidase	2.44E-08	*Igfbp4*	Insulin-like growth factor binding protein 4	0.0021
Mapk10	Mitogen-activated protein kinase 10	0.0001	*Tgfb1*	Transforming growth factor	0.0061
Pik3r1	Phosphoinositide-3-kinase regulatory subunit 1	0.0017	*Plxnd1*	Plexin D1	0.0012
Adcy9	Adenylate cyclase 9	0.0003	*Prkd2*	Protein kinase D2	0.0121
Coasy	Coenzyme A synthase	0.0055	*Adcy3*	Adenylate cyclase 3	0.0416
Trdn	Triadin	0.0167	*Kcna4*	Potassium voltage-gated channel subfamily A member 4	0.0119
Nfkb2	Nuclear factor κB subunit 2	0.0011			
Adcy7	Adenylate cyclase 7	0.0484			
Apln	Apelin	0.0019			

Figure 5.18. Selected genes of interest that were differentially expressed in female amPA hearts and *in vitro*. *(Graph)* DEGs plotted with their $\log_2$(fold-change) values. Green bars indicate DEGs that were changed in amPA females, and both propionate and butyrate *in vitro*. Red bars indicate DEGs that were changed in amPA females and propionate only *in vitro*. ***(Table)*** Full names of the DEGs and the adjusted *P* values, as determined by RNA-seq.

5.4 Discussion

The aim of this Chapter was to gain insight into the mechanisms by which propionate causes cardiac dysfunction in PA. The combined results from previous Chapters have suggested that propionate's mechanism of action involves causing long-term changes to E-C coupling, but only showing efficacy on a chronic timescale. Since propionate has been shown to be an epigenetic modifier in other tissue systems, it was hypothesised that propionate's actions involve changing cardiac gene expression. Experiments were performed in wild-type cardiomyocytes treated with propionate and also heart samples (snap-frozen ventricular tissue) from 8-week-old male and female PA mice.

The major findings from this Chapter were as follows. (i) The application of propionate *in vitro* has a major effect on cardiac gene expression, with genes differentially expressed either due to mechanisms similar, or dissimilar to those evoked by butyrate; (ii) the DEGs are predicted to associate with H3K9ac and H3K27ac and propionate increases these histone marks in cardiomyocytes *in vitro*; (iii) histone acetylation occurs in a dose-dependent manner to propionate, in a highly organised manner in cardiomyocyte nuclei; (iv) lysine propionylation is modestly increased in the proteome and histones of the PA mouse heart; (v) cardiac gene expression in the PA mouse is significantly affected, with many DEGs in common with propionate-evoked DEGs *in vitro*, via mechanisms both similar and dissimilar to butyrate (canonical vs non-canonical); (vi) sex has a profound effect on cardiac gene expression in both amPA and amWT.

5.4.1 RNA-seq reveals major effect of propionate on cardiac gene expression *in vitro*

The transcriptome is the complete set of transcripts in a cell, and their quantity, which can differ according to the developmental stage and physiological condition (Wang *et al.*, 2009). Studying the transcriptome is complex, as it includes not only mRNA, but also ribosomal, small, and non-coding RNAs. A common experimental approach however is to sequence RNA samples enriched for poly(A) tails (long chains of adenine), which are typically only found in messenger RNA to increase their stability (Wang *et al.*, 2009).

To determine the effect of propionate on cardiac gene expression, poly(A)+ RNA-seq was performed on wild-type NRVMs treated in propionate or butyrate for 24 hrs. Both propionate and butyrate were found to have a major effect on gene expression. KEGG pathways such as '*cardiac muscle contraction*' and '*MAPK signalling*' were found to be significantly annotated in enrichment analysis of propionate-evoked DEGs. However, detailed analysis and interpretation of this dataset was not shown, since, as the thesis developed, the *in vitro* RNA-seq became more important as a tool to determine which DEGs *in vivo* (RNA-seq in PA mouse heart) were propionate-sensitive, and to gain insight into the mechanism underlying their differential expression. That is, propionate and butyrate had DEGs that were both unique, and common between each other. Interestingly, 3-hydroxypropionate, the hydroxylated derivative of propionate that is typically increased in physiological fluids of PA patients, or fluoroacetate, a

structural mimetic of propionate, had no effect on gene expression, providing further evidence that propionate itself is a bioactive epigenetic modifier.

Although not formally tested in this thesis, it is proposed that the DEGs that were both affected by propionate *and* butyrate are due to the canonical mechanism of HDAC inhibition, and that DEGs that were *only* affected by propionate are due to the non-canonical mechanism of histone propionylation, as discussed in subsequent sections.

5.4.2 Gene expression is epigenetically regulated by propionate *in vitro*

5.4.2.1 Cardiomyocyte HDAC inhibition and histone acetylation

Propionate as a HDAC inhibitor in cardiomyocytes. Although HDAC activity was not directly measured in this thesis, it is extremely likely that propionate-evoked DEGs shared with butyrate are due to the inhibition of HDACs in the heart for several reasons: (1) Butyrate is a well-established HDAC inhibitor (Davie, 2003; Steliou *et al.*, 2012); (2) these two molecules are in the same homologous series differing by only one methylene group (propionate, $CH_3CH_2COO^-$; butyrate, $CH_3CH_2CH_2COO^-$); (3) propionate has been shown to have HDAC inhibition properties, albeit mild compared to butyrate (Waldecker *et al.*, 2008). Butyrate primarily acts as a class I/II HDAC inhibitor (Davie, 2003) and these are the classes of HDACs most highly expressed in cardiomyocytes (Bagchi & Weeks, 2019). Given the structural similarity between these molecules, it is credible that propionate affects cardiac gene expression in PA by inhibiting these HDACs in the heart. The HDACs inhibited would presumably be

HDAC2 and HDAC3 (class I), the isoforms both localised to the nucleus and most abundantly expressed in cardiomyocytes (Steliou *et al.*, 2012; Bagchi & Weeks, 2019).

Although it is possible to measure HDAC activity *in vitro* in tissue extracts through fluorometric assays (Nott *et al.*, 2008), this would be a challenging experiment for this study since the PA chemical milieu (i.e. propionate) would be lost from any collected extracts. Furthermore, since there would be an inherent variability in the concentration of propionate from PCC disruption *in vivo*, the only other possibility would be to perform an *in vitro* assay in which pre-defined concentrations of propionate are added to extracted lysates, which would indeed not reliably model propionate's inhibition of HDACs *in vivo*. As such, it is not possible to accurately measure HDAC activity, and the degree to which HDACs are inhibited by propionate, in the PA mouse heart.

Histone acetylation marks increased by propionate. Enrichment analysis was performed for DEGs from the *in vitro* RNA-seq, which strongly predicted H3K9ac and H3K27ac as associated histone marks. Although no propionylation marks were predicted, presumably this was because there is far less data available for this PTM. In keeping with the hypothesis that propionate acts as a HDAC inhibitor in the heart, H3K9ac and H3K27ac were increased in cardiomyocytes treated with propionate *in vitro* (combination of immunoblotting, ELISA and immunofluorescence). Histone Kac is typically regarded as transcriptionally active. More importantly, H3K9ac and H3K27ac are known as histone modifications in the heart involved

in driving adverse cardiac remodelling (Papait *et al.*, 2013; Liu & Tang, 2019). Thus, these histone marks may be driving the change in cardiac gene expression in PA.

Propionate-evoked histone acetylation shows dose-dependence. The concentrations of propionate used for the majority of the *in vitro* experiments in this Chapter were high (3-6 mM). Such concentrations of propionate are very high and expected only during situations of acute metabolic decompensation in PA patients (Chapter 1). Therefore, an important experiment was to determine whether there was a minimum 'dose' of propionate required for it to exert its epigenetic actions on the heart. To do so, whole-cell ELISA was performed for H3K9ac at concentrations more relevant to 'stable' compensated PA patients. H3K9ac increased sharply up to 1 mM propionate before plateauing. This result demonstrates that H3K9ac (and probably other histone acetylation marks) increases dose-dependently at the most physiologically important and relevant propionate concentrations.

Indeed, an important point to consider was that an unavoidable contaminant of the NRVM prep are fibroblasts. The proportion of fibroblasts in the cell population is approximately 10% (Loonat *et al.*, 2019). To determine whether fibroblast contamination would influence the concentration-dependence of propionate-evoked H3K9ac in myocytes, ELISA experiments were repeated in fibroblasts (obtained during the pre-plating stage of the isolation). These experiments also showed that H3K9ac also increased in a concentration-dependent manner to propionate (n = 2 litters; not shown). Thus, fibroblast contamination does not affect the interpretation of this experiment.

As a side experiment, fluoroacetate, a structural mimetic of propionate, was included as an extra treatment group in this experiment. Fluoroacetate is included in weed-killers and has been shown to cause a PA-like cardiotoxicity (Goncharov *et al.*, 2006; Proudfoot *et al.*, 2006). However, fluoroacetate had no effect on H3K9ac, demonstrating that despite being structurally similar, propionate's action as a HDAC inhibitor is unique.

Propionate-evoked histone acetylation has a consistent spatial pattern in the nucleus. The organisation of the genome is not random and the three-dimensional conformation of chromatin is highly complex (Zheng & Xie, 2019). This principle applies to virtually every cell type, including cardiomyocytes (Bertero & Rosa-Garrido, 2021). Perhaps one of the most striking observations from the data presented in this Chapter was that propionate-evoked histone acetylation occurred in a highly consistent and organised manner in the nucleus.

Propionate-evoked acetylation consistently occurred toward the nuclear core of adult myocytes, whilst in neonatal myocytes it reproducibly occurred toward the nuclear periphery. Given the clear effect of propionate on gene expression (RNA-seq), these observations may be related to histone acetylation increasing in regions of active euchromatic chromatin (compartment A). Indeed, it has been shown that in adult cardiomyocytes, compartment A is generally toward the centre of the nucleus (Rosa-Garrido *et al.*, 2017). There are no data available in neonatal cardiomyocytes, however developmental stage has been known to influence the relative position of compartments (van Steensel & Furlong, 2019; Bertero & Rosa-Garrido, 2021). Since developing myocytes are more transcriptionally active (Maroli & Braun, 2021), presumably

compartment A is toward the periphery of developing myocytes based on the data from this Chapter.

Indeed, further experiments would be required to fully determine whether the propionate-evoked acetylation is occurring in active chromosomal compartments using chromosome conformation capture technologies, such as Hi-C (Bonev & Cavalli, 2016). However, given its remarkable consistency, it seems highly unlikely that the location of histone acetylation in the nucleus evoked by propionate is purely phenomenological.

A point to note is that propionate-evoked histone acetylation in adult myocytes occurred even with a short treatment time (4 hrs in adult vs 24 hrs in neonatal myocytes). This finding has relevance, demonstrating that even short durations of decompensation and propionate overload *in vivo* could evoke epigenetic modifications in the heart.

5.4.2.2 Cardiomyocyte histone propionylation

Chemically, propionylation is analogous to acetylation. That is, they are both short-chain hydrophobic modifications that neutralise the lysine positive charge (Sabari *et al.*, 2017). Thus, Kpr and Kac are considered to be biochemically similar and serve similar or overlapping functions (Trefely *et al.*, 2020). Propionylation at histone 3 lysine 14 (H3K14pr) has been recently shown to be a mark of transcriptionally active chromatin in the liver of *Pcca*$^{-/-}$ A138T mice (amPA) (Kebede *et al.*, 2017). However, whether histone Kpr occurs in the heart has not been investigated. Propionylation is a relatively new PTM and the selection of available

commercial antibodies is currently poor, thus reports that have characterised propionylation have mainly relied on bespoke antibodies. Using a pan-propionyllysine antibody, lysine propionylation was found to be increased in histones extracted from NRVMs treated with propionate, at bands corresponding to the molecular weights of H3 and H4. This finding is in agreement with propionylation sites having already been identified on both H3 and H4 in non-cardiac tissues (Sabari *et al.*, 2017).

Whereas propionate is the active form inhibiting HDAC enzymes to increase Kac, propionyl-CoA is used as the substrate for Kpr. Exogenously applying propionate (or PCC deficiency; see next, Section 5.4.3) would increase propionyl-CoA bioavailability, facilitating the reaction. Further experiments would be required to determine which specific histone lysine residues are being propionylated (tandem mass spectrometry of histone extracts) and importantly, which ones are functionally important and are transcriptionally active (chromatin immunoprecipitation; ChIP). Thereafter, experiments could be performed to investigate which specific KATs mediate histone propionylation in the heart.

5.4.3 Cardiac gene expression is significantly altered in mice with PCC disruption *in vivo*

The aim of the RNA-seq experiment in the PA mouse heart was (1) to characterise how gene expression is altered in the heart by disrupted propionate metabolism *in vivo* and (2) to determine which genes are sensitive to propionate. Although the first question was simple to answer, the second question was more difficult to address. Following PCC disruption, there is

an accumulation of propionate, as well as other related metabolites (e.g. MeCit). Therefore, cell culture systems are necessary to establish a defined and controlled environment; when propionate is applied to wild-type cardiomyocytes (with PCC intact), it would be expected for propionate and propionyl-CoA to be the dominant metabolites.

Like cardiomyocytes treated with propionate *in vitro,* PCC disruption *in vivo* was found to have a major effect on cardiac gene expression, as assessed by poly(A)+ RNA-seq in sex-balanced samples. To then determine which genes are propionate-sensitive, the RNA-seq data from the PA mouse heart were compared with that of NRVMs cultured in propionate.

Indeed, there are two obvious differences between these models: species and developmental stage. However, the rat and mouse are similar both in their genome (Gibbs *et al.*, 2004) and cardiac physiology (Bers, 2002a). In terms of developmental stage, the primary changes in maturing cardiomyocytes are the switching of metabolism (from glycolytic to oxidative) and the isoform switching of contractile genes (Cui *et al.*, 2018; Maroli & Braun, 2021), therefore unlikely to affect the interpretation of DEGs (Section 5.5.3.3).

A critical observation was that, *in vivo*, the quantitatively important mechanism of modifying gene expression was the canonical butyrate-like mechanism (HDAC inhibition), as opposed to non-canonical mechanisms unique to propionate (e.g. propionylation).

Technical considerations. Prior to discussing the data, some technical points should first be considered. It is worth noting that the heart consists not only of cardiomyocyte, but multiple

cell-types including fibroblasts, neurons and endothelial cells. To add another level to this, it was recently shown using single-cell RNA-seq that there is heterogeneity in the transcriptome, even between cardiomyocytes of different anatomical regions (Litviňuková *et al.*, 2020). Indeed, the RNA-seq in the mouse heart in this thesis was bulk RNA-seq, performed in snap-frozen ventricular tissue. However, to address the aims of this Chapter–how the transcriptome is affected by propionate, which is inherently labile–snap-frozen tissue was technically favoured as opposed to isolated ventricular myocytes to preserve the metabolic state.

Although major DEGs of cardiac interest were detected in amPA hearts (see Section 5.5.3.3), there is a possibility that other genes of interest were not resolved due to a limit of detection and sequencing depth. Thus, although cardiomyocytes quantitatively contribute the highest 'volume' to the heart, the detected DEGs may include those of different cell types (like endothelial cells). There is currently no standardised method for studying the transcriptome in the heart (Robinson *et al.*, 2021). However, it would be worth considering in future studies the enrichment for cardiomyocyte nuclei only, which is possible in frozen samples, for example by utilising the INTACT nuclear profiling method (Amin *et al.*, 2014).

5.4.3.1 Epigenetic mechanisms in vivo

In cardiomyocytes treated with propionate *in vitro*, there was a sharp increase in H3K9ac and propionylation on western blotting of histone extracts. However, when the experiment was repeated in histones extracted from amPA hearts, only a modest change in propionylation was seen. This may be related to several reasons, ultimately related to the prevailing concentration

of propionate and propionyl-CoA in the cell and kinetics of the enzymes involved, or possibly, compensatory mechanisms *in vivo*. This point is discussed separately for acetylation and propionylation, below.

HDAC inhibition and histone acetylation in vivo. An increase in H3K9ac was not seen by western blot in cardiac histones from PA mice. This may be related the PA mouse model being a relatively mild model of PA (the A138T point mutation was from a patient with a mild-to-moderate dysfunction of PCC) (Guenzel *et al.*, 2013). Thus, these mice do not accumulate extremely high concentrations of propionate as in decompensated PA patients (which were concentrations used in the *in vitro* cardiomyocyte studies). The IC_{50} for propionate inhibiting HDACs is estimated as being in the millimolar range (Lu *et al.*, 2004), therefore there may not be sufficient increase in H3K9ac to be detected by immunoblotting. Nonetheless, due to the high degree of overlap between the DEGs *in vivo* and DEGs *in vitro* induced by both propionate *and* butyrate, it appears that there is indeed histone acetylation (due to HDAC inhibition by propionate), which is simply not being resolved. A sensible approach to address whether histone Kac marks have a role in epigenetic modification of the transcriptome *in vivo* would be to either perform ChIP-qPCR for selected DEGs, or ChIP-seq for specific histone acetylation marks of interest (e.g. H3K9ac, H3K27ac).

Histone propionylation in vivo. Although histone Kpr has been shown in the liver of amPA animals (Kebede *et al.*, 2017), it has not been investigated whether it occurs in the heart. Indeed, the concentration of propionyl-CoA is usually substantially higher in liver, compared to heart

tissue (Sadhukhan *et al.*, 2016), and ~90% of propionate is metabolised in the liver (Wilson *et al.*, 2017). Therefore, it was unclear whether this PTM would occur in the heart. However, the data from this thesis is the first to provide evidence for this PTM in the heart *in vivo*.

There is a high correlation between the abundance of a particular acyl-CoA and their corresponding acyl-PTM. That is, acyl-PTMs have been shown to increase in a dose-dependent manner with the prevailing acyl-CoA concentration (Simithy *et al.*, 2017). Therefore, the increased concentration of propionate and propionyl-CoA due to disrupted PCC would be expected to result in more Kpr. Indeed, fibroblasts from PA patients have been shown to have increased protein propionylation (Pougovkina *et al.*, 2014).

The reason for histone propionylation being observed on immunoblotting, but not H3K9ac, could be related to the IC_{50} for HDAC inhibition by propionate being substantially higher (millimolar range) than the K_m of the enzyme (KATs) that catalyse Kpr (micromolar range) (Reid et al., 2017). Further experiments would be required to determine which KATs are involved in the cardiac histone Kpr. As previously mentioned, there are several KATs that can mediate Kpr, albeit with reduced kinetics compared to Kac. For example, p300 (KAT3B) has been shown to be able to catalyse Kpr, although its kinetic activity has been found to be progressively slower with increasing acyl-chain lengths (fastest for Kac) (Kaczmarska *et al.*, 2017).

Indeed, the data presented thus far are correlative. To investigate the functional role of propionylation in the heart, the histone Kpr sites would first need to be mapped (MS-MS) and ChIP experiments performed for these propionylation sites.

5.4.3.2 Sex effect

There are prominent sex differences in cardiac function, including its structure, Ca^{2+} handling, as well as its metabolism (Murphy *et al.*, 2017). Accordingly, there has been increasing evidence over the years that there are also a large number of sex differences in cardiac gene expression (Murphy *et al.*, 2017; Regitz-Zagrosek & Kararigas, 2017). Surprisingly, the greatest source of variation in the amPA heart RNA-seq dataset came from sex as opposed to genotype (PA), and there was a clear division between male and female samples. Epigenetic mechanisms, including differences in histone acetylation, methylation and non-coding RNAs, have been implicated as major factors causing sex differences in cardiac gene expression (Regitz-Zagrosek & Kararigas, 2017). For example, KAT3A (CBP; CREB binding protein) and KAT3B (p300) have been shown to be recruited to DNA by androgen and oestrogen receptors, demonstrating that there is potential for sex-specific regulation of histone K_{ac} (Regitz-Zagrosek & Kararigas, 2017). Thus, there is a possibility that steroid hormone signalling plays a role in remodelling of cardiac gene expression in PA.

Of note, there was high variability within samples from male animals, particularly for male amPA. An explanation for this could be related to potential differences in the level of propionate that accumulates in males and females. It was not ascertained in the metabolomics experiment presented in Chapter 3 whether the chemical milieu is the same between male and female amPA hearts. However, there is some evidence suggesting possibly higher propionate accumulation in female vs male amPA, based on previous measurements of plasma MeCit and

C3 (Guenzel *et al.*, 2015). If true, the relative difference in [propionate] between WT and PA would then be less in males, compared to females. Since evidence has been presented in this Chapter for propionate being a direct epigenetic modifier in the heart, in a dose-dependent manner, a smaller accumulation of propionate in male amPA could account for the lack of clustering (greater variability) in male samples. In other words, there may be more clustering (less variability) in female amPA due to a stronger stimulus.

5.4.3.3 DEGs of cardiac interest

DEGs that were changed both *in vivo* and *in vitro* were used to discover propionate-sensitive targets. Based on the number genes that were differentially expressed, the most physiologically-relevant mechanism by which propionate affects cardiac gene expression *in vivo* appears to be via the canonical mechanism shared with butyrate (HDAC inhibition).

There were several genes relevant to cardiac physiology that were differentially expressed in PA hearts. In female amPA animals (where an E-C coupling phenotype was seen), there were several significant DEGs related to different aspects of cardiac physiology (Figure 5.18). Triadin (*Trdn*) has been identified as important for LTCC-RyR coupling (Chopra *et al.*, 2009). Plexin D1 (*Plxnd1*) is critical in LV compaction (Sandireddy *et al.*, 2019), and possible cases of LV non-compaction have been reported in PA (Park *et al.*, 2020). Plexin D1 has also recently been shown to be a mechanosensor in endothelial cells required for their responses to shear stress (Mehta *et al.*, 2020). Since this was bulk RNA-seq in ventricular tissue (which includes endothelial cells), the downregulation of *Plxnd1* suggests a possible involvement of endothelial dysfunction. Importantly, apelin (*Apln*) was downregulated in amPA (log_2FC -0.659; $P = 0.0019$), which is a potent endogenous positive inotrope, also involved in a variety of signalling roles (Wysocka *et al.*, 2018).

It is noteworthy that, despite the pronounced changes to cardiomyocyte Ca^{2+} handling observed in female amPA, there was no differential expression of the genes encoding key Ca^{2+} handling proteins, such as *Cacna1c* (LTCC), *Ryr2* (RyR), *Atp2a2* (SERCA), *Pln* (PLN) and *Slc8a1* (NCX).

However, taking all DEGs into consideration, a process that clearly appeared to be implicated was cyclic nucleotide signalling (Figure 5.18). Three adenylate cyclase isoforms were differentially expressed, including *Adcy9*, which has been implicated in diastolic dysfunction (Li *et al.*, 2017). *Mme*, encoding membrane metalloendopeptidase (MME) was the second most significant DEG (log_2FC +0.564; adjusted *P* = 2.44E-08). MME is one of two mechanisms by which atrial and brain natriuretic peptides (ANP, BNP) are degraded (Pereira *et al.*, 2010).

Pde9a. Notably, the most significant DEG in female amPA was *Pde9a* (log_2FC +1.43; adjusted *P* = 2.01E-09), which was commonly changed by both propionate and butyrate *in vitro*. Whilst it appears likely that the epigenetic mechanism responsible for the differential expression of *Pde9a* is related to HDAC inhibition (i.e. increase in Kac), further experiments would be required to confirm this (e.g. by ChIP-qPCR for *Pde9a*).

Due to the impact of the COVID-19 pandemic and the timing of data availability, it was not possible to validate any DEGs at the time of writing. However, an upregulation of *Pde9a* provides an explanation for the cardiac phenotype observed in PA. *Pde9a* encodes PDE9A, a cGMP-selective phosphodiesterase found to be a critical driver of cardiac disease, and upregulated in human HFpEF samples (Lee *et al.*, 2015). Since the study by Lee *et al.*, other high-profile reports had been published, whereby *in vivo* administration of PDE9A inhibitors that are currently in human clinical trials, reversed murine diastolic dysfunction (Methawasin *et al.*, 2020; Richards *et al.*, 2021). Thus, changes in cyclic nucleotide signalling appears to be a critical component in the pathophysiology of PA, at least in females. The implications of

upregulated *Pde9a* and dysregulated cyclic nucleotide signalling is discussed further in the final integrated discussion in Chapter 6.

5.4.4 Protein propionylation as a post-translational modification in the heart

Although not related to gene expression, evidence of cardiac non-histone protein Kpr was presented in this Chapter. Indeed, there is some evidence for increased protein Kpr in PA patients (Pougovkina *et al.*, 2014). Whilst the functional relevance of cardiac protein Kpr is yet to be determined, by being biochemically similar to acetylation, it is possible that propionylation of cytoplasmic non-histone proteins contributes to the cardiac PA phenotype.

In general, non-histone protein Kac is recognised as an important PTM in a variety of cell-types (Narita *et al.*, 2019). Importantly, Ca^{2+} handling proteins and myofilament proteins have been shown to be acetylated in the heart (Foster *et al.*, 2013). Furthermore, recently, K492 acetylation of SERCA by cytoplasmic p300 (KAT3B) has been shown to be the molecular driver of SERCA inhibition in heart failure (Gorski *et al.*, 2019). Since Kpr and Kac are biochemically analogous and they have been shown (at least in histones) to be functionally similar, it is possible that cardiac proteins modulated by Kac are also modulated by Kpr. However, a more sensitive method than immunoblotting would be required to test this hypothesis. The first step would be to identify which proteins are propionylated by performing MS on samples enriched for propionylated lysines.

5.5 Summary

There were several important findings from this Chapter. Propionate, and not its structural analogues, can epigenetically modify gene expression *in vitro*, either by acting as direct or indirect substrates that modify histone structure, through propionylation or HDAC inhibition (presumably HDAC 2 and 3), respectively. H3K9ac and H3K27ac, two histone Kac marks known to be involved in adverse cardiac remodelling, were increased in a dose-dependent manner by propionate and occurred with a consistent, non-random, spatial pattern in the nucleus. The first evidence for propionylation of histone and non-histone proteins in the heart was also presented.

Cardiac gene expression was significantly altered by PCC disruption and a large number of DEGs were determined to be propionate-sensitive, including genes of cardiac interest. The most physiologically important effect of propionate on cardiac gene expression *in vivo*, appears to be mediated via the butyrate-like canonical mechanism of HDAC inhibition, whereas non-canonical mechanisms unique to propionate (e.g. propionylation) appear to play a smaller part. In addition, sex had a profound effect on gene expression. In female hearts, the most significant DEG (which was, via a butyrate-like mechanism) was upregulated *Pde9a* (phosphodiesterase 9a), the cGMP-specific phosphodiesterase known to drive diastolic dysfunction. A summary schematic of the epigenetic mechanisms involved in the remodelling of cardiac gene expression is shown in Figure 5.19.

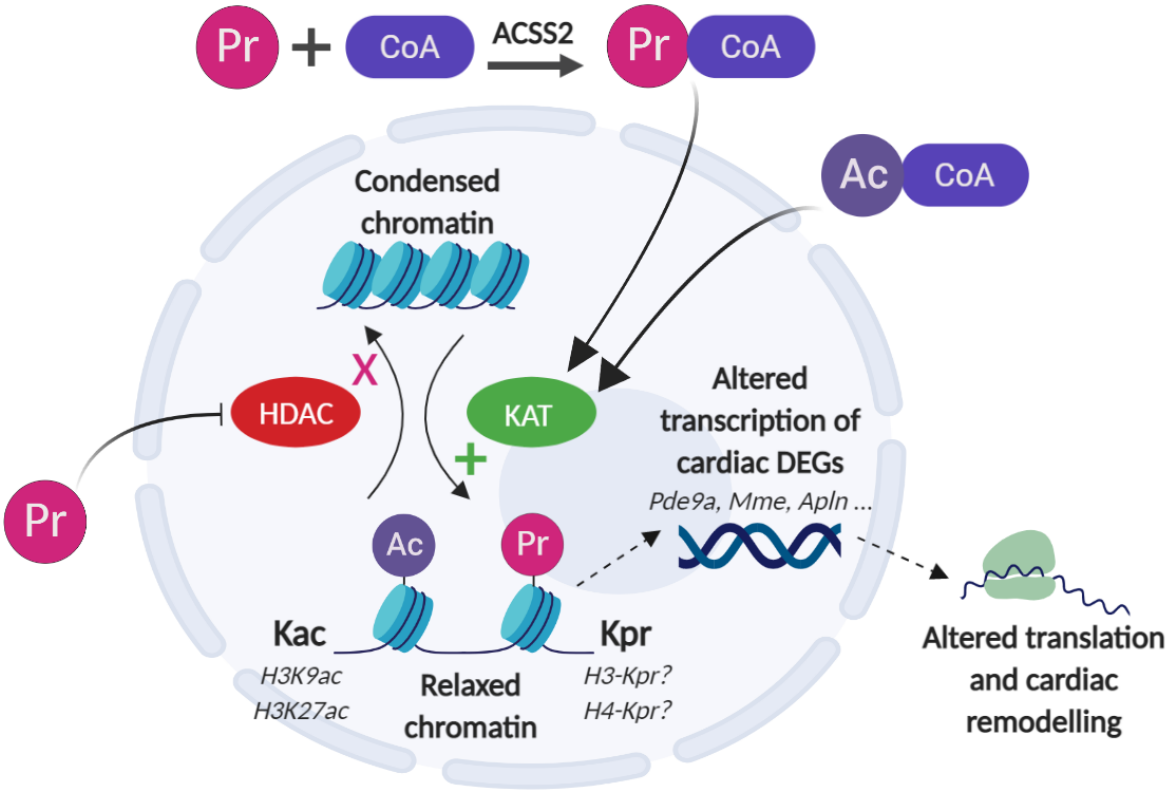


Figure 5.19. Summary of mechanisms involved in epigenetic remodelling of cardiac gene expression by propionate. Condensed chromatin is transcriptionally inactive. Propionate inhibits HDACs causing net acetylation by KATs, and an increase in histone K_{ac} marks (e.g. H3K9ac and H3K27ac), causing chromatin to be in a relaxed conformation, causing differential expression of important cardiac genes (e.g. *Pde9a*). Propionate can also be esterified by ACSS2 in the cytoplasm or nucleus to form propionyl-CoA. Propionyl-CoA acts as a substrate for KATs and histone propionylation, putatively contributing to the open conformational state of chromatin and hence active transcription. Ac, acetate; ACSS2, acyl-CoA synthetase short-chain family member 2; CoA, coenzyme A; DEGs, differentially expressed genes; H3, histone 3; H3K9ac, histone 3 lysine 9 acetylation; H3K27ac, histone 3 lysine 27 acetylation; H4, histone 4; Pr, propionate; KAT, lysine acetyl-transferase; Kac, lysine acetylation; Kpr, lysine propionylation.

Chapter 6. Final summary and integrated discussion

6.1 Summary of key findings

The aim of this thesis was to characterise the effects of dysregulated propionate metabolism on the heart. This was primarily addressed by using a mouse model of PA (*Pcca*$^{-/-}$ A138T), in which the levels of propionate generated *in vivo* are sufficient to produce a metabolic signature of the human disease, but allows the animal to reach adulthood, thereby facilitating the study of cardiac physiology *in vivo* and in isolated cells. However, contrary to other studies that use this model for PA research, there were three major differences in experimental approach undertaken herein: (i) experiments were performed in 8-week-old young-adult mice (vs 5 to 8-month-old animals used by others), in order to capture early changes in response to propionate accumulation, before compensatory mechanisms are likely to have confounded the ensemble phenotype; (ii) to account for any sex differences, which are increasingly recognised as having important influences on cardiac physiology and cardiometabolic disorders, experiments were sex-balanced and analysed according to sex; (iii) heterozygous dams were used for breeding, as opposed to homozygous PA dams, in order to model the consequences of post-natal, rather than *in utero*, propionate accumulation, as is the case in human PA. The key findings from this thesis were, that in 8-week-old animals:

i. Like in plasma, the heart accumulates metabolites canonically attributed to the human PA condition, albeit orders of magnitude lower;

ii. There are early signs of contractile dysfunction *in vivo*, in the form of raised LV end-diastolic and end-systolic volumes, that precede any resolvable electrophysiological changes;

iii. Isolated ventricular myocytes from female mice have dysregulated Ca^{2+} handling, manifesting as raised diastolic $[Ca^{2+}]$ but unaltered systolic $[Ca^{2+}]$ at 8 weeks, which progresses to a normalised diastolic $[Ca^{2+}]$ but raised systolic $[Ca^{2+}]$ by 20 weeks;

iv. Anionic propionate applied exogenously *in vitro* remodels the AP and CaT in wild-type cardiomyocytes;

v. There is a significant change in cardiac gene expression and the majority of propionate-sensitive DEGs can be associated with the butyrate-like canonical mechanism of HDAC inhibition. The DEG that had the greatest statistical significance was *Pde9a* upregulation in female hearts, which likely involves propionate acting as a HDAC inhibitor (versus non-canonical mechanisms such as histone propionylation);

vi. Propionate evokes increases in H3K9ac and H3K27ac *in vitro*, two histone marks known to be involved in adverse cardiac remodelling, in a dose-dependent manner, and following a consistent spatial pattern in the nucleus.

6.2 Integrated discussion and implications of findings

6.2.1 Ca^{2+} handling and contractile function

6.2.1.1 At 8 weeks of age, early changes are being detected

Cardiac function measured *in vivo* (cine-MRI) demonstrated an increase in LV EDV and ESV at the 8-week timepoint. Numerous experiments from Chapter 3 excluded maladaptive hypertrophy as a mechanism in PA (e.g. myocyte size, SRB assay). Whilst end-diastolic and end-systolic pressures were not measured, the increase in EDV and ESV are a manifestation of a rightward shift in the left-ventricular pressure-volume loop. Such changes could be attributed to increased effective circulating volume, valvular disease (e.g. mitral valve regurgitation), but they also resemble the response observed in DCM (Konstam & Abboud, 2017).

It is not suggested however that 8-week-old PA mice have a DCM *per se*, or rather, any severe perturbation of function. Instead, it appears that at 8 weeks of age, early deficits in contractile function and Ca^{2+} handling are being detected, that may be a prelude to more severe dysfunction. There was no evidence of gross LV chamber dilatation, or evidence of overt systolic dysfunction at this early timepoint. Although there were no statistically significant changes in the ECG, there was a trend toward a shorter QT interval (in females). Because APD was shorter in neonatal myocytes treated with high concentrations of propionate *in vitro*, one may expect changes in the ECG to appear at a later timepoint, when the cumulative effects of propionate result in electrophysiological changes.

At the cardiomyocyte-level, changes to Ca^{2+} handling were only statistically significant in female mice, indicating a meaningful interaction between sex and genotype. The key change was an increase in diastolic Ca^{2+} at 8 weeks of age, whilst systolic Ca^{2+} remained unchanged. The rise in diastolic and resting Ca^{2+} in 8-week-old amPA can be explained by a greater influx and/or reduced efflux across the sarcolemma. All things being equal, a rise in diastolic Ca^{2+} should result in greater SR Ca^{2+} filling, and therefore, a rise in systolic Ca^{2+} is expected. However, by conducting hierarchical statistical analyses, within the resolving power of the testing in this thesis, no change in systolic Ca^{2+} was noted, suggesting that there was a decrease in the gain in E-C coupling. This could be attributed to reduced SERCA activity, reduced $I_{Ca,L}$, and/or higher RyR leak. Another plausible mechanism may be increased buffering capacity for Ca^{2+}, although several lines of indirect evidence argue against this. Put together, higher diastolic Ca^{2+} and unchanged systolic Ca^{2+}, may indicate negative lusitropy and negative inotropy, respectively, resulting in a rightward shift in the pressure-volume loop (Katz, 1988).

A possible explanation for a rightward shift in volumes is a bradycardia, which allows greater ventricular filling. Indeed, a small bradycardia was observed in amPA, although the extent of this was relatively small (~9% in males, 7% in females). Whether this change would be sufficient to affect volumes, to the extent that they were affected (e.g. ESV; ~18% in males, ~15% in females), is unclear, particularly when both ESV and EDV are shifted in tandem by comparable amounts. An increase in afterload would shift ESV rightward, but without necessarily affecting

EDV, and thus seemed unlikely. Regardless, definitive evidence would require measuring pressure-volume loops and haemodynamics (Lindsey *et al.*, 2018).

Taken collectively, the best explanation for the phenotype at 8 weeks of age is a form of diastolic dysfunction, more evident in females, in conjunction with suppressed contractile strength. Dysregulated Ca^{2+} handling and raised diastolic Ca^{2+} have been implicated as features of diastolic dysfunction (Zile & Gaasch, 2011; Adeniran et al., 2015; Runte et al., 2017). LV diastolic dysfunction is characterised by an impairment in relaxation, an increase in chamber stiffness, or a combination of these two factors (Obokata *et al.*, 2020). Since SERCA rate was significantly reduced in amPA myocytes, this may contribute to an impairment in relaxation. Lusitropy is also determined by the status of myofilament proteins, such as troponin I phosphorylation, which could be affected in amPA hearts (Bers, 2002a). In a similar manner, there indeed may be an element of increased chamber stiffness, due to hypo-phosphorylation of other important myofilament proteins, such as titin. These two effects (impairment in relaxation and increase in chamber stiffness), can be explained by increased PDE9A (see Section 6.2.1.2). Indeed, should there be a diastolic dysfunction, a leftward shift of the pressure-volume relation would be expected (Katz, 1988; Katz & Rolett, 2016). Thus, in amPA, it may be that the effect of negative inotropy (from reduced CaT amplitude) offsets this with ultimately a rightward shift (increased EDV and ESV).

A common complication of diastolic dysfunction is the development of heart failure, often with an unchanged EF (HFpEF) (Obokata *et al.*, 2020). Elevated filling pressures (e.g. LV end-

diastolic pressure) are typical in HFpEF, and is associated with dyspnoea, pulmonary congestion, and impaired exercise capacity (Valero-Munoz *et al.*, 2017). The absence of pulmonary congestion or systolic dysfunction in 8-week-old PA mice (Chapter 3), suggest that there are no major increases in filling pressure at this timepoint, and also supports the idea of early changes and mild perturbation in function being detected at 8 weeks.

The hypothesis of diastolic dysfunction would be consistent with clinical findings from a longitudinal observational monocentric study of cardiac function in PA patients by Kovacevic *et al.* (2020). This was the first study to report diastolic function in PA patients, using pulsed-wave Doppler to measure the mitral E/A wave ratio, a readout of the ventricular filling pattern representing the ratio of peak velocity mitral flow from LV relaxation in early diastole (E wave), to the peak velocity flow from LA contraction in late diastole (Nagueh, 2020). E/A decreases when relaxation is impaired, but rises again with the progression of diastolic dysfunction when LA pressure increases, in a process termed pseudo-normalisation (Schnelle *et al.*, 2018). Kovacevic *et al.* found evidence for diastolic dysfunction in 61% (11/18) of their PA patient cohort, in the absence of mitral valve disease. Importantly, 45% of the patients with diastolic dysfunction did not have any LV systolic dysfunction (5/11), whilst the remainder later went on to develop LV systolic dysfunction and HNDC (6/11; 55%); 2 patients with HNDC thereafter developed DCM.

One study has been published to-date in which diastolic function was assessed in 5-month-old and 8-month-old male amPA animals (Fulgencio-Covian *et al.*, 2020). Interestingly, Fulgencio-

Covian *et al.* found no effect on diastolic function (E/A ratio). This may be related to the data from this thesis demonstrating a more pronounced cardiac phenotype in female amPA. Furthermore, the diastolic Ca^{2+} mishandling observed at 8-weeks was compensated for by 20 weeks of age, suggesting that any early deficits to diastolic function may be normalised in >5-month-old amPA. The sex effect of PA is discussed in Section 6.2.3.

An important experiment would be to perform transmitral Doppler echocardiography in 8-week-old amPA animals. Since E/A (acquired by pulsed-wave Doppler) is susceptible to pseudo-normalisation, myocardial motion in early diastole (as assessed by the peak early-diastolic mitral annular velocity; e'), should be obtained by tissue Doppler to determine E/e', a more reliable readout of LV filling pressures and diastolic function (Zacchigna *et al.*, 2021). However, in the first instance, existing cine-MRI images captured from 8-week-old amPA animals could be re-analysed to assess diastolic function (Roberts *et al.*, 2017). Furthermore, the images acquired from cardiomyocyte CaTs could be re-analysed for cell shortening kinetics (Carnicer *et al.*, 2021), whereby slower cell relaxation would be expected if diastolic dysfunction was present.

6.2.1.2 PDE9A, cGMP-PKG signalling, and diastolic dysfunction

The most significant DEG was upregulated *Pde9a* in amPA female hearts (log_2FC +1.43; adjusted P = 2.01E-09), which lends further support to the idea that 8-week-old amPA animals may have a diastolic dysfunction. The seminal study by Lee *et al.* (2015) showed that upregulated PDE9A was a critical driver of cardiac dysfunction and also increased in human HFpEF. Since the study by Lee *et al.*, other high-profile reports had been published whereby *in*

vivo administration of PDE9A inhibitors (currently in human clinical trials) reversed diastolic dysfunction in murine models (Methawasin *et al.*, 2020; Richards *et al.*, 2021).

PDE9A is a high-affinity cGMP-selective phosphodiesterase, which preferentially hydrolyses cGMP generated from natriuretic peptide stimulation of particulate guanylate cyclase at the cell membrane, as opposed to that generated by nitric oxide-coupled soluble guanylate cyclase (Methawasin *et al.*, 2020). As such, if PDE9A were upregulated, there would be greater degradation of cGMP, and thus reduced activity of cGMP-dependent protein kinase (PKG).

The consequences of reduced PKG activity have mainly been studied in the context of diastolic dysfunction and HFpEF (Lewis *et al.*, 2017). Increased LV stiffness in human HFpEF patients, has been attributed to reduced PKG activity and hypo-phosphorylation of the sarcomeric protein, titin, and both *in vitro* and *in vivo* PKG activation improved LV chamber compliance (van Heerebeek *et al.*, 2012). Furthermore, cGMP-dependent phosphorylation of troponin I by PKG is known to be positively lusitropic due to myofilament Ca^{2+} desensitisation (Mayourian *et al.*, 2018). Therefore, reduced PKG activity (due to increased PDE9A and cGMP degradation), would be expected to reduce troponin I phosphorylation and be negatively lusitropic.

cGMP-PKG signalling is also implicated in E-C coupling. PKG has been shown to phosphorylate and inhibit LTCC activity (Balligand & Hammond, 2013). Reduced PKG activity due to upregulated PDE9A in amPA could, in theory, result in dysinhibition of LTCC,

thus increasing Ca^{2+} influx, and contributing to the increase in E-C coupling gain observed in 20-week amPA females.

Collectively, reduced cGMP-PKG signalling may be a critical driver in the cardiac dysfunction observed in female amPA. This is supported by the observation that the second most significant propionate-evoked DEG *in vivo* was upregulated *Mme*, encoding membrane metalloendopeptidase (log_2FC +0.564; adjusted P = 2.44E-08). MME is one of two mechanisms by which atrial and brain natriuretic peptides (ANP, BNP) are degraded (Pereira *et al.*, 2010). Therefore, should MME be increased, one would expect increased degradation of natriuretic peptides and less stimulation of particulate guanylate cyclase (hence reduced cGMP). Indeed 8-month-old amPA hearts were previously shown to have increased *Nppb* (BNP) transcript levels (Guenzel *et al.*, 2013). This seems consistent with a compensatory response to restore cGMP levels.

6.2.2 Epigenetics and gene expression

There was a major change in cardiac gene expression in 8-week-old amPA animals. By comparing these datasets with DEGs identified from *in vitro* responses to exogenous propionate or butyrate, a proportion of these DEGs were determined as being propionate-sensitive, with evidence for propionate acting via two separate mechanisms: (1) the canonical butyrate-like mechanism of HDAC inhibition (and hence increased histone acetylation); (2) a non-canonical mechanism involving histone propionylation. The canonical mechanism of HDAC inhibition

appears to be quantitatively important *in vivo*. Several genes of cardiac interest were differentially expressed by this mechanism, notably *Pde9a*. Although not directly assayed, presumably the mechanism involves inhibition of class I HDACs (HDAC2/HDAC3), as these are the HDACs that possess deacetylase activity and are the most abundantly expressed in cardiomyocytes (Bagchi & Weeks, 2019).

The DEGs from *in vitro* propionate-treated cardiomyocytes were predicted to associate with H3K9ac and H3K27ac, two histone marks associated with adverse cardiac remodelling (Papait *et al.*, 2013). Indeed, propionate increased H3K9ac/H3K27ac in a dose-dependent manner and strikingly, in a consistent, non-random, spatial pattern in the nucleus. However, these Kac marks could not be resolved in histones extracted from amPA hearts. In contrast, Kpr was detected in both *in vitro* propionate-treated cardiomyocytes and histones extracted from amPA hearts. This difference likely relates to the IC_{50} for HDAC inhibition being in the millimolar range, vs the K_m for KATs being in the micromolar range. Indeed, to determine the true functional significance of histone modifications in amPA, the specific Kac and Kpr sites first need to be mapped, to facilitate ChIP-based targeted studies in the future. However, the different lines of evidence presented in this thesis, together, strongly suggest that changes in cardiac gene expression in PA involves histone modifications.

Aside from the epigenetic mechanisms, one that should be mentioned is the influence of Ca^{2+} on gene expression. Raised Ca^{2+} can be a substrate for altering gene expression by activating Ca^{2+}-dependent transcriptional pathways, through what is referred to as excitation-transcription

coupling in the heart (Wu *et al.*, 2006). The effector for this process is CaMKII, and a key excitation-transcription pathway involves CaMKII-dependent phosphorylation of class IIa HDACs (e.g. HDAC5; note, lacks deacetylase activity). Since, when these HDACs are dephosphorylated, they repress key transcription factors (e.g. MEF2), CaMKII-dependent phosphorylation of HDACs relieve this repression. Indeed, this pathway is mainly pro-hypertrophic (Wu *et al.*, 2006), and maladaptive hypertrophy was excluded in amPA. Furthermore, there was no change to PLN_{pThr17}, a key target of CaMKII. Regardless, the contribution of Ca^{2+}-dependent transcription pathways cannot be excluded, especially since other important phosphorylation targets of CaMKII weren't examined (e.g. LTCC and RyR) (Dewenter *et al.*, 2017).

6.2.3 Sex-dependence of cardiac dysfunction in PA

Sex differences are well recognised in cardiac physiology, for example in Ca^{2+} handling and gene expression (Murphy *et al.*, 2017). Indeed, the cardiac phenotype, with respect to Ca^{2+} handling and gene expression, was primarily observed in amPA females. However, since the experiments were sex-balanced, comparing female WT and female PA mice, it is unlikely that sex differences in physiology *per se*, is the contributing factor for the observed remodelling. Rather, this effect appears to be related to the PCC lesion and the accumulation of PA metabolites. Although the metabolomics experiment (Chapter 3) was underpowered for analysis by sex, there is evidence suggesting greater accumulation of propionate metabolites in females (plasma C3 and MeCit) (Guenzel *et al.*, 2015).

An important question, therefore, is whether the sex effect is only observed in experimental models, or whether there is an effect of sex on the prevalence of cardiac disease in human PA. However, based on the available evidence, it is unclear whether there are sex differences in PA. There have been five major clinical studies published to-date on cardiac complications in PA, summarised in Table 6.1. Whilst the sex of the total patient cohort is reported as standard, less information is available on which patients experience heart disease. Thus, it is inconclusive whether there is a sex effect in heart disease in human PA.

Table 6.1. Analysis for sex differences in the occurrence of heart disease in PA.

Study	Total study cohort (N)	Total % *(N)* with heart disease	% *(N)* with heart disease, by sex	
			Male	Female
Massoud and Leonard (1993)	19 (sex unknown)	Cardiomyopathy: 32% *(6)*	50% *(3)*	50% *(3)*
		LQTS: 5% *(1)*		100% *(1)*
Romano *et al.* (2010)	20 (12 M, 8 F)	DCM: 30% *(6)*	33% *(2)*	67% *(4)*
Baumgartner *et al.* (2007)	10 (6 M, 4F)	LQTS: 70% *(7)*	Unknown	
Grünert *et al.* (2013)	55 (35 M, 20 F)	Cardiomyopathy: 9% *(5)*	Unknown	
		LQTS: 22% *(12)*	Unknown	
Kovacevic *et al.* (2020)	18 (10 M, 8F)	HNDC: 39% *(7)*	71% *(5)*	29% *(2)*
		DCM: 11% *(2)*	100% *(2)*	-
		Diastolic dysfunction: 61% *(11)*	64% *(7)*	36% *(4)*

DCM, dilated cardiomyopathy; F, female; HNDC, hypokinetic non-dilated cardiomyopathy; LQTS, long-QT syndrome; M, male.

6.2.4 Other potential mechanisms

Non-histone protein propionylation. Immunoblotting of amPA total ventricular lysates indicated an increase in non-histone protein propionylation. Furthermore, there is some evidence for increased protein Kpr in PA patients (Pougovkina *et al.*, 2014). It is difficult to know how cytoplasmic protein Kpr may impact function, given that the identity of propionylated proteins are yet to be identified. However, it is useful to note that Kpr and Kac are considered to be biochemically similar PTMs and can occur on the same site (Sabari *et al.*, 2017), since there is more information available for the role of Kac in the heart. Notably, Kac of cardiac proteins, including those involved in E-C coupling, is recognised to have a modulatory role on cardiac function (Foster *et al.*, 2013). For example, recently, K492ac of SERCA was shown to significantly reduce its activity, and to be a molecular signature of failing hearts (Gorski *et al.*, 2019).

Free-fatty acid receptor signalling. It should be acknowledged that SCFAs, such as propionate, can act as G-protein-coupled receptor agonists and activate free fatty acid receptors (FFARs) (Kimura *et al.*, 2020). Propionate has been shown to activate G-protein coupled receptors GPR41 (FFAR3; $G_{i/o}$-coupled) and GPR43 (FFAR2; G_i/G_q-coupled) (Brown *et al.*, 2003). Although no changes to Ca^{2+} handling were observed on an acute scale by propionate, there is still the possibility that, on a chronic timescale, or *in vivo*, there is activation of FFARs. Interestingly, sympathetic ganglia have been shown to heavily express FFAR3 (GPR41), and propionate has been shown activate FFAR3 in sympathetic ganglia, which led to increased

noradrenaline release and increased HR (Kimura *et al.*, 2011). Since there is increased propionate in PA, one would expect increased activation of sympathetic ganglia, increased noradrenaline release, and activation of β-ARs. However, based on the cine-MRI experiment, the mechanism described by (Kimura *et al.*, 2011) does not appear to be applicable, since HR was not increased.

Endoplasmic reticulum stress & miRNAs. A recent study by Alonso-Barroso *et al.* (2021) characterised induced pluripotent stem cell (iPSC)-derived cardiomyocytes from a PA patient with defective PCCA. In their study, iPSC-derived PA cardiomyocytes exhibited reduced oxygen consumption and an accumulation of lipid droplets. The authors also observed increased expression of proteins associated with endoplasmic reticulum (ER) stress, such as homocysteine-inducible ER stress protein. Furthermore, reductions in several miRNAs were observed, such as miR-133a and miR-30c, which are regarded as being involved in adverse cardiac remodelling (van Rooij & Olson, 2012). However, it is unclear to what extent these changes can be directly attributed to propionate, since the major source of propionate metabolites *in vivo* is the liver (Wong *et al.*, 2006; Wilson *et al.*, 2017), and significant propionate accumulation may not be expected from a monolayer of cardiomyocytes, especially given that the authors state culture media was replaced every two days. Regardless, the possibility of ER stress and differential expression of miRNAs contributing to the cardiac phenotype *in vivo* in amPA, cannot be excluded without further study.

6.3 Summary of mechanisms

The phenotype of the PA mouse arises from disrupted PCC activity, which can produce a plethora of actions, evoked by the accumulation of propionate. These actions could be evoked by anionic propionate, propionate conjugates such as propionyl-CoA, or related substances such as 2-methylcitrate. Whilst all these triggers are relevant to the human disease, from the point of view of this investigation, the focus was to isolate early responses that may be amenable to proactive pharmacological therapy, in order to alleviate the onset/progression of severe dysfunction. The study was limited to the heart, but recognised that cardiac function can be influenced by extrinsic factors, such as haemodynamics.

The lead hypothesis of this study was that propionate is a biologically active substance. To test which aspects of the mouse phenotype could be attributable to this, experiments were also performed in isolated cardiomyocytes treated with propionate. It is important to consider that experimental noise and batch-effects can compromise power to resolve biological effects, and the analyses shown herein demonstrate a range of statistical significance. It is plausible, that some important early remodelling was below the detection threshold, particularly since a recently described compulsory hierarchical testing approach, was taken for cardiomyocyte-based experiments. Despite the vast complexity of the heart, its physiology can be characterised by a relatively small number of functional readouts, such as metabolism, electrophysiology, and contraction. For the purposes of simplicity, this thesis used readouts including the ECG,

contractile function, and Ca^{2+} signalling to assess the heart. Whilst not exhaustive, this was a necessary first step, in light of there being only a few studies in the area.

Propionate may affect the heart by directly acting on proteins in an allosteric manner, or by post-translational modifications such as propionylation, and these were the mechanisms primarily explored in this thesis. Whilst propionate is recognised to act as surface GPR agonists, if their actions are rapid, these are unlikely to be related to cardiomyocytes, given that propionate did not have an acute effect on Ca^{2+} handling. However, slower-onset actions, for example, on non-cardiomyocyte targets (e.g. sympathetic ganglia), cannot be excluded. One example however, of an 'acute' inhibitory action, that has longer-term readouts, is the inhibition of HDACs by propionate, causing epigenetic responses. Evidence for this mechanism was provided in this thesis through *in vitro* studies, by demonstrating propionate-evoked increases in histone Kac in a dose-dependent manner, and a large proportion of DEGs evoked by propionate being common with butyrate (canonical HDAC inhibitor). A significant number of DEGs in the PA mouse heart were also identified to align with those from *in vitro* studies, implicating HDAC inhibition as an important epigenetic mechanism *in vivo*. It remains to be seen however, whether the histone marks *in vitro* are observed *in vivo*. Indeed, a fraction of DEGs in the mouse heart were not *in vitro*, and these may reflect a response to other accumulated PA metabolites, a general stress response in the animal, or a product of compensatory mechanisms. Histone propionylation may also be relevant, although only a small fraction of DEGs in the mouse heart were putatively identified as genes sensitive to this

mechanism. Finally, a change in the activity of cardiac proteins such as those involved in E-C coupling through post-translational propionylation, cannot be excluded at this stage. MS of propionyllysine-enriched peptides to identify said proteins, would first be required.

6.4 Future perspectives

There are several avenues for future investigation which had been eluded to throughout this thesis. The key experiments are outlined below, in order of priority:

1. ***Diastolic function***: The raised LV EDV and ESV (cine-MRI), and increased cardiomyocyte diastolic [Ca^{2+}], implicates diastolic dysfunction as a key mechanism driving cardiac dysfunction in amPA. Diastolic function should be assessed in 8-week-old amPA animals by transmitral pulsed-wave and tissue Doppler echocardiography (E/e' ratio). However, the cine-MRI images from 8-week-old amPA should first be re-analysed to assess diastolic function (Roberts *et al.*, 2017), as well as the re-analysis of cardiomyocyte CaT images for cell shortening kinetics (Carnicer *et al.*, 2021).
2. ***Pde9a***: Upregulation of the cGMP-specific cardiac phosphodiesterase *Pde9a,* was the most significant DEG from the RNA-seq in amPA hearts. Increased PDE9A has been shown to be a critical driver of diastolic dysfunction. There are PDE9A inhibitors currently in human clinical trials for non-cardiac diseases. These inhibitors were recently repurposed in pre-clinical studies and were shown to reverse diastolic dysfunction in mouse models (Methawasin *et al.*, 2020; Richards *et al.*, 2021). Therefore, PDE9A inhibition could be a promising therapeutic target in PA and warrants prompt investigation. The next step would be to confirm the *Pde9a* hit via protein- and transcript-level analyses in 8-week-old amPA hearts. If the *Pde9a* hit is confirmed, echocardiography experiments should include an arm administering PDE9A inhibitors.

3. ***Epigenetics and histone modification sites:*** Whilst substantial evidence has been provided in this thesis demonstrating that (i) propionate evokes a change in cardiac histone modifications, and that (ii) there is a major change in cardiac gene expression in amPA, the mechanistic link has yet to be proven. ChIP-based methods are necessary in order to demonstrate the functional relevance of the changes in histone marks. ChIP-sequencing or ChIP-qPCR for selected genes (e.g. *Pde9a* after immunoprecipitating with H3K27ac), should be performed in 8-week-old amPA hearts. Furthermore, whilst this thesis focussed on selected histone Kac marks (based on findings from enrichment analysis), the involvement of other histone marks cannot be excluded. The histone acetylation and propionylation sites should be mapped in amPA hearts by histone MS-MS analysis using published methods (Mackeen *et al.*, 2010; Kebede *et al.*, 2017).
4. ***Propionylated proteome:*** It would be fascinating if lysine propionylation occurred on key E-C coupling proteins such as SERCA, troponin I, and titin. This should be investigated by MS analyses of total cardiac lysates enriched for propionylated lysines, for which there are already available commercially enrichment kits.
5. ***Sex differences in PA metabolic profile:*** A key piece of information missing from the metabolomics experiment was whether there was a sex-effect in the metabolite profile of PA mice. To determine this, IC-MS metabolomics should be repeated using a sex-balanced cohort of 8-week-old amPA heart and plasma samples.

6.5 Final conclusion

The work in this thesis sought to characterise the cardiac consequences of dysregulated propionate metabolism using a mouse model of PA, in which the levels of propionate generated *in vivo* produce a metabolic signature of PA, whilst allowing the animal to reach adulthood. Young adult PA mice manifested early signs of contractile dysfunction and changes to cardiomyocyte Ca^{2+} handling, preceding changes to electrophysiology. Although there is insufficient clinical information available to determine whether there is a sex-dependence of cardiac dysfunction in human PA, the evidence presented in this thesis demonstrate that, at least in the animal model, female PA mice have a more profound cardiac phenotype, compared to males, which may be related to sex differences in propionate metabolism.

Dysregulated propionate metabolism has a major effect on cardiac gene expression, including those critical to normal function. This effect is likely to be elicited through epigenetic mechanisms, with propionate acting canonically as a HDAC inhibitor, or non-canonically as the ligand for protein propionylation. This thesis sheds light on a potentially important mechanism underlying early diastolic dysfunction in PA, in which upregulation of *Pde9a*, and reduced cGMP-PKG signalling, provides a compelling explanation for the cardiac phenotype observed at the cellular and organ level. The upregulation of *Pde9a* is likely to involve propionate acting canonically as a HDAC inhibitor in the heart. PDE9A inhibitors are currently in clinical trials for non-cardiac diseases, opening the possibility for drug-repurposing in PA patients for the treatment of cardiac disease.

References

Adeniran I, MacIver DH, Hancox JC & Zhang H. (2015). Abnormal calcium homeostasis in heart failure with preserved ejection fraction is related to both reduced contractile function and incomplete relaxation: an electromechanically detailed biophysical modeling study. *Front Physiol* **6,** 78.

Adhikari AN, Gallagher RC, Wang Y, Currier RJ, Amatuni G, Bassaganyas L, Chen F, Kundu K, Kvale M, Mooney SD, *et al.* (2020). The role of exome sequencing in newborn screening for inborn errors of metabolism. *Nat Med* **26,** 1392-1397.

Aiken CGA. (2013). History of medical understanding and misunderstanding of Acid base balance. *J Clin Diagn Res* **7,** 2038-2041.

Allis CD, Berger SL, Cote J, Dent S, Jenuwien T, Kouzarides T, Pillus L, Reinberg D, Shi Y, Shiekhattar R, *et al.* (2007). New nomenclature for chromatin-modifying enzymes. *Cell* **131,** 633-636.

Alonso-Barroso E, Pérez B, Desviat LR & Richard E. (2021). Cardiomyocytes Derived from Induced Pluripotent Stem Cells as a Disease Model for Propionic Acidemia. *Int J Mol Sci* **22.**

Amin AS, Pinto YM & Wilde AAM. (2013). Long QT syndrome: beyond the causal mutation. *J Physiol* **591,** 4125-4139.

Amin NM, Greco TM, Kuchenbrod LM, Rigney MM, Chung MI, Wallingford JB, Cristea IM & Conlon FL. (2014). Proteomic profiling of cardiac tissue by isolation of nuclei tagged in specific cell types (INTACT). *Development* **141,** 962-973.

Ando T, Rasmussen K, Nyhan WL & Hull D. (1972a). 3-hydroxypropionate: significance of β-oxidation of propionate in patients with propionic acidemia and methylmalonic acidemia. *Proc Natl Acad Sci U S A* **69,** 2807-2811.

Ando T, Rasmussen K, Wright JM & Nyhan WL. (1972b). Isolation and identification of methylcitrate, a major metabolic product of propionate in patients with propionic acidemia. *J Biol Chem* **247,** 2200-2204.

Antzelevitch C & Shimizu W. (2002). Cellular mechanisms underlying the long QT syndrome. *Curr Opin Cardiol* **17,** 43-51.

Arbustini E, Favalli V, Narula N, Serio A & Grasso M. (2016). Left Ventricular Noncompaction: A Distinct Genetic Cardiomyopathy? *J Am Coll Cardiol* **68,** 949-966.

Argmann CA, Houten SM, Zhu J & Schadt EE. (2016). A Next Generation Multiscale View of Inborn Errors of Metabolism. *Cell Metab* **23,** 13-26.

Armstrong AJ, Collado MS, Henke BR, Olson MW, Hoang SA, Hamilton CA, Pourtaheri TD, Chapman KA, Summar MM, Johns BA, *et al.* (2021). A novel small molecule approach for the treatment of propionic and methylmalonic acidemias. *Mol Genet Metab*.

Bagchi RA & Weeks KL. (2019). Histone deacetylases in cardiovascular and metabolic diseases. *J Mol Cell Cardiol* **130,** 151-159.

Balligand JL & Hammond J. (2013). Protein kinase G type I in cardiac myocytes: unmasked at last? *Eur Heart J* **34,** 1181-1185.

Baruteau J, Hargreaves I, Krywawych S, Chalasani A, Land JM, Davison JE, Kwok MK, Christov G, Karimova A, Ashworth M, *et al.* (2014). Successful reversal of propionic acidaemia associated cardiomyopathy: evidence for low myocardial coenzyme Q10 status and secondary mitochondrial dysfunction as an underlying pathophysiological mechanism. *Mitochondrion* **17,** 150-156.

Bassani JW, Bassani RA & Bers DM. (1994). Relaxation in rabbit and rat cardiac cells: species-dependent differences in cellular mechanisms. *J Physiol* **476,** 279-293.

Bastos MB, Burkhoff D, Maly J, Daemen J, den Uil CA, Ameloot K, Lenzen M, Mahfoud F, Zijlstra F, Schreuder JJ, *et al.* (2020). Invasive left ventricle pressure-volume analysis: overview and practical clinical implications. *Eur Heart J* **41,** 1286-1297.

Baumgartner D, Scholl-Bürgi S, Sass JO, Sperl W, Schweigmann U, Stein J-I & Karall D. (2007). Prolonged QTc Intervals and Decreased Left Ventricular Contractility in Patients with Propionic Acidemia. *J Pediatr* **150,** 192-197.e191.

Baumgartner MR, Hörster F, Dionisi-Vici C, Haliloglu G, Karall D, Chapman KA, Huemer M, Hochuli M, Assoun M, Ballhausen D, *et al.* (2014). Proposed guidelines for the diagnosis and management of methylmalonic and propionic acidemia. *Orphanet J Rare Dis* **9,** 130.

Beale AL, Meyer P, Marwick TH, Lam CSP & Kaye DM. (2018). Sex Differences in Cardiovascular Pathophysiology: Why Women Are Overrepresented in Heart Failure With Preserved Ejection Fraction. *Circulation* **138,** 198-205.

Berend K, de Vries AP & Gans RO. (2014). Physiological approach to assessment of acid-base disturbances. *N Engl J Med* **371,** 1434-1445.

Berry GT, Blume ED, Wessel A, Singh T, Hecht L, Marsden D, Sahai I, Elisofon S, Ferguson M, Kim HB, *et al.* (2020). The re-occurrence of cardiomyopathy in propionic acidemia after liver transplantation. *JIMD Rep* **54,** 3-8.

Bers DM. (2001). *Excitation-Contraction Coupling and Cardiac Contractile Force*. Kluwer Academic Publishers.

Bers DM. (2002a). Cardiac excitation-contraction coupling. *Nature* **415,** 198-205.

Bers DM. (2002b). *Excitation-Contraction Coupling and Cardiac Contractile Force (2nd Ed.)*. Kluwer Academic Press, Dordrecht, Netherlands.

Bers DM. (2011). Ca^{2+}-calmodulin-dependent protein kinase II regulation of cardiac excitation-transcription coupling. *Heart Rhythm* **8,** 1101-1104.

Bertero A & Rosa-Garrido M. (2021). Three-dimensional chromatin organization in cardiac development and disease. *J Mol Cell Cardiol* **151,** 89-105.

Blaustein MP & Lederer WJ. (1999). Sodium/calcium exchange: its physiological implications. *Physiol Rev* **79,** 763-854.

Bodi I, Grunert SC, Becker N, Stoelzle-Feix S, Spiekerkoetter U, Zehender M, Bugger H, Bode C & Odening KE. (2016). Mechanisms of acquired long QT syndrome in patients with propionic academia. *Heart Rhythm* **13,** 1335-1345.

Bohnen MS, Peng G, Robey SH, Terrenoire C, Iyer V, Sampson KJ & Kass RS. (2017). Molecular Pathophysiology of Congenital Long QT Syndrome. *Physiol Rev* **97,** 89-134.

Bondarenko VE, Szigeti GP, Bett GC, Kim SJ & Rasmusson RL. (2004). Computer model of action potential of mouse ventricular myocytes. *Am J Physiol Heart Circ Physiol* **287,** H1378-1403.

Bonev B & Cavalli G. (2016). Organization and function of the 3D genome. *Nat Rev Genet* **17,** 661-678.

Bootman MD, Rietdorf K, Collins T, Walker S & Sanderson M. (2013). Ca2+-sensitive fluorescent dyes and intracellular Ca2+ imaging. *Cold Spring Harb Protoc* **2013,** 83-99.

Bora-Tatar G, Dayangaç-Erden D, Demir AS, Dalkara S, Yelekçi K & Erdem-Yurter H. (2009). Molecular modifications on carboxylic acid derivatives as potent histone deacetylase inhibitors: Activity and docking studies. *Bioorg Med Chem* **17,** 5219-5228.

Boukens BJ, Rivaud MR, Rentschler S & Coronel R. (2014). Misinterpretation of the mouse ECG: 'musing the waves of Mus musculus'. *J Physiol* **592,** 4613-4626.

Braunwald E. (2008). Biomarkers in heart failure. *N Engl J Med* **358,** 2148-2159.

Brown AJ, Goldsworthy SM, Barnes AA, Eilert MM, Tcheang L, Daniels D, Muir AI, Wigglesworth MJ, Kinghorn I, Fraser NJ, *et al.* (2003). The Orphan G protein-coupled receptors GPR41 and GPR43 are activated by propionate and other short chain carboxylic acids. *J Biol Chem* **278,** 11312-11319.

Bustin SA, Benes V, Garson JA, Hellemans J, Huggett J, Kubista M, Mueller R, Nolan T, Pfaffl MW, Shipley GL, *et al.* (2009). The MIQE guidelines: minimum information for publication of quantitative real-time PCR experiments. *Clin Chem* **55,** 611-622.

Butte NF, Liu Y, Zakeri IF, Mohney RP, Mehta N, Voruganti VS, Goring H, Cole SA & Comuzzie AG. (2015). Global metabolomic profiling targeting childhood obesity in the Hispanic population. *Am J Clin Nutr* **102,** 256-267.

Carnicer R, Duglan D, Ziberna K, Recalde A, Reilly S, Simon JN, Mafrici S, Arya R, Roselló-Lletí E, Chuaiphichai S, *et al.* (2021). BH4 Increases nNOS Activity and Preserves Left Ventricular Function in Diabetes. *Circ Res* **128,** 585-601.

Casey JR, Grinstein S & Orlowski J. (2010). Sensors and regulators of intracellular pH. *Nat Rev Mol Cell Biol* **11,** 50-61.

Chapman KA. (2019). Practical management of organic acidemias. *Transl Sci Rare Dis* **4,** 121-131.

Chapman KA, Gropman A, MacLeod E, Stagni K, Summar ML, Ueda K, Ah Mew N, Franks J, Island E, Matern D, *et al.* (2012). Acute management of propionic acidemia. *Mol Genet Metab* **105,** 16-25.

Chapski DJ, Rosa-Garrido M, Hua N, Alber F & Vondriska TM. (2018). Spatial Principles of Chromatin Architecture Associated With Organ-Specific Gene Regulation. *Front Cardiovasc Med* **5,** 186.

Charbit-Henrion F, Lacaille F, McKiernan P, Girard M, de Lonlay P, Valayannopoulos V, Ottolenghi C, Chakrapani A, Preece M, Sharif K, *et al.* (2015). Early and late complications after liver transplantation for propionic acidemia in children: a two centers study. *Am J Transplant* **15,** 786-791.

Cheema-Dhadli S, Leznoff CC & Halperin ML. (1975). Effect of 2-methylcitrate on citrate metabolism: implications for the management of patients with propionic acidemia and methylmalonic aciduria. *Pediatr Res* **9,** 905-908.

Chen-Izu Y, McCulle SL, Ward CW, Soeller C, Allen BM, Rabang C, Cannell MB, Balke CW & Izu LT. (2006). Three-dimensional distribution of ryanodine receptor clusters in cardiac myocytes. *Biophys J* **91,** 1-13.

Chen Y, Sprung R, Tang Y, Ball H, Sangras B, Kim SC, Falck JR, Peng J, Gu W & Zhao Y. (2007). Lysine propionylation and butyrylation are novel post-translational modifications in histones. *Mol Cell Proteomics* **6,** 812-819.

Cheng H & Lederer WJ. (2008). Calcium sparks. *Physiol Rev* **88,** 1491-1545.

Cheng H, Lederer WJ & Cannell MB. (1993). Calcium sparks: elementary events underlying excitation-contraction coupling in heart muscle. *Science* **262,** 740-744.

Cheng Z, Tang Y, Chen Y, Kim S, Liu H, Li SS, Gu W & Zhao Y. (2009). Molecular characterization of propionyllysines in non-histone proteins. *Mol Cell Proteomics* **8,** 45-52.

Childs B, Nyhan WL, Borden M, Bard L & Cooke RE. (1961). Idiopathic hyperglycinemia and hyperglycinuria: a new disorder of amino acid metabolism. I. *Pediatrics* **27,** 522-538.

Chopra N, Yang T, Asghari P, Moore ED, Huke S, Akin B, Cattolica RA, Perez CF, Hlaing T, Knollmann-Ritschel BE, *et al.* (2009). Ablation of triadin causes loss of cardiac Ca2+ release units, impaired excitation-contraction coupling, and cardiac arrhythmias. *Proc Natl Acad Sci U S A* **106,** 7636-7641.

Cingolani OH & Kass DA. (2011). Pressure-volume relation analysis of mouse ventricular function. *Am J Physiol Heart Circ Physiol* **301,** H2198-2206.

Coude FX, Ogier H, Grimber G, Parvy P, Pham Dinh D, Charpentier C & Saudubray JM. (1982). Correlation between blood ammonia concentration and organic acid accumulation in isovaleric and propionic acidemia. *Pediatrics* **69,** 115-117.

Critelli K, McKiernan P, Vockley J, Mazariegos G, Squires RH, Soltys K & Squires JE. (2018). Liver Transplantation for Propionic Acidemia and Methylmalonic Acidemia: Perioperative Management and Clinical Outcomes. *Liver Transpl* **24,** 1260-1270.

Cui M, Wang Z, Bassel-Duby R & Olson EN. (2018). Genetic and epigenetic regulation of cardiomyocytes in development, regeneration and disease. *Development* **145**.

Dai M, Xiao B, Zhang H, Ye J, Qiu W, Zhu H, Wang L, Liang L, Zhan X, Ji W, *et al.* (2020). Biochemical and genetic approaches to the prenatal diagnosis of propionic acidemia in 78 pregnancies. *Orphanet J Rare Dis* **15,** 276-276.

Davey PP. (2000). Which lead for Q-T interval measurements? *Cardiology* **94,** 159-164.

Davie JR. (2003). Inhibition of histone deacetylase activity by butyrate. *J Nutr* **133,** 2485s-2493s.

Davies SE, Iles RA, Stacey TE, de Sousa C & Chalmers RA. (1991). Carnitine therapy and metabolism in the disorders of propionyl-CoA metabolism studied using 1H-NMR spectroscopy. *Clinica chimica acta; international journal of clinical chemistry* **204,** 263-277.

Davis J, Maillet M, Miano JM & Molkentin JD. (2012). Lost in transgenesis: a user's guide for genetically manipulating the mouse in cardiac research. *Circ Res* **111,** 761-777.

de Keyzer Y, Valayannopoulos V, Benoist JF, Batteux F, Lacaille F, Hubert L, Chrétien D, Chadefeaux-Vekemans B, Niaudet P, Touati G, *et al.* (2009). Multiple OXPHOS deficiency in the liver, kidney, heart, and skeletal muscle of patients with methylmalonic aciduria and propionic aciduria. *Pediatr Res* **66,** 91-95.

Dempsey GA, Lyall HJ, Corke CF & Scheinkestel CD. (2000). Pyroglutamic acidemia: a cause of high anion gap metabolic acidosis. *Crit Care Med* **28,** 1803-1807.

Deodato F, Boenzi S, Santorelli FM & Dionisi-Vici C. (2006). Methylmalonic and propionic aciduria. *Am J Med Genet C Semin Med Genet* **142c,** 104-112.

Desviat LR, Perez B, Perez-Cerda C, Rodriguez-Pombo P, Clavero S & Ugarte M. (2004). Propionic acidemia: mutation update and functional and structural effects of the variant alleles. *Mol Genet Metab* **83,** 28-37.

Dewenter M, von der Lieth A, Katus HA & Backs J. (2017). Calcium Signaling and Transcriptional Regulation in Cardiomyocytes. *Circ Res* **121,** 1000-1020.

Di Virgilio F, Steinberg TH & Silverstein SC. (1990). Inhibition of Fura-2 sequestration and secretion with organic anion transport blockers. *Cell Calcium* **11,** 57-62.

Dimitrov B, Molema F, Williams M, Schmiesing J, Mühlhausen C, Baumgartner MR, Schumann A & Kölker S. (2020). Organic acidurias: Major gaps, new challenges, and a yet unfulfilled promise. *J Inherit Metab Dis*, 1-13.

Dobin A, Davis CA, Schlesinger F, Drenkow J, Zaleski C, Jha S, Batut P, Chaisson M & Gingeras TR. (2013). STAR: ultrafast universal RNA-seq aligner. *Bioinformatics* **29,** 15-21.

Dutta S & Sengupta P. (2016). Men and mice: Relating their ages. *Life Sci* **152,** 244-248.

Eisner DA. (2021). Pseudoreplication in physiology: More means less. *J Gen Physiol* **153**.

Eisner DA, Caldwell JL, Kistamás K & Trafford AW. (2017). Calcium and Excitation-Contraction Coupling in the Heart. *Circ Res* **121,** 181-195.

Eisner DA, Caldwell JL, Trafford AW & Hutchings DC. (2020). The Control of Diastolic Calcium in the Heart: Basic Mechanisms and Functional Implications. *Circ Res* **126,** 395-412.

Fabiato A. (1983). Calcium-induced release of calcium from the cardiac sarcoplasmic reticulum. *Am J Physiol* **245,** C1-14.

Falk M, Feodorova Y, Naumova N, Imakaev M, Lajoie BR, Leonhardt H, Joffe B, Dekker J, Fudenberg G, Solovei I, *et al.* (2019). Heterochromatin drives compartmentalization of inverted and conventional nuclei. *Nature* **570,** 395-399.

Finnin MS, Donigian JR, Cohen A, Richon VM, Rifkind RA, Marks PA, Breslow R & Pavletich NP. (1999). Structures of a histone deacetylase homologue bound to the TSA and SAHA inhibitors. *Nature* **401,** 188-193.

Fosang AJ & Colbran RJ. (2015). Transparency Is the Key to Quality. *J Biol Chem* **290,** 29692-29694.

Foster DB, Liu T, Rucker J, O'Meally RN, Devine LR, Cole RN & O'Rourke B. (2013). The cardiac acetyl-lysine proteome. *PLoS One* **8,** e67513-e67513.

Fraser JL & Venditti CP. (2016). Methylmalonic and propionic acidemias: clinical management update. *Curr Opin Pediatr* **28,** 682-693.

Fulgencio-Covian A, Alonso-Barroso E, Guenzel AJ, Rivera-Barahona A, Ugarte M, Perez B, Barry MA, Perez-Cerda C, Richard E & Desviat LR. (2020). Pathogenic implications of dysregulated miRNAs in propionic acidemia related cardiomyopathy. *Transl Res* **218,** 43-56.

Gallego-Villar L, Pérez-Cerdá C, Pérez B, Abia D, Ugarte M, Richard E & Desviat LR. (2013). Functional characterization of novel genotypes and cellular oxidative stress studies in propionic acidemia. *J Inherit Metab Dis* **36,** 731-740.

Gallego-Villar L, Rivera-Barahona A, Cuevas-Martin C, Guenzel A, Perez B, Barry MA, Murphy MP, Logan A, Gonzalez-Quintana A, Martin MA, *et al.* (2016). In vivo evidence of mitochondrial dysfunction and altered redox homeostasis in a genetic mouse model of propionic acidemia: Implications for the pathophysiology of this disorder. *Free Radic Biol Med* **96,** 1-12.

Galletly DC, Westenberg AM, Robinson BJ & Corfiatis T. (1994). Effect of halothane, isoflurane and fentanyl on spectral components of heart rate variability. *Br J Anaesth* **72,** 177-180.

Gao X, Zhang W, Wang Y, Pedram P, Cahill F, Zhai G, Randell E, Gulliver W & Sun G. (2016). Serum metabolic biomarkers distinguish metabolically healthy peripherally obese from unhealthy centrally obese individuals. *Nutr Metab* **13,** 33.

Garciarena CD, Youm JB, Swietach P & Vaughan-Jones RD. (2013). H^+-activated Na^+ influx in the ventricular myocyte couples Ca^{2+}-signalling to intracellular pH. *J Mol Cell Cardiol* **61,** 51-59.

Georgakopoulos D & Kass D. (2001). Minimal force-frequency modulation of inotropy and relaxation of in situ murine heart. *J Physiol* **534,** 535-545.

Gerdts E & Regitz-Zagrosek V. (2019). Sex differences in cardiometabolic disorders. *Nat Med* **25,** 1657-1666.

Gibbs RA, Weinstock GM, Metzker ML, Muzny DM, Sodergren EJ, Scherer S, Scott G, Steffen D, Worley KC, Burch PE, *et al.* (2004). Genome sequence of the Brown Norway rat yields insights into mammalian evolution. *Nature* **428,** 493-521.

Gillette TG & Hill JA. (2015). Readers, writers, and erasers: chromatin as the whiteboard of heart disease. *Circ Res* **116,** 1245-1253.

Gompertz D, Storrs CN, Bau DC, Peters TJ & Hughes EA. (1970). Localisation of enzymic defect in propionicacidaemia. *Lancet* **1,** 1140-1143.

Goncharov NV, Jenkins RO & Radilov AS. (2006). Toxicology of fluoroacetate: a review, with possible directions for therapy research. *J Appl Toxicol* **26,** 148-161.

Görlich D & Kutay U. (1999). Transport between the cell nucleus and the cytoplasm. *Annu Rev Cell Dev Biol* **15,** 607-660.

Gorski PA, Jang SP, Jeong D, Lee A, Lee P, Oh JG, Chepurko V, Yang DK, Kwak TH, Eom SH, *et al.* (2019). Role of SIRT1 in Modulating Acetylation of the Sarco-Endoplasmic Reticulum Ca(2+)-ATPase in Heart Failure. *Circ Res* **124,** e63-e80.

Griffin JL, Atherton H, Shockcor J & Atzori L. (2011). Metabolomics as a tool for cardiac research. *Nat Rev Cardiol* **8,** 630-643.

Grünert SC, Müllerleile S, De Silva L, Barth M, Walter M, Walter K, Meissner T, Lindner M, Ensenauer R, Santer R, *et al.* (2013). Propionic acidemia: clinical course and outcome in 55 pediatric and adolescent patients. *Orphanet J Rare Dis* **8,** 6-6.

Grünert SC, Wendel U, Lindner M, Leichsenring M, Schwab KO, Vockley J, Lehnert W & Ensenauer R. (2012). Clinical and neurocognitive outcome in symptomatic isovaleric acidemia. *Orphanet J Rare Dis* **7,** 9-9.

Guenzel AJ, Collard R, Kraus JP, Matern D & Barry MA. (2015). Long-term sex-biased correction of circulating propionic acidemia disease markers by adeno-associated virus vectors. *Hum Gene Ther* **26,** 153-160.

Guenzel AJ, Hofherr SE, Hillestad M, Barry M, Weaver E, Venezia S, Kraus JP, Matern D & Barry MA. (2013). Generation of a hypomorphic model of propionic acidemia amenable to gene therapy testing. *Mol Ther* **21,** 1316-1323.

Haan C & Behrmann I. (2007). A cost effective non-commercial ECL-solution for Western blot detections yielding strong signals and low background. *J Immunol Methods* **318,** 11-19.

Haberland M, Montgomery RL & Olson EN. (2009). The many roles of histone deacetylases in development and physiology: implications for disease and therapy. *Nat Rev Genet* **10,** 32-42.

Halestrap AP & Wilson MC. (2012). The monocarboxylate transporter family--role and regulation. *IUBMB Life* **64,** 109-119.

Han P, Hang CT, Yang J & Chang CP. (2011). Chromatin remodeling in cardiovascular development and physiology. *Circ Res* **108,** 378-396.

Haws SA, Leech CM & Denu JM. (2020). Metabolism and the Epigenome: A Dynamic Relationship. *Trends Biochem Sci* **45,** 731-747.

Herring N & Paterson DJ. (2018). *Levick's Introduction to Cardiovascular Physiology (6th edn)*. CRC Press.

Hiess F, Detampel P, Nolla-Colomer C, Vallmitjana A, Ganguly A, Amrein M, Ter Keurs H, Benítez R, Hove-Madsen L & Chen SRW. (2018). Dynamic and Irregular Distribution of RyR2 Clusters in the Periphery of Live Ventricular Myocytes. *Biophys J* **114,** 343-354.

Ho D, Zhao X, Gao S, Hong C, Vatner DE & Vatner SF. (2011). Heart Rate and Electrocardiography Monitoring in Mice. *Curr Protoc Mouse Biol* **1,** 123-139.

Hommes FA, Kuipers JR, Elema JD, Jansen JF & Jonxis JH. (1968). Propionicacidemia, a new inborn error of metabolism. *Pediatr Res* **2,** 519-524.

Hong T & Shaw RM. (2017). Cardiac T-Tubule Microanatomy and Function. *Physiol Rev* **97,** 227-252.

Hsia YE, Scully KJ & Rosenberg LE. (1969). Defective propionate carboxylation in ketotic hyperglycinaemia. *Lancet* **1,** 757-758.

Hsia YE, Scully KJ & Rosenberg LE. (1971). Inherited propionyl-Coa carboxylase deficiency in "ketotic hyperglycinemia". *J Clin Invest* **50,** 127-130.

Huang DW, Sherman BT & Lempicki RA. (2009). Systematic and integrative analysis of large gene lists using DAVID bioinformatics resources. *Nat Protoc* **4,** 44-57.

Jameson E & Walter J. (2008). Cardiac arrest secondary to long QT(C)in a child with propionic acidemia. *Pediatr Cardiol* **29,** 969-970.

Jefferies JL & Towbin JA. (2010). Dilated cardiomyopathy. *Lancet* **375,** 752-762.

Kaczmarska Z, Ortega E, Goudarzi A, Huang H, Kim S, Márquez JA, Zhao Y, Khochbin S & Panne D. (2017). Structure of p300 in complex with acyl-CoA variants. *Nat Chem Biol* **13,** 21-29.

Kaese S & Verheule S. (2012). Cardiac electrophysiology in mice: a matter of size. *Front Physiol* **3,** 345.

Kasahara M, Sakamoto S, Kanazawa H, Karaki C, Kakiuchi T, Shigeta T, Fukuda A, Kosaki R, Nakazawa A, Ishige M, *et al.* (2012). Living-donor liver transplantation for propionic acidemia. *Pediatr Transplant* **16,** 230-234.

Katz AM. (1988). Influence of altered inotropy and lusitropy on ventricular pressure-volume loops. *J Am Coll Cardiol* **11,** 438-445.

Katz AM & Rolett EL. (2016). Heart failure: when form fails to follow function. *Eur Heart J* **37,** 449-454.

Kebede AF, Nieborak A, Shahidian LZ, Le Gras S, Richter F, Gomez DA, Baltissen MP, Meszaros G, Magliarelli HF, Taudt A, *et al.* (2017). Histone propionylation is a mark of active chromatin. *Nat Struct Mol Biol* **24,** 1048-1056.

Kimura I, Ichimura A, Ohue-Kitano R & Igarashi M. (2020). Free Fatty Acid Receptors in Health and Disease. *Physiol Rev* **100,** 171-210.

Kimura I, Inoue D, Maeda T, Hara T, Ichimura A, Miyauchi S, Kobayashi M, Hirasawa A & Tsujimoto G. (2011). Short-chain fatty acids and ketones directly regulate sympathetic nervous system via G protein-coupled receptor 41 (GPR41). *Proc Natl Acad Sci U S A* **108,** 8030-8035.

Koh A, De Vadder F, Kovatcheva-Datchary P & Backhed F. (2016). From Dietary Fiber to Host Physiology: Short-Chain Fatty Acids as Key Bacterial Metabolites. *Cell* **165,** 1332-1345.

Kohlhaas M, Nickel AG & Maack C. (2017). Mitochondrial energetics and calcium coupling in the heart. *J Physiol* **595,** 3753-3763.

Kolwicz SC, Jr., Purohit S & Tian R. (2013). Cardiac metabolism and its interactions with contraction, growth, and survival of cardiomyocytes. *Circ Res* **113,** 603-616.

Konstam MA & Abboud FM. (2017). Ejection Fraction: Misunderstood and Overrated (Changing the Paradigm in Categorizing Heart Failure). *Circulation* **135,** 717-719.

Korhonen T, Hänninen SL & Tavi P. (2009). Model of excitation-contraction coupling of rat neonatal ventricular myocytes. *Biophys J* **96,** 1189-1209.

Kovacevic A, Garbade SF, Hoffmann GF, Gorenflo M, Kölker S & Staufner C. (2020). Cardiac phenotype in propionic acidemia – Results of an observational monocentric study. *Mol Genet Metab* **130,** 41-48.

Kranias EG & Hajjar RJ. (2012). Modulation of cardiac contractility by the phospholamban/SERCA2a regulatome. *Circ Res* **110,** 1646-1660.

Kravtsov GM, Kam KW, Liu J, Wu S & Wong TM. (2007). Altered Ca(2+) handling by ryanodine receptor and Na(+)-Ca(2+) exchange in the heart from ovariectomized rats: role of protein kinase A. *Am J Physiol Cell Physiol* **292,** C1625-1635.

Kujoth GC, Hiona A, Pugh TD, Someya S, Panzer K, Wohlgemuth SE, Hofer T, Seo AY, Sullivan R, Jobling WA, *et al.* (2005). Mitochondrial DNA mutations, oxidative stress, and apoptosis in mammalian aging. *Science* **309,** 481-484.

Kuleshov MV, Jones MR, Rouillard AD, Fernandez NF, Duan Q, Wang Z, Koplev S, Jenkins SL, Jagodnik KM, Lachmann A, *et al.* (2016). Enrichr: a comprehensive gene set enrichment analysis web server 2016 update. *Nucleic Acids Res* **44,** W90-97.

Kupittayanant P, Trafford AW, Díaz ME & Eisner DA. (2006). A mechanism distinct from the L-type Ca current or Na-Ca exchange contributes to Ca entry in rat ventricular myocytes. *Cell Calcium* **39,** 417-423.

Landstrom AP, Dobrev D & Wehrens XHT. (2017). Calcium Signaling and Cardiac Arrhythmias. *Circ Res* **120,** 1969-1993.

Lanpher B, Brunetti-Pierri N & Lee B. (2006). Inborn errors of metabolism: the flux from Mendelian to complex diseases. *Nat Rev Genet* **7,** 449-460.

Lee DI, Zhu G, Sasaki T, Cho GS, Hamdani N, Holewinski R, Jo SH, Danner T, Zhang M, Rainer PP, *et al.* (2015). Phosphodiesterase 9A controls nitric-oxide-independent cGMP and hypertrophic heart disease. *Nature* **519,** 472-476.

Lee TM, Addonizio LJ, Barshop BA & Chung WK. (2009). Unusual presentation of propionic acidaemia as isolated cardiomyopathy. *J Inherit Metab Dis* **32 Suppl 1,** S97-S101.

Lee TM, Hsu DT, Kantor P, Towbin JA, Ware SM, Colan SD, Chung WK, Jefferies JL, Rossano JW, Castleberry CD, *et al.* (2017). Pediatric Cardiomyopathies. *Circ Res* **121,** 855-873.

Leonard JV. (1995). The management and outcome of propionic and methylmalonic acidaemia. *J Inherit Metab Dis* **18,** 430-434.

Leonard JV. (1997). Stable isotope studies in propionic and methylmalonic acidaemia. *Eur J Pediatr* **156,** S67-69.

Lewis GA, Schelbert EB, Williams SG, Cunnington C, Ahmed F, McDonagh TA & Miller CA. (2017). Biological Phenotypes of Heart Failure With Preserved Ejection Fraction. *J Am Coll Cardiol* **70,** 2186-2200.

Li H, Handsaker B, Wysoker A, Fennell T, Ruan J, Homer N, Marth G, Abecasis G & Durbin R. (2009). The Sequence Alignment/Map format and SAMtools. *Bioinformatics* **25,** 2078-2079.

Li L, Louch WE, Niederer SA, Andersson KB, Christensen G, Sejersted OM & Smith NP. (2011). Calcium dynamics in the ventricular myocytes of SERCA2 knockout mice: A modeling study. *Biophys J* **100,** 322-331.

Li P, Ge J & Li H. (2020). Lysine acetyltransferases and lysine deacetylases as targets for cardiovascular disease. *Nat Rev Cardiol* **17,** 96-115.

Li X, Egervari G, Wang Y, Berger SL & Lu Z. (2018). Regulation of chromatin and gene expression by metabolic enzymes and metabolites. *Nat Rev Mol Cell Biol* **19,** 563-578.

Li Y, Baldwin TA, Wang Y, Subramaniam J, Carbajal AG, Brand CS, Cunha SR & Dessauer CW. (2017). Loss of type 9 adenylyl cyclase triggers reduced phosphorylation of Hsp20 and diastolic dysfunction. *Sci Rep* **7,** 5522-5522.

Liao Y, Smyth GK & Shi W. (2014). featureCounts: an efficient general purpose program for assigning sequence reads to genomic features. *Bioinformatics* **30,** 923-930.

Lindsey ML, Kassiri Z, Virag JAI, de Castro Brás LE & Scherrer-Crosbie M. (2018). Guidelines for measuring cardiac physiology in mice. *Am J Physiol Heart Circ Physiol* **314,** H733-h752.

Lipshultz SE, Law YM, Asante-Korang A, Austin ED, Dipchand AI, Everitt MD, Hsu DT, Lin KY, Price JF, Wilkinson JD, *et al.* (2019). Cardiomyopathy in Children: Classification and Diagnosis: A Scientific Statement From the American Heart Association. *Circulation* **140,** e9-e68.

Litviňuková M, Talavera-López C, Maatz H, Reichart D, Worth CL, Lindberg EL, Kanda M, Polanski K, Heinig M, Lee M, *et al.* (2020). Cells of the adult human heart. *Nature* **588,** 466-472.

Liu C-F & Tang WHW. (2019). Epigenetics in Cardiac Hypertrophy and Heart Failure. *JACC Basic Transl Sci* **4,** 976-993.

Livak KJ & Schmittgen TD. (2001). Analysis of relative gene expression data using real-time quantitative PCR and the 2(-Delta Delta C(T)) Method. *Methods* **25,** 402-408.

Loonat AA, Curtis MK, Richards MA, Nunez-Alonso G, Michl J & Swietach P. (2019). A high-throughput ratiometric method for imaging hypertrophic growth in cultured primary cardiac myocytes. *J Mol Cell Cardiol* **130,** 184-196.

Love MI, Huber W & Anders S. (2014). Moderated estimation of fold change and dispersion for RNA-seq data with DESeq2. *Genome Biol* **15,** 550.

Lu Q, Yang YT, Chen CS, Davis M, Byrd JC, Etherton MR, Umar A & Chen CS. (2004). Zn2+-chelating motif-tethered short-chain fatty acids as a novel class of histone deacetylase inhibitors. *J Med Chem* **47,** 467-474.

Mackeen MM, Kramer HB, Chang KH, Coleman ML, Hopkinson RJ, Schofield CJ & Kessler BM. (2010). Small-molecule-based inhibition of histone demethylation in cells assessed by quantitative mass spectrometry. *J Proteome Res* **9,** 4082-4092.

MacLennan DH & Kranias EG. (2003). Phospholamban: a crucial regulator of cardiac contractility. *Nat Rev Mol Cell Biol* **4,** 566-577.

MacQuaide N, Dempster J & Smith GL. (2007). Measurement and modeling of Ca2+ waves in isolated rabbit ventricular cardiomyocytes. *Biophys J* **93,** 2581-2595.

Mardach R, Verity MA & Cederbaum SD. (2005). Clinical, pathological, and biochemical studies in a patient with propionic acidemia and fatal cardiomyopathy. *Mol Genet Metab* **85,** 286-290.

Maroli G & Braun T. (2021). The long and winding road of cardiomyocyte maturation. *Cardiovasc Res* **117,** 712-726.

Massoud AF & Leonard JV. (1993). Cardiomyopathy in propionic acidaemia. *Eur J Pediatr* **152,** 441-445.

Mayourian J, Ceholski DK, Gonzalez DM, Cashman TJ, Sahoo S, Hajjar RJ & Costa KD. (2018). Physiologic, Pathologic, and Therapeutic Paracrine Modulation of Cardiac Excitation-Contraction Coupling. *Circ Res* **122,** 167-183.

Mehta V, Pang KL, Rozbesky D, Nather K, Keen A, Lachowski D, Kong Y, Karia D, Ameismeier M, Huang J, *et al.* (2020). The guidance receptor plexin D1 is a mechanosensor in endothelial cells. *Nature* **578,** 290-295.

Merinero B, DelValle JA, Jimenez A, Garcia MJ, Ugarte M, Solaguren R, Lopez O & Condado I. (1981). Late onset type of propionic acidaemia: case report and biochemical studies. *J Inherit Metab Dis* **4,** 71-72.

Methawasin M, Strom J, Borkowski T, Hourani Z, Runyan R, Smith JE, 3rd & Granzier H. (2020). Phosphodiesterase 9a Inhibition in Mouse Models of Diastolic Dysfunction. *Circ Heart Fail* **13,** e006609.

Michl J, Park KC & Swietach P. (2019). Evidence-based guidelines for controlling pH in mammalian live-cell culture systems. *Commun Biol* **2,** 144.

Mihalik SJ, Goodpaster BH, Kelley DE, Chace DH, Vockley J, Toledo FG & DeLany JP. (2010). Increased levels of plasma acylcarnitines in obesity and type 2 diabetes and identification of a marker of glucolipotoxicity. *Obesity (Silver Spring)* **18,** 1695-1700.

Miller TA, Witter DJ & Belvedere S. (2003). Histone deacetylase inhibitors. *J Med Chem* **46,** 5097-5116.

Mitchell GF, Jeron A & Koren G. (1998). Measurement of heart rate and Q-T interval in the conscious mouse. *Am J Physiol* **274,** H747-751.

Mitcheson JS, Chen J, Lin M, Culberson C & Sanguinetti MC. (2000). A structural basis for drug-induced long QT syndrome. *Proc Natl Acad Sci U S A* **97,** 12329.

Miyazaki T, Ohura T, Kobayashi M, Shigematsu Y, Yamaguchi S, Suzuki Y, Hata I, Aoki Y, Yang X, Minjares C, *et al.* (2001). Fatal propionic acidemia in mice lacking propionyl-CoA carboxylase and its rescue by postnatal, liver-specific supplementation via a transgene. *J Biol Chem* **276,** 35995-35999.

Moss AJ & Kass RS. (2005). Long QT syndrome: from channels to cardiac arrhythmias. *J Clin Invest* **115,** 2018-2024.

Mulla W, Gillis R, Murninkas M, Klapper-Goldstein H, Gabay H, Mor M, Elyagon S, Liel-Cohen N, Bernus O & Etzion Y. (2018). Unanesthetized Rodents Demonstrate Insensitivity of QT Interval and Ventricular Refractory Period to Pacing Cycle Length. *Front Physiol* **9,** 897-897.

Murphy E, Amanakis G, Fillmore N, Parks RJ & Sun J. (2017). Sex Differences in Metabolic Cardiomyopathy. *Cardiovasc Res* **113,** 370-377.

Nagueh SF. (2020). Left Ventricular Diastolic Function: Understanding Pathophysiology, Diagnosis, and Prognosis With Echocardiography. *JACC Cardiovasc Imaging* **13,** 228-244.

Nakamura M & Sadoshima J. (2018). Mechanisms of physiological and pathological cardiac hypertrophy. *Nat Rev Cardiol* **15,** 387-407.

Naranjo JR & Mellström B. (2012). Ca2+-dependent transcriptional control of Ca2+ homeostasis. *J Biol Chem* **287,** 31674-31680.

Narita T, Weinert BT & Choudhary C. (2019). Functions and mechanisms of non-histone protein acetylation. *Nat Rev Mol Cell Biol* **20,** 156-174.

Nerbonne JM. (2004). Studying cardiac arrhythmias in the mouse--a reasonable model for probing mechanisms? *Trends Cardiovasc Med* **14,** 83-93.

Neubauer S. (2007). The failing heart--an engine out of fuel. *N Engl J Med* **356,** 1140-1151.

Nott A, Watson PM, Robinson JD, Crepaldi L & Riccio A. (2008). S-Nitrosylation of histone deacetylase 2 induces chromatin remodelling in neurons. *Nature* **455,** 411-415.

Nyhan WL, Borden M & Childs B. (1961). Idiopathic hyperglycinemia: a new disorder of amino acid metabolism. II. The concentrations of other amino acids in the plasma and their modification by the administration of leucine. *Pediatrics* **27,** 539-550.

Oberholzer VG, Levin B, Burgess EA & Young WF. (1967). Methylmalonic aciduria. An inborn error of metabolism leading to chronic metabolic acidosis. *Arch Dis Child* **42,** 492-504.

Obokata M, Reddy YNV & Borlaug BA. (2020). Diastolic Dysfunction and Heart Failure With Preserved Ejection Fraction: Understanding Mechanisms by Using Noninvasive Methods. *JACC Cardiovasc Imaging* **13,** 245-257.

Omar HR, El-Khabiry E, Mangar D & Camporesi EM. (2016). The effect of various stages of hypothermia on the ECG. *Cardiovasc Endocrinol Metab* **5**.

Ongstad E & Kohl P. (2016). Fibroblast-myocyte coupling in the heart: Potential relevance for therapeutic interventions. *J Mol Cell Cardiol* **91,** 238-246.

Palladino AA, Chen J, Kallish S, Stanley CA & Bennett MJ. (2012). Measurement of tissue acyl-CoAs using flow-injection tandem mass spectrometry: acyl-CoA profiles in short-chain fatty acid oxidation defects. *Mol Genet Metab* **107,** 679-683.

Pan W, Yang Z, Cheng J, Qian C & Wang Y. (2018). Contractile heterogeneity in ventricular myocardium. *Journal of cellular physiology* **233,** 6273-6279.

Pandit SV, Clark RB, Giles WR & Demir SS. (2001). A mathematical model of action potential heterogeneity in adult rat left ventricular myocytes. *Biophys J* **81,** 3029-3051.

Papait R, Cattaneo P, Kunderfranco P, Greco C, Carullo P, Guffanti A, Vigano V, Stirparo GG, Latronico MV, Hasenfuss G, *et al.* (2013). Genome-wide analysis of histone marks identifying an epigenetic signature of promoters and enhancers underlying cardiac hypertrophy. *Proc Natl Acad Sci U S A* **110,** 20164-20169.

Papait R, Serio S & Condorelli G. (2020). Role of the Epigenome in Heart Failure. *Physiol Rev* **100,** 1753-1777.

Park KC, Gaze DC, Collinson PO & Marber MS. (2017). Cardiac troponins: from myocardial infarction to chronic disease. *Cardiovasc Res* **113,** 1708-1718.

Park KC, Krywawych S, Richard E, Desviat LR & Swietach P. (2020). Cardiac Complications of Propionic and Other Inherited Organic Acidemias. *Front Cardiovasc Med* **7,** 617451.

Park PJ. (2009). ChIP-seq: advantages and challenges of a maturing technology. *Nat Rev Genet* **10,** 669-680.

Parks RJ, Ray G, Bienvenu LA, Rose RA & Howlett SE. (2014). Sex differences in SR Ca(2+) release in murine ventricular myocytes are regulated by the cAMP/PKA pathway. *J Mol Cell Cardiol* **75,** 162-173.

Pavlović D, McLatchie LM & Shattock MJ. (2010). The rate of loss of T-tubules in cultured adult ventricular myocytes is species dependent. *Exp Physiol* **95,** 518-527.

Pena L, Franks J, Chapman KA, Gropman A, Ah Mew N, Chakrapani A, Island E, MacLeod E, Matern D, Smith B, *et al.* (2012). Natural history of propionic acidemia. *Mol Genet Metab* **105,** 5-9.

Peoples JN, Saraf A, Ghazal N, Pham TT & Kwong JQ. (2019). Mitochondrial dysfunction and oxidative stress in heart disease. *Exp Mol Med* **51,** 1-13.

Pereira NL, Aksoy P, Moon I, Peng Y, Redfield MM, Burnett JC, Jr., Wieben ED, Yee VC & Weinshilboum RM. (2010). Natriuretic peptide pharmacogenetics: membrane metallo-endopeptidase (MME): common gene sequence variation, functional characterization and degradation. *J Mol Cell Cardiol* **49,** 864-874.

Peterson LR, Soto PF, Herrero P, Mohammed BS, Avidan MS, Schechtman KB, Dence C & Gropler RJ. (2008). Impact of gender on the myocardial metabolic response to obesity. *JACC Cardiovasc Imaging* **1,** 424-433.

Pietrocola F, Galluzzi L, Bravo-San Pedro JM, Madeo F & Kroemer G. (2015). Acetyl coenzyme A: a central metabolite and second messenger. *Cell Metab* **21,** 805-821.

Pinto YM, Elliott PM, Arbustini E, Adler Y, Anastasakis A, Böhm M, Duboc D, Gimeno J, de Groote P, Imazio M, *et al.* (2016). Proposal for a revised definition of dilated cardiomyopathy, hypokinetic non-dilated cardiomyopathy, and its implications for clinical practice: a position statement of the ESC working group on myocardial and pericardial diseases. *Eur Heart J* **37,** 1850-1858.

Piper HM. (2000). The calcium paradox revisited: an artefact of great heuristic value. *Cardiovasc Res* **45,** 123-127.

Pougovkina O, Te Brinke H, Wanders RJ, Houten SM & de Boer VC. (2014). Aberrant protein acylation is a common observation in inborn errors of acyl-CoA metabolism. *J Inherit Metab Dis* **37,** 709-714.

Proudfoot AT, Bradberry SM & Vale JA. (2006). Sodium fluoroacetate poisoning. *Toxicol Rev* **25,** 213-219.

Rafique M. (2013). Clinical spectrum of propionic acidaemia. *J Nutr Metab* **2013,** 975964.

Ramirez FD, Motazedian P, Jung RG, Di Santo P, MacDonald Z, Simard T, Clancy AA, Russo JJ, Welch V, Wells GA, *et al.* (2017). Sex Bias Is Increasingly Prevalent in Preclinical Cardiovascular Research: Implications for Translational Medicine and Health Equity for Women: A Systematic Assessment of Leading Cardiovascular Journals Over a 10-Year Period. *Circulation* **135,** 625-626.

Rasmussen K, Ando T, Nyhan WL, Hull D, Cottom D, Donnell G, Wadlington W & Kilroy AW. (1972). Excretion of propionylglycine in propionic acidaemia. *Clin Sci* **42,** 665-671.

Regitz-Zagrosek V & Kararigas G. (2017). Mechanistic Pathways of Sex Differences in Cardiovascular Disease. *Physiol Rev* **97,** 1-37.

Reid MA, Dai Z & Locasale JW. (2017). The impact of cellular metabolism on chromatin dynamics and epigenetics. *Nat Cell Biol* **19,** 1298-1306.

Richard E, Gallego-Villar L, Rivera-Barahona A, Oyarzábal A, Pérez B, Rodríguez-Pombo P & Desviat LR. (2018). Altered Redox Homeostasis in Branched-Chain Amino Acid Disorders, Organic Acidurias, and Homocystinuria. *Oxid Med Cell Longev* **2018,** 1246069.

Richard E, Pérez B, Pérez-Cerdá C & Desviat LR. (2015). Understanding molecular mechanisms in propionic acidemia and investigated therapeutic strategies. *Expert Opin Orphan Drugs* **3,** 1427-1438.

Richards DA, Aronovitz MJ, Liu P, Martin GL, Tam K, Pande S, Karas RH, Bloomfield DM, Mendelsohn ME & Blanton RM. (2021). CRD-733, a Novel PDE9 (Phosphodiesterase 9) Inhibitor, Reverses Pressure Overload-Induced Heart Failure. *Circ Heart Fail* **14,** e007300.

Riemersma M, Hazebroek MR, Helderman-van den Enden A, Salomons GS, Ferdinandusse S, Brouwers M, van der Ploeg L, Heymans S, Glatz JFC, van den Wijngaard A, *et al.* (2017). Propionic acidemia as a cause of adult-onset dilated cardiomyopathy. *Eur J Hum Genet* **25,** 1195-1201.

Ringnér M. (2008). What is principal component analysis? *Nat Biotechnol* **26,** 303-304.

Ritterhoff J & Tian R. (2017). Metabolism in cardiomyopathy: every substrate matters. *Cardiovasc Res* **113,** 411-421.

Rivera-Barahona A, Alonso-Barroso E, Perez B, Murphy MP, Richard E & Desviat LR. (2017a). Treatment with antioxidants ameliorates oxidative damage in a mouse model of propionic acidemia. *Mol Genet Metab* **122,** 43-50.

Rivera-Barahona A, Fulgencio-Covian A, Perez-Cerda C, Ramos R, Barry MA, Ugarte M, Perez B, Richard E & Desviat LR. (2017b). Dysregulated miRNAs and their pathogenic implications for the neurometabolic disease propionic acidemia. *Sci Rep* **7,** 5727.

Rivera-Barahona A, Navarrete R, García-Rodríguez R, Richard E, Ugarte M, Pérez-Cerda C, Pérez B, Gámez A & Desviat LR. (2018). Identification of 34 novel mutations in propionic acidemia: Functional characterization of missense variants and phenotype associations. *Mol Genet Metab* **125,** 266-275.

Roberts TA, Price AN, Jackson LH, Taylor V, David AL, Lythgoe MF & Stuckey DJ. (2017). Direct comparison of high-temporal-resolution CINE MRI with Doppler ultrasound for assessment of diastolic dysfunction in mice. *NMR Biomed* **30**.

Robinson EL, Baker AH, Brittan M, McCracken I, Condorelli G, Emanueli C, Srivastava KP, Gaetano C, Thum T, Vanhaverbeke M, *et al.* (2021). Dissecting the transcriptome in cardiovascular disease. *Cardiovasc Res*.

Roe CR, Millington DS, Maltby DA, Bohan TP & Hoppel CL. (1984). L-carnitine enhances excretion of propionyl coenzyme A as propionylcarnitine in propionic acidemia. *J Clin Invest* **73,** 1785-1788.

Romaine SPR, Tomaszewski M, Condorelli G & Samani NJ. (2015). MicroRNAs in cardiovascular disease: an introduction for clinicians. *Heart* **101,** 921.

Romano S, Valayannopoulos V, Touati G, Jais JP, Rabier D, de Keyzer Y, Bonnet D & de Lonlay P. (2010). Cardiomyopathies in propionic aciduria are reversible after liver transplantation. *J Pediatr* **156,** 128-134.

Rosa-Garrido M, Chapski DJ, Schmitt AD, Kimball TH, Karbassi E, Monte E, Balderas E, Pellegrini M, Shih TT, Soehalim E, *et al.* (2017). High-Resolution Mapping of

Chromatin Conformation in Cardiac Myocytes Reveals Structural Remodeling of the Epigenome in Heart Failure. *Circulation* **136,** 1613-1625.

Rosenberg LE, Lilljeqvist AC & Hsia YE. (1968). Methylmalonic aciduria. An inborn error leading to metabolic acidosis, long-chain ketonuria and intermittent hyperglycinemia. *N Engl J Med* **278,** 1319-1322.

Roussel J, Champeroux P, Roy J, Richard S, Fauconnier J, Le Guennec JY & Thireau J. (2016). The Complex QT/RR Relationship in Mice. *Sci Rep* **6,** 25388.

Runte KE, Bell SP, Selby DE, Haussler TN, Ashikaga T, LeWinter MM, Palmer BM & Meyer M. (2017). Relaxation and the Role of Calcium in Isolated Contracting Myocardium From Patients With Hypertensive Heart Disease and Heart Failure With Preserved Ejection Fraction. *Circ Heart Fail* **10,** 1-15.

Sabari BR, Zhang D, Allis CD & Zhao Y. (2017). Metabolic regulation of gene expression through histone acylations. *Nat Rev Mol Cell Biol* **18,** 90-101.

Sadhukhan S, Liu X, Ryu D, Nelson OD, Stupinski JA, Li Z, Chen W, Zhang S, Weiss RS, Locasale JW, *et al.* (2016). Metabolomics-assisted proteomics identifies succinylation and SIRT5 as important regulators of cardiac function. *Proc Natl Acad Sci U S A* **113,** 4320-4325.

Saegusa N, Moorhouse E, Vaughan-Jones RD & Spitzer KW. (2011). Influence of pH on Ca^{2+} current and its control of electrical and Ca^{2+} signaling in ventricular myocytes. *J Gen Physiol* **138,** 537-559.

Sah R, Ramirez RJ, Oudit GY, Gidrewicz D, Trivieri MG, Zobel C & Backx PH. (2003). Regulation of cardiac excitation-contraction coupling by action potential repolarization: role of the transient outward potassium current (I(to)). *J Physiol* **546,** 5-18.

Salama G & Bett GC. (2014). Sex differences in the mechanisms underlying long QT syndrome. *Am J Physiol Heart Circ Physiol* **307,** H640-648.

Salway JG. (2017). *Metabolism at a Glance (4th edn)*. Wiley Blackwell.

Samsa LA, Yang B & Liu J. (2013). Embryonic cardiac chamber maturation: Trabeculation, conduction, and cardiomyocyte proliferation. *Am J Med Genet C Semin Med Genet* **163c,** 157-168.

Sandireddy R, Cibi DM, Gupta P, Singh A, Tee N, Uemura A, Epstein JA & Singh MK. (2019). Semaphorin 3E/PlexinD1 signaling is required for cardiac ventricular compaction. *JCI Insight* **4,** e125908.

Santana LF, Cheng EP & Lederer WJ. (2010). How does the shape of the cardiac action potential control calcium signaling and contraction in the heart? *J Mol Cell Cardiol* **49,** 901-903.

Sauer SW, Okun JG, Hoffmann GF, Koelker S & Morath MA. (2008). Impact of short- and medium-chain organic acids, acylcarnitines, and acyl-CoAs on mitochondrial energy metabolism. *Biochimica et biophysica acta* **1777,** 1276-1282.

Schiattarella GG, Altamirano F, Tong D, French KM, Villalobos E, Kim SY, Luo X, Jiang N, May HI, Wang ZV, *et al.* (2019). Nitrosative stress drives heart failure with preserved ejection fraction. *Nature* **568,** 351-356.

Schneider CA, Rasband WS & Eliceiri KW. (2012). NIH Image to ImageJ: 25 years of image analysis. *Nat Methods* **9,** 671-675.

Schnelle M, Catibog N, Zhang M, Nabeebaccus AA, Anderson G, Richards DA, Sawyer G, Zhang X, Toischer K, Hasenfuss G, *et al.* (2018). Echocardiographic evaluation of diastolic function in mouse models of heart disease. *J Mol Cell Cardiol* **114,** 20-28.

Scholl-Bürgi S, Sass JO, Zschocke J & Karall D. (2012). Amino acid metabolism in patients with propionic acidaemia. *J Inherit Metab Dis* **35,** 65-70.

Schonichen A, Webb BA, Jacobson MP & Barber DL. (2013). Considering protonation as a posttranslational modification regulating protein structure and function. *Annu Rev Biophys* **42,** 289-314.

Schroder E, Byse M & Satin J. (2009). L-type calcium channel C terminus autoregulates transcription. *Circ Res* **104,** 1373-1381.

Schwab MA, Sauer SW, Okun JG, Nijtmans LGJ, Rodenburg RJT, van den Heuvel LP, Dröse S, Brandt U, Hoffmann GF, Ter Laak H, *et al.* (2006). Secondary mitochondrial dysfunction in propionic aciduria: a pathogenic role for endogenous mitochondrial toxins. *Biochem J* **398,** 107-112.

Seymour AM, Giles L, Ball V, Miller JJ, Clarke K, Carr CA & Tyler DJ. (2015). In vivo assessment of cardiac metabolism and function in the abdominal aortic banding model of compensated cardiac hypertrophy. *Cardiovasc Res* **106,** 249-260.

Shattock MJ, Ottolia M, Bers DM, Blaustein MP, Boguslavskyi A, Bossuyt J, Bridge JHB, Chen-Izu Y, Clancy CE, Edwards A, *et al.* (2015). Na+/Ca2+ exchange and Na+/K+-ATPase in the heart. *J Physiol* **593,** 1361-1382.

Shattock MJ, Park KC, Yang HY, Lee AWC, Niederer S, MacLeod KT & Winter J. (2017). Restitution slope is principally determined by steady-state action potential duration. *Cardiovasc Res* **113,** 817-828.

Shechter D, Dormann HL, Allis CD & Hake SB. (2007). Extraction, purification and analysis of histones. *Nat Protoc* **2,** 1445-1457.

Sikkel MB, Francis DP, Howard J, Gordon F, Rowlands C, Peters NS, Lyon AR, Harding SE & MacLeod KT. (2017). Hierarchical statistical techniques are necessary to draw reliable conclusions from analysis of isolated cardiomyocyte studies. *Cardiovasc Res* **113,** 1743-1752.

Siliprandi N, Di Lisa F & Menabò R. (1991). Propionyl-L-carnitine: biochemical significance and possible role in cardiac metabolism. *Cardiovascular drugs and therapy* ***5* Suppl 1,** 11-15.

Simithy J, Sidoli S, Yuan ZF, Coradin M, Bhanu NV, Marchione DM, Klein BJ, Bazilevsky GA, McCullough CE, Magin RS, *et al.* (2017). Characterization of histone acylations links chromatin modifications with metabolism. *Nat Commun* **8,** 1141.

Sivanand S, Viney I & Wellen KE. (2018). Spatiotemporal Control of Acetyl-CoA Metabolism in Chromatin Regulation. *Trends Biochem Sci* **43,** 61-74.

Smith GL & Eisner DA. (2019). Calcium Buffering in the Heart in Health and Disease. *Circulation* **139,** 2358-2371.

Steliou K, Boosalis MS, Perrine SP, Sangerman J & Faller DV. (2012). Butyrate Histone Deacetylase Inhibitors. *Biores Open Access* **1,** 192-198.

Stuckey DJ, Carr CA, Tyler DJ & Clarke K. (2008). Cine-MRI versus two-dimensional echocardiography to measure in vivo left ventricular function in rat heart. *NMR Biomed* **21,** 765-772.

Sun B, Leem CH & Vaughan-Jones RD. (1996). Novel chloride-dependent acid loader in the guinea-pig ventricular myocyte: part of a dual acid-loading mechanism. *J Physiol* **495,** 65-82.

Sun S, Li H, Chen J & Qian Q. (2017). Lactic Acid: No Longer an Inert and End-Product of Glycolysis. *Physiology* **32,** 453-463.

Sutton VR, Chapman KA, Gropman AL, MacLeod E, Stagni K, Summar ML, Ueda K, Ah Mew N, Franks J, Island E, *et al.* (2012). Chronic management and health supervision of individuals with propionic acidemia. *Mol Genet Metab* **105,** 26-33.

Swietach P, Spitzer KW & Vaughan-Jones RD. (2010). Modeling calcium waves in cardiac myocytes: importance of calcium diffusion. *Front Biosci (Landmark Ed)* **15,** 661-680.

Swoap SJ, Li C, Wess J, Parsons AD, Williams TD & Overton JM. (2008). Vagal tone dominates autonomic control of mouse heart rate at thermoneutrality. *Am J Physiol Heart Circ Physiol* **294,** H1581-1588.

Takimoto E & Kass DA. (2007). Role of oxidative stress in cardiac hypertrophy and remodeling. *Hypertension* **49,** 241-248.

Tamayo M, Fulgencio-Covian A, Navarro-Garcia JA, Val-Blasco A, Ruiz-Hurtado G, Gil-Fernandez M, Martin-Nunes L, Lopez JA, Desviat LR, Delgado C, *et al.* (2020).

Intracellular calcium mishandling leads to cardiac dysfunction and ventricular arrhythmias in a mouse model of propionic acidemia. *Biochim Biophys Acta Mol Basis Dis* **1866,** 165586.

Tan NS, Bajaj RR, Morel C & Singh SM. (2018). Metabolic cardiomyopathy from propionic acidemia precipitating cardiac arrest in a 25-year-old man. *CAMJ* **190,** E883.

Tanaka K, Budd MA, Efron ML & Isselbacher KJ. (1966). Isovaleric acidemia: a new genetic defect of leucine metabolism. *Proc Natl Acad Sci U S A* **56,** 236-242.

Tang WHW, Li DY & Hazen SL. (2019). Dietary metabolism, the gut microbiome, and heart failure. *Nat Rev Cardiol* **16,** 137-154.

Taverna SD, Li H, Ruthenburg AJ, Allis CD & Patel DJ. (2007). How chromatin-binding modules interpret histone modifications: lessons from professional pocket pickers. *Nat Struct Mol Biol* **14,** 1025-1040.

Thireau J, Zhang BL, Poisson D & Babuty D. (2008). Heart rate variability in mice: a theoretical and practical guide. *Exp Physiol* **93,** 83-94.

Trafford AW, Diaz ME & Eisner DA. (1999). A novel, rapid and reversible method to measure Ca buffering and time-course of total sarcoplasmic reticulum Ca content in cardiac ventricular myocytes. *Pflugers Arch* **437,** 501-503.

Trefely S, Lovell CD, Snyder NW & Wellen KE. (2020). Compartmentalised acyl-CoA metabolism and roles in chromatin regulation. *Mol Metab* **38,** 100941.

Tyler DJ, Lygate CA, Schneider JE, Cassidy PJ, Neubauer S & Clarke K. (2006). CINE-MR imaging of the normal and infarcted rat heart using an 11.7 T vertical bore MR system. *J Cardiovasc Magn Reson* **8,** 327-333.

Ugarte M, Perez-Cerda C, Rodriguez-Pombo P, Desviat LR, Perez B, Richard E, Muro S, Campeau E, Ohura T & Gravel RA. (1999). Overview of mutations in the PCCA and PCCB genes causing propionic acidemia. *Hum Mutat* **14,** 275-282.

Ussher JR, Elmariah S, Gerszten RE & Dyck JR. (2016). The Emerging Role of Metabolomics in the Diagnosis and Prognosis of Cardiovascular Disease. *J Am Coll Cardiol* **68,** 2850-2870.

Valero-Munoz M, Backman W & Sam F. (2017). Murine Models of Heart Failure with Preserved Ejection Fraction: a "Fishing Expedition". *JACC Basic Transl Sci* **2,** 770-789.

van Heerebeek L, Hamdani N, Falcão-Pires I, Leite-Moreira AF, Begieneman MP, Bronzwaer JG, van der Velden J, Stienen GJ, Laarman GJ, Somsen A, *et al.* (2012). Low myocardial protein kinase G activity in heart failure with preserved ejection fraction. *Circulation* **126,** 830-839.

van Rooij E & Olson EN. (2012). MicroRNA therapeutics for cardiovascular disease: opportunities and obstacles. *Nat Rev Drug Discov* **11,** 860-872.

van Steensel B & Furlong EEM. (2019). The role of transcription in shaping the spatial organization of the genome. *Nat Rev Mol Cell Biol* **20,** 327-337.

Vara R, Turner C, Mundy H, Heaton ND, Rela M, Mieli-Vergani G, Champion M & Hadzic N. (2011). Liver transplantation for propionic acidemia in children. *Liver Transpl* **17,** 661-667.

Varró A, Tomek J, Nagy N, Virag L, Passini E, Rodriguez B & Baczkó I. (2020). Cardiac Transmembrane Ion Channels and Action Potentials: Cellular Physiology and Arrhythmogenic Behavior. *Physiol Rev*.

Vaughan-Jones RD, Spitzer KW & Swietach P. (2009). Intracellular pH regulation in heart. *J Mol Cell Cardiol* **46,** 318-331.

Vichai V & Kirtikara K. (2006). Sulforhodamine B colorimetric assay for cytotoxicity screening. *Nat Protoc* **1,** 1112-1116.

Wakabayashi S, Hisamitsu T & Nakamura TY. (2013). Regulation of the cardiac Na^+/H^+ exchanger in health and disease. *J Mol Cell Cardiol* **61,** 68-76.

Waldecker M, Kautenburger T, Daumann H, Busch C & Schrenk D. (2008). Inhibition of histone-deacetylase activity by short-chain fatty acids and some polyphenol metabolites formed in the colon. *J Nutr Biochem* **19,** 587-593.

Walsby-Tickle J, Gannon J, Hvinden I, Bardella C, Abboud MI, Nazeer A, Hauton D, Pires E, Cadoux-Hudson T, Schofield CJ, *et al.* (2020). Anion-exchange chromatography mass spectrometry provides extensive coverage of primary metabolic pathways revealing altered metabolism in IDH1 mutant cells. *Commun Biol* **3,** 247.

Wang Y, Christopher BA, Wilson KA, Muoio D, McGarrah RW, Brunengraber H & Zhang GF. (2018). Propionate-induced changes in cardiac metabolism, notably CoA trapping, are not altered by l-carnitine. *Am J Physiol Endocrinol Metab* **315,** E622-e633.

Wang Z, Gerstein M & Snyder M. (2009). RNA-Seq: a revolutionary tool for transcriptomics. *Nat Rev Genet* **10,** 57-63.

Waters D, Adeloye D, Woolham D, Wastnedge E, Patel S & Rudan I. (2018). Global birth prevalence and mortality from inborn errors of metabolism: a systematic analysis of the evidence. *J Glob Health* **8,** 021102-021102.

Watkins H, Ashrafian H & Redwood C. (2011). Inherited cardiomyopathies. *N Engl J Med* **364,** 1643-1656.

Wehrens XH, Kirchhoff S & Doevendans PA. (2000). Mouse electrocardiography: an interval of thirty years. *Cardiovasc Res* **45,** 231-237.

Wikoff WR, Gangoiti JA, Barshop BA & Siuzdak G. (2007). Metabolomics identifies perturbations in human disorders of propionate metabolism. *Clin Chem* **53,** 2169-2176.

Wilson KA, Han Y, Zhang M, Hess JP, Chapman KA, Cline GW, Tochtrop GP, Brunengraber H & Zhang GF. (2017). Inter-relations between 3-hydroxypropionate and propionate metabolism in rat liver: relevance to disorders of propionyl-CoA metabolism. *Am J Physiol Endocrinol Metab* **313,** E413-e428.

Winter J & Shattock MJ. (2016). Geometrical considerations in cardiac electrophysiology and arrhythmogenesis. *Europace* **18,** 320-331.

Wishart DS, Feunang YD, Marcu A, Guo AC, Liang K, Vázquez-Fresno R, Sajed T, Johnson D, Li C, Karu N, *et al.* (2018). HMDB 4.0: the human metabolome database for 2018. *Nucleic Acids Res* **46,** D608-d617.

Wolf B, Hsia YE, Sweetman L, Gravel R, Harris DJ & Nyhan WL. (1981). Propionic acidemia: A clinical update. *J Pediatr* **99,** 835-846.

Wong JM, de Souza R, Kendall CW, Emam A & Jenkins DJ. (2006). Colonic health: fermentation and short chain fatty acids. *J Clin Gastroenterol* **40,** 235-243.

Wongkittichote P, Ah Mew N & Chapman KA. (2017). Propionyl-CoA carboxylase - A review. *Mol Genet Metab* **122,** 145-152.

Wu X, Zhang T, Bossuyt J, Li X, McKinsey TA, Dedman JR, Olson EN, Chen J, Brown JH & Bers DM. (2006). Local InsP3-dependent perinuclear Ca2+ signaling in cardiac myocyte excitation-transcription coupling. *J Clin Invest* **116,** 675-682.

Wysocka MB, Pietraszek-Gremplewicz K & Nowak D. (2018). The Role of Apelin in Cardiovascular Diseases, Obesity and Cancer. *Front Physiol* **9,** 557-557.

Yan K, Rousseau J, Machol K, Cross LA, Agre KE, Gibson CF, Goverde A, Engleman KL, Verdin H, De Baere E, *et al.* (2020). Deficient histone H3 propionylation by BRPF1-KAT6 complexes in neurodevelopmental disorders and cancer. *Sci Adv* **6,** eaax0021.

Zacchigna S, Paldino A, Falcão-Pires I, Daskalopoulos EP, Dal Ferro M, Vodret S, Lesizza P, Cannatà A, Miranda-Silva D, Lourenço AP, *et al.* (2021). Towards standardization of echocardiography for the evaluation of left ventricular function in adult rodents: a position paper of the ESC Working Group on Myocardial Function. *Cardiovasc Res* **117,** 43-59.

Zaccolo M & Movsesian MA. (2007). cAMP and cGMP signaling cross-talk: role of phosphodiesterases and implications for cardiac pathophysiology. *Circ Res* **100,** 1569-1578.

Zhang D, Tang Z, Huang H, Zhou G, Cui C, Weng Y, Liu W, Kim S, Lee S, Perez-Neut M, *et al.* (2019). Metabolic regulation of gene expression by histone lactylation. *Nature* **574,** 575-580.

Zheng H & Xie W. (2019). The role of 3D genome organization in development and cell differentiation. *Nat Rev Mol Cell Biol* **20,** 535-550.

Zhou B & Tian R. (2018). Mitochondrial dysfunction in pathophysiology of heart failure. *J Clin Invest* **128,** 3716-3726.

Zile MR & Gaasch WH. (2011). Abnormal calcium homeostasis: one mechanism in diastolic heart failure. *J Am Coll Cardiol* **58,** 155-157.

Zwickler T, Riderer A, Haege G, Hoffmann GF, Kolker S & Burgard P. (2014). Usefulness of biochemical parameters in decision-making on the start of emergency treatment in patients with propionic acidemia. *J Inherit Metab Dis* **37,** 31-37.

Appendix: research during the COVID-19 pandemic

Sadly, during the final year of this DPhil, the world was hit by the COVID-19 pandemic. The SARS-CoV-2 coronavirus had a catastrophic impact on humankind and has led to (and still causing at the time of writing), a dramatic loss of human life worldwide. The world was met by unprecedented challenges to public health and the economy. At the height of the pandemic, the only way to control infection rates was to initiate a lockdown and for people to stay isolated in their homes. Isolation posed an extraordinary challenge to people's way of life and their mental health. However, this challenge was met by the astonishing kindness, generosity and resilience that is inherent to every human.

One of the greatest achievements in science, will forever be the development and validation of safe vaccines against SARS-CoV-2, at an extraordinary timescale. Never before has the scientific community come together at such haste and homed in on a single goal.

A key clinical feature of the SARS-CoV-2 infection is severe hypoxaemia, often in the presence of normal lung mechanics. In 2020, several research groups had proposed that a derangement of convective O_2 transport by red blood cells (RBCs) was an explanation for COVID-19 hypoxaemia. However, this had not been tested, and it was unknown whether RBC O_2 handling by was affected by SARS-CoV2. Around that time, our research group had developed single-cell oxygen saturation imaging, to assess O_2 handling at the single-cell level (Richardson *et al*. *Proc Natl Acad Sci USA* 2020). After suspending my DPhil studies for a Term, this method was applied to examine O_2 handling in RBCs from SARS-CoV-2 patients. A challenge was developing a protocol that would ensure our safety and inactivate the virus, whilst preserving RBC function. In our study, RBC O_2 unloading kinetics, O_2 binding capacity, and RBC radius were not different in COVID-19 patients, compared to healthy volunteers. We concluded the cause of hypoxaemia in COVID-19 patients is unlikely to be related to impaired RBC O_2 handling. This publication (Park *et al. Br J Haem* 2020) is attached to the Appendix of this thesis.

It was a privilege to be a scientist at the time of COVID-19 and to be able to contribute to the global research effort.